Dissertation

submitted to the

Combined Faculty of Natural Sciences and Mathematics

of Heidelberg University, Germany

for the degree of

Doctor of Natural Sciences

Put forward by

Robert Mark Chojowski

born in Ludwigshafen am Rhein

Oral examination: 23.01.2024

Elastic phase field approach for modelling cell mechanics and mechanotransduction

Referees: Prof. Dr. Ulrich S. Schwarz

Prof. Dr. Tristan Bereau

Elastic phase field approach for modelling cell mechanics and mechanotransduction

Biological cells constantly sense and adapt to the mechanical properties of their environment. While traditionally the cytoskeleton has been considered to be the prime determinant of cell mechanics, more recently it has been shown that the nucleus is also an essential element. In this thesis, we propose continuum models to investigate the effect of nuclear rigidity on whole-cell elasticity, the mechanosensitive accumulation of proteins in the nucleus as well as the formation of thick cytoskeletal filament bundles, so-called stress fibres. These aspects are modelled using a diffuse interface approach, the phase field method, coupled to standard elasticity theory and are numerically solved by a combination of spectral and matrix methods. First, we demonstrate the applicability of the approach to standard biological situations of single cells and cell monolayers without internal structures. We than extent it for single cells to include a nucleus and illustrate that nuclear mechanics has important implications on the mechanical response of cells for a selection of relevant situations. Combining this method with a reaction-diffusion system, we propose a model that shows that nuclear rigidity affects nuclear protein import. Lastly, we present a continuum model for the mechanosensitive formation of stress fibres by coupling a dynamic nematic order parameter tensor, as suggested by liquid crystal theory, to the elastic phase field method. This combined model can qualitatively capture prominent experimental observations. In conclusion, we developed a versatile continuum framework that can describe and quantify several important effects of mechanobiology.

Elastische Phasenfeldmethode zur Modellierung von Zellmechanik und Mechanotransduktion

Biologische Zellen nehmen ständig die mechanischen Eigenschaften ihrer Umgebung wahr und passen sich diesen an. Während traditionell das Zytoskelett als bestimmend für die Zellmechanik angesehen wurde, hat sich in jüngster Zeit gezeigt, dass auch der Zellkern ein wesentliches Element ist. In dieser Arbeit schlagen wir Kontinuumsmodelle vor, um die Auswirkung der Zellkernsteifigkeit auf die Elastizität der ganzen Zelle, die mechanosensitive Anreicherung von Proteinen im Zellkern sowie die Bildung von dicken Filamentbündeln des Zytoskeletts, sogenannten Stressfasern, zu untersuchen. Diese Aspekte werden mit der Phasenfeldmethode modelliert, welche an die lineare Elastizitätstheorie gekoppelt ist. Die Modellgleichungen werden numerisch durch eine Kombination aus Spektral- und Matrixmethoden gelöst. Wir demonstrieren die Anwendbarkeit dieser Methode auf biologische Standardsituationen von Einzelzellen und Zellmonoschichten ohne interne Strukturen. Anschließend erweitern wir die Methode für Einzelzellen um einen Zellkern und zeigen für eine Auswahl relevanter Situationen, dass die Kernmechanik wichtige Auswirkungen auf die mechanische Reaktion von Zellen hat. Dieses Modell kombinieren wir mit einem Reaktions-Diffusions-System und schlagen so ein Modell vor, das zeigt, dass die Kernsteifigkeit den Import von Proteinen in den Zellkern beeinflusst. Schließlich stellen wir ein Kontinuumsmodell für die mechanosensitive Bildung von Spannungsfasern vor, indem wir einen dynamischen nematischen Ordnungstensor, wie er von der Flüssigkristalltheorie vorgeschlagen wird, mit der elastischen Phasenfeldmethode koppeln. Dieses kombinierte Modell kann prominente experimentelle Beobachtungen qualitativ erfassen. In Summe, haben wir eine vielseitiges Kontinuumsmethode entwickelt, mit dem wichtige Effekte der Mechanobiologie beschrieben und quantifiziert werden können.

Contents

List of Figures

List of Tables

List of Abbreviations

ADP . . . . . Adenosine diphosphate
ATP . . . . . Adenosine triphosphate
AFM . . . . . Atomic force microscopy
Arp2/3 . . . . . Actin related protein 2/3
DNA . . . . . Deoxyribonucleic acid
ECM . . . . . Extracellular matrix
FG nups . . . . . Phenylalanin-Glycin amino-acid polymers (nucleoporins)
GDP . . . . . Guanosine diphosphate
GTP . . . . . Guanosine triphosphate
INM . . . . . Inner nuclear membrane
LBR . . . . . Lamin B-receptor
LC . . . . . Liquid crystal
LINC . . . Linker of Nucleoskeleton and Cytoskeleton
MTOC Microtubule-organizing centre
nesprin . . . . nuclear envelope spectrin repeat protein
NE . . . . . Nuclear envelope
NES . . . . . Nuclear export signal
NPC . . . . . Nuclear pore complex
NLS . . . . . Nuclear localization signal
Nups . . . . . nucleoporins
NTF2 . . . . . Nuclear transport factor 2
ONM . . . . . Outer nuclear membrane
PNS . . . . . Perinuclear space
Ran . . . . . Ras-related nuclear protein
RanGAP . . . . . Ran GTPase-activating protein
RanGEF . . . . . Ran guanine nucleotide exchange factor
RanGDP Ran guanosine diphosphate
RanGTP Ran guanosine triphosphate
RCC1 . . . . . Regulator of chromosome condensation 1
RhoA . . Ras homolog family member A
SUN . . . . . Sad1p and UNC-84 protein
TAZ Transcriptional co-activator with PDZ-binding motif
YAP . . . . . Yes-associated protein 1

1 Introduction

Animal cells constantly interact with their environment to collect information on it and to rapidly react to changing physiological conditions. One important aspect are the material properties of the cellular surrounding. Force production by the cell itself and transmission of these forces to the outside allow it to sense the mechanical characteristics of the environment. The conversion of these mechanical stimuli into biochemical signals, termed mechanotransduction, then triggers adequate cellular responses.

A plethora of biological processes on a single cell and tissue scale are highly dependent on this informational pathway, like development, organogenesis and migration of immune cells, metastatic cancer cells or epithelial cells in wound healing. The correct perception of and adaptability to mechanical cues by individual cells and cell collectives scales up to be vital for complex multicellular organisms such as the human body with its approximately 10^{13} cells [1]. Dysfunctions often result in diseases and the progression of malignancies, which can ultimately lead to death [2].

Although more light has been shed on the role of cell and environmental mechanics in various biological processes, many questions still remain unanswered. In particular, how individual cellular substructures impact whole-cell rheology. It is nowadays well-known, that the main determinant of cell mechanics is the cytoskeleton, a highly cross-linked but dynamic polymer network, giving the cell stability while at the same time allowing a fast cellular reaction to the outside world. Nevertheless, certain aspects of the mechanisms guiding the formation of thick contractile polymer bundles, called stress fibres, and their mechanical feedback within a cell, are still not fully understood.

Over the last years, the mechanics of a second cellular structure has attracted a lot of attention: the cell nucleus. Due to its prominent role as the container of a cell's genetic information, nuclear influence on whole-cell mechanics has been overlooked for a long time. However, there is an increasing amount of evidence of a dramatic impact of the nucleus on cellular mechanical responses. Additionally, the discovery of physical connections between the cytoskeleton and the nucleus enabling direct transmission of mechanical stimuli to the gene expression machinery [3–5] manifests that cell rheology

and associated reactions cannot be considered without this cellular compartment.

Recently, it has also been shown that nuclear deformations and arising tensions are involved in the opening of nuclear pores [6, 7], facilitating the influx of transcriptionally active proteins into and out of the nucleus; a major ingredient in mechanotransduction [8, 9].

Despite the thriving number of evidence for the biological and physical significance of the nucleus, models regarding whole-cell mechanics that specifically account for nuclear mechanical properties are still rare, often due to the lack of suitable theoretical modelling frameworks.

In this thesis, we aim to contribute a versatile modelling approach for cell mechanics, including internal cell structures, in stationary as well as dynamic situations. Our modelling framework of choice is the so-called phase field method, an efficient approach for treating deformable and/or moving boundary problems. We use a formulation able to describe full (reversible) elasticity and show its application to the cases of single cells and cohesive cell monolayers [10]. Further, we incorporate an elastic nucleus, studying its effect on whole-cell mechanics and the implications of associated nuclear straining on the spatio-temporal transport of molecules through the nuclear boundary. Lastly, we consider the mechanosensitive reorganization of the cytoskeleton, especially regarding the formation of stress fibres and their feedback on cell elasticity.

Outline of the thesis

In **Chapter 2**, the biological background on the structural mechanics of cells is presented, by introducing the cytoskeleton and the nucleus. The three major polymeric structures of the cytoskeleton (actin cytoskeleton, intermediate filaments and microtubules) are discussed, with focus on the actin cytoskeleton. Especially stress fibres as distinct mechanical elements in cells will be of importance in one of the projects discussed later.

Regarding the nucleus, the composition of its envelope and interior are outlined. Here, the structure of nuclear pore complexes (NPCs) and the protein transport mechanism through them is of special interest.

Following the biological background, we give an overview on the theory of continuum mechanics, specializing to linear elasticity, which provides the theoretical basis for describing cell deformations.

Chapter 3 introduces the phase field approach, a diffuse interface method, used for modelling the problems of interest throughout this thesis. The idea of interface-based

methods and the basics of the phase field method are presented.

Next, in **Chapter 4**, we continue with the presentation of our developed *reversible elastic phase field approach* [10]. First, we explain why the standard formulation of coupling phase field dynamics and elasticity is not able to describe elastic reversibility. This means, when a deforming force is removed from a modelled elastic object, the deformation does not go back and the object does not return to its undeformed reference state. We then present an alternative approach in two-dimensions, which accounts for this reversibility, and apply it to paradigmatic geometries for single cells and cell monolayers, both to verify the correct description of elasticity and for demonstrating its applicability.

In **Chapter 5**, we propose a two-phase field approach, extending the one of Chapter 4 for modelling elastic cells with an internal compartment representing the nucleus. Using analytical solutions, we again verify that this approach correctly describes elastic behaviour. Subsequently, we examine the mechanical effect of an elastic nucleus in a selection of biologically highly relevant situations and experimental setups, ranging from spread cells in varying adhesion geometries to the description of cell compression between two plates and micropipette aspiration. For the latter two, the model is used to extract effective moduli of the cell-nucleus composite.

Complementing the model from the previous part, **Chapter 6** focuses on modelling the nucleocytoplasmic import of proteins in mechanically strained cells. Here, a system of reaction-diffusion equations is employed and coupled to the elastic phase field method in order to model mechanosensitive protein import into the nucleus. The sensitivity of the transport process to nuclear rigidity is explored for spread cells.

Chapter 7 shifts the focus from the nucleus to the cytoskeleton. Here, a continuum theory for nematic liquid crystals is used to describe the cytoskeletal reorganization and the formation of stress fibres in response to stress. We model contractile cells adhered to well-defined geometries and show that the presented continuum approach captures qualitative experimental observations regarding the assembly of stress fibres, *i.e.* the regions of their occurrence and alignment direction. Further, a mechanical feedback of those structures on the elastic properties of the cell are included.

We close in **Chapter 8** with a general discussion and prospects on further interesting applications.

2 Structural mechanics of cells

Cell mechanics and a cell's ability to sense environmental mechanical properties allow a cell to adequately respond to its surrounding, which is essential in a large number of biological processes. Substrate stiffness has been shown to influence the spreading behaviour of cells, evoking larger spread areas on stiffer substrates [11–13]. Migratory cells are guided by the properties of their environment [14], *e.g.* tending to move in the direction of increasing stiffness, a phenomenon termed durotaxis [15–17]. Furthermore, cells are known to adapt their stiffness to the rigidity of their environment [18, 19], which is also observed in the differentiation of stem cells [20, 21]. Having different mechanical characteristics than the environment may also be advantageous for cells. Special cell types, like migratory immune and cancer cells, respond to increased confinement by softening to facilitate their migration through constrictions [22], making cellular stiffness a marker for determining the malignancy of cancer cells [23].

The importance of the interplay between cells and their neighbourhood extends to tissues, where organogenesis [24], tissue homeostasis [25] and collective cell migration in wound healing [26, 27] are to a high degree mechanically driven and organized [28, 29].

What determines cellular mechanics? The interior of a cell is a highly heterogeneous and crowded environment, containing many different structures and an elusive number of proteins [1]. Three of these structures have a major influence on cellular mechanical properties and the process of mechanotransduction[1]: the cell plasma membrane, the cytoskeleton (a cross-linked polymer network) and the nucleus (containing the genetic information of a cell). The cell plasma membrane is a 4 nm thick [1] phospholipid bilayer containing many proteins and which separates the interior of the cell from the outside world [30]. As the outer envelope, it determines the volume and surface area of a cell. The plasma membrane affects cell mechanics mostly indirectly by guiding the formation of a mechanically stabilizing cytoskeletal cortex beneath it, which encloses the entire

[1] Mechanotransduction means the conversion of mechanical stimuli into biochemical information, possibly triggering a cellular response.

cell [31]. Main determinants of cellular rigidity are the cytoskeleton and the nucleus. Out of this relevance, an overview on both is given in this chapter.

2.1 The cell cytoskeleton

Cellular rigidity stems primarily from a stiff but at the same time dynamic polymer network spanning the entire cell: the cytoskeleton [32, 33].

It consists of three major polymeric substructures formed by actin filaments, intermediate filaments and microtubules (*cf.* Fig. 2.1). Their distinct physical and chemical properties are used by a cell to perform specialized tasks. Nevertheless, all three subsystems are highly interconnected and mutually influence each other [32, 34]. The cytoskeleton not only ensures the stability and integrity of cells and tissues under mechanical load, but also permits cells to exert forces, central to processes like mechanosensing, cell division or migration [32, 33, 35, 36]. Polymerization of cytoskeletal filaments can induce pushing forces, while their depolymerization and interplay with specific molecular motors can result in pulling forces [37]. Additionally, its reorganization capacity adjusts cell shape and mechanics to the properties of the extracellular environment [38–42].

In this section, we will provide an overview on the cytoskeletal substructures, particularly focusing on the actin cytoskeleton, which is the most relevant one in our context. Further information can be found in the literature this section is based on: for books and reviews on the cytoskeleton see Refs. [30, 32, 33, 37]; specialized reviews on actin filaments are Refs. [36, 43, 44]; for intermediate filaments see Refs. [45–47] and for microtubules see Refs. [48–51].

2.1.1 Actin cytoskeleton

The actin cytoskeleton is a generic term for different intracellular structures formed by so-called actin filaments, organized into networks and linear filament bundles (*cf.* Fig. 2.2) [30, 32]. Cell mechanics is mainly determined by the actin cytoskeleton, which is also central to cellular force generation [36, 43].

The basic subunit of actin filaments is the globular and polar protein actin (G-actin) [30]. Binding via non-covalent interactions, the actin monomers polymerize into two protofilaments wound around one another in parallel into a right-handed helix [30]. The resulting actin filament (also filamentous actin or F-actin) has a diameter of around 7 nm [30] (*cf.* Fig. 2.1 B left).

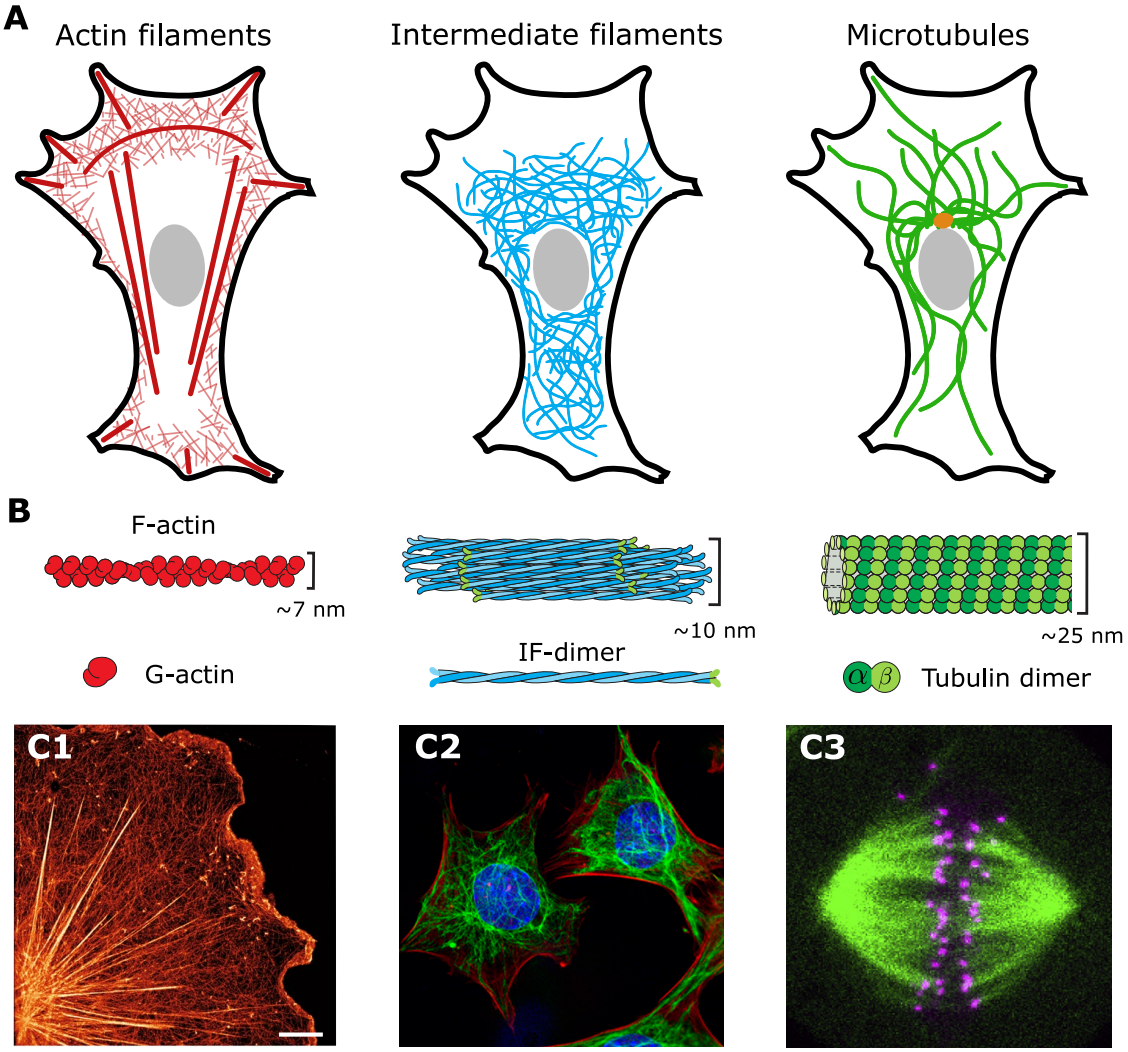

Figure 2.1: **A** Sketch of the three major polymeric substructures of the cell's cytoskeleton: actin filaments (left), intermediate filaments (middle) and microtubules (right). Actin filaments are organized into a highly cross-linked network (actin cortex) enveloping the whole cell and into thick bundles of filaments (stress fibres). Intermediate filaments are flexible polymers forming a network within the cell. Microtubules are very stiff, rod-like polymers originating at the microtubule-organizing centre (centrosome in orange). **B** Depiction of the molecular structure of the three cytoskeletal polymer types with their typical diameters. **C1** Super-resolution STORM microscopy image of the actin cytoskeleton (red), clearly showing the cortical network and thick stress fibres visible as bright, straight lines. **C2** Fluorescence microscopy image showing actin (red), intermediate filaments (green) and the nucleus (blue). **C3** Microtubule structure (green) observed during mitosis. This so-called mitotic spindle is anchored to chromatids and separates them during cell division. Panel **A** adpated from [34]; Panels in **B** adapted from [30]; **C1** taken from [52]; **C2** taken from [53]; **C3** adapted from [54].

Polymerization of actin is a non-equilibrium process [37], which is energetically fuelled by the hydrolysis of G-actin bound adenosine triphosphate (ATP) into adenosine diphosphate (ADP) during monomer association [30]. This lowers the binding affinity of G-actin, enabling a rapid assembly and disassembly of actin filaments [30]. In fact, the actin cytoskeleton can be reorganized by filament turnover on the time scales of minutes [35, 55].

As a consequence of the polarity of the monomers, actin filaments are also polar, which manifests itself in two structurally different ends: a fast growing *plus (barbed) end* and a slower growing *minus (pointed) end* [30]. When encountering a barrier, extending F-actin can exert pushing forces on the order of pN [1]. Filament growth can be stopped by capping proteins binding to the filament ends, inhibiting further monomer addition.

In the context of polymer mechanics, the resistance to bending is important and can be quantified by the persistence length l_p.[2] For actin $l_p \approx 10\,\mu\text{m}$ [1], making it semiflexible on the scale of a cell.

Actin networks

In cells, actin filaments are assembled into branched (partially aligned) networks or non-aligned networks, via a variety of cross-linking proteins connecting neighbouring filaments [44].

Most animal cells posses a thin and dense F-actin meshwork beneath the cell plasma membrane, also being physically connected to it, which wraps the whole cell [31]. This actin cortex has a thickness of tens to hundreds of nanometers, depending on the cell type, cell cycle stage as well as the actual adhesion geometry [31]. Cross-linkers such as filamin and non-muscle myosin II motor proteins provide physical connections between adjacent filaments in the generally non-aligned network [44].

Myosin II motors perform mechanical work by converting chemical energy in form of ATP [37]. Upon ATP consumption and hydrolysis, they move along actin filaments, sliding cross-linked and antiparallel aligned polymers against each other, leading to an effective contraction of the system and putting the cortex under tension. This cell contractility enables the cell to generate pulling forces [37]. In addition, the actin cortex is mainly responsible for cellular rigidity.

[2] The persistance length l_p measures the distance over which orientational correlations between subunits of the polymers are lost due to thermal fluctuations. Defined as $l_p = EI/k_BT$, it is linearly related to the Young's modulus (stiffness) E of the polymer, with area moment of inertia I, Boltzmann constant k_B and temperature T [56]. The product EI is the bending stiffness. Due to the above relation, l_p is commonly used as a measure for polymer flexibility.

During cell motility, the formation of a quasi-two dimensional planar network in the direction of migration, *i.e.* the leading edge of the cell, is initiated [30]. This so-called *lamellipodium* has a branched structure evoked by another important cross-linking protein, namely the actin related protein 2/3 complex (Arp2/3 complex) [30]. Binding to the side of an already present filament, it initiates the nucleation of a new one at an angle of 70° to the mother filament [44]. The pushing forces generated at the cell membrane result in the formation of a characteristic protrusion. Capping proteins regulate the polymerization dynamics [44]. The different association and dissociation rates at the ends of the actin filaments effectively transport the meshwork of the lamellipodium from the cell periphery towards the centre of the cell, where it depolymerizes, allowing a recycling of actin monomers at the leading edge. This phenomenon is known as *retrograde flow* [30]. Cell locomotion is the outcome of the interplay of the actin polymerization dynamics in the lamellipodium with intermingled myosin II motors and force transmission to the extracellular surrounding via adhesive connections [57].

Actin bundles - Stress fibres

In addition to these networks, actin can be organized into more discrete bundle-like structures. At the cell periphery, a small number of filaments bundled by fascin form filopodia; small finger-like protrusions with which a cell explores its vicinity [30].

Cells can also assemble thick actin bundles, also called *stress fibres* [58–63]. They consist of 10 to 30 highly aligned filaments, mainly tied together by α-actinin and myosin II minifilaments [60]. The diameter of these fibres is on the order of several hundred nanometres with intrafilament distances of around 35 to 50 nm, depending on the dimensions of the cross-linking proteins [62].

Three main classes of actin bundles can be distinguished: ventral stress fibres, dorsal stress fibres and transverse arcs (*cf.* Fig. 2.2 A) [58, 59, 61–63]. Their distinction is based on the number of fibre ends attached to the extracellular environment via so-called focal adhesions (*cf.* Sect. 2.1.3), their molecular structure and also location in the cell [58, 59, 61].

Ventral stress fibres are at both ends attached to a substrate and consist of antiparallel aligned actin filaments. They display a periodic pattern of α-actinin and myosin II, where the activity of the latter renders them contractile. These fibres can be polymerized from scratch at adhesive spots, *i.e.* their latter attachment points. Some ventral stress fibres span over the nucleus and are called *perinuclear actin caps*, constituting a

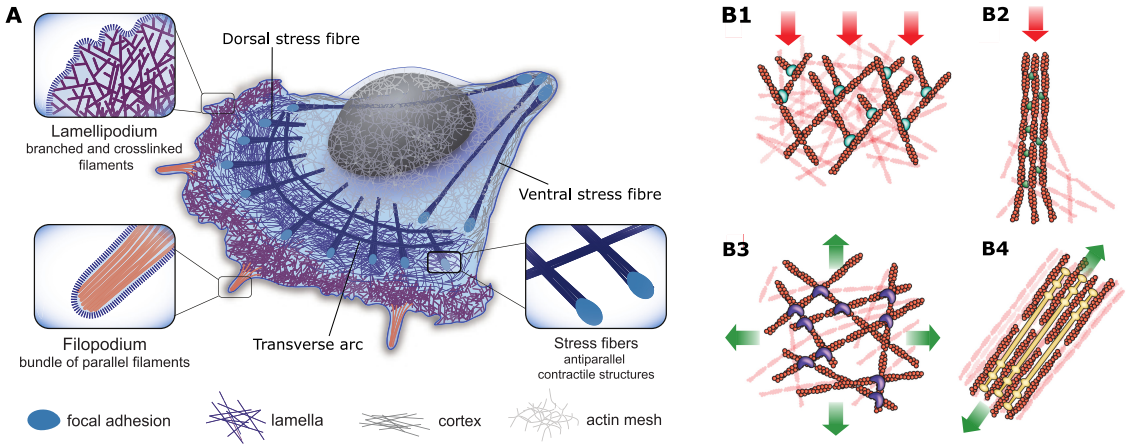

Figure 2.2: A The actin cytoskeleton is organized in different structures ranging from the lamellipodial and cortical networks to filament bundles like filopodia and various kinds of stress fibres. Some stress fibres can even span over the nucleus (in dark grey). These are called perinuclear caps. **B1**-**B4** Sketches of the different actin filament structures and the forces they are experiencing (compressive forces as red arrows and tensional forces as green arrows). **B1** Branched actin network as encountered in the lamellipodium of a migrating cell. The filaments are cross-linked by Arp 2/3. Upon encountering a barrier, such as the cell plasma membrane, the growing filaments lead to its protrusion and experience compressive forces due to mechanical resistance of the membrane. **B2** Filopodia are thin filament bundles cross-linked by fascin. When growing against the plasma membrane, they lead to slender protrusions, facing compressive forces. **B3** The actin cortex is located beneath the cell membrane and consists of non-aligned filaments interconnected via proteins like filamin and myosin II motors. The activity of the latter puts the network under tension. **B4** Stress fibres consist of highly aligned actin filaments bundled by α-actinin and myosin II minifilaments. Stress fibres containing myosin II motors encounter tensional forces. Panel **A** adapted from [55] and panels **B1**-**B4** adapted from [32].

subtype of ventral stress fibres [63].[3] Perinuclear actin caps have been shown to control the shape of the cell nucleus mediated by physical connections, so-called LINC complexes [4], transmitting forces to the nucleus (*cf.* Sect. 2.2.1) [5, 65]. This makes perinuclear actin caps crucial in the context of mechanotransduction.

Dorsal stress fibres primarily assemble at the leading edge of a migrating cell [60]. They are only with one end connected to a focal adhesion and extend into the cell interior, generally rising with their free end towards the upper cell surface (dorsal surface). In contrast to ventral stress fibres, they consist of parallel aligned actin filaments and do not contain myosin II motors, which makes them non-contractile.

The third member of the stress fibre family, transverse arcs, are not anchored di-

[3] Recently, Lehtimäki et al. [64] observed actin bundles, with a structure reminiscent to ventral stress fibres, forming predominantly beneath the nucleus. They suggested that these are a new type of actin bundles, which they named cortical stress fibres.

rectly to the ECM. Instead, they are connected to dorsal stress fibres, mediated by the cross-linker Arp2/3. With a similar molecular structure as ventral stress fibres, i.e. anti-paralell actin filaments and a periodic α-actinin-myosin II pattern, transverse arcs are contractile filament bundles. However, the generated forces are transmitted to the environment via the dorsal stress fibres and their focal adhesion points. Transverse arcs form at the leading edge of migratory cells and are transported towards to the cell centre by the growing dorsal stress fibres and the retrograde flow. Furthermore, these F-actin bundles are important for assembling new ventral stress fibres, as several transverse arcs can associate with a dorsal stress fibre to form a ventral one [66].

Mechanically, stress fibres are one of the most rigid structures within the cell with a tensile stiffness up to the MPa-range [67]. In general, their rigidity is limited by the load-bearing capacity of the cross-linking proteins, leading to a lower rigidity compared to single actin filaments [68]. Nevertheless, being multi-stranded makes them more stable against bending and breaking [37]. Their primary purpose is the absorption of mechanical stresses and the exertion of forces due to their internal tension. Actin stress fibres associated with focal adhesions have been shown to generate stresses of up to $5.5\,\mathrm{pN}/\mu\mathrm{m}^2$ [69].

In general, stress fibres assembly is a mechanosensitive process promoted by the protein RhoA regulating actin polymerization [70]. RhoA further promotes the activity of ROCK, which in turn stimulates myosin II motor activity [71] by mediating the phosphorylation of the myosin light chain (MLC) [58]. The latter drives focal adhesion and stress fibre assembly [70].

Although it appears that actin networks and bundles are separated structures, it has recently been demonstrated that they are highly connected and that stress fibres may even form out of the cortex by filament bundling [52].

2.1.2 Microtubules and intermediate filaments

Besides to the already complex actin cytoskeleton, cells posses subsystems of intermediate filaments and microtubules (*cf.* Fig. 2.1). In addition to their specific tasks, they also contribute to cellular morphology, mechanical properties and mechanosensing.

Microtubules

Microtubules are long and hollow cylinders, with outer and inner diameters of 25 nm and 17 nm, respectively [48, 49]. Due to their structure and persistence length of $l_p \geq 1$ mm

[1, 32, 48], they are the stiffest of all three cytoskeletal filament types [48].[4] Their mechanical stability makes them important in the context of preserving and supporting cell morphology, in particular protrusions like cilia and dendrites [48].

These long filaments originate in *microtubule-organizing centres* (MTOC)[5] and are polymerized from tubulin, a dimer of α- and β-tubulin, by weak non-covalent interactions [30]. Similar to ATP/ADP in actin polymerization, unbound tubulin contains a guanosine triphosphate (GTP) which is converted to guanosine diphosphate (GDP) upon binding, altering the affinity of tubulin [30]. Together, this allows microtubules to be assembled and dissembled easily and quickly. Microtubules are typically made of 13 to 16 protofilaments laterally bound together, forming the aforementioned cylindrical outline [47]. Due to the polarity of the tubulin monomers and their head-to-tail association, the resulting microtubule is also polar, with a faster growing and shrinking *plus end* and a slower *minus end* [30]. Characteristic for microtubule polymerization dynamics is a (stochastically) occurring rapid shrinkage of the polymer, termed *catastrophe*, which can subsequently change back to growth. This phenomenon is known as *dynamic instability* [73]. Microtubule assembly and disassembly can induce pushing and pulling forces in the pN-range [37], used in the organization of the cell interior by moving organelles. Nuclear positioning and the separation of sister chromatids during mitosis by the *mitotic spindle* are two examples [49]. In cell migration, the direction of motion is influenced by the microtubule distribution [51]. Moreover, they serve as transport routes for cargo by the motor proteins kinesin and dynein [30].

Intermediate filaments

The third cytoskeletal polymer type are intermediate filaments, representing a large protein family categorized in 5 major forms (type I to V). They can be found in the cytoplasm (type I to IV, like vimentin, desmin, keratin) as well as in the nucleus (type V, nuclear lamins A/C and B) [45–47]. Historically, the name 'intermediate filaments' refers to their characteristic diameter of 10 nm [30, 46] , with places them between actin filaments and microtubules.[6]

Structurally, their basic subunit are polar coiled-coil dimers, which can form a non-

[4] Nevertheless, microtubules are known to buckle under compressive load in cells, despite their rigidity [72].

[5] In most animal cells, this MTOC is the centrosome in the vicinity of the nucleus [30].

[6] Originally, the name referred to their diameter being in between the one of actin and myosin filaments in muscle [47, 74]. The references changed to actin and microtubules after the discovery of intermediate filaments in non-muscle cells [47]

polar tetramer by antiparallel and half-staggered binding [45, 46]. First, these tetramers rapidly form approx. 60 nm-long unit length fibres (ULFs), which then longitudinally associate to long, non-polar intermediate filaments [45, 46]. With a persistence length of $l_p \leq 1$ µm, they are more flexible than actin filaments and microtubules [30, 46, 47]. However, they are very extensible and can be strained to 3.5 times their original length, withstanding tensile stresses of up to 2 nN before breakage [45].

The main purpose of intermediate filaments is to assist the actin cytoskeleton in the absorption of externally applied stresses and the stabilization of cell shapes, also by adapting to the mechanical properties of the environment [45, 46]. A special role is attributed to nuclear lamins, which form a protective cage enclosing the DNA in the nuclear interior [75]. Cytoplasmic intermediate filaments are also assumed to take part in the process of mechanotransduction by being attached to the nucleus [46, 75]. Just like microtubules, these polymers are also involved in organizing the cell interior and directing cell motility [46]. Furthermore, they are indispensable for ensuring tissue integrity, where intermediate filament networks of neighbouring cells are connected by cell-cell junctions (desmosomes) [30, 45].

2.1.3 Cell adhesion

Cells sense and interact with the environment, for instance by chemical signals, exchanged through respective channels, or mechanical stimuli, transmitted by physical connections between the cytoskeleton and the cellular physiological surrounding. This can be the (three-dimensional) extracellular matrix (ECM), which is a network of polymers and proteins such as collagen and fibronectin, providing an anchoring substrate for the cell or neighbouring cells in a tissue [30].

Cell-matrix connections

Cell-matrix adhesion, termed focal adhesions, primarily involves the connection of the actin cytoskeleton with the ECM based on the transmembrane protein integrin (*cf.* Fig. 2.3 A) [30, 77]. On the cytoplasmic side, integrin is connected to actin filaments, in particular stress fibres [60], over adapter proteins such as vinculin and talin. Outside of the cell, it establishes links with complementary proteins like fibronectin in the ECM. Beginning with the formation of small and short-lived nascent adhesions (also known as focal complexes), these first precursors mature under mechanical load to fully grown focal adhesions. With these adhesion sites, cells are able to mechanically sense their

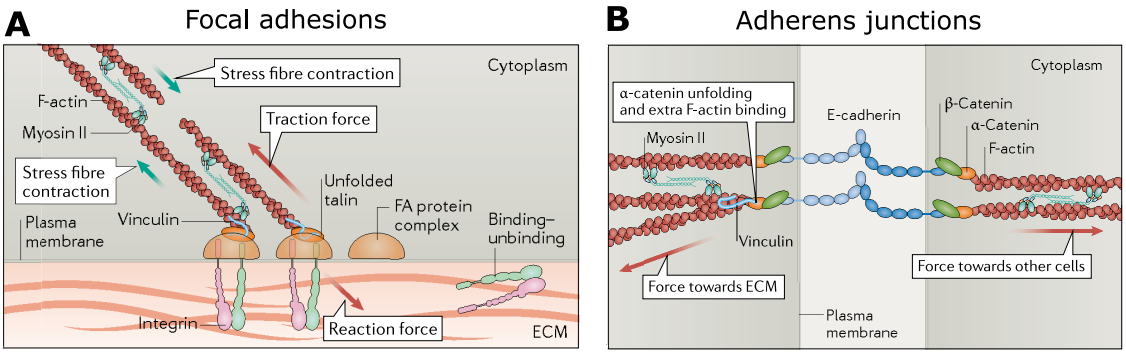

Figure 2.3: A Focal adhesions are protein complexes based on the transmembrane protein integrin and adapter proteins such as vinculin and talin. They connect the actin cytoskeleton, especially stress fibres, with the ECM. **B** Adherens junctions connect via the transmembrane protein E-cadherin and adaptor proteins, such as vinculin and catenin, the actin cytoskeletons of neighbouring cells. Adapted from [76].

surrounding and to migrate by transmitting internally generated forces and stresses to the outside. Cells are known to exert constant stresses of approximately 5.5 kPa per focal adhesion [69], also depending on the substrate stiffness, as this feeds back to the maturation state of stress fibres. Stiff substrates lead to larger *focal adhesions* and the assembly of thicker actin bundles generating larger forces.

In addition to focal adhesions, some cell types, like epithelial cells, also form links between intermediate filaments and the ECM. These connections are called hemidesmosomes and keep the cells tightly on the substrate.

Cell-cell connections

Neighbouring cells in a tissue establish mechanical connections between their cytoskeletons, based on the transmembrane protein cadherin, responsible for tissue cohesiveness (*cf.* Fig. 2.3 B) [30]. These so-called adherens junctions couple the actin cytoskeletons with each other, allowing force-based communication and sensing between neighbours [30]. Desmosomes connect the intermediate filament networks of neighbouring cells and are indispensable for tissue integrity [30]. Cell-cell adhesions are further important in the context of collective cell migration [78].

2.2 The cell nucleus

Single cell organisms are divided into two distinct groups: prokaryotes and eukaryotes. The central difference between both is that eukaryotic cells contain a large number of mostly membrane-enclosed substructures, which to a large part lack in prokaryotes [30].

The most prominent of all organelles in eukaryotic cells is the nucleus [79]. It is the largest cellular compartment, reaching a cell type-dependent diameter of 5 µm to 20 µm [79], typically occupying up to 30 % of the total cell volume [1, 80, 81]. However, not only its size makes it a distinct structure within a cell. With a mechanical stiffness 2 to 10-fold higher compared to the surrounding cytoskeleton and cytoplasm, the nucleus is one of the most rigid cellular structures [75, 82, 83].

The nucleus primarily serves as container of the cellular genetic information, separating it from the surrounding cytoplasm and the proteins therein, protecting it at the same time [30]. In recent years, it has become clear that nuclear mechanical properties are also important in many cellular processes, particularly in the context of mechanosensing [84, 85]. Direct physical connections between nucleus and cytoskeleton allow a nearly instantaneous transmission of forces to the nucleus [4, 5]. This leads to an influx of transcriptionally relevant proteins and the possible subsequent onset of biochemical cascades triggering gene expression and cellular reactions to the received mechanical stimuli [8, 86, 87].

Motivated by this importance of the nucleus, an overview on its structure, giving rise to its mechanical characteristics, is provided. Further, the mechanosensitive nuclear-cytoplasmic transport of proteins is described.

This section is based on Refs. [30, 75, 79, 88].

2.2.1 Building plan of the nucleus

The nuclear structure can be divided into two major parts: the interior, containing the DNA in form of densely packed chromatin, and the nuclear envelope as boundary layer.

Nuclear envelope

Cytoplasm and nuclear content, *i.e.* nucleoplasm and the DNA, are spatially separated by the nuclear envelope, which consists of two layers (*cf.* Fig. 2.4 A). The first peel are the outer and inner nuclear membrane, each having the well-known width of approximately 4 nm [75]. These two concentric lipid bilayers have a 20 nm to 50 nm wide lumen

between them, referred to as perinuclear space [75]. However, both membranes are contiguous as they are joined at pores, so-called nuclear pore complexes (NPC), perforating the nuclear envelope. The outer nuclear membrane is also continuously connected to the endoplasmic reticulum, which can serve as a membrane reservoir for the nuclear surface upon deformation [75]. Over this, inner and outer nuclear membrane serve as anchoring surfaces for a vast number of different proteins on the cytoplasmic as well as nucleoplasmic side.

The second layer, below the inner nuclear membrane, is the nuclear lamina. It is a 14 nm to 30 nm [75] thick and dense network of nuclear lamins (type V intermediate filaments), exclusive to the nucleus. Similar to the actin cortex being connected to the cell plasma membrane, this network is connected to the inner nuclear membrane by the protein emerin and mechanically stabilizes the nuclear envelope and therefore the whole nucleus.

Nuclear lamins have the characteristic 10 nm diameter of intermediate filaments [79]. The nuclear lamina of animal cells is formed by two types: the A-type lamin A and C and the B-type lamins B1 and B2. Both are forming separate meshworks, which are interconnected. Lamin-A/C is only expressed in fully differentiated cells. They are the load-bearing elements of the nuclear envelope, determining to a large part the stiffness of the nucleus, as has been shown by decreased nuclear rigidity in lamin-A/C knockdown cells. Furthermore, the lamin-A level in the nuclear lamina, and therefore the nuclear stiffness, positively correlates with the substrate rigidity guiding cell differentiation [89]. Lamins-A/C are mostly localized to the nuclear periphery, but were also found in the nuclear interior, where they are assumed to be involved in the positioning and stabilization of the chromatin structure. B-tpye lamins are present in all cells, i.e. also undifferentiated stem cells. They contribute little to the mechanics of the cell nucleus, however, they have a vital role in establishing the nuclear-cytoskeletal coupling.

In addition to the responsibility in determining nuclear mechanics and morphology, the nuclear lamina takes part in various biological processes such as cell division, differentiation, chromatin organization, DNA replication, and also DNA repair. Its physical connections to the cytoskeleton and also to the DNA structure in the nucleus, makes the lamina a key component in mechanotransduction. For unstressed nuclei (i.e. low nuclear surface tension), the nuclear envelope is wrinkled [90–93], providing an additional surface reservoir [75]. During mitosis, the nuclear envelope is disassembled, facilitating gene separation, and afterwards the nucleus and its envelope are rebuild [30, 94].

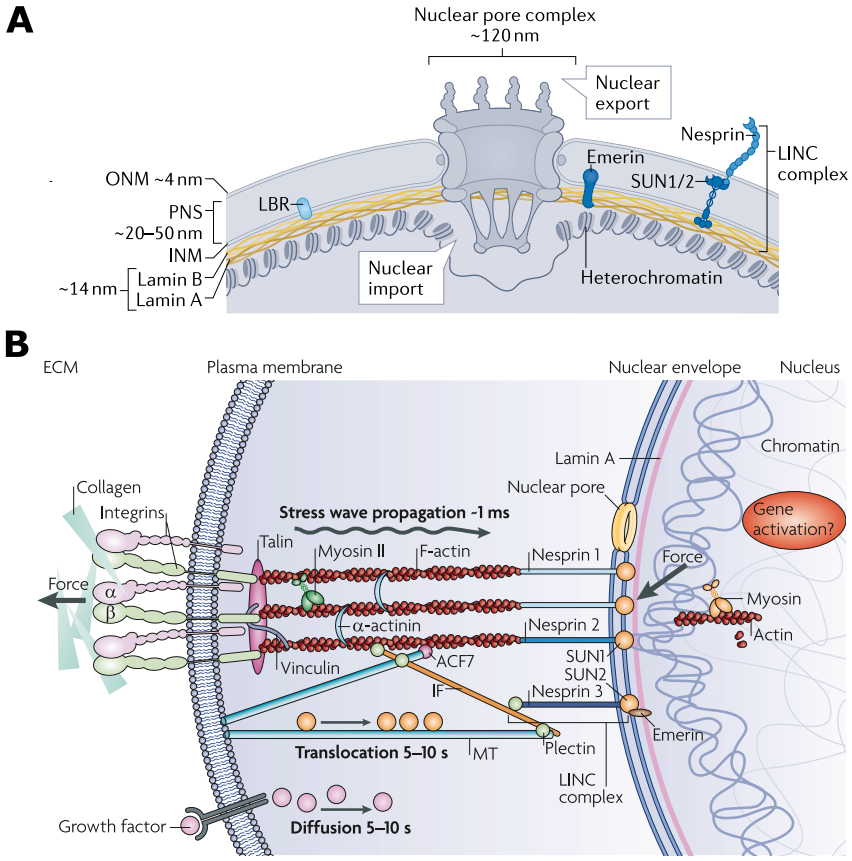

Figure 2.4: A The nuclear envelope (NE) consists of the outer (ONM) and inner nuclear membrane (INM), separated by the perinuclear space (PNS), and the nuclear lamina. Nuclear pore complexes (NPCs) allow nuclear-cytoplasmic transport across the NE. The Lamina and INM are connected via proteins like lamin B receptor (LBR) and emerin. They also establish links between the NE and chromatin. LINC complexes provide anchoring points for the cytoskeleton on the nuclear surface. **B** Cartoon of the mechanotransduction pathway allowing direct force transmission from the ECM to the nucleus. External forces are transmitted via integrins to the actin CSK and further via LINC complexes to the NE and chromatin, possibly triggering gene expression. This signalling pathway is up to 4 orders of magnitude faster than diffusional transport in the cytoplasm or active transport along intermediate filaments (IF) and microtubules (MT). Panel **A** adapted from [75]; panel **B** adapted from [95]

Nuclear-cytoskeletal coupling - the LINC complex

Forces originating from the cytoskeleton or the extracellular environment can be directly transmitted to the nucleus [3]. This is enabled by physical connections, known as LINC complexes (Linker of Nucleoskeleton and Cytoskeleton), between the cytoskeleton and the nuclear envelope (*cf.* Fig. 2.4 B) [4, 5].

LINC complexes are composed of members of the nesprin protein family (nuclear

envelope spectrin repeat protein), which are localized to the outer nuclear membrane, and SUN 1/2 proteins, anchored to the inner nuclear membrane. Both bind across the perinuclear space with each other. On the cytoplasmic side, nesprins bind directly to actin filaments such as stress fibres, while connections to the other two cytoskeletal polymers require respective bridging proteins.[7] On the other end of the complex, the SUN proteins provide the link to the lamin network of the nucleoskeleton below the inner nuclear membrane. Additionally, SUN proteins are known to directly interact with NPCs and chromatin [75].

LINC complexes are crucial for adapting the nuclear shape, for example by compression via perinuclear actin caps, which has been shown by LINC complex disruption to severely alter the cytoskeletal organization [5, 65]. Similar experiments indicated their crucial role in nuclear mechanosensing, where decreased nuclear deformation by LINC complex rupture resulted in decreased nuclear accumulation of mechanosensitive transcription regulators [8]. Nuclear straining mediated by LINC complexes has also been observed during cell migration through a confined environment, facilitating the passage [96]. Davidson et al. [96] demonstrated that in such situations LINC complexes predominantly form at the front of the nucleus, providing anchor points for actin filaments, which pull the nucleus across the constriction.

Nuclear interior

The interior of the nucleus, encaged by the nuclear envelope, is mainly occupied by the DNA of the cell and the nucleoplasm containing a large variety of proteins involved *e.g.* in DNA-transcription and repair [30].

The DNA of eukaryotic cells is a double helix structure [97] of nucleotides, encoding the genetic information [30]. It is a long chain with a width of 2 nm and a length of approximately 2 m, in the case of humans [30]. In order to fit the long genome into the nucleus, it is wound around so-called nucleosomes and further arranged into higher organizational fibrous structures, called chromatin. The resulting dense packing contributes to the mechanical rigidity of the nucleus.

Two types of chromatin can be distinguished, related to their condensation state, *i.e.* packing density: euchromatin and heterochromatin. Euchromatin has a lower density, providing better gene accessibility for transcription regulators, and is predominantly located in the nuclear interior and near NPCs. The short distance to the pores decreases

[7] In the case of microtubules kinesin and dynein motors are used for establishing a connection to nesprins. For intermediate filaments, plectrin forms this bridge.

the reaction time of a cell to stimuli. Heterochromatin has a much higher packing density and is therefore thought to be transcriptionally inactive. In contrast to euchromatin, it is primarily localized at the nuclear rim region.

Specific regions of the genome associate with the nuclear lamina (LAD - lamina-associated chromatin domains), altering the packing density of chromatin upon nuclear deformation and thereby possibly enabling subsequent gene transcription activity [98]. This decondensation is associated with a decrease in nuclear stiffness. However, large nuclear deformations may also cause DNA damage (e.g. double-strand breaks), either by nuclear envelope rupture and following exposition of the DNA to cytoplasmic proteins [99–101] or by increased replication stress without envelope rupture [101].

2.2.2 Nuclear pore complexes (NPCs)

Gene expression to mechanical and biochemical stimuli often involves proteins, which are natively cytoplasmic and have to cross the nuclear envelope to reach the DNA and trigger transcription. The transcription of the genes than have to exit the nucleus, in order to reach the ribosomes in the cytoplasm [30]. Here, the proteins are build according to this blue print as a response to the stimuli.

Nucleocytoplasmic protein transport is mediated by nuclear pore complexes (NPCs) perforating the nuclear envelope. NPCs are on a coarse scale homogeneously distributed [75] with nuclei having hundreds to thousands of these pores, depending on the cell type [30, 88]. Each of them can translocate up to 1000 molecules per second [102, 103] with translocation times of 10 ms [103] in and out of the nucleus at the same time. Despite this bidirectional, high-throughput protein transport, NPCs are highly selective. While allowing passive diffusion of small molecules up to a molecular mass of approximately 40 kDa, larger ones need adaptor proteins and are actively transported through the NPC [75]. However, this permeability barrier is not a hard one, but above the translocation probability shows a high dependence on molecule size.

NPC architecture

NPCs are build from up to 1000 copies of approx. 30 different and evolutionary highly conserved proteins, called nucleoporins (Nups), with a total mass of $60 - 125$ MDa [104, 105], making NPCs the largest molecular complexes in cells [88]. The constituting Nups are organized to a scaffold with 8-fold rotational symmetry [106–108] and a length in the range of 100 nm [88] with an outer diameter of around 120 nm [75] (*cf.* Fig. 2.4 A).

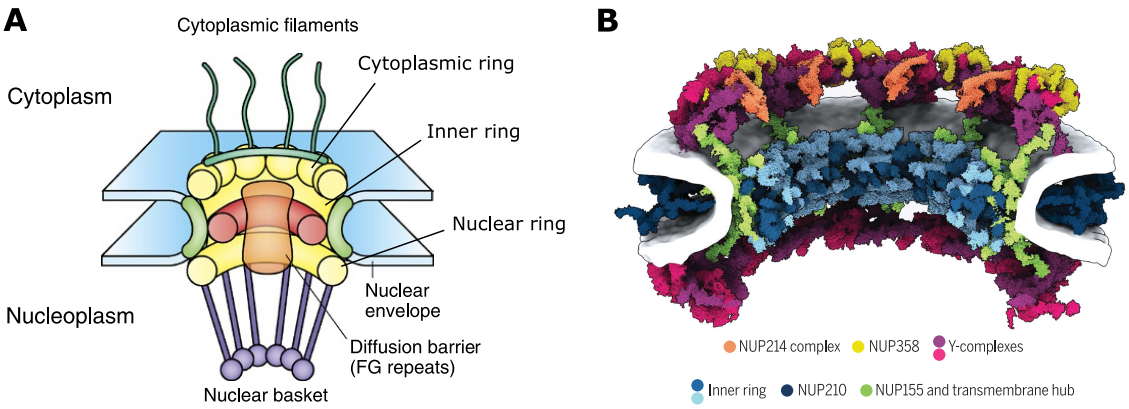

Figure 2.5: A Cartoon of the architecture of a NPC providing a transport channel through the NE between cytoplasm and nucleus. The NPC is anchored via a transmembrane scaffold of Nups to the NE. The central channel is filled with so-called FG nups, intrinsically disordered proteins, in a gel-like state responsible for the permeability barrier preventing passive diffusional passage of molecules above a mass of ~40 kDa. **B** High-resolution, AI-based reconstruction of the NPC scaffold. Visible are the two outer and the inner ring as well as the NE anchoring structures. Panel **A** adapted from [109]; panel **B** adapted from [110]

In this structure a cytoplasmic ring, a nuclear ring and an inner ring are distinguished (*cf.* Fig. 2.5). Located at the fusion area of inner and outer nuclear membrane, the inner ring anchors the NPC via transmembrane proteins to the nuclear envelope. Long filaments of intrinsically disordered proteins , attached to the cytoplasmic ring, extended into the cytoplasm, thought to serve as tentacles catching cargo for transport. On the nucleoplasmic side, such extensions form a basket-like structure.

The inner ring represents the central transport channel with a width of 35 – 60 nm[6, 7, 88]. It is filled with 200 – 300 intrinsically disordered Phenylalanin-Glycin amino-acid polymers (FG nups; repeats of nucleoporins) forming a gel-like barrier [88]. They are responsible for the high selectivity of the transport process by forming the aforementioned permeability barrier for molecules larger than ~40 kDa. An open/closed two-state system controlling the in- and outflux does not exist for NPCs.

NPC-mediated nuclear-cytoplasmic protein transport

The description of the nuclear-cytoplasmic transport cycle in this section is based on Refs. Hoogenboom et al. [88] and Cautain et al. [111] and Fig. [**fig: NPC transport**].

Larger proteins exceeding the permeability barrier need transport receptors in order to be actively translocated through the NPC. Depending on the transport direction, these are called importins (for nuclear import) and exportins (for nuclear export). Trans-

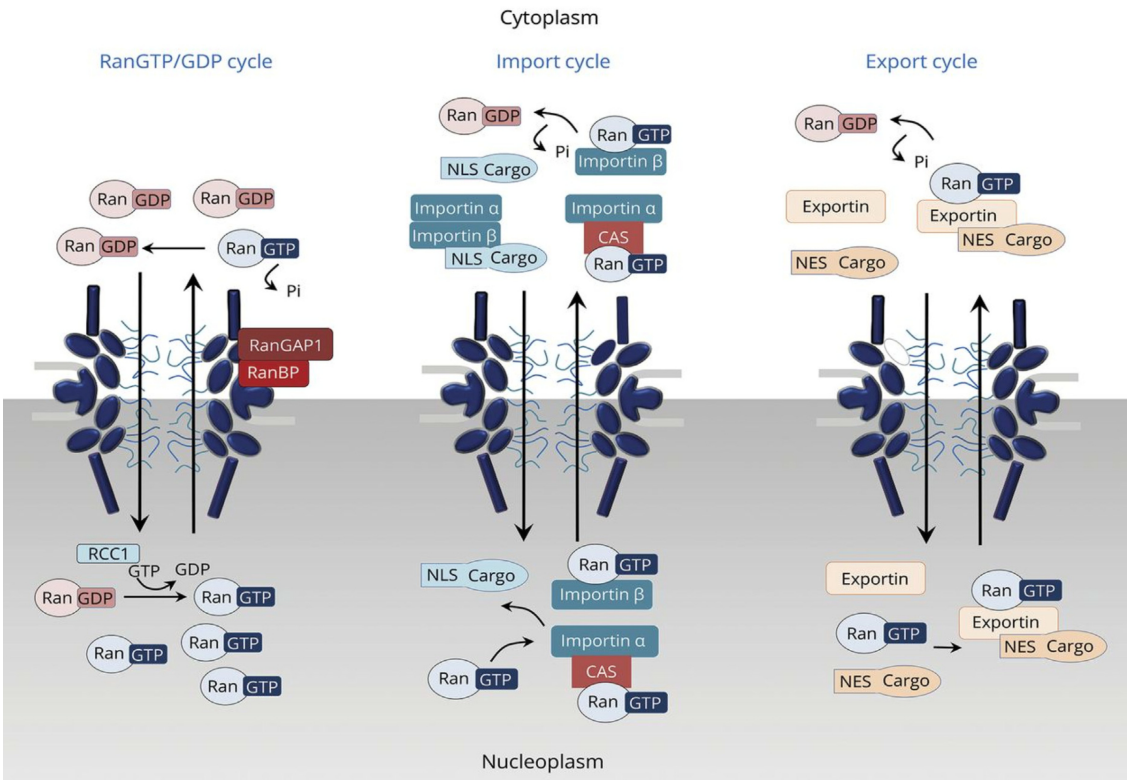

Figure 2.6: Shown are the three cycles of the active transport mechanism through NPCs: the RanGTP/GDP cycle, the import cycle and the export cycle. Molecules with masses above the nuclear permeability barrier (~40 kDa) cannot passively diffuse through NPCs, but have to be actively transported. Proteins equipped with special signal sequences, nuclear localization (NLS) or nuclear export signals (NES), are targetted by transport receptors. These importins and exportins interact with the FG-Nups in the central channel of the NPC facilitating the translocation. The direction of transport is given by the cytoplasmic localization of RanGAP and nuclear localization of RCC1, establishing a RanGTP gradient with low RanGTP concentration in the cytoplasm and high RanGTP concentration in the nucleus; vice versa for RanGDP. All reactions, with the exception of the conversion of RanGTP to RanGDP, are thermodynamically reversible [88]. Taken from [88].

port receptors recognize cargo by special sequences, namely nuclear localization signals (NLS) and nuclear export signals (NES). Regarding nuclear import, cargo proteins containing an NLS sequence, in general, first associate to the adaptor protein importin-α which than recruits importin-β enabling the NPC-transport process. [8] A cargo may even posses more than one NLS allowing the binding of multiple importins. Upon entering the NPC, the cargo-importin complex interacts with the FG nups in the central channel, in a way which is up to now still under investigation, weakening the diffusion barrier

[8] However, it is also known, that for certain cargo importin-β can associate without importin-α.

and allowing for passage. The transport motion of the complex within the channel still exhibits diffusion-like behaviour, and is referred to as facilitated diffusion. Reaching the nuclear side, the cargo-importin complex rapidly dissociates by RanGTP, omnipresent in the nucleus, displaying a high affinity for importins. The RanGTP-bound importins, sometimes with other adpator proteins, can leave the nucleus again. Back in the cytoplasm, the importins are released from RanGTP by its hydrolysis to RanGDP and can begin the next import cycle.

Export is functioning in a similar way, where exportins bind to cargo having NES sequences, facilitating nuclear export. These complexes often require RanGTP association. On the cytoplasmic side, RanGTP is hydrolysed to RanGDP, leading to the break up of the cargo-exportin complex.

Directionality of the transport is determined by a RanGTP/GDP gradient established by the spatial localization of two RanGTPases, RanGAP and RanGEF (RCC1). RangGAP is exclusively cytoplasmic and rapidly hydrolizes RanGTP to RanGDP, while RanGEF is localized to the nucleus and converts RanGDP to RanGTP. Physiologically, this results in a high RanGDP concentration in the cytoplasm and a high RanGTP concentration in the nucleus.[9] Due to the export of importin-bound RanGTP into the cytoplasm after the nuclear import of one cargo, RanGDP has to be brought actively into the nucleus via the nuclear transport factor 2 (NTF2) in order to maintain the RanGTP gradient and directionality of transport. This happens in addition to its passive diffusional passage. Apart from the RanGAP-mediated hydrolysis of RanGTP to RanGDP, all other processes described above are thermodynamically reversible [88]. This commonly accepted picture of the transport process can be split into three cycles, the RanGTP/GDP cycle, the import cycle and the export cycle as summarized in Fig. 2.6.

[9] Nuclear accumulation of cargo proteins can be inverted to cytoplasmic accumulation by switching the direction of the RangGTP gradient [112].

2.3 A primer of continuum mechanics

The theoretical framework to describe cellular mechanical responses on a macroscopic level is continuum mechanics. In this thesis, we describe cell deformations in the context of elasticity theory, in particular resorting to its linearised version. Here, an overview is given on the relevant concepts of continuum mechanics and the specification to linear elasticity theory. This section is based on the textbooks on continuum mechanics by Landau & Lifschitz [113], Howell et al. [114] and Sadd [115, 116].

2.3.1 Describing deformations

Forces applied to continuous elastic bodies lead to their deformation and changes in their morphology. This can be uniquely described by specific quantities, which we will introduce in the following.

Eulerian and Lagrangian framework

Consider a solid body as a continuous collection of material points each located at a point $\boldsymbol{X}$ at time $t = t_0$ in euclidean space. This state can be defined as *initial* or *reference configuration* of the solid. If the body is not subject to forces and moments, this state can be considered the *undeformed configuration*. However, the choice of the reference configuration is arbitrary. Upon the action of forces or moments the material points are displaced to new positions $\boldsymbol{x}(\boldsymbol{X}, t)$ for $t > t_0$. The new state is the *current* or *deformed configuration* of the body. Between both the reference and current configuration a unique, invertible mapping

$$\boldsymbol{x} = \chi(\boldsymbol{X}, t) \tag{2.1}$$

can be defined [116].

If the initial configuration of a body is known, it is possible to fix the position of a material point $\boldsymbol{X}$ within the body and to follow its trajectory in time to $\boldsymbol{x}(\boldsymbol{X}, t)$ This description is called the *Lagrangian* or *material description* and is the common framework in solid mechanics, since in general the initial configuration is known. Alternatively, it is possible to express the evolution of quantities with time at fixed spatial positions $\boldsymbol{x}$. This is the *Eulerian* or *spatial framework*, the natural description in fluid dynamics, where a reference material configuration is generally unknown.

Displacement

The displacement of a material point from its initial coordinate $\boldsymbol{X}$ to its current one $\boldsymbol{x}(\boldsymbol{X}, t)$ is defined as

$$\boldsymbol{u}(\boldsymbol{X}, t) = \boldsymbol{x}(\boldsymbol{X}, t) - \boldsymbol{X}. \tag{2.2}$$

This is the fundamental measure in continuum mechanics. Due to the continuity of the material, a neighbouring point, initially at distance $d\boldsymbol{X}$ from the previous one, is also displaced by

$$\boldsymbol{u}(\boldsymbol{X} + d\boldsymbol{X}, t) = (\boldsymbol{x} + d\boldsymbol{x}) - (\boldsymbol{X} + d\boldsymbol{X}). \tag{2.3}$$

By rearranging Eq. (2.3) and using Eq. (2.2) we can write

$$\begin{aligned} d\boldsymbol{x} &= d\boldsymbol{X} + \boldsymbol{u}(\boldsymbol{X} + d\boldsymbol{X}, t) - \boldsymbol{u}(\boldsymbol{X}, t) \\ &= d\boldsymbol{X} + \frac{\partial \boldsymbol{u}}{\partial \boldsymbol{X}} d\boldsymbol{X} \\ &= (\boldsymbol{I} + \nabla \boldsymbol{u}) d\boldsymbol{X} \end{aligned} \tag{2.4}$$

and define another fundamental measure in continuum mechanics, the *deformation gradient tensor*

$$\boldsymbol{F} = \boldsymbol{I} + \nabla \boldsymbol{u} = \frac{\partial \boldsymbol{x}}{\partial \boldsymbol{X}}, \tag{2.5}$$

which is the Jacobian matrix of the mapping $\chi(\boldsymbol{X}, t)$. It measures local relative position changes. The quantity $\nabla \boldsymbol{u}$ is called *displacement gradient tensor*. $\boldsymbol{F}$ allows to determine the volume change of an infinitesimal element of the body due to a deformation by $J = det(\boldsymbol{F})$ with $0 < J < \infty$, meaning that the material cannot intersect itself. An important insight from the deformation gradient tensor is, that uniform translations of a body with $\boldsymbol{u} = const.$ result in $\boldsymbol{F} = \boldsymbol{I}$, i.e. reference and current configuration of the body are identical. Rigid body motions do not change the deformation state.

Strain

Relative changes of distances between two material points can be derived from the above introduced quantities. Suppose, two points in a body are separated by the distances $|d\boldsymbol{X}|$ and $|d\boldsymbol{x}|$ in initial and deformed configuration, respectively. Taking the difference of the squared distances and using the relation $d\boldsymbol{x} = \boldsymbol{F}\, d\boldsymbol{X}$ we find

$$\begin{aligned} |d\boldsymbol{x}|^2 - |d\boldsymbol{X}|^2 &= (\boldsymbol{F} d\boldsymbol{X}) \cdot (\boldsymbol{F} d\boldsymbol{X}) - d\boldsymbol{X} \cdot d\boldsymbol{X} \\ &= d\boldsymbol{X}^T \left(\boldsymbol{F}^T \boldsymbol{F} - \boldsymbol{I} \right) d\boldsymbol{X} \end{aligned} \tag{2.6}$$

with the symmetric Green-Lagrange strain tensor

$$\boldsymbol{E} = \frac{1}{2}\left(\boldsymbol{F}^T\boldsymbol{F} - \boldsymbol{I}\right), \tag{2.7}$$

where $\boldsymbol{F}^T\boldsymbol{F} = \boldsymbol{C}$ is known as the right Cauchy-Green strain tensor. By use of Eq. (2.5) the Green-Lagrange strain tensor can be written as

$$\boldsymbol{E} = \frac{1}{2}\left[\nabla\boldsymbol{u} + \nabla\boldsymbol{u}^T + (\nabla\boldsymbol{u}^T)\,(\nabla\boldsymbol{u})\right]. \tag{2.8}$$

For later purposes the same considerations can be made for the Eulerian description

$$|d\boldsymbol{x}|^2 - |d\boldsymbol{X}|^2 = d\boldsymbol{x}\left[\boldsymbol{I} - \left(\boldsymbol{F}^{-1}\right)^T\left(\boldsymbol{F}^{-1}\right)\right]d\boldsymbol{x} \tag{2.9}$$

leading to the definition of the Euler-Almansi strain tensor

$$\boldsymbol{e} = \frac{1}{2}\left[\boldsymbol{I} - \left(\boldsymbol{F}^{-1}\right)^T\left(\boldsymbol{F}^{-1}\right)\right] \tag{2.10}$$

where $d\boldsymbol{X} = \boldsymbol{F}^{-1}\boldsymbol{x}$ was used. In the absence of any deformation both quantities $\boldsymbol{E}$ and $\boldsymbol{e}$ vanish. More general, pure rigid body transformations, such as uniform translations and rotations, lead to vanishing strains as they do not induce internal deformations.

Stress tensor

Deformations of a body lead to the emergence of internal restoring forces and stresses. To describe them, a body is divided into infinitesimal volume elements dV. On each of its surface elements dA a force

$$d\boldsymbol{f} = \boldsymbol{t}\,dA \tag{2.11}$$

is acting, where $\boldsymbol{t}$ is called *traction vector*. It depends on the position and orientation of the considered surface element, where the latter is given by the normal vector $\boldsymbol{n}$ of dA. The traction vector $\boldsymbol{t}$ is defined as

$$\boldsymbol{t} = \boldsymbol{\sigma}\cdot\boldsymbol{n} \tag{2.12}$$

with $\boldsymbol{\sigma}$ being the symmetric second-order *Cauchy stress tensor*. Each of its components σ_{ij} describes the stress acting in direction j on a surface element with normal vector in direction i. Per definition, positive stresses always point out of the considered volume element. Traction $\boldsymbol{t}$ as well as the stress components σ_{ij} bear the unit force/area (N/m^2) as can be inferred from eqs. (2.11) and (2.12).

Linear momentum conservation

Newton's second law demands that the sum of all momenta of the material points of a considered solid body balances all external forces acting on it. Therefore, we can consider an arbitrary volume element $\Omega(t)$ of a solid of denisty ρ and state that the momentum of it equals the sum of all body force densities $\boldsymbol{f}$ on $\Omega(t)$ and traction forces $\boldsymbol{t}$ on its surface $\partial\Omega(t)$,*i.e.*

$$\frac{d}{dt}\int_{\Omega(t)} \rho \frac{\partial \boldsymbol{u}}{\partial t} d\boldsymbol{x} = \int_{\Omega(t)} \boldsymbol{f} d\boldsymbol{x} + \int_{\partial\Omega(t)} \boldsymbol{\sigma}\boldsymbol{n} d\boldsymbol{A} \tag{2.13}$$

where relation (2.12) was used in the last term. Realizing that the mass of the considered fixed volume $\Omega(t)$ remains constant under deformation, i.e the mass density ρ is independent of t, and using the divergence theorem[10] gives

$$\int_{\Omega(t)} \rho \frac{\partial^2 \boldsymbol{u}}{\partial t^2} d\boldsymbol{x} = \int_{\Omega(t)} \boldsymbol{f} d\boldsymbol{x} + \int_{\Omega(t)} \nabla \cdot \boldsymbol{\sigma} d\boldsymbol{x}. \tag{2.14}$$

As the chosen volume $\Omega(t)$ is arbitrary, the above holds true for any other portion of the body under consideration. We arrive therefore at the governing equations of motion for an elastic material

$$\rho \frac{\partial^2 \boldsymbol{u}}{\partial t^2} = \nabla \cdot \boldsymbol{\sigma} + \boldsymbol{f}. \tag{2.15}$$

For soft matter, like biological cells and tissue, the inertial term can be neglected[11], resulting in the equation of mechanical equilibrium

$$\nabla \cdot \boldsymbol{\sigma} + \boldsymbol{f} = 0. \tag{2.16}$$

2.3.2 Linear elasticity

The above introduced elasticity theory can be specified to the case of small strains leading to its linearization. This linear elasticity theory is a widely used approximative description for the mechanical behaviour of cells and also used throughout this thesis.

The origin of linear elasticity theory is the assumption that all relative length changes within a deformed body are small. Hence, for all components of the displacement gra-

[10] The divergence theorem (Gauss's theorem) is $\int_\Omega \nabla \cdot \boldsymbol{a}\, dV = \int_{\partial\Omega} \boldsymbol{a} \cdot \boldsymbol{n} dA$ for an arbitrary vector $\boldsymbol{a}$.

[11] The associated wave velocity is $c \propto \sqrt{E/\rho}$, where the Young's modulus E is the stiffness of the material. For cells, which have a size of 5-50 µm [1], it is on the order of m/s, assuming E =1 kPa and a water-like density ρ =1 kg/m^3.

dient tensor $\nabla \boldsymbol{u}$ it is assumed that

$$\frac{\partial u_i}{\partial X_j} \ll 1. \tag{2.17}$$

First consequence of this approximation is that the deformation gradient tensor $\boldsymbol{F} \approx \boldsymbol{I}$ and therefore $d\boldsymbol{X} \approx d\boldsymbol{x}$, meaning that reference and current configuration fall onto each other and do not need to be differentiated. This obviously propagates to the strain tensors, where now eqs. (2.8) and (2.10) are equal and from now on denoted as $\boldsymbol{\epsilon}$.[12] Furthermore, the higher-order terms in the symmetric strain tensor $\boldsymbol{\epsilon}$ can be neglected, resulting in the linearized version

$$\epsilon = \frac{1}{2}\left(\nabla \boldsymbol{u} + \nabla \boldsymbol{u}^T\right) \tag{2.18}$$

or in index notation

$$\epsilon_{ij} = \frac{1}{2}\left(\frac{\partial u_i}{\partial x_j} + \frac{\partial u_j}{\partial x_i}\right). \tag{2.19}$$

Additionally to the above assumption, a linear relation between stress and strain tensor is assumed, known as Hooke's law

$$\sigma_{ij} = C_{ijkl}\epsilon_{ij}, \tag{2.20}$$

where C_{ijl} is a fourth-order tensor. It contains all characteristic parameters to describe the mechanics of a material and is known as the *elasticity* or *stiffness tensor*. Its 81 components can be reduced to 36 independent entries by acknowledging the symmetry of stress and strain tensor. Further reductions are achieved by considering special material symmetries. Isotropic materials, i.e. solids mechanically behaving the same way in any direction, only have two entries such that

$$C_{ijkl} = 2\mu\delta_{ik}\delta_{jl} + \lambda\delta_{ij}\delta_{kl} \tag{2.21}$$

and the stress tensor can be written in terms of the strain tensor as

$$\sigma_{ij} = 2\mu\epsilon_{ij} + \lambda\epsilon_{kk}\delta_{ij} \tag{2.22}$$

where the Einstein summation rule over identical indices is assumed, if not mentioned

[12] This follows from: $\frac{\partial u_i}{\partial X_j} = \frac{\partial u_i}{\partial x_k}\frac{\partial x_k}{\partial X_j} = \frac{\partial u_i}{\partial x_k}\left(\frac{\partial u_k}{\partial X_j} + \delta_{kj}\right) \approx \frac{\partial u_i}{\partial x_k}\delta_{kj} = \frac{\partial u_i}{\partial x_j}$.

otherwise. The material parameters

$$\mu = \frac{E}{2(1+\nu)} \qquad \text{and} \qquad \lambda = \frac{\nu E}{(1+\nu)(1-2\nu)}. \tag{2.23}$$

are called *Lamé coefficients* and are combinations of the *Young's modulus* or stiffness E of the material with unit $\mathrm{N/m^2}$ and the unitless *Poisson's ratio* ν, measuring the compressibility of the material.[13]

Lastly, the elastic free energy stored within a deformed object is given by

$$\mathcal{F}_{el} = \int \frac{1}{2}\sigma_{ij}\epsilon_{ij} dV = \int \left[\mu\epsilon_{ij}\epsilon_{ij} + \frac{\lambda}{2}\epsilon_{jj}\epsilon_{kk}\right] dV, \tag{2.24}$$

where the integrand is the elastic free energy density f_{el}.

2.3.3 From 3D to 2D: Plane stress and plane strain

In many biological situations cells are widely spread, which allows to consider them as thin elastic sheets. In this special case, the three-dimensional elasticity theory can be reduced to effectively two dimensions, simplifying its treatment. The most common 2D approximations are the plane stress and plane strain theories.

Plane stress

The plane stress theory can be applied to thin objects, whose height d (assumed to be in Cartesian z-direction) is much smaller than their extension in the other two orthonormal spatial directions. It is assumed, that the components of the stress tensor

$$\sigma_{xz} = \sigma_{yz} = \sigma_{zz} = 0 \tag{2.25}$$

and that z-variations of the other stress components are negligible small. Therefore, the stress tensor reduces to $\sigma_{ij} = \sigma_{ij}(x, y)$ with $i, j = \{x, y\}$.

However, the out-of-plane strain component

$$\epsilon_{zz} = \frac{\partial u_z}{\partial z} = -\frac{\nu}{E}\left(\sigma_{xx} + \sigma_{yy}\right) \tag{2.26}$$

[13] The Poisson ratio is defined via uniaxial extension experiments as the ratio between the lateral contraction of a material and its longitudinal dilation. A material with Poisson's ratio $\nu = 0.5$ is said to be incompressible, i.e. its volume does not change under deformation.

is in general not zero. To rescue the two-dimensional description, all quantities and Eq. (2.16) can be height-averaged under the assumption that the average of the out-of-plane displacement u_z vanishes. This procedure modifies the Lamé coefficients to

$$\mu = \frac{Ed}{2(1+\nu)} \qquad \text{and} \qquad \lambda = \frac{\nu Ed}{(1-\nu^2)}, \tag{2.27}$$

which can be found by expressing the out-of-plane strain ϵ_{zz}, *cf.* Eq. (2.26), in terms of the in-plane strains ϵ_{xx} and ϵ_{yy} and insertion into Hooke's law, *cf.* Eq. (2.22). The two-dimensional Lamé coefficients, and hence the stress tensor, have the unit N/m.

Plane strain

In the second two-dimensional approximation, the considered body is assumed to be of cylindrical shape, being much longer in one spatial direction than its extension in the other two. In the simplest case, it is assumed to be infinitely long.[14] Again, consider this direction to be the Cartesian z-direction, without loss of generality. All strain components associated with this spatial direction vanish, *i.e.*

$$\epsilon_{xz} = \epsilon_{yz} = \epsilon_{zz} = 0, \tag{2.28}$$

and the displacement components $u_x(x,y)$ and $u_y(x,y)$ should be independent of z. With this, the deformation state is completely described in the (x,y)-plane without out-of-plane deformations. Consequently, the mid-plane solution is valid throughout the body length.

A comparison with Hooke's law shows that the Lamé coefficients in plane strain are equal to the three-dimensional ones, *cf.* Eq. (2.23), again with unit N/m^2. Note that the mechanical equilibrium Eq. (2.16) is of the same form for plane stress and plane strain, despite their different geometrical assumptions. They can be transformed into each other by appropriate substitutions of the material parameters. For example, a transformation from plane stress to plane strain is achieved by substituting $E \longrightarrow E/(1-\nu^2)$ and $\nu \longrightarrow \nu/(1-\nu)$ in the Lamé coefficients for plane stress, *cf.* Eq. (2.27) [115].

[14] Otherwise, the ends of a body of finite length require special attention to obtain a full solution [115].

3 Phase field method

Physical problems and especially continuum ones can often be described by resorting to their translation into the language of partial differential equations (PDEs). Most often, these systems are not analytically solvable, unless the exploitation of special symmetries allow for it, and numerics have to be used for examining them. A plethora of different numerical methods exists for solving systems of PDEs, each with their own advantages and disadvantages. When it comes to moving boundary problems, especially in combination with complex shapes, implicit interface methods have proved to be a suitable approach for efficient numerical treatment. We will apply and develop further such an implicit method, namely the phase field approach, in order to solve complex and dynamic situations involved in cell mechanics. For this purpose, we discuss in this chapter the concept of boundary methods. First, the idea of sharp interface approaches is outlined, focussing on the implicit level-set method. We than introduce a diffuse interface approach, the phase field method, which is used throughout this thesis.

3.1 Sharp interface approaches

In sharp interface methods, the central feature is the well-defined interface position, where jumps in physical quantities occur when the interface is crossed. One distinguishes between explicit and implicit interface approaches, where the latter is numerically easier to implement.

3.1.1 Explicit interface

Explicit interface methods require to resolve the interfaces of a system by a sufficiently large number of points often called markers. The discretization accuracy has to ensure to capture the boundary motion in sufficient detail, especially to keep the physical integrity of the interface. Like discretization points in the bulk of a system, these boundary points are moved according to the underlying system of PDEs and respective

boundary conditions, which can be time- and space-dependent. Because the discretization grid is not fixed in space, but rather in the material itself, explicit interface methods rely on a Lagrangian (material) description. The markers have to be tracked in space at every point of time in order to apply the respective (dynamic) boundary conditions, which makes explicit interface methods a computationally expensive task. Complex geometries add further difficulties to the interface discretization, particularly for regions with high curvature. Especially topological changes, such as breaking or merging of phases, are difficult to model with explicit interface methods.

3.1.2 Level-set method

The numerical complexity arising by explicitly tracking interface marker points can be remedied by describing the interface implicitly via a so-called level-set function, whose evolution is dictated by the PDEs of the considered system. The level-set method was first proposed by Osher and Sethian (1988) [117] as a computational tool for solving problems involving the motion interfaces, such as incompressible two-phase flow [118]. In the biological context, it has been for instance used to model cell motility [119] and cell deformation [120]. The following description is based on Refs. [121, 122].

Consider for simplicity a two-dimensional domain Ω containing a (dynamic) interface $\Gamma(t)$ separating two subdomains $\Omega^{(1)}$ and $\Omega^{(2)}$ (*cf.* Fig. 3.1 B). In general, these two subdomains do not need to be simply connected, i.e. they can exhibit holes[1]. A smooth function $\varphi(\boldsymbol{x}, t)$, the level-set function, is introduced, which is of higher dimensionality than Ω. The intersection of the surface of $\varphi(\boldsymbol{x}, t)$ with the plane Ω is defined as the zero level-set of $\varphi(\boldsymbol{x}, t)$ and identified as the interface, i.e. $\Gamma(t) = \{\boldsymbol{x} | \varphi(\boldsymbol{x}, t) = 0\}$ (*cf.* Fig. 3.1 A). While traditionally set to zero, the exact value of the level-set characterizing $\Gamma(t)$ is in principle arbitrary.

Additionally, the exact form of $\varphi(\boldsymbol{x}, t)$ is free to choose and most often a signed distance function $\varphi(\boldsymbol{x}, t) = \pm d$ is used, with d being the distance to $\Gamma(t)$ [122, 123]. All points $\boldsymbol{x}$ of the computational domain can now be uniquely assigned to one subdomain

[1] A simply connected set is a topological space where any two points can be connected by a path and any loop within this set can be contracted to a point. A not simply connected set is called multiply connected.

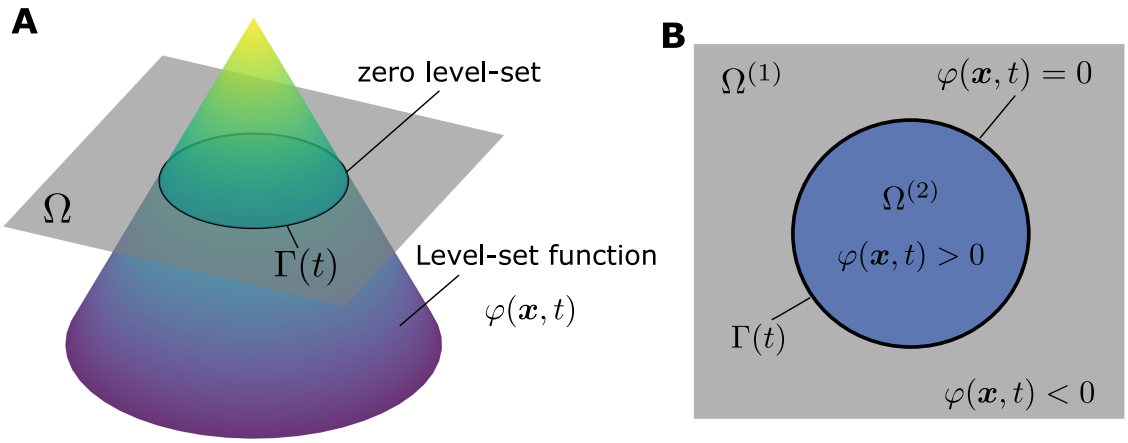

Figure 3.1: Sketch of the level-set method in 2D. **A** The intersection of the level-set function $\varphi(\boldsymbol{x}, t)$ with the plane of the domain Ω is identified with the boundary $\Gamma(t)$ (zero level-set) between two subdomains $\Omega^{(1)}$ and $\Omega^{(2)}$ of the considered system. **B** The level-set function $\varphi(\boldsymbol{x}, t)$ allows to assign each point of the domain Ω to a respective subpart, *i.e.* one of the two bulk domains $\Omega^{(1)}$ and $\Omega^{(2)}$ or the interface $\Gamma(t)$ associated with the zero level-set $\varphi(\boldsymbol{x}, t) = 0$.

or the interface by defining (*cf.* Fig. 3.1 B) [121–123]

$$\varphi(\boldsymbol{x}, t) \begin{cases} < 0 & \text{for } \boldsymbol{x} \in \Omega^{(1)}(t) \\ = 0 & \text{for } \boldsymbol{x} \in \Gamma(t) \\ > 0 & \text{for } \boldsymbol{x} \in \Omega^{(2)}(t). \end{cases} \tag{3.1}$$

The motion of $\Gamma(t)$ under a velocity field $\mathbf{v}$, given by the evolution equations of the physical system, can now be described by

$$\frac{\partial \varphi}{\partial t} + \mathbf{v} \cdot \nabla \varphi = 0 \tag{3.2}$$

with $\varphi(\boldsymbol{x}, t) = 0$ being the quantity of interest, describing the interface(s). This is the central equation of the level-set approach. The physical values of $\mathbf{v}$ are only required on the interface, while it is otherwise arbitrarily extended on the rest of the domain.

This implicit sharp interface formulation is especially suited for problems in which topological changes of the subsets of Ω occur, as those mentioned in the foregoing section, *e.g.* droplet splitting in a jet. Further advantages of this approach are the straightforward calculation of geometrical quantities of the interface like the normal vector $\boldsymbol{n} = \nabla\varphi/|\nabla\varphi|$and curvature $\kappa = -\nabla \cdot \boldsymbol{n}$ [122]. Additionally, the implicit formulation of interfaces via a level-set function enables to discretize the model PDEs on a

fixed grid, without the need of remeshing, rendering it an Eulerian formulation. All this makes the level-set approach numerically more efficient than explicit interface tracking methods. Nevertheless, as a sharp interface method, sophisticated numerical algorithms are needed for dealing with discontinuities of physical quantities at the interface $\Gamma(t)$. Moreover, often one has to reset/redefine the level set from time to time [123].

3.2 Phase field method - a diffuse interface approach

An alternative to implicit sharp interface methods for efficiently modelling moving boundary problems is the diffuse interface approach. This so-called phase field method also omits the necessity of explicit interface tracking for applying boundary conditions, showing similarities to the level-set method. It is the modelling approach used throughout this thesis to model cell mechanics in stationary and dynamic situations. We will therefore give here an overview on the basic principles of the phase field method.

3.2.1 Making interfaces diffuse

The phase field method was originally developed for modelling solidification processes such as crystal growth out of a solution [124, 125]. Its basic idea is to replace the sharp boundary (depending on the system, this can be angstrom or nanometer scale) between two distinguished phases (subdomains) of a system by a continuous one. For this purpose, a smooth regularized function $\rho(\boldsymbol{x}, t)$, the phase field, is introduced. This auxiliary field is constant in the bulk of the two phases, distinguishing both by assigning each of them a different numerical value (*cf.* Fig. 3.2 A). At the position of the interface $\Gamma(t)$ between the two phases it varies rapidly but continuously, in a small but finite region of width ϵ, from one bulk value to the other. Hence, the previously sharp boundary and its dynamics are implicitly described by the variation and evolution of the order parameter field $\rho(\boldsymbol{x}, t)$, making the interface 'diffuse'. Therefore, the phase field method is also known as diffuse interface approach.

The phase field dynamics can be coupled to the equations of motion of the modelled system, which then evolves according to these. If coupled properly, boundary conditions at interfaces are inherently described in the phase field-translated system of PDEs and only at the boundary of the computational domain they have to be stated explicitly.

In addition to facilitating the computational treatment of moving boundaries, the phase field approach omits the numerical difficulties arising from discontinuities of

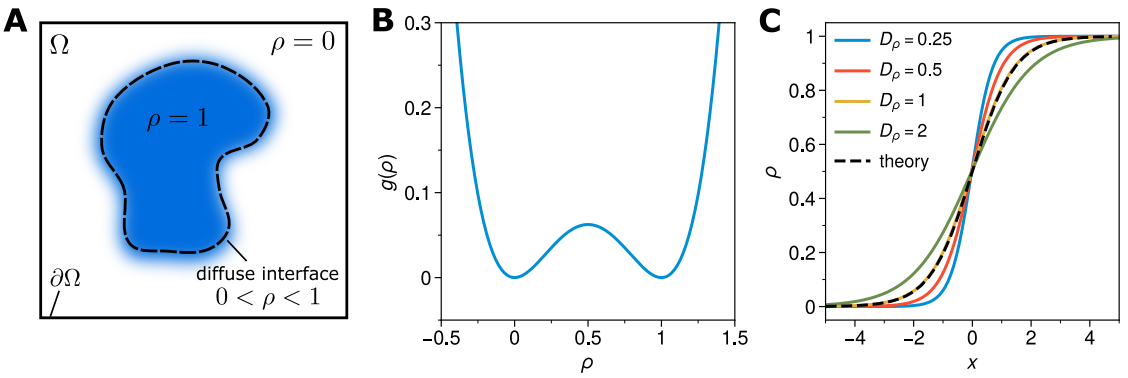

Figure 3.2: A Sketch of the phase field method for a two-phase system. In a domain Ω with boundary $\partial\Omega$ the phase field $\rho(\boldsymbol{x}, t)$ takes on constant values in the bulk phases. Here, $\rho(\boldsymbol{x}, t) = 0$ in the white (outside) phase and $\rho(\boldsymbol{x}, t) = 1$ in the blue (inside) phase. At the position of the sharp interface (black dashed line) it continuously changes between these values. **B** Double well potential $g(\rho) = \rho^2(1-\rho)^2$ with minima at $\rho = 0$ and $\rho = 1$ associated with two distinct bulk phases. The interface is identified with the $\rho = 1/2$-isocurve or the maximum of $|\nabla\rho|$. **C** One-dimensional phase field profiles as steady-state solutions to Eq. (3.8) for different interface widths set by the phase field diffusion coefficient D_ρ. The numerical phase field profile agrees with the analytical solution (black dashed line), *cf.* Eq. (3.9), as exemplified for the case $D_\rho = 1$ and $x_0 = 0$. For simulation parameters to **C** see Table B.1.

physical quantities at the interface due to its regularized description. Like the level-set method, the phase field approach is an Eulerian method, allowing the use of a fixed discretization grid. However, its numerical simplicity and efficiency compared to other methods comes with the expense of reduced accuracy. The latter can be partially regained by a higher degree of discretization and reduction of the interface width ϵ. In fact, in the sharp interface limit $\epsilon \to 0$ the 'sharp interface equations' for each considered phase are recovered and the phase field solution approaches the exact one.[2]

Since its first appearance, the phase field method has been applied to a large variety of different physical problems, proving its versatility and usefulness. Apart from microstructure evolution [126], solidification [127] and crystallization processes [125, 128, 129], the phase field approach has also been successfully applied to model fracture mechanics [130–133], stress-induced instabilities of the surface of a solid with its melt (Grinfeld instability) [134, 135] or fluid-structure interaction [136]. In the last decade, it attracted attention in the soft matter [137] and biological context and was for instance used to model vesicles in fluid flow [138, 139], actin gel growth [140] and the motility of single cells [123, 141–149]. Its efficiency and ease of implementation made it even

[2]This procedure is also known as asymptotic analysis and is exemplified in Appendix A.1 for the elastic phase field equation used in this thesis, *cf.* Chapter 4.

possible to model multiple cells at the same time; from pairs of cells [150] up to cell collectives and tissues [151–158]. In general, the models used in soft matter and biological systems do not account for cell elasticity. Only recently, phase field models for single cell [10] and tissue mechanics [159] have been proposed.

The success and flexibility make the phase field approach an important element for numerical studies of dynamic complex systems.

3.2.2 Theoretical framework of the phase field method

Having described the principal idea of the phase field approach, we now introduce the scaffolding structure of the associated dynamic equation.

Time-dependent Ginzburg-Landau equation

The derivation of a PDE describing the evolution of the order parameter field $\rho(\boldsymbol{x}, t)$ for a two-phase system starts from associating a Ginzburg-Landau free energy functional

$$\mathcal{F}[\rho] = \int_V f(\rho) d\boldsymbol{x} = \int_V \left[\frac{1}{2} D_\rho \left(\nabla\rho\right)^2 + g(\rho) \right] d\boldsymbol{x} \tag{3.3}$$

to it, where the first term penalizes the formation of interfaces and the second term is the energy contribution of the distinguished bulk phases. Via the diffusion parameter D_ρ the width of the interface $\epsilon \propto \sqrt{D_\rho}$ is controlled. The bulk contribution $g(\rho)$ is a double well potential, whose minima represent the two phases. Its exact form is arbitrary [3] and hence it is convenient to choose the simplest form [140]

$$g(\rho) = \rho^2 \left(1 - \rho\right)^2, \tag{3.4}$$

with minima at $\rho = 0$ and $\rho = 1$ (*cf.* Fig. 3.2 B).

The time-dependent Ginzburg-Landau equation follows from the minimization of the energy functional (3.3). For an a non-conserved order parameter field $\rho(\boldsymbol{x}, t)$, a so-called Allen-Cahn type equation is obtained.

$$\frac{\partial\rho}{\partial t} + \mathbf{v} \cdot \nabla\rho = -M^{-1} \frac{\delta\mathcal{F}}{\delta\rho}. \tag{3.5}$$

[3] Consequently, the numerical values of the minima associated to the bulk phases can be set freely.

Here, M^{-1} is a mobility coefficient, $\mathbf{v}$ is a possible advection velocity and

$$\frac{\delta \mathcal{F}[\rho]}{\delta \rho} = \frac{\partial f}{\partial \rho} - \nabla \cdot \left(\frac{\partial f}{\partial (\nabla \rho)} \right) \tag{3.6}$$

is the functional derivative of the free energy. Similarly, the dynamic equation for a conserved phase field $\rho(\boldsymbol{x}, t)$ is given by the Cahn-Hilliard equation

$$\frac{\partial \rho}{\partial t} + \mathbf{v} \cdot \nabla \rho = \nabla \cdot \left(M^{-1} \nabla \frac{\delta \mathcal{F}}{\delta \rho} \right). \tag{3.7}$$

To solve this fourth-order PDE, appropriate computational methods are required as it is prone to numerical instabilities. Thus, often the Allen-Cahn formulation (3.5) is used and mass conservation is enforced by adding additional terms [142] or employing Lagrangian multipliers. Inserting the free energy functional (3.3) into Eq. (3.5) results in

$$\frac{\partial \rho}{\partial t} + \mathbf{v} \cdot \nabla \rho = D_\rho \Delta \rho - \frac{\partial g(\rho)}{\partial \rho}. \tag{3.8}$$

with $\partial g(\rho)/\partial \rho = 4\rho(1-\rho)(1/2-\rho)$. The sharp interface position is assumed to coincide with the maximum of the gradient $|\nabla \rho|$, or simpler, with the isoline $\rho = 0.5$. In steady state and $\mathbf{v} = 0$, the solution to Eq. (3.8) in one dimension under the conditions that $\rho(x \to -\infty) = 0$ and $\rho(x \to +\infty) = 1$ is

$$\rho(x) = \frac{1}{2} \left[1 + \tanh \left(\frac{x - x_0}{\sqrt{2 D_\rho}} \right) \right], \tag{3.9}$$

where x_0 can be identified with the interface position (Fig. 3.2 C; for derivation see Appendix A.2).

Correcting for surface tension

In two and higher dimensions, the phase field formulation presented above has no stationary state for non-planar interfaces. This circumstance stems from an inherent surface tension energy, leading to an effective normal force at the interface proportional to its local mean curvature and pointing towards the centre of curvature [160]. Under this force, curved interfaces tend to shrink, in order to reduce their surface area. Parallel to this shrinking, phases of arbitrary (convex) geometry will evolve into a sphere [161], which has the lowest surface-to-volume ratio (Fig. 3.3 top row). The radius $r(t)$ of an

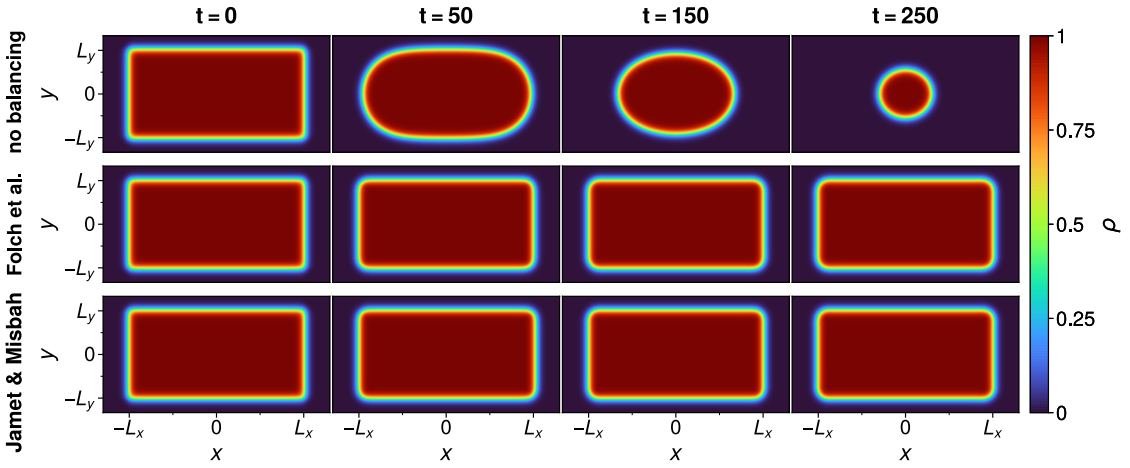

Figure 3.3: The phase field formulation, as presented in Eq. (3.8), is endowed with an inherent surface tension which tends to shrink curved interfaces in order to reduce the surface area, as shown in the example for a phase of rectangular shape (top row). During this shrinking, the rectangle deforms into a sphere, which has the optimal surface-to-volume ratio. It is possible to counteract this effect up to first order by adding a respective balancing term. Folch et al. [160] (middle row) and later Jamet and Misbah [162] (bottow row) introduced such terms. In absence of any other driving forces, both possibilities stabilize the phase field interface for sufficiently long times. For simulation parameters see Appendix B.1 Table B.2.

area equivalent sphere in d dimensions shrinks with the velocity

$$\frac{dr(t)}{dt} = -\frac{D_\rho(d-1)}{r(t)} \tag{3.10}$$

where $1/r(t) = \kappa(t)$ is the time-dependent curvature of the d-dimensional sphere. From Eq. (3.10) follows that

$$r(t) = \sqrt{R_0^2 - 2D_\rho(d-1)t} \tag{3.11}$$

with $t \in \left[0, \frac{R_0^2}{2D_\rho(d-1)}\right)$ and R_0 being the initial sphere radius at $t = 0$ (*cf.* Fig. 3.4 black dashed and yellow solid lines). For some physical problems, this surface tension might pose an undesired feature. Folch et al. [160] found that the surface tension can be balanced to first order by adding a term that is linearly dependent on the interface curvature κ_ρ to the phase field equation

$$\frac{\partial\rho}{\partial t} + \mathbf{v}\cdot\nabla\rho = D_\rho\Delta\rho - \frac{\partial g(\rho)}{\partial\rho} + D_\rho\kappa_\rho|\nabla\rho|. \tag{3.12}$$

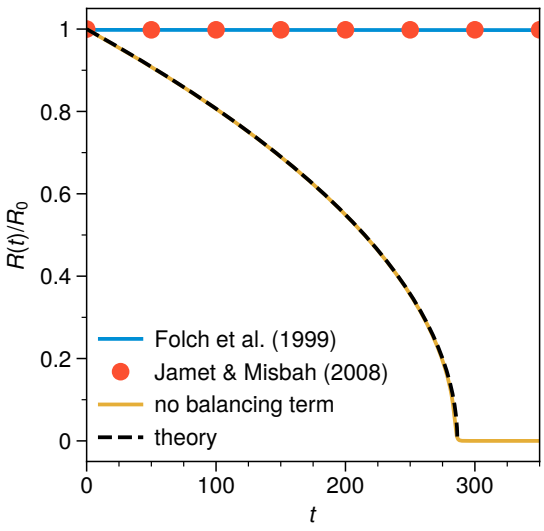

Figure 3.4: Time evolution of the radius $R(t)$ of the rectangle area for the simulations shown in Fig. 3.3 normalized by the initial radius R_0. Without correction of the surface tension (yellow solid line) the rectangle shrinks according to the theoretical expectation (black dashed line), *cf.* Eq. (3.11). The balancing terms by Folch et al. [160] (solid blue line) and by Jamet and Misbah [162] (red symbols) prevent the shrinkage for times that are sufficient long for most purposes. For simulation parameters see Appendix B.1 Table B.2.

This term acts only in the interface indicated by $|\nabla\rho|$. The curvature κ_ρ is given by

$$\kappa_\rho = -\nabla \cdot \boldsymbol{n} = -\nabla \cdot \left(\frac{\nabla\rho}{|\nabla\rho|} \right) \tag{3.13}$$

with the normal vector

$$\boldsymbol{n} = \frac{\nabla\rho}{|\nabla\rho|}. \tag{3.14}$$

Practically, the normal vector field and the curvature are calculated in a tube around the interface.[4] The sharp interface limit of Eq. (3.12) naturally shows that the 'Folch term' counteracts the surface tension energy up to first order in interface width ϵ (cf. Appendix A.1). However, no energy functional can be associated to it. Jamet and Misbah [162] introduced a thermodynamic consistent alternative[5], which is up to first order in interface width ϵ identical to the expression by Folch et al. [160]. The corresponding phase field equation reads

$$\frac{\partial\rho}{\partial t} + \mathbf{v} \cdot \nabla\rho = D_\rho \Delta\rho - \frac{\partial g(\rho)}{\partial\rho} + \sqrt{2D_\rho g(\rho)}\kappa_\rho. \tag{3.15}$$

Both balancing terms can be used equivalently, and stabilize the phase field for sufficiently long times as shown in Fig. 3.3 (middle and bottom row) and Fig. 3.4 (blue line and red symbols). Equations (3.12) and (3.15) both provide the basic structure of the phase field equation. If thermodynamic consistency is required, Eq. (3.15) should be

[4] For example, in the region where $|\nabla\rho| \geq 10^{-4}$.

[5] The corresponding energy reads $\mathcal{F}_{surface} = -\int_V \sqrt{2Dg(\rho)}|\nabla\rho| d\boldsymbol{x}$ [162].

used. Otherwise, when the phase field is regarded as a numerical tool as in our case, the choice is a matter of taste. Both versions are used in this thesis, demonstrating the insensitivity of the proposed phase field model to this choice.

3.2.3 Multi-phase field approach

The above formulation can be extended straightforwardly to situations involving more than two "phases". A prominent example in the biological context are cell collectives [151–153, 155]. Here, each cell i is represented by its own phase field ρ_i in the same manner as described above. The free energy functional of the system is the sum of the free energies of each of the N cell phase fields

$$\mathcal{F}[\rho_0, ..., \rho_N] = \sum_{i=0}^{N} \mathcal{F}[\rho_i] \tag{3.16}$$

which leads to the respective dynamic equations

$$\frac{\partial \rho_i}{\partial t} + \mathbf{v_i} \cdot \nabla \rho_i = D_{\rho_i} \Delta \rho_i - \frac{\partial g(\rho_i)}{\partial \rho_i} + f(\rho_i, \rho_j) \tag{3.17}$$

for each cell phase field ρ_i. The term $f(\rho_i, \rho_j)$ denotes all possible additional terms such as the correction for surface tension or interactions between cell i and a neighbouring cell j. We will use this approach (for $N = 2$) in Chapter 5, when we will model a cell with an additional internal compartment, the nucleus. The whole cell and the nucleus will each be represented by an own phase field.

4 Reversible elastic phase field approach and application to cell monolayers

Having introduced the concepts of elasticity theory and the phase field method, we now want to discuss how both can be combined into an elastic phase field approach, enabling the prediction of the dynamics of elastic cells and cell monolayers in two-dimensions. First, we will briefly summarize the commonly used elastic phase field method and an alternative formulation (as described in the Master's thesis [163] and in Chojowski et al. [10]), which accounts for the reversibility of elastic deformations. This *reversible elastic phase field approach* is than verified by being applied to a selection of biologically relevant situations and comparison to analytical solutions. It is the formulation used throughout this thesis.

This chapter is based on the publication Chojowski, R., Schwarz, U. S., and Ziebert, F. "Reversible elastic phase field approach and application to cell monolayers". *European Physical Journal E* 43.10 (2020), p. 63.

4.1 Introduction

Cell and tissue mechanics is an essential element of many physiological processes, including development, tissue homeostasis and wound healing [24, 29]. Both single cells and cell collectives are highly dynamic. For animal cells, fluorescence-based experiments have shown that subcellular structures like the actomyosin cortex, lamellipodia and adhesion complexes turn over on the timescale of minutes, despite their function to provide mechanical stability to cells and tissues [164–166]. In most developing and even in some homeostatic tissues (notably skin and intestine), there exists a constant flow of cells [167]. Together, these observations suggest that biological systems should be viscous rather than elastic on large time scales, at least in the absence of an extracellular

matrix [168].

Surprisingly, recent experiments with epithelial monolayers did reveal elastic signatures despite the high cellular and subcellular dynamics. The standard setup in this context is the so-called wound healing assay. In these experiments, cell monolayers of well-defined geometry migrate into free space created by the removal of a straight barrier. This setup has been used to quantify cellular velocity fields, traction forces and intramonolayer tension [26, 169, 170]. Several new effects have been discovered, including plithotaxis [171], where cells tend to migrate in the direction of maximal principal stress within the tissue, and collective durotaxis [17], where cells follow a stiffness gradient of the underlying substrate.

Very important in our context, it has been shown that one can extract a linear relation between stress and strain, thus defining an elastic modulus [172]. This agrees with the results of experiments that stretch free-standing monolayers without adhesion, from which a well-defined elastic modulus can be extracted [173, 174]. Later it has been argued that the seemingly elastic signature in expanding monolayers can also be explained as an emergent property of an active fluid with a purely viscous material law [175].

Three phenomena have received special attention in the context of the wound healing assay: mechanical waves, interface protrusions with leader cells and monolayer organization at boundaries. Mechanical waves in expanding epithelial monolayers were discovered with traction force microscopy and initially explained by repeated cycles of cytoskeleton fluidization and reinforcement [176]. Later it was shown that both an elastic material law [177] or a viscous material law [178] can explain their origin. A similar situation exists for the finger-like protrusions that are often observed to form at the wound margin [26]. Reminiscent of fingering in flow cells, these protrusions are often explained by viscous theories that include mechanisms for wavelength selection [179]. Some years ago, however, it has been shown that these protrusions tend to have a characteristic distance between each other that can be explained by the elastic properties of the monolayer [27]. Experiments with circular wounds and monolayer flow around obstacles have also provided evidence for both elastic and viscous processes in cell monolayers. While flow around a circular obstacle has been shown to be described best by the Maxwell model for viscoelastic fluids [180], the mechanical properties around a gap seem to correspond more to those of the Kelvin-Voigt model for a viscoelastic solid [181–183].

Taken together, a growing body of experimental and modelling results suggest that

cell monolayers are highly dynamic and reconcile both viscous and elastic signatures. However, the identification of the appropriate material law is often not clear and might strongly depend on context. Rather than extending the ongoing discussion of viscous versus elastic laws in a continuum mechanics framework, here we present an approach that brings together these two aspects in a different mathematical framework, namely the phase field method. It is nowadays widely used in the biological context, as has been discussed in Sect. 3.2.1, but has not been applied to the (bulk) elastic aspects of cells and cell monolayers. For these elastic aspects, we resort to standard elasticity theory, which is turned into a dynamic description by coupling it to the phase field. In fact, the phase field method has already a tradition for problems involving elasticity, especially for fracture mechanics [130, 132] and stress-induced instabilities [134, 135]. However, because they address irreversible problems like fracture, these existing implementations are typically not reversible under a removal of the forces and stresses. They hence are not adapted to the biological situation described above, which requires the combination of dynamics and reversible elasticity. Reversibility has been shown *e.g.* by optogenetics, when cells return to a homeostatic level of contraction after transient stimulation of motor activity [184].

In this chapter, we first briefly review how elastic stresses can be defined in the phase field sense and how elastic effects have been incorporated in previous studies, arguing why the reversibility of elastic deformations after a release of the applied forces, one of the hallmarks of elasticity, is not recovered in the existing (commonly used) approaches. Afterwards we present an alternative way of coupling elasticity to the phase field via an imbalance of forces at short times that allows to drive the phase field interfaces [10]. The method is than applied to a few simple model problems inspired by single cell and cell monolayer experiments, including a contractile cell (or cell sheet) adhering to a substrate, a hole in a contractile cell monolayer and a contractile cell pinned via strong focal adhesions, in order to verify and demonstrate the approach.

4.2 Coupling elasticity and phase field dynamics

The phase field equation can be coupled to model equations describing the evolution of a physical system. This coupling will lead the phase field domain to deform as predicted by these equations. In the biological context, the incorporation of continuum mechanics is of particular interest. Here we will present the aforementioned standard method of combining elasticity and phase field dynamics and the alternative approach, able to

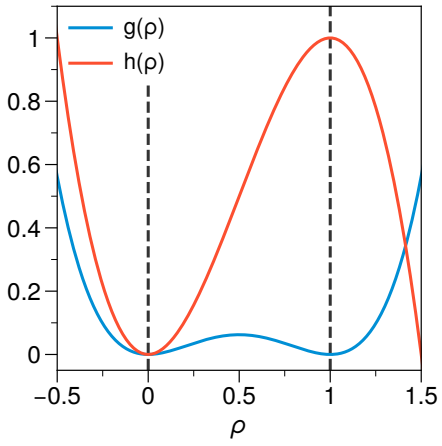

Figure 4.1: Plot of the weighting function $h(\rho) = \rho^2(3-2\rho)$ (red curve) and the double well potential $g(\rho) = \rho^2(1-\rho)^2$ (blue curve) for reference. The chosen interpolation function has extrema at $\rho = 0$ and $\rho = 1$, coinciding with the minima of $g(\rho)$, *i.e.* with the bulk phases. This is highlighted by the black dashed lines.

account for elastic reversibility.

4.2.1 Standard elastic phase field approach

Consider a system of two elastic materials represented by the bulk regions $\rho = 0$ and $\rho = 1$ of a phase field $\rho(\boldsymbol{x}, t)$. In order to couple the phase field to the elastic variables, first an expression for the stress field in the whole domain is needed. Assuming both materials are linearly elastic and isotropic, for each phase one has Hooke's law [113],

$$\sigma_{ij} = 2\mu\epsilon_{ij} + \lambda\epsilon_{kk}\delta_{ij}, \tag{4.1}$$

with the strain field ϵ_{ij} and Lamé coefficients μ and λ that can be different in the two materials, and the respective elastic energy density

$$f_{el} = \frac{1}{2}\sigma_{ij}\epsilon_{ij} = \frac{1}{2}\lambda\epsilon_{jj}\epsilon_{kk} + \mu\epsilon_{ij}\epsilon_{ij}. \tag{4.2}$$

To define the stress tensor in the whole domain, one interpolates by writing

$$\Sigma_{ij}(\rho) = h(\rho)\,\sigma^1_{ij} + [1 - h(\rho)]\,\sigma^0_{ij}, \tag{4.3}$$

with σ^0_{ij} and σ^1_{ij} the stresses in the materials described by $\rho = 0$ and $\rho = 1$, respectively, and an interpolation function $h(\rho) = \rho^2(3-2\rho)$ [135, 140]. This function is not unique, but it should have values $h(0) = 0$ and $h(1) = 1$ for the phases $\rho = 0$ and $\rho = 1$, respectively. The given choice has in addition a minimum for $\rho = 0$ and a maximum for $\rho = 1$ (*cf.* Fig. 4.1), *i.e.* $\partial_\rho h(\rho)_{|\rho=0} = \partial_\rho h(\rho)_{|\rho=1} = 0$.

Equation (4.3) can also be interpreted as an interpolation of the Lamé coefficients of

both material phases

$$\begin{aligned}\mu(\rho) &= h(\rho)\mu^1 + [1 - h(\rho)]\,\mu^0 \\ \lambda(\rho) &= h(\rho)\lambda^1 + [1 - h(\rho)]\,\lambda^0.\end{aligned} \tag{4.4}$$

where the superscripts denote the respective material phase.

The equations of mechanical equilibrium $\nabla \cdot \boldsymbol{\sigma} + \boldsymbol{F} = 0$ (*cf.* Eq. (2.16), where the external force density $\boldsymbol{f}$ will be from now an denoted by $\boldsymbol{F}$ to avoid confusion with the energy densities) should still hold for the stress in the phase field formulation, *i.e*

$$\nabla \cdot \Sigma + \boldsymbol{F} = 0, \tag{4.5}$$

with Σ being defined in Eq. (4.3). Note that the divergence operator then generates several terms, including derivatives of the interpolation field $h(\rho)$ and hence of ρ. Similar to the stress field, the elastic energy can be interpolated by replacing σ_{ij} by Σ_{ij} in Eq. (4.2), resulting in

$$f_{el}(\rho) = h(\rho)\, f_{el}^1 + [1 - h(\rho)]\, f_{el}^0. \tag{4.6}$$

The standard approach to couple elasticity to the phase field dynamics is to add the interpolated (and hence phase field-dependent) elastic energy to the free energy density of the phase field defined in Eq. (3.3), *i.e.* $f_{tot} = f(\rho) + f_{el}(\rho)$ [129, 132–135, 140, 185]. Performing the functional derivative results in

$$\frac{\partial \rho}{\partial t} = D\Delta\rho - \frac{\partial g(\rho)}{\partial \rho} - \frac{\partial h(\rho)}{\partial \rho}\left(f_{el}^1 - f_{el}^0\right) \tag{4.7}$$

where the new term can be interpreted as a driving force for the phase field due to elasticity. In principle, it has also to be accounted for a balancing of the phase field inherent surface tension. To preserve the thermodynamic consistency of the above formulation, the term by Jamet & Misbah [162] (*cf.* Eq. (3.15)) would be the most obvious choice. Since $\partial h(\rho)/\partial\rho$ for $\rho \in [0, 1]$ is a positive function peaked at the phase field interface, the phase field (associated to phase $\rho = 1$) will advance if $f_{el}^1 > f_{el}^0$ and retract otherwise, according to Eq. (4.7). For example, consider the stress-induced surface instability (Grinfeld instability) [134, 135], where phase $\rho = 0$ is the outside, non-material phase (hence $f_{el}^0 = 0$) and phase $\rho = 1$ is under stress (hence $f_{el}^1 > 0$). Consequently, phase $\rho = 1$ will grow – in fact, because of incompressibility, by undulating its surface – to release the stress. Note that Eq. (4.7) has to be solved together with Eq. (4.5) describing mechanical equilibrium.

The standard elastic phase field approach describes situations in which elastic defor-

mations drive changes in the position of a domain. However, it does not describe any elastic relaxation back to the original configuration. The reason is that in Eq. (4.7) only the elastic energy enters, which is quadratic in deformation (or, equivalently, in stress). Hence a sign change of the applied force $\boldsymbol{f}$ does not lead to a sign change in the driving force term (last term of Eq. (4.7)) and the interface does not go back. We should note that for the problems treated with Eq. (4.7) so far, this "non-reversibility" was not a problem: in fracture mechanics problems of brittle materials, when the material is broken, it does not close under release of the force [132, 133]. Similarly, in Ref. [140] the growth of an actin gel was modelled, but the healing/depolymerisation of the gel was not considered. However, for many other situations of interest, and in particular for single cells and cell monolayers, as extensively discussed in the introduction, a phase field approach with elastic reversibility is highly desirable.

4.2.2 Reversible elastic phase field approach

We will now describe an alternative approach for coupling elasticity to the phase field dynamics, which is able to recover the reversibility of linear elasticity. First, the phase field should be regarded as a numerical method to describe deforming or moving boundaries. As such, although this may be convenient, its dynamics does not need to be the functional derivative of a potential. Keeping the phase field potential defined in Eq. (3.3), the coupling to elasticity can be implemented via forces instead of energy. Hence, the phase field dynamics in two and higher dimensions can be written as

$$\frac{\partial \rho}{\partial t} = D\Delta\rho - \frac{\partial g(\rho)}{\partial \rho} + \sqrt{2Dg(\rho)}\kappa - \frac{1}{\xi}\left(\nabla \cdot \Sigma + \boldsymbol{F}\right) \cdot \nabla\rho, \tag{4.8}$$

where we stick to the surface tension elimination term by Jamet & Misbah [162]. Equivalently, the term by Folch et al. [160] can be used as thermodynamic consistency for the phase field is not necessarily demanded. The last term in brackets is the sum of internal elastic forces and an external force density. At mechanical equilibrium, this sum is zero and hence the whole term vanishes, and the interface described by the phase field is stationary. If there is an imbalance of forces, however, the interface will be advected in the direction of this force imbalance due to the term $\nabla\rho$. This proceeds until the phase field has attained a new shape fulfilling force balance, where mechanical equilibrium again holds and the movement stops. The prefactor $1/\xi$ is a coupling parameter (a mobility or inverse friction) setting the characteristic velocity of this movement.

To implement the elastic movement during the times of force imbalance, various

choices are possible, depending on the system to be modelled. In the soft matter and biology context, one would argue that motion should be overdamped. The simplest assumption then is a relaxational (overdamped) dynamics for the displacement field,

$$\xi \frac{\partial \boldsymbol{u}}{\partial t} = \nabla \cdot \Sigma + \boldsymbol{F} \tag{4.9}$$

where ξ is a friction coefficient setting the relaxation timescale into mechanical equilibrium.

The dynamics of Eqs. (4.8) and (4.9) then is as follows: let us assume we start with a stationary phase field (for the standard phase field, this corresponds to a $\tanh(x)$-like profile) and vanishing displacement field $\boldsymbol{u}(\boldsymbol{x}) = 0$. If we apply a force density $\boldsymbol{F}$ at the phase field boundary, as the stress in Eq. (4.9) is zero, $\boldsymbol{u}$ will increase with a certain timescale proportional to ξ. This will lead to a build-up of stress until mechanical equilibrium is reached via Eq. (4.9) and at the same time the phase field interface moves via Eq. (4.8) because of the transient force imbalance. When the applied force is removed, the accumulated internal stresses (having opposite sign than $\boldsymbol{F}$) will lead to a sign change in front of the driving force in Eq. (4.8) and the body relaxes back to its initial equilibrium configuration before force application.

To ensure the independence of the phase field dynamics on ξ, the coupling parameter of the elastic driving force in Eq. (4.8) is chosen to be the inverse of ξ. This becomes clear by recognizing that the right-hand side of Eq. (4.9) is the driving term of Eq. (4.8). This choice yields consistent results, meaning that the phase field interface moves as far as the displacement field at the initial boundary indicates, independent of ξ. In turn, ξ should be chosen as small as possible to minimize computational costs, although for a specific system of interest, the exact choice should depend on microscopic details.

From this point onwards, we will always assume that phase $\rho = 1$ describes an elastic material (like a cell) and phase $\rho = 0$ the outside, *i.e.* empty space, where $\boldsymbol{\sigma}^0 = 0$. Hence, the phase field stress simplifies to

$$\Sigma_{ij}(\rho) = h(\rho)\, \sigma^1_{ij}. \tag{4.10}$$

Finally, we have to take into account that if the interface moves backwards, *i.e.* if the domain shrinks, it has to be assured that the displacement field is suppressed in what will become the outside of the domain, where no material and hence no displacement field exists. This problem is easy to remedy by adding a suppression term to Eq. (4.9)

for the displacement field

$$\xi \frac{\partial \boldsymbol{u}}{\partial t} = \nabla \cdot \Sigma + \boldsymbol{F} - \gamma(\boldsymbol{F}) \left[1 - h(\rho)\right] \boldsymbol{u}. \tag{4.11}$$

This suppression term is active only in the outside, is linear in $\boldsymbol{u}$ and has a rate $\gamma(\boldsymbol{F})$. We write the damping rate as $\gamma(\boldsymbol{F}) = \gamma_0 + \gamma_1(\boldsymbol{F})$. While γ_0 is always active, $\gamma_1(\boldsymbol{F})$ is only non-zero when forces are applied to the interface. The use of two terms makes the procedure more flexible and in particular allows to adapt to the Poisson effect, which leads to movement at free boundaries that are not directly pulled by an external force.[1] Since the suppression term is active also in the interface region, as a consequence the total force actually applied to the domain is reduced. Therefore, $\gamma(\boldsymbol{F})$ has to be taken as small as possible.[2] Its effect can be partially compensated by decreasing the interface width (decreasing D) and increasing spatial accuracy by a finer grid. We will call the forces/stresses modulated in such a way *effective force/stress* in the following. Lastly, we note that we use an implicit matrix relaxation scheme (Crank-Nicolson) to solve Eq. (4.9), while the phase field dynamics is solved by the Fourier pseudo-spectral method (*cf.* Appendix C).

4.3 Application to cells and cell monolayers

Having described the reversible elastic phase field approach, we will discuss its specification and usefulness to describe biological systems that deform themselves due to active internal forces in the plane stress approximation (*cf.* Sect. 2.3.3). Afterwards, the elastic phase field approach will be used to investigate several archetypical experimental geometries.

4.3.1 Introducing cell contractility and substrate adhesion

Cells and cell monolayers continuously generate internal forces to probe the mechanics of their environment, to stabilize their interactions with the environment and to control their shape and mechanics. In order to address this biological situation, two important aspects have to be included in our modelling approach, namely internal contractility and adhesion to the underlying surface. Regarding contractility, single cells and cell

[1] The presented formulation works best for large Poisson ratios ν (*cf.*) Ref. [10]. This poses no weakness for treating biological materials, as these are in general nearly incompressible, *i.e.* $\nu \approx 0.5$.

[2] In a simple 1D example the new effective force can be calculated to be $F_{eff} = \int \left[F - \gamma(1 - h(\rho))u\right] dx$.

sheets are known to be contractile due to myosin II motors actively contracting the actin cytoskeleton [37]. For epithelial monolayers, this contraction is coherent over very large distances (hundreds of micrometres) due to the strong cohesion provided by the cadherin-based adherens junctions [27, 186]. Such a global contractility can be modelled on a coarse scale by adding an isotropic contractile stress $\sigma_0 < 0$ to the constitutive relation from Eq. (4.1):

$$\sigma_{ij} = 2\mu\epsilon_{ij} + (\lambda\epsilon_{kk} + \sigma_0 d)\,\delta_{ij}. \tag{4.12}$$

For simplicity, we here consider only a homogeneous, time-independent contractile stress, but clearly the method is also applicable for time-dependent and spatially inhomogeneous active stresses $\sigma_0(x, y, t)$.

Regarding adhesion, cells and cell monolayers are connected to the substrate through a layer of integrin-mediated adhesions. This adhesion layer allows for exchange of information and for mechanical coupling between cells and their substrates [187]. Cell-matrix adhesion to the substrate has been extensively characterized with traction force microscopy [188, 189]. A simple approach to model an adhesive soft interface that transmits force is the so-called elastic foundation [71, 190–193]. Here one assumes a homogeneous surface coverage with springs of spring constant density Y (measured in $\mathrm{N/m^3}$) positioned between a stiff substrate and the cell. This leads to an additional contribution to the force balance, Eq. (4.5), reading

$$\boldsymbol{F}_{adh} = -Y\boldsymbol{u}. \tag{4.13}$$

In the dynamics, this term simply enters the right-hand side of Eq. (4.11). In principle, this adhesion strength can also vary in time and space, *i.e.* $Y = Y(\boldsymbol{x}, t)$. Note, Y is determined by two contributions, namely the properties of the engaged adhesions modelled as the springs and the mechanical properties of the substrate [192]. In the case of very stiff substrates, the adhesions springs dominate. For our purpose this simplification is sufficient and we will neglect the substrate details.

Finally, the case of very strong adhesions can also be modelled by defining regions A where both the phase field and the displacement field are pinned, *i.e.* via the boundary condition

$$\partial_t \rho_{|A} = 0, \qquad \partial_t \boldsymbol{u}_{|A} = 0 \qquad \text{and} \qquad \boldsymbol{u}_{|A} = 0. \tag{4.14}$$

For modelling cell monolayers, cell-cell junctions are inherently treated by not re-

solving individual cells but by describing the tissue as a coherent material.

With these ingredients added, we continue with modelling specific geometries relevant for single cells and cell monolayers.

4.3.2 Contractile cell adhered to a substrate

We first address the problem of a contractile elastic disk on an elastic foundation (*cf.* Fig. 4.2 A) which constitutes a simple model for an adherent cell or cell monolayer [71, 191–193]. Generally, the disk is assumed to adhere on a ring at its periphery of inner radius $R_Y < R_C$ with a constant adhesion strength Y, *i.e.*

$$Y(\boldsymbol{x}) = \begin{cases} Y > 0 & \text{for} \quad R_Y \leq r \leq R_C \\ 0 & \text{for} \quad 0 \leq r < R_Y. \end{cases} \tag{4.15}$$

For $R_Y \to 0$, the cell is completely and homogeneously adhered. This model has been used before to explain the characteristic localization of traction forces at the cell or cell layer periphery [191].

First, Edwards & Schwarz [191] derived an analytical solution for the homogeneously adhered disk (*i.e.* $R_Y \to \infty$ in Fig. 4.2 A), where the radial displacement field is given by

$$u_r(r) = -l \frac{\sigma_0 d}{2\mu + \lambda} \frac{I_1\left(\frac{r}{l}\right)}{I_0\left(\frac{R_C}{l}\right) - \frac{2\mu}{2\mu+\lambda} I_1\left(\frac{R_C}{l}\right)}. \tag{4.16}$$

Here $l = \sqrt{E_C d / Y\left(1 - \nu_C^2\right)}$ is the localization length [191], which combines the moduli and dimension of the disk with the substrate stiffness, *i.e.* the spring stiffness density, Y. I_0 and I_1 are the modified Bessel functions of the first kind.

Later, an analytical solution was given for the case of adhesion on a ring geometry [194] being of the form

$$u_r(r) = \begin{cases} A\, I_1\left(\frac{r}{l}\right) + B\, K_1\left(\frac{r}{l}\right) & \text{for} \quad R_Y \leq r \leq R_C \\ C\, r & \text{for} \quad 0 \leq r < R_Y \end{cases}, \tag{4.17}$$

where A, B and C are constants determined by respective boundary conditions. Note, the radial displacement field is linear for the non-adhered cell part. Due to its complexity, the reader is referred to Solowiej-Wedderburn et al. [194] for the full solution. In the phase field model, the adhesion of the diffuse cell boundary has to be smoothly

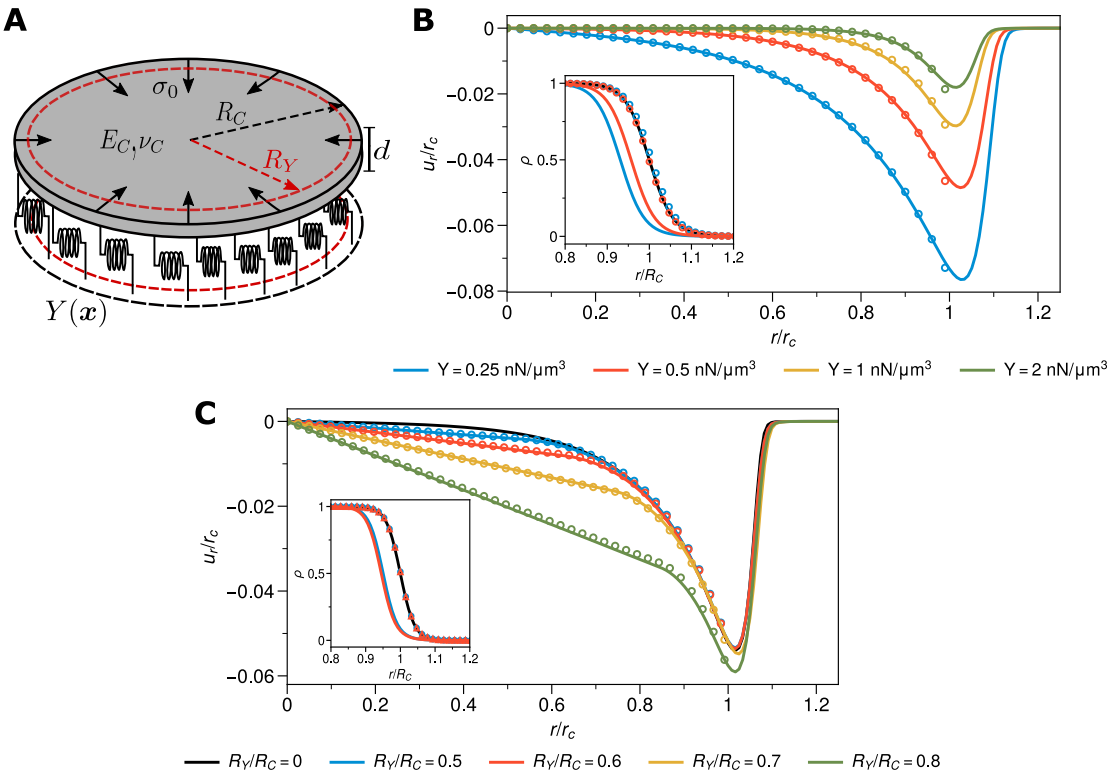

Figure 4.2: A Sketch of a radial symmetric, elastic cell (E_C, ν_C) of radius R_C and height d. The cell is subject to an isotropic contractile stress σ_0, while being adhered to an adhesive substrate via a layer of springs with spring stiffness density Y on a ring $R_Y \leq r \leq R_C$. For $R_Y \longrightarrow 0$ the case of complete homogenous adhesion is recovered. Shown are the phase field (solid lines) and corresponding analytical solutions (symbols in same colour) for the radial displacement field u_r, normalized by the cell radius r_c in mechanical equilibrium, for **B** a completely adhered cell ($R_Y = 0$) for different adhesion strengths Y and for **C** adhesion on a ring for different inner ring radii R_Y/R_C and $Y = 0.5\,\mathrm{nN/\mu m^3}$. The inset in **B** shows the phase field profiles for the cases $Y = 0.25\,\mathrm{nN/\mu m^3}$ (blue) and $Y = 0.5\,\mathrm{nN/\mu m^3}$ (red) at three different time points: the initial profiles before contraction (black), in mechanical equilibrium after stress application (coloured lines) and after stress removal and elastic relaxation (coloured symbols). The same is shown in the inset of **C** for the cases $R_Y/R_C = 0.5$ (blue) and $R_Y/R_C = 0.6$ (red). This demonstrates reversibility in both cases. Simulations were performed on $N = 512 \times 512$ grid points on a domain of $100\,\mu\mathrm{m} \times 100\,\mu\mathrm{m}$. If not specified above or in the figures, other relevant mechanical parameters are $R_C = 25\,\mu\mathrm{m}$, $E_C = 5\,\mathrm{kPa}$, $\nu_C = 0.45$, $\sigma_0 = 3.182\,\mathrm{kPa}$. The obtained disk radii at mechanical equilibrium are $r_c = 23.24\,\mu\mathrm{m}$ ($Y = 0.25\,\mathrm{nN/\mu m^3}$), $r_c = 23.83\,\mu\mathrm{m}$ ($Y = 0.5\,\mathrm{nN/\mu m^3}$), $r_c = 24.41\,\mu\mathrm{m}$ ($Y = 1\,\mathrm{nN/\mu m^3}$) and $r_c = 24.61\,\mu\mathrm{m}$ ($Y = 2\,\mathrm{nN/\mu m^3}$). Further parameters as in Appendix B.2.2 Table B.3.

continued towards the outside phase $\rho = 0$. Arguing that the displacement field $\boldsymbol{u}$ is suppressed in phase $\rho = 0$, a straightforward possibility is to define the adhesion strength $Y(\boldsymbol{x}) = Y$ in the whole computational domain. This corresponds to the case of complete

adhesion. The ring adhesion geometry can then be modelled by setting $Y(\boldsymbol{x}) = 0$ for $r < R_Y$ without the need of a smooth change as the phase field ρ is constant in the cell.

Figure 4.2 B shows results of phase field simulations (solid lines) for a completely adhered, elastic disk of radius $R_C = 25\,\mu\text{m}$ under the action of a strong homogeneous contractile stress and for different values of the substrate spring stiffness density $Y = 0.25 - 2\text{nN}/\mu\text{m}^3$. Note that this leads to localization lengths in the range $l \approx 0.8{-}2.3\,\mu\text{m}$ for a cell of stiffness $E_C = 1\,\text{kPa}$. The agreement of the displacement field, which by symmetry is only radial, with the analytical solution (symbols) is very good inside the bulk material. At the interface, the displacement smoothly crosses over to zero in the no-material region.

The inset of Fig. 4.2 B investigates the reversibility of the phase field method. Shown are the phase field profiles for the cases $Y = 0.25\,\text{nN}/\mu\text{m}^3$ (blue) and $Y = 0.5\,\text{nN}/\mu\text{m}^3$ (red) for three time points: the initial profile (equal for both cases) before applying the contractile stress (black solid line), the phase field profile in mechanical equilibrium with applied stress (coloured solid lines) and after removal of the stress.

It should be noted that the used stress value for the simulations in Fig. 4.2 B and C is rather high, so deformations are only small for large stiffnesses Y. Nevertheless, the reversibility is well captured down to $Y = 0.25\,\text{nN}/\mu\text{m}^3$ implying displacements of order 10 %. We nevertheless should give the warning that for too large displacements (*i.e.* large σ_0 and/or small Y), reversibility may be no longer complete, because the phase field model includes non-linear effects associated to the large-scale motion of its interface that go beyond linear elasticity.

Figure 4.2 C shows results of phase field simulations (solid lines) and analytical solutions (symbols) for cells adhered on a ring at their periphery with inner ring radii $R_Y/R_C = 0.5 - 0.8$ and $Y = 0.5\,\text{nN}/\mu\text{m}^3$. Again, both are in very good agreement with each other. As expected, increasing the adhesion area by decreasing R_Y, decreases the deformation within the cell, approaching the solution of a completely adhered disk (solid black line), *i.e.* $R_Y/R_C = 0$. Note, the linear deformation in the non-adhered cell part is obtained as predicted by Eq. (4.17).

The inset of Fig. 4.2 C shows phase field profiles for the cases $R_Y/R_Y = 0.5$ and $R_Y/R_Y = 0.6$ for three different time points as in Fig. 4.2 B. Again, elastic reversibility is recovered.

To make the above comparisons, in Eqs. (4.16) and (4.17) it has to be accounted for two effects. First, the initial disk radius R_C has to be replaced by r_c, the current radius, since the displacement field moves with the phase field. Second, the suppression term

in Eq. (4.9) reduces the applied contractile stress, hence an effective (radial) stress is acting given by

$$\sigma_{0,eff} d = \sigma_0 d - \frac{\gamma_0 + Y}{r_c} \int \left[1 - h(\rho)\right] u_r r dr, \tag{4.18}$$

where r_C is again the current radius of the disk. Note that to get this good agreement, the contribution of the substrate spring stiffness density Y in the interface region has also to be accounted for. The interpretation is that, while inside the cell's domain (i.e. underneath the cell) the springs reduce the displacement as elastic elements should do, their effect outside the cell and in the diffuse interface is indistinguishable of the implemented damping term $\propto \gamma$. Note that the effect is large in the given case, since the displacement is largest at the boundary and Y is large, but it can be reduced by decreasing the interface width of the phase field.

4.3.3 Contractile cell monolayer with a hole

Motivated by earlier work on wound closure [182, 183, 195–199] (*cf.* Fig. 4.3 A1 and A2), as a second test case we model a hole (devoid of cells) of radius R_h in a cell monolayer under isotropic contraction, sketched in Fig. 4.3 B.

If adhesion to the substrate is not considered, the analytical solution for a hole of radius R_h in an infinite monolayer under an isotropic stress σ_0 is given by [115]

$$u_r(r) = \frac{1 - \nu_C}{E_C} \frac{\sigma_0 R_h^2}{r} \tag{4.19}$$

yielding a long-ranged $1/r$-decay. In the numerical implementation we have to apply periodic boundary conditions, corresponding to a regular array of holes.

The result for the radial displacement field for a hole of $R_h = 100\,\mu\text{m}$ is shown in Fig. 4.3 C for three different system sizes $L = 2\,\text{mm}$, $3\,\text{mm}$, $4\,\text{mm}$ (coloured curves) and compared to the analytical solution (dashed). One can see that the – most interesting – part of the displacement close to the hole is well captured, while the long-ranged decay suffers from finite size effects that become smaller for larger system sizes. The inset of Fig. 4.3 C again confirms the reversibility after the release of the stress.

Note, again the for comparing the analytical and phase field solutions the stress σ_0 and initial hole radius R_h in the analytical solution have to be replaced by the actually applied stress $\sigma_{0,eff}$ and the final radius r_c in mechanical equilibrium, equivalent to the previous example of the contractile disk.[3]

[3] For the effective stress see again Eq. (4.18) with $Y = 0$ as adhesion is not considered here.

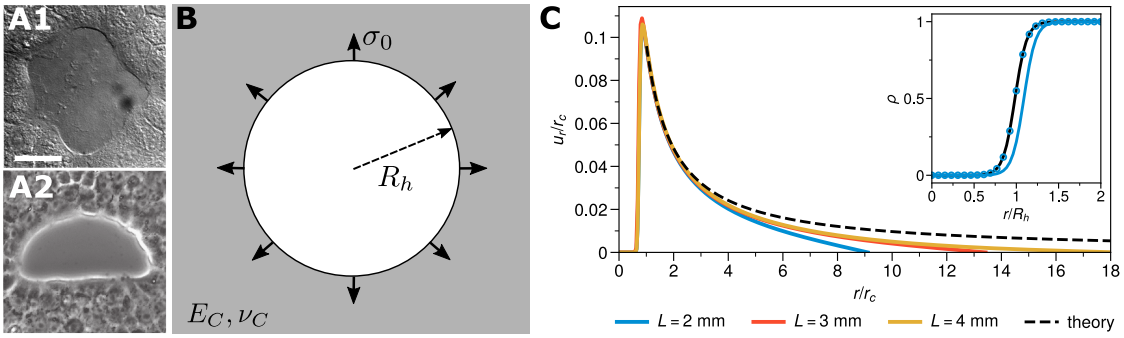

Figure 4.3: A1/A2 Examples of gaps/wounds of different, circle-like geometries in cell monolayers. **B** Simple model for a circular hole of radius R_h in an infinite, elastic monolayer (E_C, ν_C). The monolayer contracts isotropically with the stress σ_0. No substrate adhesion is assumed, *i.e* $Y = 0$. **C** Radial displacement u_r normalized by the current hole radius r_c in mechanical equilibrium after applying the contractile stress σ_0. Shown are the phase field solutions for domain sizes $L = 2\,\text{mm}$, $3\,\text{mm}$, $4\,\text{mm}$ (coloured lines) and the theoretical solution for an infinite monolayer(black dashed line), *cf.* Eq. (4.19). The behaviour close to the hole is well captured, while far away finite size effects are visible due to the applied periodic boundary conditions. The inset shows the phase field profile ρ before stress application (black line), in mechanical equilibrium after contraction (blue line) and after stress removal and relaxation (blue symbols) for $L = 2\,\text{mm}$. This demonstrates again the elastic reversibility. Simulations were performed on $N = 512 \times 512$ ($N = 1024 \times 1024$ for $L = 4\,\text{mm}$) grid points. If not specified above or in the figures, other relevant mechanical parameters are $R_h = 100\,\mu\text{m}$, $E_C = 1\,\text{kPa}$, $\nu_C = 0.5$, $\sigma_0 = 75\,\text{Pa}$. Final hole radii: $r_c = 109.4\,\mu\text{m}$ ($L = 2\,\text{mm}$), $r_c = 111.3\,\mu\text{m}$ ($L = 3\,\text{mm}$), $r_c = 109.4\,\mu\text{m}$ ($L = 2\,\text{mm}$). Further parameters as in Appendix B.2.2 Table B.3. Panel **A1** adapted from [183]; **A2** adapted from [182].

Note that to make this comparison – as already explained in the previous section – in Eq. (4.19) one again has to use the current radius r_c instead of R_h and $\sigma_{0,eff}$ as given by Eq. (4.18), where $Y = 0$ in the present case.

4.3.4 Contractile cell pinned at focal adhesions

Studying cells on micropatterned adhesive substrates has a long tradition in cell biology and biophysics [200–202]. Today this approach is used on a routine level to mimic the behaviour of different cell types in their physiological environment, which is more structured than a glass or plastic dish [187].

We begin with a cell pinned to the corners of a $50\,\mu\text{m} \times 50\,\mu\text{m}$ square pattern by strong focal adhesions. The latter were implemented as being centred around the four corners, where we draw circles of radius $r_A = 3\,\mu\text{m}$ wherein the rigid boundary condition, Eq. (4.14), was applied. We then allowed the cell to contract under an isotropic stress

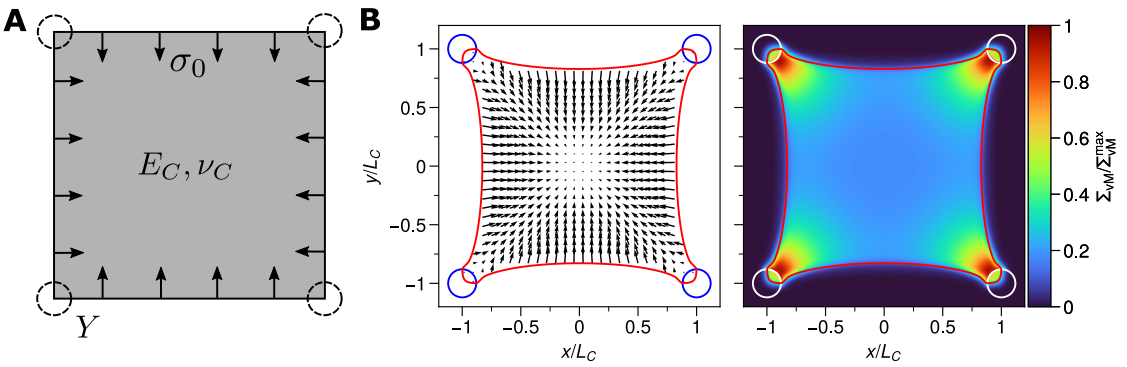

Figure 4.4: A Sketch of a contractile cell (E_C, ν_C), which is fixed to a square-shaped adhesion pattern with half-edge length L_C. The adhesive spots of radius r_A are centred at the cell corners. The cell is contracting under the homogenous stress σ_0. **B** Shown is the displacement field $\boldsymbol{u}$ for $\rho > 0.5$ (left panel) and the von Mises stress field Σ_{vM} normalized with respect to its maximal value Σ_{vM}^{max} (right panel) in mechanical equilibrium. The isocontour $\rho = 0.5$ is drawn as red line and the adhesive areas as blue and white circles, respectively. Visible are the in such experiments ubiquitous invaginated arcs and stress condensation at the the focal adhesions. Simulations were performed on $N = 512 \times 512$ grid points on a domain of size $100\,\mu\text{m} \times 100\,\mu\text{m}$. Relevant mechanical parameters are $L_C = 25\,\mu\text{m}$, $E_C = 1\,\text{kPa}$, $\nu_C = 0.5$, $\sigma_0 = 0.4\,\text{kPa}$ and $r_A = 3\,\mu\text{m}$. Further parameters as in Appendix B.2.2 Table B.3.

(here $\sigma_0 = 0.4$ kPa).

In mechanical equilibrium the cell's boundaries displayed invaginated arcs as shown in Fig. 4.4 B in red (corresponding to the $\rho = 1/2$–isocurve). The displacement field is shown as arrows and the adhesion sites, where the cell is pinned, as blue circles. To get a scalar quantification of the stress inside the cell, we calculated the von Mises stress, which is defined (in plane stress) as

$$\sigma_{vM} = \sqrt{\sigma_{xx}^2 + \sigma_{yy}^2 - \sigma_{xx}\sigma_{yy} + 3\sigma_{xy}^2}. \tag{4.20}$$

Note that in the phase field sense, σ_{ij} was replaced by the interpolated stress Σ_{ij}. A stress accumulation at the focal adhesions is visible.

Applying a small substrate adhesion below the rest of the cell, in addition to the strong pinning, does not change the overall quantitative picture. In contrast, when implementing only substrate adhesion via a spring stiffness density Y, but no pinning, the square-shaped cell just contracts homogeneously (in an affine fashion), *i.e.* without displaying invaginations, and the stress was highest in the centre, as expected (*cf.* Appendix B.2.1 Fig. B.1).

Next, we consider again an isotropically contracting circular cell, which is fixed via

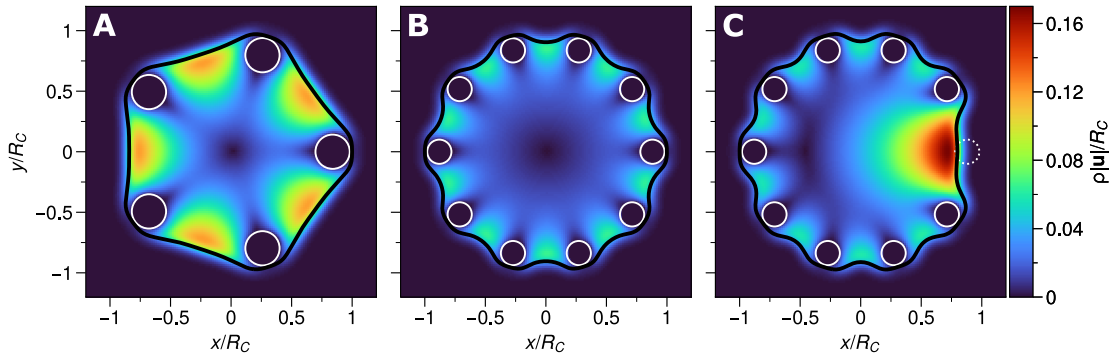

Figure 4.5: An initially circular, contractile cell of initial radius R_C adhered to 5 (**A**) and 10 (**B**) adhesion spots of radius r_A (white circles). The focal adhesions are evenly distributed with their centres lying on a circle $r = 0.98R_C - r_A$, having in both geometries equal total area corresponding to 10 % of the cell area. Shown is the total deformation field $\rho|\boldsymbol{u}|$ in the cell phase normalized by R_C. Decreasing adhesive spot distance reduces the deformation at the free edges. **C** Upon removal of one focal adhesion (here the most right one, shown as dotted white circle), for instance by dissolution or rupture, a substantial increase in deformation is observed. In all panels the isocontour $\rho = 0.5$ is drawn as black solid line. Simulations were performed on $N = 256 \times 256$ grid points on a domain of size $100\,\mu\text{m} \times 100\,\mu\text{m}$. Other relevant mechanical parameters are $R_C = 25\,\mu\text{m}$, $E_C = 1\,\text{kPa}$, $\nu_C = 0.5$, $\sigma_0 = 0.4\,\text{kPa}$. Further parameters as in Appendix B.2.2 Table B.3.

the boundary conditions Eqs. (4.14) to a varying number N of circular adhesive spots of radius r_A. The centres of these mimicked focal adhesions are equally distributed on a circle of radius $R = 0.98R_C - r_A$ [194]. The total area of the adhesive spots A_{tot} is assumed to be constant, hence $r_A = \sqrt{A_{tot}/(N\pi)}$.

In Fig. 4.5 the normalized total deformation field in the cell phase $\rho|\boldsymbol{u}|/R_C$ for $N = 5$ (Fig. 4.5 A) and $N = 10$ (Fig. 4.5 B) adhesive patches, indicated by white circles, is shown. Like for the square-shaped cell, invaginated arcs are forming between neighbouring focal adhesions with reduced deformation for increasing adhesion spot number, as has been reported previously [194].

The phase field method makes it possible to model dynamically changing boundary conditions. To demonstrate this, we again modelled the situation in Fig. 4.5 B. After mechanical equilibrium has been reached, we remove one focal adhesion (the most right one, dotted circle) and let the cell evolve into an equilibrium. The removal of one adhesion spot is a simple model for its rupture or dissolution. Figure 4.5 C shows the total deformation field in equilibrium after the removal of the adhesion patch. At the liberated edge high deformation occurs, associated with a considerable stress relaxation.

4.4 Discussion and conclusion

Cells and cell monolayers are both elastic and dynamic at the same time, making it very challenging to develop appropriate mathematical models. The phase field approach is very suitable for describing moving interfaces and versions accounting for elasticity have already been developed. However, existing elastic phase field approaches are not reversible under release of forces. As this is crucial in the biological context, *e.g.* when a protrusion first forms and then relaxes again in a wound healing assay, here we presented an alternative approach. It is based not on a total phase field energy that includes the elastic energy, but rather implements elasticity on the level of forces.

We applied the method to several standard situations that are often studied experimentally for both single cells and cell monolayers. Important features of biological systems, namely active stresses generated inside the layer as well as both weak adhesion and strong pinning to an underlying substrate can be integrated easily into the method. All tests worked well, including reversibility, and several features observed experimentally were well captured, such as the appearance of invaginated arcs and stress focusing for strongly pinned contractile cells.

Care has to be taken when using strong damping outside of the domain (to ensure good reversibility) and when implementing an elastic foundation, since both involve a rescaling of the forces/stresses for finite widths of the phase field interface. Accounting for this, we have shown that the method is in agreement with all tests against analytical results performed and is completely reversible for not too large forces and stresses. Reversibility may become only partial (*i.e.* the system does not go back completely to its initial state) for higher forces or stresses. This is to be expected since the phase field moving under the action of elastic forces is an effect going beyond linear elasticity, and the more so, the further the phase field boundaries move.

In the future, the method should prove very useful to investigate dynamically self-organized forces and stresses, especially concerning contractile cells pinned at focal adhesions or finger formation and dynamics at monolayer boundaries. Building on existing cellular phase field models, as additional features relevant to cell dynamics one could implement actin filament orientation [142], concentration fields [141], the effects of biochemical signalling like the Rho-pathway [203], as well as adhesion and traction force dynamics. The latter have been modelled previously within the phase field approach [143, 145] by introducing reaction-diffusion kinetics for the engaged adhesive bonds, transmitting traction forces on an elastic substrate, while elasticity of the cell

was disregarded. In the framework proposed here, the simplest approach would be to let the distribution of engaged adhesive bonds modulate the substrate's spring stiffness density. Further on, in view of the viscoelastic flow behaviour of monolayers migrating around an obstacle [180], a generalization of the approach to different viscoelastic models [136] would be highly interesting. The approach can be extended to multicellular situations in which single cell resolution is required, by using different phase fields for different cells [149, 151, 152, 154, 204]. The approach could be generalized to three dimensions, to model *e.g.* cell spheroids or cells moving in strong confinement [146, 148, 205]. In summary, the new method of reversible elastic phase fields introduced here should find many interesting applications in modelling biological systems.

5 The role of the nucleus for cell mechanics: an elastic phase field approach

Cells contain a large variety of substructures with varying size and material characteristics [30]. It is not far-fetched to assume that this heterogeneity influences the mechanical response and perception of a cell and thereby many biological processes. In the last decades, it has become clear that the nucleus as the largest and one of the stiffest compartments of a cell is here of primary interest [75]. Here, we present an elastic two-phase field approach, using the formulation presented in the previous chapter, incorporating the nucleus as a second field associated with nuclear elastic properties. We investigate the mechanical role of a nucleus for a selection of relevant experimental setups including micro-patterning, cell compression and micropipette aspiration. For the last two, we are able to extract effective elastic moduli for the cell-nucleus composite. Lastly, we give an outlook on modelling cell migration through narrow channels.

This chapter is based on the manuscript Chojowski, R., Schwarz, U. S., and Ziebert, F. "The role of the nucleus for cell mechanics: an elastic phase field approach". *arXiv preprint arXiv:2309.12777* (2023), which has been submitted for publication. Further, the method and some results discussed in this chapter have been presented on the 03/06/2023 as a contributed talk at the APS March Meeting 2023 in Las Vegas (Nevada, USA) and the abstract is published in the Bulletin of the American Physical Society [207].

5.1 Introduction

Many essential biological processes depend on the mechanical properties of animal cells and their ability to dynamically react to mechanical cues from their environment. Classical examples include the spreading behaviour of cells on substrates of variable stiffness [11, 13], cell migration in the direction of larger rigidity [15, 17] and cell dif-

ferentiation in response to environmental stiffness [20, 21]. A typical cell response to variable environmental stiffness is to adapt the own stiffness to match the one of the environment [18, 19]. However, there are also situations in which it is favourable for cells to work with a different stiffness then the surrounding. One prominent example are migratory immune and cancer cells in confined spaces, which tend to increase their softness to more easily squeeze through the pores in their environment [23, 208, 209].

The main determinant of cell mechanics is the cytoskeleton, a crosslinked and highly dynamical polymer network, giving the cell stability and the ability to quickly change its mechanics [33, 36, 43]. In particular, the cytoskeleton allows cells to generate forces, mainly pushing forces through polymerization and pulling forces through motor activity, both of which convert chemical energy into mechanical work and thus make the cell an active system [36, 71]. Although the plasma membrane typically does not contribute much to cell mechanics directly, it is important in the sense that it determines cell volume and surface area; in addition, it provides guidance for the organization of the cell cortex generated by the cytoskeleton as a thin polymeric network wrapping the whole cell [31, 166].

In recent years, it has become clear that a third important mechanical component of animal cells is the nucleus [75]. The nucleus harbours the genetic information of the cell and is separated from the cytoplasm by its nuclear envelope. Due to its overarching role for gene expression, it has long been overlooked that the nucleus also plays an important role in mechanics. Having a cell-type dependent diameter of several micrometres and occupying a large fraction of the overall cell volume (typically up to 30%), the nucleus is the largest and most prominent of all cellular organelles [79]. Since it is so densely packed with chromatin, the nucleus can be up to 10-fold stiffer than the rest of the cell [83], which together with its size already suggests its importance in whole-cell mechanics.

During recent years, it has been shown in many experimental studies that the nucleus indeed has very specific mechanical roles in animal cells. In matrix-driven cell differentiation, the nuclear stiffness correlates with tissue and matrix compliance, leading to stiffer cell nuclei on stiffer substrates and pointing at its ability of perceiving mechanical cues and adapting to it [89]. Recently, it has been demonstrated that nuclear deformations instruct migratory behaviour of cells in confined spaces, indicating that the nucleus serves as a ruler and mechanosensor [92, 93]. Moreover, the nuclear size and stiffness limits the minimal size of constrictions through which a migratory cell can squeeze through [208, 210, 211]. In turn, it has been observed that nuclear soft-

ening during passage of narrow constrictions is often associated with nuclear envelope rupture and DNA damage, which in our context are not only failure, but also signalling events [99, 100, 208]. Stresses and strains on the nucleus can also lead to structural changes in the chromatin packing and a subsequent softening of the nucleus [98]. It also has been shown that metastatic cancer cells use the nucleus as a "battering ram" to invade soft tissue [212]. In cell migration, the nucleus is positioned by the microtubule-organizing centre either at the front or the back, depending also on the properties of the environment; when positioned at the front, it can be used as a ram during cell migration. Last but not least, it is known that forces originating from the interplay between cytoskeleton and the cellular surrounding can be directly transmitted to the nuclear envelope leading to nuclear deformations, triggering transcriptional activities and cellular reactions to these stimuli. This direct mechanotransduction pathway includes the LINC protein complexes establishing a direct physical connection between nucleus and cytoskeleton [4, 5, 65].

Despite this growing body of evidence of its importance for cell mechanics and mechanotransduction, the nucleus is often neglected when modelling whole-cell mechanics, often due to lack of an appropriate theoretical framework. We here propose an extension of our previously developed elastic phase field approach for cell mechanics [10] (*cf.* Chapter 4) that also includes the nucleus. In the spirit of multi-phase field approaches [151, 152, 155], the nucleus is introduced as an additional field, as was done in previous phase field studies of cells [213, 214], but this time, we associate to the nucleus elastic material characteristics and make them different from the ones of the rest of the cell. This enables us to study the effect of the nucleus on the cell's mechanical behaviour in a variety of different and biologically highly relevant situations, including various boundary conditions between both cell and substrate and nucleus and cytoplasm.

This chapter is structured as follows. First, we present the modelling approach for an elastic cell with a nucleus. We then demonstrate its applicability for homogeneously and locally adhered cells, already pointing out an important role of the nucleus. For the simple geometry of an isotropically contracting, homogeneously adhering, disk-like cell with a nucleus, we can use analytical solutions to validate the numerical solution. We then proceed with discussing numerical studies of more complex experimental setups, namely patterned adhesion and dynamic failure of an adhesion point. Finally, we turn to cells in confinement and discuss as examples the compression of cells between two parallel plates as well as micropipette aspiration of an elastic cell. We conclude with a

discussion and outlook on possible applications and further extensions of the proposed method.

5.2 Elastic phase field model for a cell with nucleus

In order to explicitly account for the nucleus in a model for an elastic cell, we extend the elastic phase field approach described in the previous chapter and in Ref. [10]. Following the idea of multi-phase field approaches [151, 152, 155–157], we extend this model by implementing an additional phase field $\psi(\boldsymbol{x}, t)$ describing an intracellular compartment, which will be associated with nuclear elastic properties. A similar approach has been used previously to account for an explicit nucleus in phase field models for cells [213, 214]. However, Camley et al. [213] neglected mechanics by solely considering the dynamics of two intercellular chemicals, while Moure et al. [214] assumed Stokesian hydrodynamics for both cell compartments. To our knowledge, no phase field model has been proposed yet that would account for elastic continuum mechanics and allow to model several cellular compartments – here the cytoplasm and the nucleus – having different material properties.

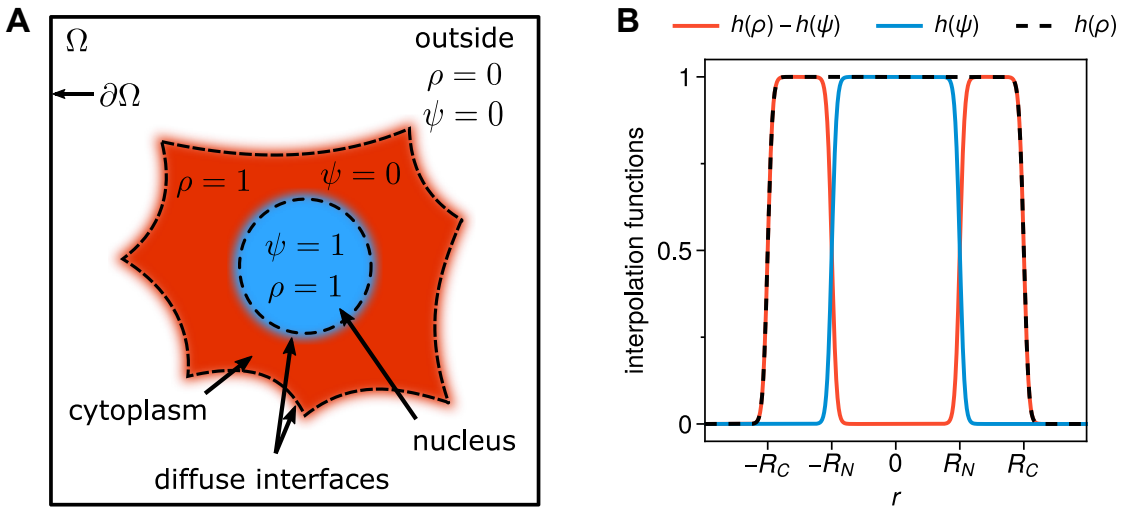

Figure 5.1: A Sketch of the two-phase field approach for modelling a cell with a nucleus. The computational domain Ω with boundary $\partial\Omega$ is divided into different compartments by use of the phase fields $\rho(\boldsymbol{x}, t)$ and $\psi(\boldsymbol{x}, t)$ for the whole cell and the nucleus, respectively. The distinguished phases are the outside of the cell ($\rho = 0, \psi = 0$), the cytoplasm ($\rho = 1, \psi = 0$), and the nucleus, ($\rho = 1, \psi = 1$). **B** Radial cut showing the interpolation functions for a cell of diameter $2R_C$ with a nucleus of diameter $2R_N$. The cell ($h(\rho)$, black dashed line) is split into two compartments, the cytoplasm ($h(\rho) - h(\psi)$, red) and the nucleus ($h(\psi)$, blue).

In our approach, the cell and its nucleus are represented by two phase fields, $\rho(\boldsymbol{x}, t)$ and $\psi(\boldsymbol{x}, t)$, respectively, *cf.* Fig. 5.1 A.
Equivalent to the previous chapter, the cell is described by the bulk phase $\rho = 1$ and the outside by the phase $\rho = 0$. Similar, the nucleus phase field $\psi(\boldsymbol{x}, t)$ takes on the value $\psi = 1$ in presence of the nucleus and $\psi = 0$ otherwise. Cell and nucleus boundary are described by a smooth tanh-like variation of the respective fields $\phi(\boldsymbol{x}, t) \in \{\rho(\boldsymbol{x}, t), \psi(\boldsymbol{x}, t)\}$, where the interface location can be identified with the location of the maximum of $|\nabla\phi|$, or simpler with the isocontour $\phi = 1/2$. Each phase field has its own evolution equation which follows an overdamped relaxational dynamics

$$\frac{\partial\phi}{\partial t} = D_\phi\Delta\phi - \frac{\partial g(\phi)}{\partial\phi} + D_\phi\kappa_\phi|\nabla\phi| - \frac{1}{\xi}\left(\nabla\cdot\Sigma + \boldsymbol{F} - \gamma(\boldsymbol{x})\left[1 - h(\rho)\right]\boldsymbol{u}\right)\cdot\nabla\phi \tag{5.1}$$

with $\phi \in \{\rho, \psi\}$, respectively. As before, the first term penalizes the formation of interfaces whose width ϵ_ϕ is set by the diffusion coefficient D_ϕ ($\epsilon_\phi \propto \sqrt{D_\phi}$). In general, the two interface widths, set by D_ϕ, could be chosen to be different. The second term in Eq. (5.1) is the derivative of a double-well potential of the form $g(\phi) = \phi^2(1-\phi)^2$, already used in Chapter 4.[1] Its minima are associated with the interior of the cell/the nucleus ($\phi = 1$) and the space outside the cell/the nucleus ($\phi = 0$), respectively (*cf.* Fig. 5.1 A). The third term in Eq. (5.1) is correcting for the method inherent surface tension (*cf.* Sect. 3.2.2), which is proportional to the local mean curvature $\kappa_\phi = -\nabla\cdot(\nabla\phi/|\nabla\phi|)$, as before. Different to Chapter 4, we here use the surface tension correction term by Folch et al. [160] instead of the one by Jamet & Misbah [162] (*cf.* Eq. (4.8) third term). We recall that the expressions by Folch et al. [160] and Jamet & Misbah [162] are up to first order equivalent. If thermodynamic consistency is not required, they can be interchangeably used. However, the surface tension correction by Folch et al. [160] follows directly from an asymptotic expansion (*cf.* Appendix A.1), which is why we will use it from now on. Finally, the last term in Eq. (5.1) couples the phase field dynamics to continuum mechanics. It describes a movement of the phase fields in case the mechanical force balance, $\nabla\cdot\Sigma + \boldsymbol{F} = 0$ with stress tensor Σ and applied external force $\boldsymbol{F}$, is not fulfilled.

The evolution of the displacement field $\boldsymbol{u}$ can be written, using the common assump-

[1] As mentioned in Chapter 4, the double-well potential is not unique. Here, we remain with the simplest choice.

tion of overdamped dynamics for cells and tissues, as

$$\xi \frac{\partial \boldsymbol{u}}{\partial t} = \nabla \cdot \Sigma + \boldsymbol{F} - \gamma(\boldsymbol{x}) \left[1 - h(\rho)\right] \boldsymbol{u}. \tag{5.2}$$

As previously, ξ sets the timescale of the relaxation into mechanical equilibrium, given by the force balance, and the last term suppresses $\boldsymbol{u}$ in the region outside of the cell, which is assumed to be empty space, *i.e.* without any elastic material properties.[2] Equations (5.1) and (5.2) have been verified for the biological context in Ref. [10] and Chapter 4.

The stress tensor Σ must be defined on the entire computational domain. In case of several compartments with different material properties, the phase field stress tensor has to interpolate the stress tensors $\boldsymbol{\sigma}$ (and lastly material parameters) of the individual considered phases, with smooth transitions at the respective interfaces. For this purpose, we use weighting functions of the form $h(\phi) = \phi^2(3 - 2\phi)$ – already known from the previous chapter – for the cell and the nucleus, respectively [10, 135, 140].

The total phase field stress tensor Σ is then defined as

$$\Sigma(\rho, \psi) = \left[h(\rho) - h(\psi)\right] \boldsymbol{\sigma}^{\boldsymbol{C}} + h(\psi) \boldsymbol{\sigma}^{\boldsymbol{N}} \tag{5.3}$$

where $\boldsymbol{\sigma}^{\boldsymbol{C}}$ and $\boldsymbol{\sigma}^{\boldsymbol{N}}$ are the stress tensors of the cytoplasmic ($\boldsymbol{C}$), *i.e.* the intracellular part without nucleus[3], and the nuclear compartment ($\boldsymbol{N}$). To indicate in which regions cytoplasmic and nuclear material properties are valid, an interpolation function for both compartments have to be defined. We chose the interpolation function for the cytoplasmic compartment to be $h(\rho) - h(\psi)$ (*i.e.* cell, but not nucleus), consistent with the interpolation function $h(\psi)$ for the nucleus (*cf.* Fig. 5.1 B). In general, the interpolation functions are not unique, however, they should fulfil certain conditions, namely $h(1) = 1$, $h(0) = 0$ and $\partial_\phi h(1) = \partial_\phi h(0) = 0$ (*cf.* Sect. 4.2.2). Outside of the cell we assume the stress tensor to be zero for simplicity. Note that the cytoplasmic and the nuclear compartments are mechanically coupled (only) via the phase field stress tensor, Eq. (5.3).

Finally, the constitutive relation for the cytoplasm and the nucleus have to be specified. Both compartments are assumed to be linear elastic materials (*cf.* Eq. (2.22)) with Young's moduli E_C and E_N and Poisson ratios ν_C and ν_N for cytoplasm and nucleus, respectively (*cf.* Sect. 2.3.2) [113]. Recall that the stress tensors are defined as

[2] For more details on this aspect, see Sect. 4.2.2.

[3] From now on, when the cell part without nucleus is meant, we will refer to it cytoplasm.

$\boldsymbol{\sigma}^{\alpha} = 2\mu^{\alpha}\boldsymbol{\epsilon} + \lambda^{\alpha} tr(\boldsymbol{\epsilon})\mathbf{1}$, where $\alpha = \{C, N\}$. Here, μ^{α} and λ^{α} are the Lamé coefficients of each compartment and $\boldsymbol{\epsilon}$ is the strain tensor (*cf.* Eq. (2.19)).

In this chapter, we will consider cells of different geometries and therefore different two-dimensional approximations of elasticity theory will be used: the plane stress approximation for strongly spread cells and the plain strain approximation for cells having the shape of a long cylinder (*cf.* Sect. 2.3.3). Furthermore, two of the modelled experimental setups, namely cell compression between two parallel plates and micropipette aspiration, will be described in axial symmetry, *i.e.* quasi-3D. Here, the Lamé coefficients are the three-dimensional ones (*cf.* Eq. (2.23)). We will specifically mention the used approximation for each experiment discussed in this chapter.

5.3 Modelling strongly spread cells

Having proposed the two-phase field method for modelling elastic cells containing a nucleus, we will demonstrate its applicability by studying a cell of height d spread onto a compliant substrate in the 2D plane stress approximation. This situation is biologically highly important, since cells are able to sense the mechanical properties of their environment via internal force generation and transmission of these forces to the outside [19]. The received information can then be used by the cell to adapt its mechanical properties and morphology, and possibly even to induce division, differentiation or motility (processes which are beyond the scope of this work). Similar to the situations studied in Chapter 4, active cell contractility and cell-substrate adhesion have to be included as central features into the proposed method, in order to model a spread cell.

Active stresses Σ_{act} can be straightforwardly introduced into the phase field stress tensor, Eq. (5.3), as an additive contribution. In principle, the active stress can be time- and space-dependent. As discussed in Sects. 2.1.1 and 4.3.1, contractile stresses within a cell arise due to the activity of myosin II motor proteins, which slide cytoskeletal actin filaments relatively to each other [37]. While parts of the contracting actin cytoskeleton span over the nucleus, a fraction $f \in [0, 1]$ can directly bind to it via LINC complexes (*cf.* Sect. 2.2.1) exerting direct contractile stresses on the nuclear boundary [4, 5, 65]. Using the common – and previously used – approximation of an isotropic contractile stress $\boldsymbol{\sigma}_{act} = -\sigma_0 d\mathbf{1}$, with $\sigma_0 > 0$ and $\mathbf{1}$ the identity matrix, we write the active stress tensor as

$$\Sigma_{act} = [h(\rho) - f h(\psi)]\sigma_0 d\mathbf{1}. \tag{5.4}$$

The function in the square brackets indicates in which cell compartment the contractile stress is active. Two limiting cases can be distinguished: for $f = 0$ the whole cell, including the nucleus, is actively contracting, while for $f = 1$ only the cytoplasm, but not the nuclear region, is contracting. Biologically, varying f should correspond to variable degrees of nuclear-cytoplasmic coupling of active contractility (the passive elasticity always corresponds to the one of a coherent elastic body): $f = 0$ can be interpreted as the case in which the nucleus is rather not connected to the actin cytoskeleton, so that the actin cortex is effectively contracting the whole cell body, while $f = 1$ can be interpreted as the case in which the nucleus is connected such that the contractile actin cytoskeleton pulls on it. In the following, we consider $\boldsymbol{\sigma}_{act}$ to be time-independent and homogeneous in the respective cell compartments and investigate only steady state situations.

The second feature needed to model spread cells is cell-substrate adhesion, anchoring the cell and allowing for force transmission from the cytoskeleton to the substrate via integrin-mediated adhesion sites (*cf.* Sect. 2.1.3). We here use again the concept of an elastic foundation as an approximation for a fully elastic substrate (*cf.* Sect. 4.3.1). Engaged adhesion sites are modelled as a spring stiffness density $Y(\boldsymbol{x})$ resisting cell deformations [190–192]. The associated restoring force entering the elastic Eq. (5.2) is then given by

$$\boldsymbol{F}_{adh}(\boldsymbol{x}) = -Y(\boldsymbol{x})h(\rho)\boldsymbol{u} \tag{5.5}$$

where $h(\rho)$ indicates that adhesion sites can only form underneath the cell. In principle, $Y(\boldsymbol{x})$ could be made time-dependent as well, allowing to model dynamics of bond formation [143]. Note, the above formulation of the adhesion force differs from the previous one, Eq. (4.13), by the factor $h(\rho)$. The scaling with the weighting function $h(\rho)$, *i.e.* the restriction of $\boldsymbol{F}_{adh}(\boldsymbol{x})$ to the cell interior, reduces possible effects on the suppression of the displacement field $\boldsymbol{u}$ outside of the cell, if $Y(\boldsymbol{x})$ extends into the outside phase $\rho = 0$ (*cf.* Eq. (4.18)).

5.3.1 Adhered cell of radial symmetry

We first study a circular, elastic cell of radius R_C which is spread and actively contracting on an elastic foundation, as shown in Fig. 5.2 A. Adhesion can be restricted to a ring at the cell periphery of outer radius R_C and inner radius R_Y, such that the cell adheres in the region $R_Y \leq r \leq R_C$ (*cf.* Eq. (4.15)). For $R_Y \longrightarrow 0$, the case of homogeneous adhesion of the whole cell is recovered. This geometry was originally used to explain the ex-

perimentally observed concentration of traction forces at the cell periphery from a mechanical perspective and is analytically solvable for homogeneously adhered cells [71, 191, 192]. Recently, an analytical solution for the case where adhesion is restricted to a ring at the cell's periphery has been also given [194]. Both have already been discussed in Sect. 4.3.2.

To benchmark our numerical framework, we generalized the homogeneous adhesion model ($R_Y \longrightarrow 0$) by additionally considering a disk-like nucleus of radius R_N in the cell's centre. We have calculated an analytical solution to this problem, which we here give in an abbreviated form:

$$u_r(r) = \begin{cases} -\dfrac{\sigma_N d l_N}{2\mu_N + \lambda_N} \dfrac{I_1\left(\frac{r}{l_N}\right)}{I_0\left(\frac{R_N}{l_N}\right) - \frac{2\mu_N}{2\mu_N+\lambda_N}\frac{l_N}{R_N} I_1\left(\frac{R_N}{l_N}\right)} & \text{for } 0 \le r \le R_N \\ \\ A I_1\left(\frac{r}{l_C}\right) + B K_1\left(\frac{r}{l_C}\right) & \text{for } R_N < r \le R_C, \end{cases} \tag{5.6}$$

where $I_0(x)$, $I_1(x)$ and $K_1(x)$ are modified Bessel functions of the first and second kind [215], and A, B and σ_N are long expressions following form lengthy but straightforward algebra. For a sketch of the calculation and the full solution see Appendix A.3.

We begin with the simplest case of a cell fully and homogeneously adhered to the substrate, *i.e.* $Y(\boldsymbol{x}) = Y_0$ and $R_Y \longrightarrow 0$, and with no nuclear-cytoskeletal coupling (*i.e.* $f = 0$). First, the model with a nucleus rigidity $E_N/E_C = 1$ is compared to the phase field model without an explicit nucleus from Sect. 4.3.2) and the analytical solution, Eq. (5.6). Figure 5.2 B (upper panel) shows both phase field solutions (blue curve: with explicit nucleus, red curve: without nucleus) and the analytical one (black curve) for the radial displacement field u_r normalized by the cell radius r_C in mechanical equilibrium. All three are in excellent agreement with each other. This demonstrates that for the case, where cytoplasmic and nucleus compartment are mechanically indistinguishable, the current approach and the previously verified one without nucleus yield the same results, as to be expected. This also applies to the phase field profile of $\rho(\boldsymbol{x}, t)$, as shown in Fig. 5.2 B (lower panel).

In Fig. 5.2 C (upper panel) the phase field (solid curves) and analytical solutions (dashed) for the radial displacement field u_r for different nuclear stiffnesses and radii are shown. Both are in very good agreement, further confirming our approach.

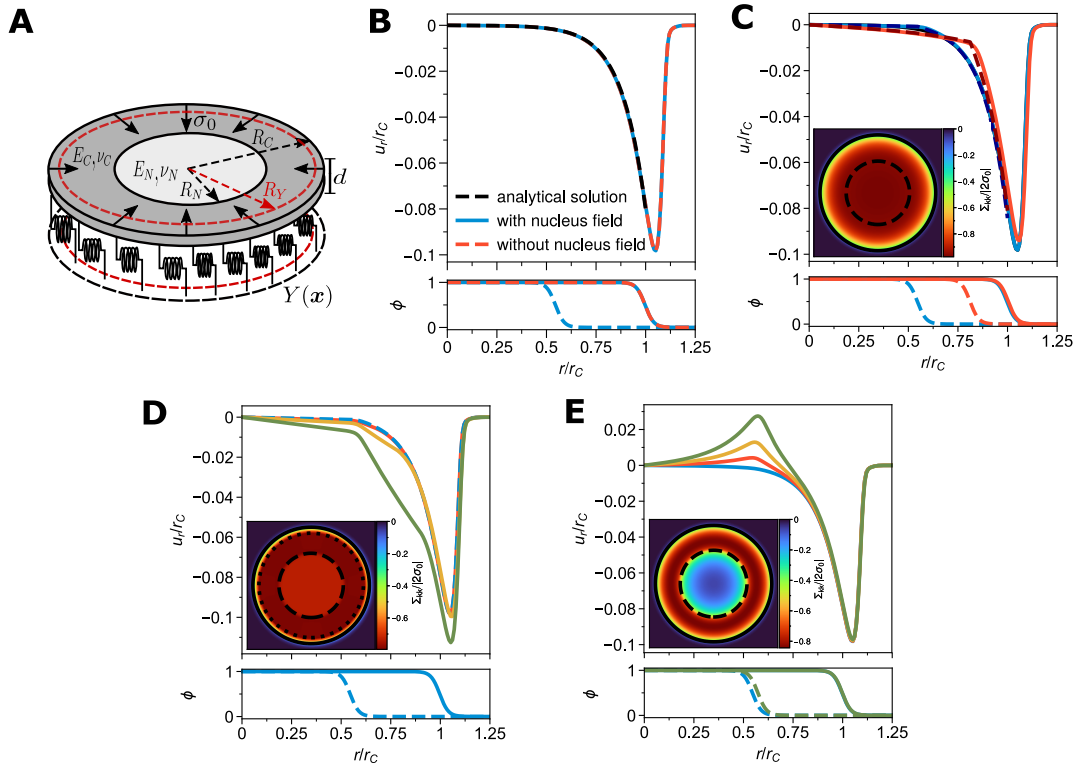

Figure 5.2: A Sketch of the model for a cell (thickness d, radius R_C) with a concentric nucleus (radius R_N). The cell is contracting isotropically with active stress σ_0 while being adhered to a substrate via a spring stiffness density $Y(\boldsymbol{x})$ on a ring $R_Y \leq r \leq R_C$. The cytoplasm (E_C, ν_C) and the nucleus (E_N, ν_N) can have different material properties. **B** Comparison of phase field models with and without nucleus. Shown in the upper panel are the phase field solution without nucleus (red dashed), with nucleus for $E_N/E_C = 1$ (blue solid) and the analytical one (black dashed) for the radial displacement field u_r, normalized by the cell radius in mechanical equilibrium r_C. The lower panel shows the radial profile of ρ (blue solid) and ψ (blue dashed) of the model with nucleus and for ρ (red dashed) without it. **C** Full homogeneous adhesion case with $R_Y = 0$. The upper panel shows the phase field (solid) and analytical (dashed) solutions for u_r/r_C, for the cases: $E_N/E_C = 10$, $R_N/R_C = 0.5$ (blue); $E_N/E_C = 10$, $R_N/R_C = 0.75$ (red); and the phase field solution for $E_N/E_C = 1$ and $R_N/R_C = 0.5$ (black, mostly covered by the blue curve). The inset shows the trace of the stress tensor, normalized by the active stress σ_0, for $E_N/E_C = 10$, $R_N/R_C = 0.5$; the contour lines correspond to $\rho = 0.5$ (cell, solid) and $\psi = 0.5$ (nucleus, dashed). The lower panel shows the radial profile of ρ (cell, solid) and ψ (nucleus, dashed) in mechanical equilibrium with colours corresponding to the upper panel. **D** Adhesion on an outer ring only. In the upper panel phase field solutions for u_r/r_C are shown for $E_N/E_C = 10$, $R_N/R_C = 0.5$ and varying $R_Y/R_C = 0.5, 0.6, 0.7.0.8$ (blue to green). The inset shows the normalized stress for $R_Y/R_C = 0.8$ (dotted line marks inner ring boundary) and the lower panel the phase field profiles for the case $R_Y/R_C = 0.5$. **E** Homogenous adhesion case for varying $f = 0, 0.2, 0.5, 1$ (blue to green) (*cf.* Eq. (5.4)) for a nucleus of radius $R_N/R_C = 0.5$. Shown are the phase field solutions for u_r/r_C. The inset shows the normalized stress for $E_N/E_C = 2$ and $f = 1$ and the lower panel the phase field profiles for $f = 0$ (blue) and $f = 1$ (green). All simulations were performed on $N = 512 \times 512$ grid points on a domain of $50\,\mu\text{m} \times 50\,\mu\text{m}$. If not specified above, the other mechanical parameters are $R_C = 12.5\,\mu\text{m}$, $d = 1\,\mu\text{m}$, $E_C = \sigma_0 = 1\,\text{kPa}$, $\nu_C = \nu_N = 0.5$ and $Y_0 = 0.8\,\text{nN}/\mu\text{m}^3$. Further parameters as in Appendix B.3.2 Table B.4.

Deviations result from the diffuse description of the nucleus-cytoplasm boundary in the phase field framework and can be reduced by decreasing its interface width. The kink at the nucleus-cytoplasm interface, occurring in both the analytical and numerical solution, is due to the different rigidities of the two considered cell compartments. Consistent with previous results, the highest deformations are visible at the cell periphery [191]. This is associated with high traction stresses at the periphery and lowered total internal stresses, as visualized in the inset of Fig. 5.2 C by plotting the trace of the stress tensor $tr(\Sigma)$, normalized by the applied active stress level σ_0.

Physiologically, nuclei of animal cells can take up to 30 % of the total cell volume and can be up to 10-fold stiffer than the rest of the cell [1, 75, 79, 83]. Hence, the question arises, how important the nucleus is for cell mechanics. For a nucleus of half the cell's radius, $R_N/R_C = 0.5$ (which is in the above volume range), the nucleus stiffness E_N has only a negligible effect on the cell's deformation, as exemplified in the upper panel of Fig. 5.2 C for a stiff nucleus ($E_N/E_C = 10$; blue curve) and a soft nucleus ($E_N/E_C = 1$; black curve, mostly hidden by the blue one). Increasing the nuclear radius, a realistically stiff ($E_N/E_C = 10$) nucleus (red curves) leads to considerably different slopes in the displacement field. However, the overall position of the cell periphery remains approximately the same, *cf.* the solid curves in the lower panel of Fig. 5.2 C, displaying the radial phase field profiles.

It is important to note that the displacement field in the nucleus always remains small. This demonstrates that strong cell adhesion protects the nucleus against large deformations and stresses. The determining factors are the distance between the nucleus and the cell boundary, $R_C - R_N$, and the characteristic distance over which stress can propagate through the cytoplasm, which for an adhering cell is given by the localization length $l_C = \sqrt{E_C d/Y(1-\nu_C^2)}$. [191] Peripheral cell adhesion seems to be sufficient for protecting the nucleus, corresponding to the experimental observation of strong adhesions forming mostly at the cell periphery, while the basal side under the nucleus is mostly adhesion free [216].

We further recall from Sect 4.3.2, that in order to compare the analytical solution, Eq. (5.6), with the numerically obtained phase field solutions, the initial radius of the nucleus (R_N) and the cell (R_C) have to be replaced by the current radius – here in mechanical equilibrium – of the nucleus (r_N) and the cell (r_C). Importantly, the applied stress is reduced by the suppression of the displacement field outside of the cell (*cf.* Sect. 4.2.2

and Eq. (5.2)) to an effective stress

$$\sigma_{0,eff} d = \sigma_0 d - \frac{\gamma_0 + Y(\boldsymbol{x}) h(\rho)}{r_c} \int \left[1 - h(\rho)\right] u_r r dr, \tag{5.7}$$

similar to Eq. (4.18). However, due to the weighting of the adhesion strength $Y(\boldsymbol{x})$ with $h(\rho)$ its impact becomes small.

The shielding observed above can have a major impact on the nuclear mechanosensing ability of stimuli originating at the cell edge. In a second study we therefore restrict the adhesion to a ring at the cell periphery of inner radius R_Y, to see whether the nuclear deformation increases, indicating a higher perception of mechanical stimuli. In most cell types, the nucleus occupies not more than a third of the cellular volume. Therefore, we fix the nucleus radius to $R_N/R_C = 0.5$, for which we found above that the nuclear stiffness has only a negligible effect on cell mechanics, and the stiffness to $E_N/E_C = 10$. We then examine the radial deformation u_r upon varying the inner radius R_Y of the adhesion ring between $R_Y/R_C = 0.5 - 0.8$ as shown in the upper panel of Fig. 5.2 D (blue to green curves). First we remark, that the deformation field is linear in the non-adhered cell parts, *i.e.* both in the nucleus and the inner part of the cytoplasm. As visible from the displacement field, a larger R_Y, and therefore a decreased adhesion area, increases the deformation the nucleus experiences. This demonstrates that adhesion restricted to the cell periphery leads to an increased stress propagation to the nucleus, as also visible in the inset of Fig. 5.2 D. Nevertheless, peripheral adhesion is sufficient to prevent large deformations as shown by the only slightly increased deformation peak compared to the fully adhered case in Fig. 5.2 C (upper panel). Similar results are obtained for soft nuclei, *i.e.* $E_N/E_C = 1$ and $E_N/E_C = 2$ with the same radius $R_N/R_C = 0.5$ (*cf.* Appendix B.3.1 Fig. B.2). This agrees with recent experiments on optogenetic activation of whole cells that showed only small differences in whole-cell contractility between cells on disk and ring adhesion geometries [217].

Having analysed the effect of adhesion geometry, we now return to the situation of a fully adhered disk, but now with a varying fraction f of actin filaments that couple to the nucleus via LINC complexes. This coupling leads to an tensile stress on the nuclear boundary upon filament contraction (*cf.* Eq. (5.4)). Figure 5.2 E (upper panel) demonstrates the radial displacement field u_r for $R_N/R_C = 0.5$ and $E_N/E_C = 2$ for different degrees of nuclear-cytoskeletal coupling ($f = 0, 0.2, 0.5, 1$). The peaks close to the nucleus-cytoplasm interface clearly show a radial stretching of the nucleus, which is also visible in the lower panel of Fig. 5.2 E showing the phase field profiles for the

cases $f = 0$ (blue) and $f = 1$ (green). Interestingly, the whole-cell deformation, *i.e.* the displacement of the cell membrane, indicated by the ρ-interface position, remains unaffected. For increasing coupling parameter f, the nucleus experiences higher tensile stresses, also visualized in the inset of Fig. 5.2 E for the case $f = 1$, in contrast to the previous discussed cases.

We also investigated the combination of the ring adhesion geometry combined with the maximal nuclear-cytoskeletal coupling $f = 1$, showing a substantial increase in the radial stretch of the nucleus due to the absence of adhesion in its vicinity (*cf.* Appendix B.3.1 Fig. B.3).

In summary, the above results verify our elastic phase field approach and indicate that the transmission of mechanical cues to the nucleus strongly depends on the actual adhesion geometry and the possible force transmission from the cytoskeleton to the nucleus.

5.3.2 Contractile cells on adhesion patterns

Micro-patterned adhesive substrates are a standard setup for studying cellular behaviour in structured environments [200–202, 218]. Adherent cells are always under contraction, as demonstrated by the ubiquitous invaginated arcs that form when cells adhere with point-like adhesions [71, 219]. Here, we investigate the impact of the nucleus on the overall cell morphology in such geometries. As a first example, we study a rectangular pattern with four (identical) circular adhesive patches of radius r_{adh} located at its corners. A 2D rectangular cell, described in plane stress is allowed to form focal adhesions at the corners and to contract isotropically under a contractile stress σ_0. The nucleus initially has a circular shape of radius R_N with physiological nucleus-to-cell volume ratio $V_N/V_C \approx 0.17$. We neglect nucleo-cytoskeletal coupling, *i.e.* $f = 0$. For the adhesion strength $Y(\boldsymbol{x})$ we use a smoothly varying field, transitioning in a tanh-like manner from the maximal value Y_0 in the focal adhesion towards zero outside of it, *i.e.*

$$Y_i(\boldsymbol{x}) = \frac{Y_0}{2}\left[1 - \tanh\left(\frac{r - r_{adh}}{\sqrt{2D_Y}}\right)\right] \tag{5.8}$$

for each adhesive spot i, where D_Y sets the steepness of the transition region. Primarily, this ensures numerical stability compared to pinning the cell completely to the focal adhesion (via the boundary condition $\boldsymbol{u} = 0$, *cf.* Eq. (4.14) and Ref. [10]). It also would allow to study different adhesive strengths in different focal adhesions.

Representative results for varying nuclear stiffness, position and shape are shown in

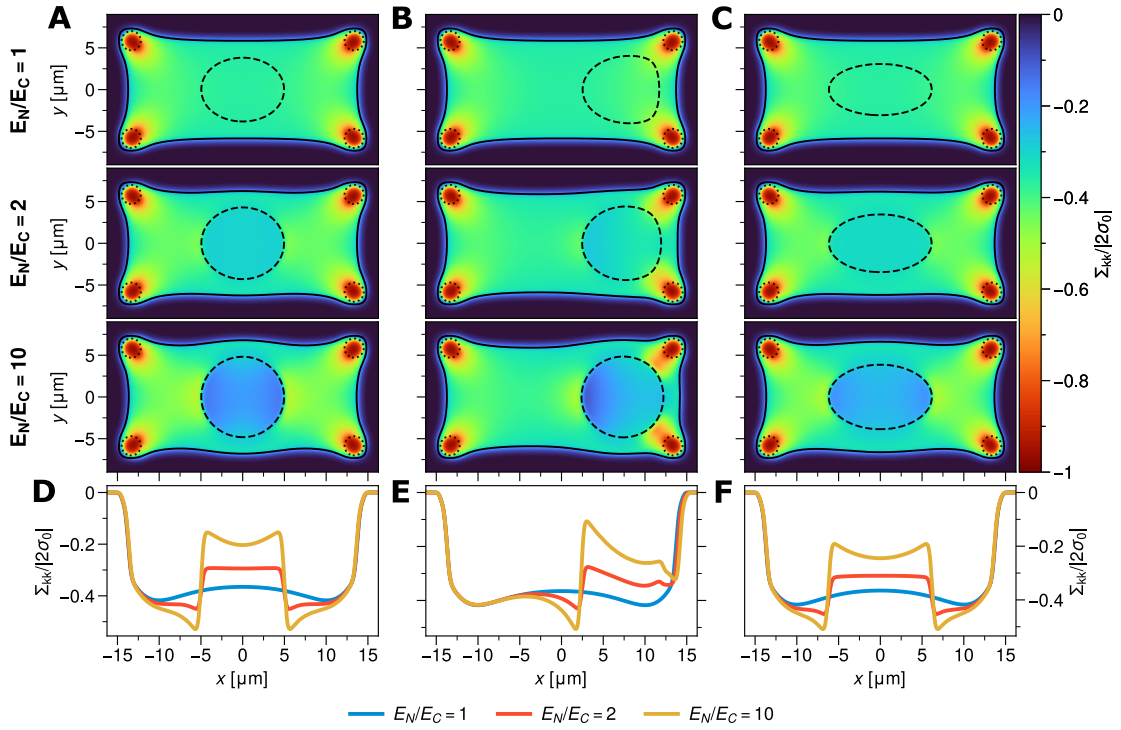

Figure 5.3: A spread cell is adhering to a rectangular shape due to adhesive spots in its corners.The adhesive spots (dotted) have a radius r_{adh} =1.15 µm with high Y =16 nN/µm^3, to prevent slipping from the adhesion sites. The cell is contracting under an isotropic contractile stress $\sigma_0/E_C = 0.4$. The trace of the normalized stress tensor $\Sigma_{kk}/|2\sigma_0|$ is shown as colour map for the cases $E_N/E_C = 1, 2, 10$ (top to bottom) with an initially round nucleus (**A**) centred in the cell, (**B**) shifted by $\Delta x = 1.5\ R_N$ in x-direction and (**C**) for an elliptical nucleus (initial eccentricity $e = 0.64$) in the cell's centre. Cell and nucleus boundary positions are marked by contour lines corresponding to $\rho = 1/2$ (solid, cell) and $\psi = 1/2$ (dashed, nucleus). **D**-**F** Shown is the trace of the stress tensor along the symmetry line $y = 0$ for the corresponding simulations shown in (**A**)-(**C**). All simulations were performed on $N = 1024 \times 512$ grid points on a domain of 50 µm × 25 µm. Initial cell dimensions are 30 µm × 15 µm with $R_N = 5$ µm, $d = 1$ µm, $E_C = 1$ kPa and $\nu_C = \nu_N = 0.5$. Rest as in Appendix B.3.2 Table B.4.

Fig. 5.3. The panels of Fig. 5.3 A study a centred and circular nucleus and demonstrate the effect of an increased nuclear-cytoplasmic stiffness ratio E_N/E_C. Clearly, the nucleus is deformed by the invaginated arcs for low nuclear stiffness. A higher nuclear stiffness rather changes the shape of the cell by perturbing the formation of invaginated arcs, demonstrating again that localized adhesion together with an increased nuclear stiffness protect the nucleus against large deformations/stresses. Similar perturbations are observable for example for cells spreading on nanonets [220]. Yet one also sees how stress bridges start to emerge between nucleus and adhesion sites, which look like precursors of stress fibres.

Similar to the previous study in circular geometry, the distance between the nucleus and the cell edge is a determining factor for the magnitude of the morphology perturbation. If the nucleus position is shifted away from the cell's centre, as shown in *cf.* Fig. 5.3 B, a stress accumulation at the cytoplasm-nucleus boundary can be observed, while the stress is lowered on the opposite side of the nucleus. Other observations made above still apply here, *i.e.* the stiffer the nucleus, the less it gets deformed and the more it perturbs the overall cell morphology. However, the asymmetry introduced by the positional shift of the nucleus clearly leads to an asymmetric deformation of the softer nuclei.

Lastly, we study the effect of nuclear shape, as nuclei are not only spherical/circular but are also known to be of oval/elliptic morphology [79]. We centre the nucleus again in the cell and change its aspect ratio $AR = b/a$, where a and b are the semi-major and semi-minor axis length of the ellipse, respectively.[4] Figure 5.3 C shows the stress distribution for $AR \approx 0.77$ and different $E_N/E_C = 1, 2, 10$. The resulting stress distribution within the cell is qualitatively very similar to Fig. 5.3 A, suggesting that in the present case the initial nuclear morphology is of minor importance. Nevertheless, the average deformation of the cell decreases the lower the aspect ratio and the higher the stiffness of the nucleus is (*cf.* Appendix B.3.1 Fig. B.4).

In Fig. 5.3 D-F the trace of the stress along the symmetry line $y = 0$ is depicted for the case shown in Fig. 5.3 A-C, clearly showing the stress decrease for higher E_N/E_C and its asymmetry when shifting the nucleus. Note again the similarity in the stress between the centred spherical and elliptical nucleus in Fig. 5.3 D and F.

Interestingly, as visible in Fig. 5.3 B, the stress "builds a bridge" between the close-by focal adhesions and the nucleus, [221] quite possibly impacting the mechanosensing of the nucleus. One can hypothesize that the asymmetric stress distribution for shifted nuclei allows the cell to differentiate between left and right, which may be important to polarize for cell migration.

5.3.3 Focal adhesion failure

Having demonstrated that the proposed modelling framework is able to describe static spread cells with nucleus in complex geometries, we now give an example of a simple dynamic response. Like in the last example, we consider a cell on a micro-patterned adhesive environment favouring a hexagonal cell shape. The adhesion spots are again

[4] For a circle $AR = 1$ and for an ellipse $AR < 1$.

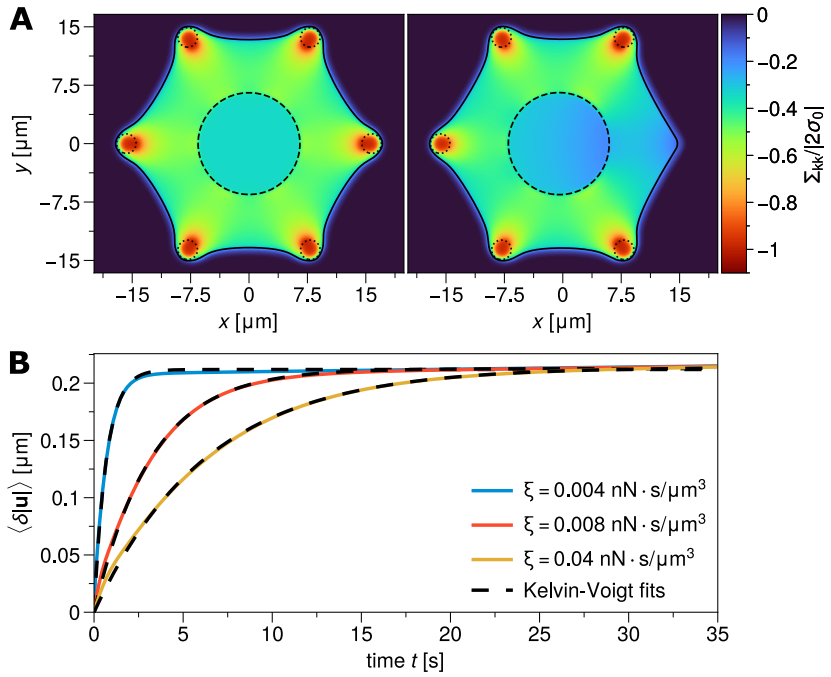

Figure 5.4: A A cell with nucleus was allowed to spread in a hexagonal adhesion pattern and to contract isotropically with $\sigma_0/E_C = 0.4$ until it reached mechanical equilibrium (left panel). Subsequently, the most right adhesion spot was removed and the cell evolved towards a new mechanical equilibrium (right panel). The colour map shows the normalized trace of the stress tensor. The cell shape (isocline $\rho = 0.5$, solid black) and nucleus shape ($\psi = 0.5$, dashed black) are also shown. **B** Shown is the average displacement $\langle\delta|\boldsymbol{u}|\rangle$, with respect to the initial reference displacement in (A), as a function of time t for different friction coefficients ξ. For all tested ξ, the behaviour is the one of a Kelvin-Voigt model. The simulations were performed on $N = 512\times512$ grid points on a domain of 50 µm × 50 µm. Initial cell edge length is 17.5 µm and $R_N = 6.65$ µm with cell height $d = 1$ µm resulting in $V_N/V_C \approx 0.17$. Further, $E_N/E_C = 10$ with $E_C = 1$ kPa, $\nu_C = \nu_N = 0.5$, $r_{adh} = 1.25$ µm and $Y_0 = 16\,\mathrm{nN/\mu m^3}$. Further parameters as in Appendix B.3.2 Table B.4.

described by a smoothly varying function, *cf.* Eq. (5.8).

The cell first contracts isotropically under a stress σ_0 until it reaches mechanical equilibrium, *i.e.* $\nabla\cdot\Sigma + \boldsymbol{F} = 0$. The resulting shape, including stress focusing at the adhesion spots and invaginated arcs in between, is shown in the left panel of Fig. 5.4 A for a nucleus-cell volume ratio $V_N/V_C \approx 0.17$ and nucleus rigidity $E_N/E_C = 10$. Subsequently, one of the adhesion spots (here, the most right one) is suddenly removed, mimicking the rupture/dissolution of a focal adhesion, and the cell deforms into a new mechanical equilibrium given by this geometry (*cf.* right panel of Fig. 5.4 A). One can clearly see that the cell relaxes a substantial amount of stress in the area of the missing adhesion

point. The stress inside the nucleus is also reduced, in the shown example by 14.5 %, and again shows an asymmetry. Because our elastic phase field model uses a reference configuration, it is attributed with a memory preventing the cell edge, which was connected to the removed adhesion, to relax fully to a new invaginated arc. Consequently, one still sees the remnants of the original adhesion in the cell morphology.

To quantify the dynamics of this relaxation, we investigated the cell-averaged displacement

$$\langle |\boldsymbol{u}| \rangle = \frac{1}{V_{cell}} \int \rho |\boldsymbol{u}| d\Omega, \tag{5.9}$$

where the cell's volume is given by $V_{cell} = \int \rho d\Omega$. Figure 5.4 B shows the deviation

$$\langle \delta |\boldsymbol{u}(t)| \rangle = \langle |\boldsymbol{u}(t)| \rangle - \langle |\boldsymbol{u}_{ref}| \rangle, \tag{5.10}$$

from the average reference displacement $\langle |\boldsymbol{u}_{ref}| \rangle$ at the time point of the removal of the focal adhesion as a function of time and for different friction coefficients ξ (*cf.* Eq. (5.2)) and $E_N/E_C = 10$. As can be seen, the displacement $\langle \delta |\boldsymbol{u}| \rangle$ always levels at the same plateau value, reflecting that mechanical equilibrium is reached, with ξ determining the relaxation time.

It should be noted that the elastodynamic formulation of Eq. (5.2) was introduced out of necessity to couple the phase field dynamics with elasticity in a reversible fashion, as explained in Chapter 4 and Ref. [10]. Hence, if one wants to describe a system with "pure" elastic behaviour, one should not probe the system on time scales τ faster than the one set by ξ. On the other hand, if one does so, the average displacement follows the relaxation behaviour of a viscoelastic material with long-term elastic behaviour. This is reflected by the dashed curves in Fig. 5.4 B where we applied a Kelvin-Voigt model, predicting

$$\langle \delta |\boldsymbol{u}(t)| \rangle = u_{max} \left[1 - \exp\left(\frac{t}{\tau_R} \right) \right] \tag{5.11}$$

to interpret the data, which fits perfectly. Here u_{max} is the maximum average displacement and τ_R the characteristic relaxation timescale. The Kelvin-Voigt model is a widely used and experimentally validated model for cellular mechanics, describing that mechanical relaxation does not occur instantaneously (as in linear elasticity), but is retarded by internal friction, stemming from viscous flow and cytoskeletal reorganization. For a Kelvin-Voigt material the relaxation timescale is given by $\tau_R = \eta/E$, where E is the Young's modulus and η the material's viscosity. We verified that the correspondence to a Kelvin-Voigt model holds for all tested nucleus stiffnesses, although slightly less

accurate for softer nuclei (*cf.* Appendix B.3.1 Fig. B.5). The above comparison hence allows to associate the friction coefficient ξ with an effective viscosity η. However, since the cell is a composite material of cytoplasm and nucleus, both E and η entering τ_R are cell-averaged quantities.

5.4 Cells in confinement and modulus measurements

We now turn to the problem of cells in confinement, again focusing on the effects of the nucleus. On the one hand, in their physiological environment, cells are often subject to (dynamic) straining induced by their surrounding. Examples include cyclic stretching in lung and vascular tissue or the migration of immune cells and metastatic cancer cells through narrow openings in tissues or fibrous networks. On the other hand, several experimental methods have been developed to probe cellular mechanical responses, including local indentation using an atomic force microscope [222, 223], compression of cells between two plates [92, 93, 224–228] and cell aspiration by micropipettes [229–234]. Here, we show how the latter two can be modelled using our framework to extract effective elastic moduli.

In both experimental setups, the interaction of the examined cell with the confining obstacles – the plates of the compression apparatus or the tube walls of the micropipette – is crucial. In the phase field method, such "obstacles" can be described by implementing another, static phase field $\varphi(\boldsymbol{x})$, also having tanh-like transitions from $\varphi = 1$ within the obstacle to $\varphi = 0$ outside, and which is assumed here to be perfectly rigid. The local presence of the obstacle is then manifesting itself by interactions of the cell's phase field with φ. Motivated by a phenomenological excluded volume potential of the form $\mathcal{F} = \frac{\alpha}{2}\rho^2\varphi^2$ presented earlier [123, 151, 152], we add the following excluded volume force to the force $\boldsymbol{F}$ entering Eqs. (5.1) and (5.2):

$$\boldsymbol{F}_{excl} = \alpha\rho\varphi^2\frac{\nabla h(\rho)}{f(h(\rho))}. \tag{5.12}$$

Here the first term, including the interaction strength α, is the derivative of the excluded volume energy. $\nabla h(\rho)$ indicates that the volume exclusion force acts orthogonal to the ρ-interface[5] and is restricted to the interface region.[6] Finally, $f(x) = \sqrt{1+\epsilon(\nabla x)^2}$

[5]The orthogonality to the ρ-interface follows from $\nabla h(\rho) = \partial_\rho h(\rho)\nabla\rho$. Hence, $\boldsymbol{F}_{excl}$ acts in the direction $\boldsymbol{n}_{h(\rho)} = \nabla h(\rho)/|\nabla h(\rho)| = \nabla\rho/|\nabla\rho| = \boldsymbol{n}_\rho$, *i.e* normal to the interface.

[6]Practically, $\boldsymbol{F}_{excl}$ is implemented to be only active if $\rho\varphi^2 \geq 10^{-2}$ to prevent 'long-range' interaction if α is large.

with a small $\epsilon \ll 1$ implements saturation of the force in case the phase field gradient becomes too steep [152].

5.4.1 Compression of cells between two parallel plates

Compressing cells between two parallel plates is nowadays a standard experimental technique to mechanically probe global cell mechanics [83, 225–228, 235, 236]. For instance, in combination with computational predictions, it has been demonstrated that for mitotic cells the cell cortex dominates cell mechanics. [228] Beyond that, also cellular responses to increased confinement have been addressed, evidencing that it can induce the mesenchymal-amoeboid transition [237] and trigger cell migration [92, 93]. In the latter studies it was suggested that the extent of nuclear compression determines the onset of this response.

We model compression experiments by implementing the upper and lower plates via the field $\varphi(\boldsymbol{x})$. Both plates are initially not in contact with the cell, such that $\boldsymbol{F}_{excl} = 0$. They are moved towards each other successively by the grid spacing Δx each time the cell has relaxed into mechanical equilibrium. Having reached the desired compression level/plate distance, this procedure can be reversed to release the cell from the confinement. Note that we study here the quasi-static, purely elastic process to be able to compare with analytical solutions; however, it is possible to also study compression that is continuous in time, where the response will then be of Kelvin-Voigt-type (*cf.* Sect. 5.3.3).

So far, in Sect. 5.3 we used an effectively 2D plane stress approach, which was justified for a thin, spread cell. In the compression experiment, the simplest effective 2D problem would be the plane strain approach, corresponding to a long cylinder with circular cross-section (*cf.* Sect. 2.3.3). To see how sensitive the compression experiment is to the geometry, we compared this simple case (unrealistic for a cell) to the axially symmetric case of a 3D sphere compressed between the plates. Note that the latter needs solving all equations defined above in cylindrical coordinates.

Figure 5.5 A shows the distribution of stresses, visualised via the trace of the stress tensor $tr(\Sigma)$, within the cross-section of a cell in plane strain (top, cylinder geometry; note that this implies that the nucleus is also a cylinder) and of a spherical cell in axial symmetry (bottom). The nuclear stiffnesses are $E_N/E_C = 1$ (left), $E_N/E_C = 2$ (middle) and $E_N/E_C = 10$ (right), respectively. For all shown cases, the nucleus radius is set to $R_N/R_C = 0.5$. In the snapshots, the plates have a distance of 90% of the initial cell diameter $2R_C$. Both cases, plane strain and axial symmetry, show an increased stress

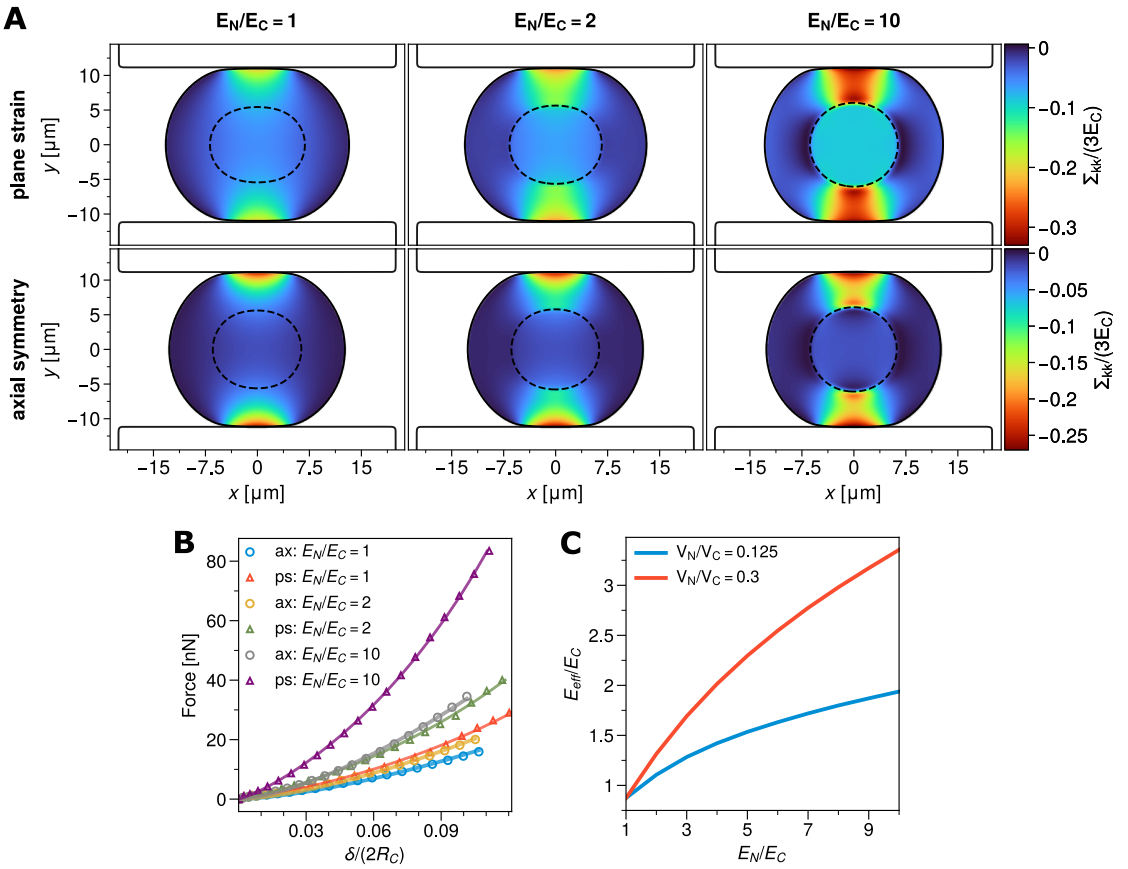

Figure 5.5: A Compression of a cell in the plane strain geometry (long cylinder, top) compared to a spherical cell (axial symmetry, bottom). Shown is the trace of the stress for the cases $E_N/E_C = 1, 2, 10$, normalized to the cytoplasm stiffness E_C. The stress tensor is only shown for $\rho > 0.5$ with the isolines corresponding to $\rho = 0.5$ (black solid line) indicating the cell boundary, $\psi = 0.5$ (black dashed line) for the nucleus boundary and $\varphi = 0.5$ marking the boundary of the plates (black solid line outside the cells). Snapshots are for a compression of ≈10 % of the initial cell diameter. **B** Numerically obtained force-compression curves. The symbols are numerical solutions for plane strain (triangles) and axial symmetry (circles), respectively, *cf.* panel **A**. The solid curves are fits to the respective analytical solutions (available in the absence of the nucleus). **C** For the case of axial symmetry, we extracted an effective elastic modulus from fits as shown in panel **B**. In the physiological range of nucleus sizes and stiffness, the effective modulus measured in compression is up to three times larger than the one of the pure cytoplasmic stiffness. Colours in **B**: $E_N/E_C = 1$ in axial symmetry (blue), $E_N/E_C = 2$ in axial symmetry (yellow), $E_N/E_C = 10$ in axial symmetry (grey); $E_N/E_C = 1$ in plane strain (red), $E_N/E_C = 2$ in plane strain (green), $E_N/E_C = 10$ in plane strain (violet). Colours in **C**: nucleus size of $V_N/V_C = 0.125$ (blue); nucleus size $V_N/V_C = 0.3$ (red). Simulations were performed on $N = 512 \times 512$ grid points on a domain of size 50 µm × 50 µm. Mechanically relevant parameters for all shown simulations (if not mentioned otherwise) are $R_N = 6.25$ µm, $E_C = 1$ kPa, $\nu_C = \nu_N = 0.48$, and $\alpha = 6$ kPa. Rest as in Appendix B.3.2 Table B.4.

concentration for increasing nuclear stiffness in the regions between the nucleus and the plates, with a band-like stress accumulation connecting the cell edge in contact with the plates and the nucleus. This is reminiscent of the 'stress bridges' between nucleus and focal adhesion as seen in Fig. 5.3 A-C, again possibly indicating a special role in the perception of mechanical stimuli by a stiffer nucleus. The plane strain case shows an overall higher stress, since it does not allow a considerable stress relaxation within the nucleus. Nevertheless, the overall behaviour is quite similar.

To further quantify the compression experiments, we obtained the force-compression curves for the results shown in Fig. 5.5 A. This was done by calculating the total force

$$F = \int |\nabla \cdot \Sigma| \rho d\Omega \tag{5.13}$$

in mechanical equilibrium for the respective total compression δ of the cell, normalized by the cell diameter $2R_C$, as shown in Fig. 5.5 B. As can be noticed, a consistently higher force is required to deform a plane strain cylinder (triangles) by the same δ as compared to a sphere in axial symmetry (circles), consistent with Fig. 5.5 A. Note that for the resulting line contact problem in plane strain, the fundamental measure for this case is the in-plane force per length F/L [238]. In order to compare the force-compression curves in both geometries, we determined the length of the cylinder $L = 4/3R_C$ in plane strain, such that the cylinder volume is equal to the sphere volume in axial symmetry and multiplied the average force per length by L.

Importantly, for both contact problems studied here, plane strain and axial symmetry, there exists an analytical solution for the force-compression relation in the absence of the nucleus [238]. The force-compression relation of an elastic sphere compressed by two rigid plates is the Hertz problem with

$$F \propto \delta^{3/2} \tag{5.14}$$

for an arbitrary pressure distribution [238, 239]. In plane strain, the relation is more complicated and can be given as

$$\delta \propto \frac{F}{L} \log\left(\frac{B}{\sqrt{F/L}}\right), \tag{5.15}$$

where B is a constant containing information about the cell size and its effective stiffness [238, 240]. Figure 5.5 B shows, apart from the numerically obtained data (symbols),

also fits to these relations (solid curves), resulting in a very good agreement for both geometries. Importantly, the Hertzian theory $F \propto \delta^{3/2}$ is still valid, even in the presence of a rather large and stiff nucleus. Throughout all tested E_N/E_C the plane strain geometry (triangles) requires a considerably higher force for the same compression δ compared to the respective axial symmetric case (circles), consistent with the previous observations.

As the two-plate setup is extensively used to measure cellular stiffnesses, we tried to infer the effective Young's modulus E_{eff} (*i.e.* cell plus nucleus as measured in the respective apparatus) of our model cell in the physically relevant axial symmetric situation. We used the full Hertzian law

$$F = \frac{\sqrt{2R_C}}{3} E' \delta^{3/2}, \tag{5.16}$$

for a parabolic pressure distribution with F the total force per plate and $E' = E_{eff}/(1 - \nu_{eff}^2)$. Here E_{eff} and ν_{eff} are the effective elastic parameters of the cell-nucleus composite for rigid plates [239]. We assumed here that $\nu_{eff} = \nu_C = \nu_N$. In general, the effective modulus in Eq. (5.16) is $1/E^{'} = (1 - \nu_P^2)/E_P + (1 - \nu_{eff}^2)/E_{eff}$, where ($E_P$, ν_P) and (E_{eff}, ν_{eff}) are the (effective) Young's moduli and Poisson ratios of the plates of the compression apparatus (P) and the compressed cell, respectively [238]. As we here consider rigid plates $E_P \to \infty$. Equation (5.16) can be derived from the original Hertz problem of an elastic sphere pressed into an elastic half-space.

Figure 5.5 C then shows that E_{eff} increases non-linearly with increasing nucleus stiffness E_N. For physiological nucleus sizes $V_N/V_C = 0.125 - 0.3$, the effective modulus E_{eff} experiences an up to three-fold increase for $E_N/E_C = 10$. Note that for $E_N/E_C = 1$ the comparison with Hertzian theory yields an effective modulus slightly $E_{eff} < 1$, resulting from the unknown pressure distribution in the phase field simulation. Nevertheless, we argue that because the deviation is small, the assumption of a parabolic pressure distribution in the Hertzian law is still sufficiently accurate.

Finally, while the above results indicate a considerable effect of nucleus size and stiffness on the mechanics of a cell, we now consider cellular shape. Figure 5.6 shows the compression of an initially pancake-like shaped cell (A) and droplet-like cell (B) in axial symmetry, for different nucleus stiffnesses $E_N/E_C = 1, 2, 10$. The pancake-like geometry is similar to the one studied in Ref. [228]. They can be directly compared to the initially spherical cell in Fig. 5.5 A (bottom). Again, for increasing nucleus stiffness a redistribution of stresses within the cell is visible. For the pancaked-like cell and $E_N/E_C = 1$, the

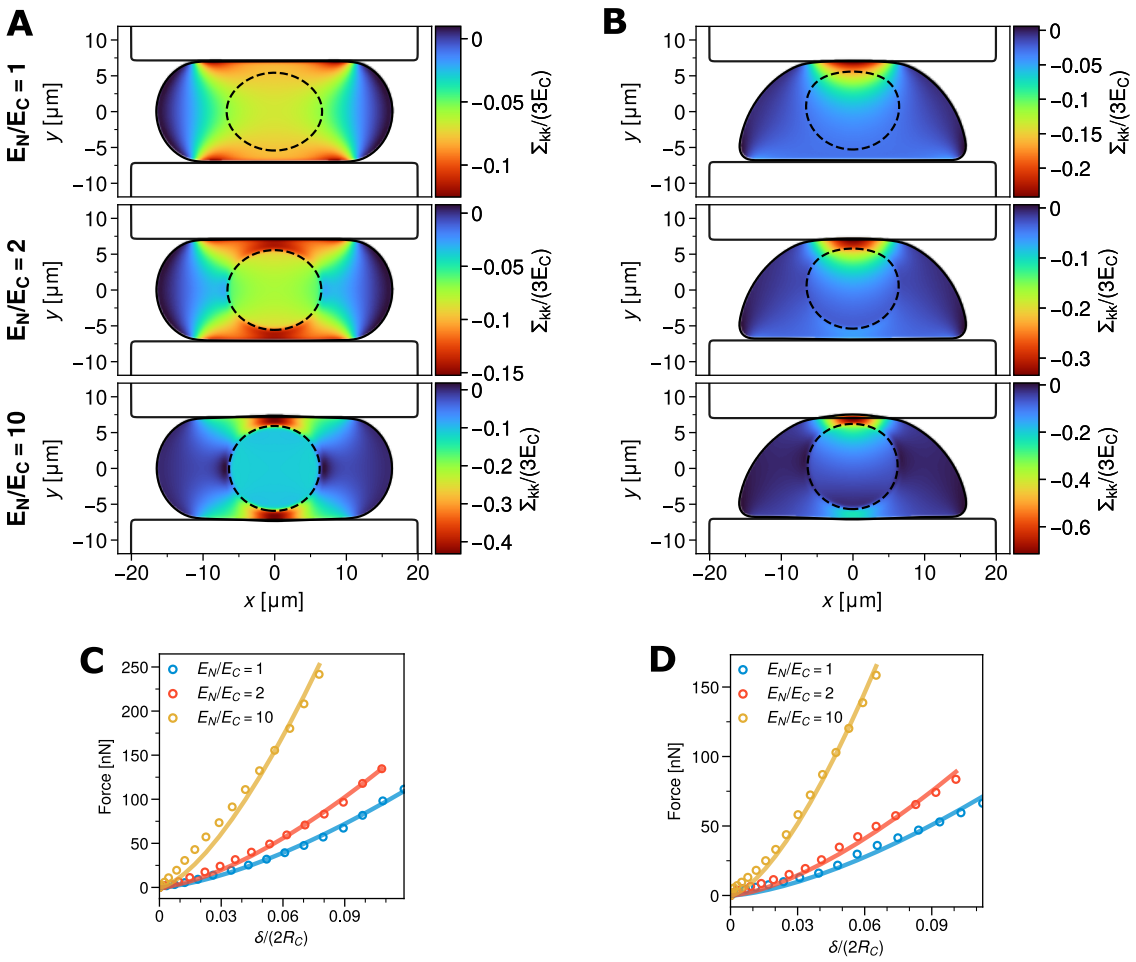

Figure 5.6: Compression experiments similar to Fig. 5.5 of (**A**) pancaked-shaped and (**B**) droplet-shaped cells with nuclei of stiffness $E_N/E_C = 1, 2, 10$ between two parallel plates in axial symmetry. Shown is the normalized trace of the stress tensor for $\rho > 0.5$. The cell boundary is indicated by the isoline $\rho = 0.5$ (black solid line), the nucleus boundary by the isoline $\psi = 0.5$ (dashed black line) and the plate boundaries by $\varphi = 0.5$ (black solid lines outside the cell). All cells are compressed to ≈90 % of their initial height. **C** Force-compression curves for the simulations shown in (**A**). **D** Force-compression curves for the simulations shown in (**B**). The symbols are the simulation results and the solid lines are fits to them according to the relation $F = A\delta^{3/2}$, where A is a fit constant. Note that the relation is in good agreement also for non-spherical cell shapes in presence of a nucleus.Simulations were performed on $N = 512 \times 256$ grid points on a domain of size 50 µm × 25 µm. Mechanically relevant parameters for all shown simulations (if not mentioned otherwise) are $R_N = 6.25$ µm, $E_C = 1$ kPa, $\nu_C = \nu_N = 0.48$, and $\alpha = 6$ kPa. Further parameters as in Appendix B.3.2 Table B.4.

regions of highest stress are located close to the cell boundary at the transition points from vanishing to finite curvature, as predicted before [228]. However, for increasing nucleus stiffness the upper and lower poles of the nucleus, nearest to the plates, be-

come the zones of highest stress. Again, a band-like stress from the cell boundary in contact with the plates to the nucleus boundary is visible. Special to the droplet-like cell (*cf.* Fig. 5.6 B), modelled as a half-sphere, is that the $\pm z$-symmetry of the cell morphology is broken. This translates to an asymmetry in the compressed nuclear morphology and the stress distribution within the cell between lower and upper half. Highest stresses are visible in the cytoplasmic region between the upper nucleus pole and the upper plate. Figure 5.6 C and D show the respective force-compression curves for the cases shown in Fig. 5.6 A and B. Higher forces are needed to compress the pancake-like cell compared to the droplet-like cell. We fitted the Hertzian relation Eq. (5.14) (solid lines), which is also valid for objects of non-spherical shape (at least without a nucleus) [113], to the numerical solution (circles). For soft nuclei, both agree well. However, the agreement is less accurate for stiff nuclei, compared to the spherical cell (*cf.* Fig. 5.5 B). We here refrained from determining effective moduli E_{eff}, as Eq. (5.16) should not apply for these geometries.

The main impact of cell morphology (sphere vs. pancake vs. droplet) on nuclear straining thereby comes from the distance between the nucleus and the cell boundary: forces are better propagated to the nucleus for flatter cell shapes. Apical-basal asymmetries in the initial cell morphology, as for the droplet-shaped cell, propagate also to the nuclear deformation, possibly allowing a cell to distinguish between top and bottom and to use the nucleus as compression sensor [92, 93].

5.4.2 Micropipette aspiration

An alternative to cell compression experiments for measuring cellular rheological responses are micropipette experiments [229, 232–234, 241]. In this setup, cells are sucked into a pipette tube by applying a pressure difference ΔP between the tube's interior and the exterior space. In this setup, forces are more locally applied compared to global straining in compression experiments. Micropipette aspiration has already been studied numerically and together with experiments showed that cells can have elastic and viscous signatures [242]. Therefore, this experiment has been used to measure both the elastic modulus E and viscosity η of cells [229].

We are again interested in the influence of the nucleus on the measurement of the effective cell stiffness, in the context of this more local force application. Considering a spherical cell with axial symmetry, the stationary pipette wall can be modelled as in the previous example by using a field $\varphi(\boldsymbol{x})$, placing it closely to the cell membrane. Before sucking the cell into the pipette, we first let the cell relax into mechanical equilibrium

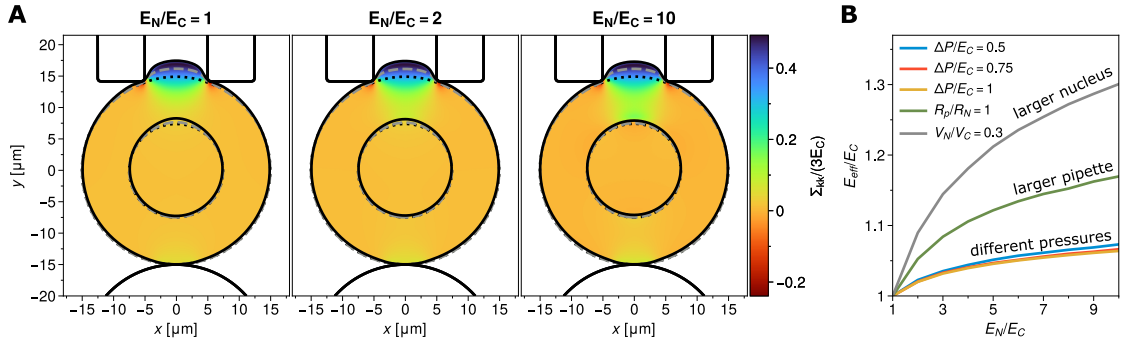

Figure 5.7: A Micropipette aspiration of a spherical cell ($R_C = 15\,\mu\text{m}$) with nucleus ($R_N = 7.5\,\mu\text{m}$) into a pipette of $R_p/R_N = 2/3$ with $\Delta P/E_C = 0.5$ in axial symmetry. Shown are the cases $E_N/E_C = 1$, $E_N/E_C = 2$ and $E_N/E_C = 10$. Cell and nucleus boundary are depicted for three different time points: before pressure application (dotted black), during pressure application (dashed grey) and in mechanical equilibrium (solid black). The solid line outside the cell marks the edges of the pipette walls (top) and the spherical bead the cell adheres to (bottom). The colour map shows the trace of the stress tensor normalized by the cytoplasmic stiffness E_C. An axial symmetric, spherical cell with nucleus is aspirated into a micropipette. The cell adheres to a spherical bead to suppress rigid body motions. **B** Effective moduli extracted from experiments as shown in **A** at $\Delta P/E_C = 0.5$ (blue), for higher pressures $\Delta P/E_C = 0.75$ (red) and $\Delta P/E_C = 1$ (yellow), and at $\Delta P/E_C = 0.5$ but for a larger nucleus $V_N/V_C = 0.3$ (grey) or for a larger pipette $R_p/R_N = 1$ (green). All cases show an increase in effective modulus with nucleus stiffness, but much smaller as compared to the compression experiment in Fig. 5.5 C. Note, due to the unknown shape factor for the micropipette, we shifted the curves slightly such that for $E_N/E_C = 1$ the expected modulus is recovered. Simulations were performed on $N = 512 \times 512$ grid points. Further parameters used are $E_C = 1\,\text{kPa}$, $\nu_C = \nu_N = 0.48$, $\alpha = 6\,\text{kPa}$ and $Y = 5\,\text{nN}/\mu\text{m}^2$ (unit for adhesion strength is now different due to phase field-type definition, Eq. (5.17)). Other parameters as in Appendix B.3.2 Table B.4.

due to the interaction with the pipette walls, *cf.* Eq. (5.12) To prevent any rigid body motion of the cell, we let it adhere to a sphere (field $\tilde{\varphi}(\boldsymbol{x})$) on the side opposite to the pipette, as also done experimentally [230, 231] using an adhesion force

$$\boldsymbol{F}_{adh} = Y(\nabla\tilde{\varphi})(\nabla h(\rho))\boldsymbol{u}. \tag{5.17}$$

Note that this is the phase field version of Eq. (5.5) modelling adhesion of the cell with strength Y when it is in contact with the sphere.

Applying now a pressure, P_1, in the micropipette tube that is smaller than the pressure P_0 in the cell's interior (the outside pressure is assumed to be P_0 as well) leads to a

boundary force acting at the cell membrane within the pipette like

$$\boldsymbol{F}_p = \Delta P(\boldsymbol{x}) \frac{\nabla h(\rho)}{f(h(\rho))} \tag{5.18}$$

where $\Delta P(\boldsymbol{x}) = (P_1 - P_0)p(\boldsymbol{x})$ and where $p(\boldsymbol{x})$ marks the micropipette interior (where P_1 is applied).

Figure 5.7 A shows results for the aspiration of spherical nucleated cells (R_C =15 µm, R_N =7.5 µm) for nucleus stiffnesses $E_N/E_C = 1, 2$ and 10 into a micropipette of radius $R_p = 2/3R_N$ =5 µm using a pressure difference of $\Delta P/E_C = 0.5$. As expected, the highest positive stresses occur at the cell membrane within the pipette, while negative stresses arise at the edges of the micropipette, where it effectively pushes against the cell. Furthermore, in the case of stiff nuclei ($E_N/E_C = 10$), stress accumulation occurs again in the vicinity of the nucleus boundary nearest to the pipette. This again suggests the possible perception of mechanical stimuli by the nucleus, even for very locally applied forces. While stiffer nuclei only deform marginally and are shifted within the cell towards the pipette position, soft nuclei ($E_N/E_C = 1, 2$) show some egg-like asymmetry in their morphology due to deformation. The black curves in the panels of Fig. 5.7 A show the cell and nucleus boundaries (1/2-phase field isocurves) for three different time points, to exemplify the dynamic nature of the problem.

Also in the micropipette geometry, one can extract an effective modulus for the cell-nucleus composite. Within the elastic regime of aspiration, the stiffness can be approximated by the relation

$$E = \frac{3\zeta}{2\pi} \Delta P \frac{R_p}{L_p}, \tag{5.19}$$

where R_p is the inner micropipette radius and ζ is a shape factor for the micropipette geometry [243]. No closed form exists for calculating the shape factor ζ [242].

To calculate the effective cell stiffness E_{eff} from the numerics, we determine the aspiration length L_p and, knowing the applied pressure difference and the micropipette radius, we estimated the effective modulus over a range of nucleus stiffnesses, nucleus sizes, pressure differences and micropipette radii, *cf.* Fig. 5.7 B. All tested cases yield $E_{eff} \approx 1$ for $E_N/E_C = 1$ with a deviation of less than 5 % for $\Delta P/E_C = 0.5$. Since the shape factor is unknown, we hence shifted all results such that for $E_C = E_N$ we get the correct modulus. There also is a slight dependence on the applied pressure. However, with increasing pressure (from blue to yellow curves in Fig. 5.7 B), the extracted effective moduli E_{eff} approach each other, indicating that the method is best suited for

sufficiently large applied pressures.

All studied cases show an increase in effective stiffness for stiffer nuclei. However, this increase is approximately 30 % for the largest and stiffest nuclei. Hence the localized force application due to the micropipette geometry leads to much lower measured E_{eff} compared to the global cell compression geometry (*cf.* Fig. 5.5). This clearly demonstrates – and quantifies – that experimentally measured effective cell stiffnesses do not only depend on the inner structure of the cell, but also on the experimental setup.

5.4.3 Outlook on modelling cells migrating through narrow channels

We here want to present a first approach on how cell migration can be modelled with the elastic phase field approach discussed in this chapter in a 2D plane stress formulation.

Migrating cells often have to squeeze through narrow channels and gaps in their surroundings. Here, the size of the cell nucleus in conjuncture with its mechanical properties pose a constraint on the minimal constriction size, which still allows a passage of the cell [208, 210, 244]. Often passage through narrow constrictions is associated with nuclear envelope rupture and therefore loss of nuclear rigidity [99, 100, 208]. However, passage can be facilitated without such an event by the formation of actin cytoskeletal structures linked to the nucleus assisting in its deformation [208, 245] and pulling it through the constriction [96, 246]. Recently, it has been proposed that nuclei can be pushed by the cytoskeleton [247] and that a transition between pushing and pulling by the cytoskeleton exists, depending on the degree of confinement [248].

Models for cell migration (containing a nucleus) need to combine elastic deformations of the cell, such as the formation of the lamellipodium or mechanical interactions with obstacles, and rigid-body motions. We note that the elastic description (of the nucleus) is supported by recent experimental observations on cell squeezing trough a constriction [248]. Rigid-body motions of the cell require the deformation field – or rather the reference configuration – to move with the cell and is not incorporated in the model equations discussed in Chapter 4 to 7.

This can be achieved by adding an advection-like term to the phase field and elasto-

dynamic equations

$$\frac{\partial \phi}{\partial t} = D_\phi \Delta \phi - \frac{\partial g(\phi)}{\partial \phi} + D_\phi \kappa_\phi |\nabla \phi| - \left[\frac{\partial \boldsymbol{u}}{\partial t} + \left(\frac{\partial \boldsymbol{r}_{com}}{\partial t} \cdot \nabla \right) \boldsymbol{u} \right] \cdot \nabla \phi - \frac{\partial \boldsymbol{r}_{com}}{\partial t} \cdot \nabla \phi \tag{5.20}$$

$$\xi \left[\frac{\partial \boldsymbol{u}}{\partial t} + \left(\frac{\partial \boldsymbol{r}_{com}}{\partial t} \cdot \nabla \right) \boldsymbol{u} \right] = \nabla \cdot \Sigma + \boldsymbol{F} - Y h(\rho) \boldsymbol{u} - \gamma(\boldsymbol{x}) \left[1 - h(\rho) \right] \boldsymbol{u}, \tag{5.21}$$

where $\phi \in \{\rho, \psi\}$ denotes the cell phase field $\rho(\boldsymbol{x}, t)$ and nucleus phase field $\psi(\boldsymbol{x}, t)$, respectively. For details on these equations see for instance Chapter 5. The term proportional to the centre of mass velocity $\partial \boldsymbol{r}_{com}/\partial t$ are the advection-like terms, allowing to describe rigid-body motions by shifting the displacement field/ reference configuration in space.

Being controlled by the strength of force transmission by the cell to an underlying substrate, the centre of mass velocity is given by

$$\chi \frac{\partial \boldsymbol{r}_{com}}{\partial t} = \begin{cases} k \left(\langle \boldsymbol{u} \rangle - \langle \boldsymbol{u} \rangle_{cr} \right) & \text{for } \langle \boldsymbol{u} \rangle > \langle \boldsymbol{u} \rangle_{cr} \\ 0 & \text{else} \end{cases}, \tag{5.22}$$

where χ is a friction coefficient setting the timescale of motion and k controls the coupling strength or force transmission efficiency to the substrate. Onset of motion occurs when the average traction force $k\langle \boldsymbol{u} \rangle$ exerted by the cell, with average displacement

$$\langle \boldsymbol{u} \rangle = \frac{1}{V_{cell}} \int_\Omega \boldsymbol{u}(\boldsymbol{x}) \rho(\boldsymbol{x}) d\Omega \qquad \text{and} \qquad V_{cell} = \int_\Omega \rho(\boldsymbol{x}) d\Omega \quad , \tag{5.23}$$

is above a critical average traction force $k\langle \boldsymbol{u} \rangle_{cr}$; otherwise, the cell is only deformed and does not move. Note that the elastic effect of substrate coupling is still introduced to the elastodynamic equation via the adhesion force $\boldsymbol{F}_{adh} = -Y(\boldsymbol{x}) h(\rho) \boldsymbol{u}$, *cf.* Eq. (5.21). Instead of considering a centre of mass velocity, a (more realistic) local velocity description could be employed.

To move the cell, we introduce an effective propulsion force $\boldsymbol{F}_{prop}(\boldsymbol{x}) \propto \nabla \rho$, spatially restricted to a part of the cell edge, into Eq. (5.21). This is a simplification for the propulsion forces exerted via internal dynamics of the cytoskeleton. A more detailed model of cell polarization and motion can be introduced by considering an internal polarization field $\boldsymbol{p}$, representing actin polymerization dynamics, as previously done by Ziebert et al. [142] without considering elasticity. The polarization field induces a force at the cell boundary, which can be written as $\boldsymbol{F}_{prop} = \alpha_p |\boldsymbol{p}|^2 \nabla \rho$, entering the force balance in Eq. (5.21).

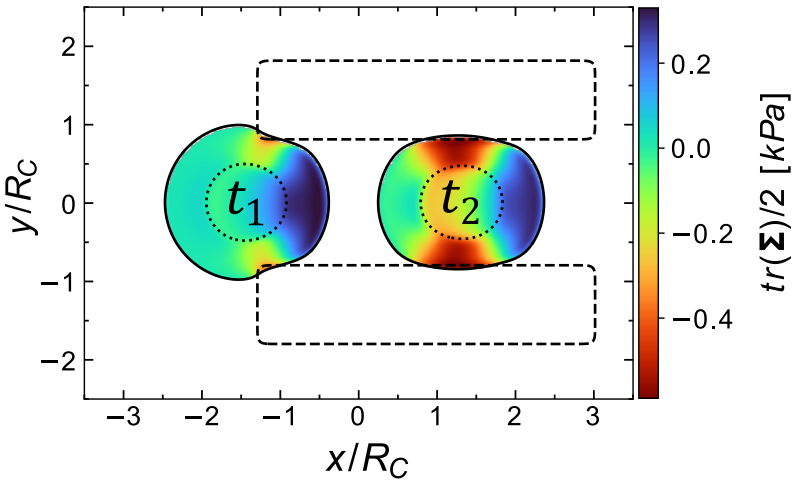

Figure 5.8: A cell of initial radius R_C with a nucleus of radius $R_N/R_C = 1/2$ and stiffness $E_N/E_C = 5$ is migrating through a channel of a width corresponding to 60 % of the initial cell diameter $2R_C$. Shown are snapshots of the trace of the stress tensor for $\rho > 1/2$ for two time points: when the cell is entering the channel (t_1) and when it is completely within the channel (t_2). The channels walls are marked by the isocontour $\varphi = 1/2$ (dashed black lines), the cell boundary by $\rho = 1/2$ (black solid line) and the nucleus boundary by $\psi = 1/2$ (dotted black line). Mechanical parameters are $E_C = 1\,\mathrm{kPa}$, $E_N = 5\,\mathrm{kPa}$, $\nu_{N/C} = 0.5$, propulsion force $F/E_C = 0.2$, $\alpha/E_C = 6$.

Figure 5.8 shows snapshots of an initially circular cell of radius R_C with a nucleus of radius $R_N/R_C = 1/2$ and stiffness $E_N/E_C = 5$ migrating through a narrow channel for two different time points. The interactions with the channel walls are modelled via Eq. (5.12). Shown is the trace of the stress tensor, showing similarities in the stress distribution observed in the compression of cells between two plates (*cf.* Fig. 5.5 A), notably the concentration of stress between channel walls and nucleus. Note that the cell gets stretched at its leading edge due to the pulling force leading to its movement.

5.5 Discussion

Cell mechanics and mechanotransduction are strongly influenced by the largest and stiffest cellular organelle, the nucleus. Despite increasing evidence of its mechanical importance, models explicitly accounting for nuclear mechanics are still rare. We here developed a two-phase field approach for modelling cell mechanics with an additional internal compartment associated with nuclear elastic properties and investigated the mechanical response of cells in a selection of biologically relevant geometries and experimental setups. We also verified our approach in cases for which analytical solutions are available to the elastic equations.

In the first part described in Sect. 5.3, we considered the case of spread cells in unstructured and structured environments using a 2D plane stress formulation. For homogeneous adhesion, the effect of a physiologically sized nucleus on the mechanical response of the cell is small as the adhesion to the substrate effectively shields the nucleus from deformations and stresses. Even peripheral adhesion on a ring pattern is still sufficient to protect the nucleus. However, in more structured environments with highly localized adhesion sites, a much higher transmission of stresses to the nucleus was observed. These observations demonstrate that the actual adhesion geometry can be sensed by cells at the nucleus. Further on, applying tensile stresses on the nucleus by letting only the cytoplasm contract (again for a homogeneously adhered cell), indicates that the geometry dependence is complemented by the manner of force transmission from the cytoskeleton to the nucleus. This agrees with previous experimental results and the role of the LINC complex in direct force transmission from the cytoskeleton to the nucleus, where it is known that its disruption dramatically impedes nuclear mechanotransduction. [8]

On micro-patterned environments, stiffer nuclei also change the cellular morphology, by perturbing the formation of the invaginated arcs. Additionally, the nuclear position largely effects the stress distribution within the cell, which may be an important input for the cell with regard to the determination of its polarity, *e.g.* when having to distinguish between front and back. For stiff nuclei, "stress bridges" resembling stress fibres form from close-by focal adhesions to the nuclear boundary, suggesting an effect on the perception of mechanical cues.

The here-proposed phase field method allows to model not only stationary but also dynamic situations. As a simple example we considered the failure of a focal adhesion for a cell on a hexagonal micro-patterned substrate. The coupling of phase field dy-

namics and elasticity made it necessary to use an elastodynamic formulation for the evolution of the displacement field (*cf.* Sect. 4.2) [10]. We here showed that the relaxation into mechanical equilibrium is of Kelvin-Voigt type (*cf.* Sect. 5.3.3). In turn, if a purely elastic behaviour of the system is desired, it should not be probed on timescales shorter than the respective relaxation time. Also note that the elastic description memorizes the initial condition of the cell before the application of forces or stresses. The cell shown in Fig. 5.4 A hence does not relax to a (deformed) pentagonal shape with an invaginated arc at the cell edge where the disappeared focal adhesion was located.

In the second part, Sect. 5.4, we modelled compression experiments of cells between two parallel plates and the aspiration of cells into micropipettes in an axial symmetric geometry. Again, stiffer nuclei showed stress accumulation near their boundary pointing towards a significant role of nuclear mechanics in determining the properties of the cellular environment. Importantly, our model allowed the extraction of effective elastic moduli of the cell-nucleus composite for both experimental methods, yielding consistently lower effective moduli for local pressure application in micropipette experiments compared to more global cell compression. This shows that the determination of effective cell moduli is not only dependent on cell geometry but also the experimental setup used. We have also shown that the cell geometry influences the distribution and possible perception of stresses. Flatter shapes allow a better force propagation to the nucleus and top-bottom asymmetries in cell morphology translate to asymmetric nuclear deformations, possibly enabling the nucleus to distinguish between top and bottom.

In the case of the compression of cells, we here used a quasi-stationary compression, allowing the comparison to analytical solutions. Nevertheless, the approach is also applicable for dynamic compression with different plate velocities. For the micropipette aspiration experiments the extraction of elastic moduli is best suited for sufficiently large pressures. Low pressure application leads to a slight underestimation in the range of 5% of the effective cell stiffness. This is partially influenced by the unknown shape factor for the pipette, cf. the discussion of Fig. 5.7 B.

In the future, the here developed method should prove useful for investigating the effect of a nucleus and/or other cellular organelles, potentially described with different material laws, in a large variety of situations. Additional new insights on mechanotransduction could be gained by examining the effect of the nuclear position within the cell in fully three-dimensional (3D) situations. In this respect, the phase field method can be extended relatively easily to 3D, making it possible to consider more complex environments like fibrous network geometries or non-symmetric constrictions [146, 205,

249].

The presented method could also be used to describe the role of cell nucleus mechanics in tissues, using the multi-phase field approach [151, 152, 155]. Note that recently, a new jamming transition due to the presence of nuclei was predicted for tissues by an active foam model [250]. It would be interesting to study the same effect in our dynamic continuum framework.

Another important context of cell and nuclear mechanics is cell migration through constrictions, where the minimal constriction size is predominantly determined by the nuclear size and stiffness [208]. A first, simple approach to model cell migration through a narrow channel was demonstrated in Sect. 5.4.3, showing similarities to the compression of a cell between two plates. We envision to supplement the current approach by self-organized internal driving forces inducing cellular motility, that could be implemented by an actin "polarization" field [142] and should naturally enter the elastodynamic equation, Eq. (5.2). In the context of mechanotransduction, the coupling of the proposed method to a system of reaction-diffusion equations should allow to model nuclear translocation of proteins like YAP/TAZ in response to nuclear straining (and opening of nuclear pore complexes [6, 8, 9]). This could elucidate further – and more directly – the role of nuclear mechanics on spatio-temporal import dynamics and mechanically induced signalling events.

In summary, the elastic phase field approach for modelling the mechanics of nucleated cells is very versatile and easy to generalize for future applications. The results presented should be useful to quantify experiments and last but not least point to many interesting implications with regarding the role of the nucleus on whole cell mechanics, mechanosensing and related subjects.

6 Modelling the spatiotemporal dynamics of nucleocytoplasmic transport in mechanically strained cells

In the previous chapter, we have proposed a phase field model for elastic cells with nuclei and examined the role of the nucleus for cell mechanics in a selection of biologically relevant experimental setups. Here, we now consider mechanotransduction, *i.e.* the mechanosensitive transport of proteins into the nucleus. We extend the model from Chapter 5 by a reaction-diffusion system for modelling nucleocytoplasmic protein transport dynamics, in order to investigate its sensitivity on nuclear rigidity.

6.1 Introduction

Cellular reactions to external mechanical stimuli are to a large part mediated by the direct transmission of forces to the nucleus. Essential in the mechanotransduction pathway is a biochemical component involved in gene transcription, namely the accumulation of transcriptionally active proteins in the nucleus. Additionally, nuclear deformations are known to disturb the chromatin organization in cells and, hence, possibly allowing transcription of previously inactive genes [98, 251].

Transport of proteins into the nucleus occurs through hundreds to thousands of nuclear pore complexes (NPCs) perforating the nuclear envelope (*cf.* Sect. 2.2.2). In the last years, the structure of these massive protein complexes has been more and more unveiled up to atomic resolution [252–254], recently assisted by artificial intelligence [110, 255]. NPCs show a high throughput capacity of around 1000 proteins per second per NPC [102] in and out of the nucleus, while still being highly selective [88]. This selectivity manifests itself by the so-called permeability barrier allowing efficient passive

diffusional passage only for macromolecules with molecular weights below 40 kDa to 60 kDa [75, 88, 256]. Above this size threshold, adaptor proteins, so-called importins and exportins, binding to the cargo molecules are needed to facilitate nuclear import and export.

Being the gateway to the cellular genome, NPCs are also used by viruses to bring their genetic information into the nucleus of cells [257]. A recent study has demonstrated that cone-shaped HIV capsids invade cell nuclei by squeezing through NPCs and releasing their cargo directly in the nucleus [258].

To understand the protein transport mechanisms, pathways and selectivity of NPCs, experiments on isolated, in vivo [108] and artificial NPCs have been performed, complemented by theoretical models. Still, many aspects of NPC-mediated nucleocytoplasmic transport have to be revealed.

During recent years, nuclear mechanics has been identified as another component in determining nucleocytoplasmic transport efficiency. An extensively studied macromolecule in this context is YAP/TAZ, which is known to be a mechanosensitive transcription regulator involved in many physiological processes, including development and wound healing [259]. With a molecular weight of 65 kDa [260], YAP lies at the edge of the NPC permeability barrier. It has been shown that nuclear accumulation of YAP occurs above a critical substrate stiffness associated with focal adhesion growth and increased traction forces [261]. In line, several studies on spread cells in 2D and 3D environments have indicated a connection between YAP accumulation in the nucleus and nuclear morphology/ deformation [8, 220, 262, 263]. Importantly, YAP nuclear translocation is highly dependent on the transmission of cytoskeletal forces to the nucleus via LINC complexes, which has been demonstrated by disruption of the latter leading to heavily decreased nuclear YAP signals [8]. However, the mechanosensitivity of the transport process depends on the differential effect of forces exerted on the nucleus on passive and facilitated diffusion through NPCs [9].

It is argued that NPC-mediated transport is (partially) facilitated by tension induced stretching of NPCs in response to nuclear deformation, weakening the permeability barrier [8, 88]. This has been recently supported by electron microscopy studies demonstrating changes in the diameter of NPCs [6, 7]. However, other aspects such, as conformational changes of the NPC structure [6], may also be important in this context.

Here, we aim at investigating the sensitivity of nucleocytoplasmic protein shuttling on nuclear rigidity using the elastic phase field model for cells with nuclei (*cf.* Chapter 5) extended by a reaction-diffusion model for the cargo transport, similar to those of An-

dreu et al. [9] and Kim et al. [264]. In contrast to these kinetic models, our approach allows to model spatiotemporal transport dynamics in moving boundary problems in two dimensions. NPC widening due to nuclear tension is accounted for by increase of the local permeability of the nuclear boundary.

This chapter is structures as follows: First, we describe a sharp interface reaction-diffusion model describing the import of proteins into the nucleus, which will then be translated into the phase field framework. We then study how nuclear tension has to influence the permeability of the nuclear boundary for increased accumulation of proteins in the nucleus. Afterwards, we consider the effect of nuclear mechanics on the accumulation of cargo in the nucleus for spread cell, focussing on molecules of a size similar to YAP.

6.2 Reaction-diffusion model for nucleocytoplasmic transport

In the following, we will propose a system of reaction-diffusion equations describing the import of cargo proteins into the nucleus in a mechanosensitive manner. This continuum approach is justified by experimentally measured fluorescence signals of transportable cargo in cells, suggesting the possibility to consider concentrations of cargo proteins [8, 9, 220]. First, the sharp interface equations of the model and later their corresponding phase field version are discussed.

6.2.1 Sharp interface model

We consider a domain Ω representing a cell, which is divided into two compartments: the nucleus (Ω_N) and the cytoplasm (Ω_C), *i.e.* the cell part without nucleus (*cf.* Fig. 6.1). The cell boundary ($\partial\Omega_C$), *i.e.* the cell plasma membrane, is assumed to be impermeable, while the nuclear envelope ($\partial\Omega_N$) can be traversed by molecules through NPCs.

Cargo proteins of interest can diffuse in both compartments and shuttle between nucleus and cytoplasm. In order to distinguish cargo proteins in the cytoplasm from those in the nucleus, we denote the cargo concentration in the cytoplasm by $c(\boldsymbol{x}, t)$ and in the nucleus by $n(\boldsymbol{x}, t)$. Similar, complexes of cargo proteins and importins, facilitating the nucleocytoplasmic transport, are referred to by $c_I(\boldsymbol{x}, t)$ in the cytoplasm and $n_I(\boldsymbol{x}, t)$ in the nucleus compartment. The general model equations with boundary conditions

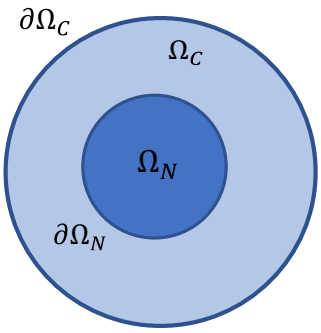

Figure 6.1: A cell is divided into two compartments: the cytoplasm (Ω_C) and the nucleus (Ω_N). The cell boundary ($\partial\Omega_C$) and is assumed to be impermeable. The nucleus boundary ($\partial\Omega_N$) is permeable due to NPCs perforating it.

for each species are

$$\frac{\partial c}{\partial t} = D_c\Delta c + k_1^- c_I - k_1 c \qquad \boldsymbol{n}\cdot\nabla c|_{\partial\Omega_N} = P_p(n-c) \qquad \boldsymbol{n}\cdot\nabla c|_{\partial\Omega_C} = 0 \tag{6.1}$$

$$\frac{\partial n}{\partial t} = D_n\Delta n + k_2^- n_I - k_2 n \qquad \boldsymbol{n}\cdot\nabla n|_{\partial\Omega_N} = -P_p(n-c) \tag{6.2}$$

$$\frac{\partial c_I}{\partial t} = D_{c_I}\Delta c_I - k_1^- c_I + k_1 c \qquad \boldsymbol{n}\cdot\nabla c_I|_{\partial\Omega_N} = P_a(n_I - c_I) \qquad \boldsymbol{n}\cdot\nabla c_I|_{\partial\Omega_C} = 0 \tag{6.3}$$

$$\frac{\partial n_I}{\partial t} = D_{n_I}\Delta n_I - k_2^- n_I + k_2 n \qquad \boldsymbol{n}\cdot\nabla n_I|_{\partial\Omega_N} = -P_a(n_I - c_I). \tag{6.4}$$

where the total number of cargo proteins N_{tot} in the entire cell, irrespective if they are in a complex or not, is conserved, *i.e.* $\partial_t N_{tot} = \partial_t(N_c + N_n + N_{n_I} + N_{c_I}) = 0$, where the N_i are the total number of cargo and cargo-importin complexes in cytoplasm and nucleus.

The above system for nuclear import is a simplified version of the transport cycle shown in Fig. 2.6. It dynamics is as follows: Cargo proteins and cargo-importin complexes diffuse through each compartment with a diffusion coefficient D_i.Cargo molecules can associate with importins to cargo-importin complexes in both compartments with a rate k_1 with units s^{-1}. Note, importins (I) are not considered explicitly as their concentration is assumed to be much higher in the cytoplasm and in the nucleus than those of the cargo proteins, such that there are always enough available importins for binding and the reaction becomes independent of the importin concentration [9].

In the cytoplasm the cargo-importin complexes dissociate with a (small) rate k_1^-, while in the nucleus the unbinding rate k_2^- is much higher due to a large nuclear concentration of RanGTP involved in separating cargo and importins. Similar to the cargo-importin association, the large RanGTP concentration in the nucleus allows to assume that it is in a steady state and the dissociation rate k_2^{-1} is constant. Additionally, we assume the RanGTP/GDP cycle (*cf.* Fig. 2.6) to be in steady state. Note that the RanGTP concentration in the cytoplasm is much smaller than in the nucleus, creating a concen-

tration gradient responsible for the directionality of the transport process [88, 265].

Lastly, no-flux boundary conditions are assumed at the cell membrane, while the nuclear membrane is permeable due to NPCs perforating it. Simple cargo can shuttle by passive diffusion due to a jump in concentration across the nuclear envelope with an efficiency given by the passive impermeability P_p with units µm/s, similar to a velocity. Cargo-importin complexes are actively transported through NPCs, also called facilitated diffusion, with a permeability $P_a > P_p$. In principle, both passive and active permeability can vary along the nuclear boundary.

6.2.2 Diffusion-reaction model in the phase field method

To couple the model equations presented in the previous section to the elastic phase field model from Chapter 5, Eqs. (6.1)-(6.4) first have to be transcript into the phase field sense.

Consistent with Chapter 5, we describe the cell domain Ω_C by a phase field $\rho(\boldsymbol{x}, t)$ and the nucleus domain Ω_N by a second phase field $\psi(\boldsymbol{x}, t)$, both taking on the value 1 in the respective domains and 0 otherwise. The cytoplasmic domain Ω_C can be represented by the difference between both fields $\Phi(\boldsymbol{x}, t) = \rho(\boldsymbol{x}, t) - \psi(\boldsymbol{x}, t)$. In the phase field framework Eqs. (6.1)-(6.4) are written as

$$\frac{\partial(\Phi c)}{\partial t} = D_c \nabla \left[\Phi \nabla c\right] + P_p(n - c)|\nabla\psi| + \Phi\left(k_1^- c_I - k_1 c\right) + \beta\Phi\left(N_{tot,0} - N_{tot}\right) \tag{6.5}$$

$$\frac{\partial(\psi n)}{\partial t} = D_n \nabla \left[\psi \nabla n\right] - P_p(n - c)|\nabla\psi| + \psi\left(k_2^- n_I - k_2 n\right) \tag{6.6}$$

$$\frac{\partial(\Phi c_I)}{\partial t} = D_{c_I} \nabla \left[\Phi \nabla c_I\right] + P_a(n_I - c_I)|\nabla\psi| - \Phi\left(k_1^- c_I - k_1 c\right) \tag{6.7}$$

$$\frac{\partial(\psi n_I)}{\partial t} = D_{n_I} \nabla \left[\psi \nabla n_I\right] - P_a(n_I - c_I)|\nabla\psi| - \psi\left(k_2^- n_I - k_2 n\right). \tag{6.8}$$

Let us discuss the structure of these equations: Assuming for now that cell and nucleus boundary are impermeable the factors ψ and Φ on the left-hand side of Eqs. (6.5)-(6.8) automatically incorporate no-flux boundary conditions [266]. Note that the concentrations may leak out of the cell compartments, but for example $\int \Phi c d\boldsymbol{x}$ is conserved, which is the relevant part [266]. This is also true for the other quantities.

On the right-hand side of Eqs. (6.5)-(6.8) the phase field factors indicate in which compartment/subdomain of the whole computational domain they are active. For instance, in the diffusion terms (first terms) the phase field factors determine where the diffusion coefficients D_i are defined and for the reaction terms where these reactions

take place. Assuming that the D_i are constant in the respective domains, they can be put in front of the first gradient in the diffusion terms, as done above. In the case that they vary spatially in the respective compartment, *i.e.* $D_i(\boldsymbol{x})$, they have to be put inside the square-brackets next to the phase field variable.

To account for the permeability of the nuclear boundary $\partial\Omega_N$, the flux boundary conditions as given in Eqs. (6.1)-(6.4) (middle column) can be directly incorporated into the phase field Eqs. (6.5)-(6.8) (second terms), thanks to the diffuse description of the nucleocytoplasmic boundary [267]. Thereby, the factor $|\nabla\psi|$ indicates the nucleus boundary. Note that this is only one possibility how boundary conditions can be implemented into the PDEs of phase field models [267].

Finally, we need to ensure the conservation of the total cargo number N_{tot}. Although no-flux boundary conditions are applied at the cell membrane, the total cargo number is not perfectly conserved. Depending on the required spatial and time resolution when solving the PDEs the loss may become considerably large. Therefore, we additionally introduce a Lagrange multiplier for the conservation of the total cargo number $N_{tot} = \int \rho(c + c_I + n + n_I)d\boldsymbol{x}$, *cf.* last term Eq. (6.5). Here, $N_{tot,0}$ is the initial reference cargo number and β is the (small) rate/strength of the conservation condition. We chose to implement the cargo number conservation in Eq. (6.5) because the cytoplasmic compartment Φ is much larger than the nuclear one, hence its relative effect here is reduced. From a biological perspective, proteins are synthesized in the cytoplasm [30] most probably without directly binding to importins, *i.e.* c is created where $\Phi = 1$. Consequently, Eq. (6.5) is a natural choice to implement total cargo number conservation.

6.2.3 Mechanosensitive import

There is increasing evidence that proteins are imported in a mechanosensitive manner into the nucleus and that this process is associated with nuclear deformations [8, 9, 75, 84, 220, 262]. An extensively studied protein in this context are YAP and TAZ [259], whose activity and accumulation in the nucleus has been shown to depend on the transmission of cytoskeletal forces to the nucleus [8, 9, 86, 268].

Lomakin et al. [93] and Venturini et al. [92] independently demonstrated that the normally wrinkled nuclear envelope can unfold in response to deformation triggering cell migration. It is hypothesized that forces applied to the nucleus stretch NPCs thereby facilitating the nucleocytoplasmic transport through them [8, 9, 256]. In fact, recent studies revealed that nuclear envelope tension leads to an expansion of NPCs [6, 7].

To incorporate mechanosensitivity into the model presented in the foregoing sections

we will consider two aspects: a stress-dependent binding rate k_1 of cargo proteins and importins and a mechanically-induced change of the local permeabilities P and P_a in Eqs. (6.5)-(6.8).

Assuming that the binding rates $k_{1/2}$ are stress-dependent (hence, they can vary in space), we write it as

$$k_{1/2}(\boldsymbol{x}) = k^0_{1/2}\frac{\Sigma_{vM}}{\Sigma_{vM,cr} + \Sigma_{vM}}, \tag{6.9}$$

where $k^0_{1/2}$ is the maximal binding rate and the (phase field) von Mises stress Σ_{vM} (*cf.* Eq. (4.20)) serves as scalar measure for the stress in the cell. The onset of the association process is controlled via a critical stress $\Sigma_{vM,cr}$. This ensures that facilitated transport can only occur in presence of stress.

Further, we assume that the passive permeability $P_p(\boldsymbol{x})$ as well as the active permeability $P_a(\boldsymbol{x})$ can locally change due to NPC dilation when the tension $\tau(\boldsymbol{x})$ on the nuclear boundary is above a threshold τ_{cr}, *i.e.*

$$P_p(\boldsymbol{x}) = \begin{cases} P_p & \text{if } \tau(\boldsymbol{x}) \leq \tau_{cr} \\ P_p' & \text{if } \tau(\boldsymbol{x}) > \tau_{cr} \end{cases} \qquad \text{and} \qquad P_a(\boldsymbol{x}) = \begin{cases} P_a & \text{if } \tau(\boldsymbol{x}) \leq \tau_{cr} \\ P_a' & \text{if } \tau(\boldsymbol{x}) > \tau_{cr} \end{cases} . \tag{6.10}$$

P_p, P_a are the permeabilities if the NPCs are constricted and P_p', P_a' are the (larger) permeabilities if the NPCs are dilated. Note, an exact value for the threshold tension τ_{cr} is not known to us. Therefore, we will always take the limiting case $\tau_{cr} = 0$, hence, as soon as tension arises on the nuclear envelope the impacted NPCs are stretched. The local tension can be calculated by [269, 270]

$$\tau = \int \boldsymbol{t} \cdot [\boldsymbol{\sigma} - (\boldsymbol{n} \cdot \boldsymbol{\sigma} \cdot \boldsymbol{n})\, \mathbf{1}] \cdot \boldsymbol{t} \quad d\boldsymbol{n} \tag{6.11}$$

where $\boldsymbol{n}$ is the interface normal, $\boldsymbol{t}$ is the tangent and an integral across the nucleocytoplasmic interface is performed. Equation (6.11) amounts to be the difference between the local stress tangential ($\sigma_{||}$) and normal ($\sigma_\perp$) to the interface, *i.e.* $\tau = \int \left(\sigma_{||} - \sigma_\perp\right) d\boldsymbol{n}$ [271]. In the phase field model, we omit the integration due to the diffuse interface description and the tension, which is from now on called Σ_τ as it will have the dimensions of a stress, can be calculated by

$$\Sigma_\tau = \boldsymbol{t} \cdot [\Sigma - (\boldsymbol{n} \cdot \Sigma \cdot \boldsymbol{n})\, \mathbf{1}] \cdot \boldsymbol{t} |\nabla\psi|, \tag{6.12}$$

where Σ is the phase field stress tensor (*cf.* Eq. (5.3)), $\boldsymbol{n}_\psi = \nabla\psi/|\nabla\psi|$ is the normal vector

of the nucleus interface and $|\nabla\psi|$ indicates the interface position.

In summary, the governing equations of the model are Eqs. (6.5)-(6.8) together with the phase field model for a cell with nucleus from the previous chapter, *i.e.*

$$\frac{\partial\phi}{\partial t} = D_\phi\Delta\phi - \frac{\partial g(\phi)}{\partial\phi} + D_\phi\kappa_\phi|\nabla\phi| - \frac{1}{\xi}\left(\nabla\cdot\Sigma + \boldsymbol{F} - \gamma(\boldsymbol{x})\left[1-h(\rho)\right]\boldsymbol{u}\right)\cdot\nabla\phi \tag{6.13}$$

$$\xi\frac{\partial\boldsymbol{u}}{\partial t} = \nabla\cdot\Sigma + \boldsymbol{F} - \gamma(\boldsymbol{x})\left[1-h(\rho)\right]\boldsymbol{u}, \tag{6.14}$$

where ϕ denotes the phase field for cell (ρ) and nucleus (ψ) and the phase field stress tensor is

$$\Sigma(\rho,\psi) = \left[h(\rho) - h(\psi)\right]\boldsymbol{\sigma}^{\boldsymbol{C}} + h(\psi)\boldsymbol{\sigma}^{\boldsymbol{N}} \tag{6.15}$$

with $\boldsymbol{\sigma}^{\boldsymbol{C}}$ and $\boldsymbol{\sigma}^{\boldsymbol{N}}$ being the stress tensors of the cytoplasmic ($\boldsymbol{C}$), *i.e.* the intracellular part without nucleus, and the nucleus ($\boldsymbol{N}$). For more detail on these equations see Chapters 4 and 5.

6.3 Model results for nuclear import

Having introduced the model equations, we will now investigate the model and its implications on the mechanosensitive import of proteins into the nucleus of spread cells. A protein frequently studied in the context of nuclear transport is the approx. 65 kDa protein YAP [260], due to its importance in mechanotransduction [8, 9, 220, 261]. Therefore, we restrict our study to molecules of this size, *i.e.* we will fix the diffusion constants accordingly.

First, we discuss how nuclear tension has to alter the relation between passive and active transport to allow for an increased protein accumulation in the nucleus in response to stress. Later, we investigate the effect of nuclear rigidity and position in different situations, including the application of local and global strain. We already note that in the performed experiments, the central quantity studied is the nucleocytoplasmic signal ratio of cargo proteins [9]

$$\frac{N}{C} = \frac{\langle n + n_I\rangle A_{cyto}}{\langle c + c_I\rangle A_{nuc}}, \tag{6.16}$$

where $\langle\cdots\rangle$ are volume integrals of the concentrations in the respective cell compartments and $A_{cyto/nuc}$ are the areas of cytoplasm and nucleus, respectively.

6.3.1 Parameters of the reaction-diffusion system

We first discuss the default parameters used in Eqs. (6.5)-(6.8) for the following simulations. The diffusion coefficient in the cytoplasm of eukaryotic cells of proteins such as YAP with a molecular weight of approx. 65 kDa can be estimated to $D_c \approx 10\,\mu m^2/s$ [272]. As importins have a molecular weight of around 100 kDa [273], we estimate the diffusion coefficient of the cargo-importin complex to be $D_{c_I} \approx 2\,\mu m^2/s$ [272]. For the diffusion coefficients of the cargo (D_n) and cargo-importin complex (D_{n_I}) in the nucleus, we use the same values as in the cytoplasm, as they have been shown to be similar [272].

The association rates of cargo-importin complexes in cytoplasm and nucleus will be always set to the same value, *i.e* we do not assume the maximal binding affinity $k^0_{1/2}$ of cargo proteins and importins (*cf.* Eq. (6.9)) to change between the cell compartments. As values we will use $k^0_{1/2} = 0.054\ s^{-1}$ [9], $k^0_{1/2} = 0.2\ s^{-1}$ [9] and $k^0_{1/2} = 0.5\ s^{-1}$ [273] for an importin concentration in the µM-range [9, 274]. In the study by Elosegui-Artola et al. [261] it has been shown that the onset of nuclear accumulation of YAP is observable above a critical substrate stiffness and traction stress (around 0.1 kPa). Therefore, we set the critical von Mises stress $\Sigma_{vM,cr} = 0.1$ kPa in Eq. (6.9).

For the dissociation rate in the cytoplasm, we set $k_1^- = 0.05\ s^{-1}$ [9], which is on the order of magnitude as reported by Catimel et al. [273]. The dissociation rate in the nucleus, in general, depends on the nuclear RanGTP concentration as it is responsible for the separation of cargo and importin [9, 88]. For an assumed RanGTP concentration of around 5 µM in steady state, we will set $k_2^- = 5\ s^{-1}$ [9, 265].

The default values for the permeabilities in absence of forces on the nucleus are estimated by measurements reported by Andreu et al. [9]. For 67 kDa molecules, they have measured passive influx rates of $0.03\ s^{-1}$ into the nucleus and facilitated, *i.e* active, influx rates of around $0.08\ s^{-1}$. These quantities can be converted to permeabilities of the nuclear envelope by the relation

$$P = k\frac{A_{nuc}}{V_{nuc}} \tag{6.17}$$

where k is the measured rate, A_{nuc} is the surface area and V_{nuc} the volume of the nucleus [275]. In 2D, we find $P = kR_N/2$, which for a spherical nucleus of radius R_N 5 µm yields for the passive permeability $P_p = 0.075\,\mu m/s$ and for the active permeability $P_a = 0.2\,\mu m/s$. The permeabilities in presence of tension will be discussed later. These are the parameters used in the following simulations, if not explicitly stated otherwise.

6.3.2 Nuclear tension has to influence passive and active import differently

Tension-induced stretch of NPCs may alter their permeability for active and passive transport. Recent experimental results suggest a differential effect of NPC dilation on the passive (P_p) and active (P_a) permeability leading to an increased nuclear influx of proteins and N/C ratio in strained cells [9].

To test our modelling approach in this direction, we first assume that P_p and P_a change by the same factor f_p in response to tension, *i.e.* they are both equally impacted by tension-induced NPC stretch. This idea is motivated by assuming that only the change in the NPC geometry, *i.e.* bigger "holes" in the nuclear envelope, influences the permeabilities. Hence, this geometrical change is naively the same for P_p and P_a.

We model a cell, which is allowed to adhere to a rectangular shape on adhesive spots of radius r_{adh} and high adhesion strength Y in its corners (*cf.* Sect. 5.3.2 Fig. 5.3 or Fig. 6.3 C). The cell has a nucleus of stiffness $E_N/E_C = 10$ in its centre and is isotropically contracting with a contractile stress $\sigma_0/E_C = 0.4$ with $E_C = 1\,\mathrm{kPa}$. Initially, we assume a uniform distribution of cargo molecules in the cell, hence $N/C(t = 0) = 1$, as has been measured for cells on soft substrates and supports [8, 220, 261]. This is also the expected N/C ratio obtained if only passive transport is allowed. We note that initially only bare cargo is present in the nucleus and the cytoplasm, which is set to $\Phi c(\boldsymbol{x}, t = 0) =!$ and $\psi n(\boldsymbol{x}, t = 0) = 1$, while $\Phi c_I(\boldsymbol{x}, t = 0) = 0$ and $\psi n_I(\boldsymbol{x}, t = 0) = 0$. The above initial conditions apply for all simulations presented.

Figure 6.2 A shows the time evolution of the N/C ratio for tension-induced changes of the passive and active permeability to $P'_p = f_p P_p$ and $P'_a = f_p P'_a$ by the factor $f_p = 1$, 1.25 and 2 (blue to yellow) for $k^0_{1/2} = 0.054\,\mathrm{s}^{-1}$ (dashed lines) and $k^0_{1/2} = 0.5\,\mathrm{s}^{-1}$ (solid lines). Interestingly, an increase of both permeabilities by the same factor f_p leads to a decrease of the N/C ratio compared to the case without NPC dilation in response to tension, *i.e* the case $f_p = 1$. This observation can be made for both tested association rates. One can explain this phenomenon by the establishment of a high gradient in bare cargo protein concentration between nucleus (n) and cytoplasm (c), increasing the passive protein flux out of the nucleus. Passive diffusion therefore seems to benefit more from NPC dilation, which decreases the N/C ratio. The influence of passive diffusion on N/C ratios has been previously demonstrated by Görlich et al. [265], whose model for Ran-driven cargo transport through NPCs yielded a dramatic decrease of the N/C ration when passive transport was allowed compared to only active transport.

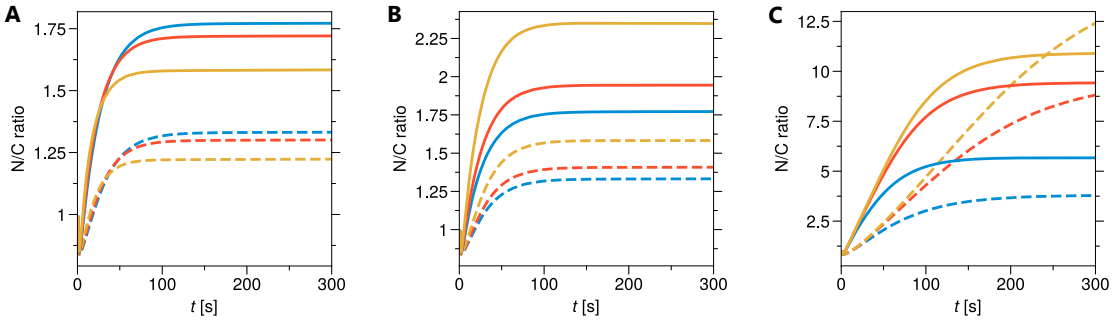

Figure 6.2: A Time evolution of the nucleocytoplasmic signal ratio (N/C ratio) in an isotropically contracting cell on a rectangular micropattern (*cf.* Sect. 5.3.2 Fig. 5.3 or Fig. 6.3 C)) with a nucleus of stiffness $E_N/E_C = 10$ for an equal response of passive and active permeability to nuclear tension ($\Sigma_\tau > 0$). Shown are the cases that both permeabilities change by the factor $f_p = 1$, 1.25 and 2 (blue to yellow) in response to tension for association rates $k^0_{1/2} = 0.054\,\mathrm{s}^{-1}$ (dashed lines) and $k^0_{1/2} = 0.5\,\mathrm{s}^{-1}$ (solid lines). **B** As in (**A**) but now only the active permeability is changing by the factor $f_p = 1$, 1.25 and 2 (blue to yellow), while the passive permeability is constant. **C** Shown is the N/C ratio with time for $P_a = 0.1\,\mu\mathrm{m/s}$, $P'_a = 0.5\,\mu\mathrm{m/s}$ and varying $P_a/P_p = 5$, 20 and 50 (blue to yellow) for $k^0_{1/2} = 0.054\,\mathrm{s}^{-1}$ (dashed lines) and $k^0_{1/2} = 0.5\,\mathrm{s}^{-1}$ (solid lines). Other parameters as in Appendix B.4.2 Table B.5.

Next, we consider the case where tension impacts P_p and P_a differently. For proteins with a size similar to YAP, Andreu et al. [9] reported approximately equal passive influx and efflux rates for cells on soft and stiff substrates, *i.e.* with and without forces exerted on the nucleus. On the other hand, active influx rates increased in response to forces [9]. Following these results, we assume the passive permeability not to change in response to tension, *i.e.* $P'_p = P_p = 0.075\,\mu\mathrm{m/s}$. However, the active permeability is allowed to increase from $P_a = 0.2\,\mu\mathrm{m/s}$ to $P'_a = f_p P_a$.

In Fig. 6.2 B, the time evolution of the N/C ratio is shown for the case, that only the active permeability is affected by tension for $f_p = 1, 1.25$ and 2 (blue to yellow) and two different cargo-importin association rates $k^0_{1/2}$ as before. In contrast to the previous observation, the different response of the permeabilities to tension leads to an increase of the stead state value of the N/C ratio compared to the case without tension-induced NPC stretch ($f_p = 1$). This is true for the tested association rates $k^0_{1/2}$. This is in agreement with the previously mentioned experimental results [9], that a different response of passive and facilitated transport to tension is responsible for increased N/C ratios.

We note that the magnitude of the steady state N/C ratio depends on the cargo-importin association rates $k^0_{1/2}$ (*cf.* Fig. 6.2 A and B) and should also depend on the ratio between active and passive permeability as shown by Kim et al. [264]. To ver-

ify our modelling approach regarding this aspect, we here set for testing purposes the active permeability in absence of stress to a lower value $P_a = 0.1\,\mu m/s$ which changes in presence of tension to $P'_a = 0.5\,\mu m/s$, which is the by Ribbeck et al. [102] estimated velocity with which cargo-transportin complexes can traverse NPCs. The passive permeability is varied and kept constant, irrespective of the tension. Figure 6.2 C shows again the evolution of the N/C ratio for association rates $k^0_{1/2} = 0.054\,s^{-1}$ (dashed lines) and $k^0_{1/2} = 0.5\,s^{-1}$ (solid lines) and ratios $P_a/P_p = 5$, 20 and 50 (blue to yellow). One sees the expected increase of the signal ratio with increasing P_a/P_p ratio [264]. Note that for low association rates larger N/C ratios can be reached for high ratios P_a/P_p, as active and passive efflux are severely reduced. Active efflux is reduced due to the rapid dissociation of cargo-importin complexes in the nucleus.

6.3.3 Effect of nuclear stiffness

In the previous section, our model showed that only if passive and active permeability react differently to nuclear tension, *i.e.* the ratio $P'_a/P'_p > P_a/P_p$, the accumulation of proteins in the nucleus is higher compared to the case without a permeability change due to tension, consistent with recently published experimental results [9].

We here want to investigate the effect of nuclear stiffness on the obtained N/C ratio in spread cells. The values for the different permeabilities are fixed as previously to $P'_p = P_p = 0.075\,\mu m/s$, $P_a = 0.2\,\mu m/s$ and $P'_a = 0.5\,\mu m/s$. Again, we first consider a contractile cell adhered to a rectangular shape with a nucleus of stiffness E_N/E_C, which is centred in the cell.

Figure 6.3 A shows the evolution of the N/C ratio with time for physiological nucleus stiffnesses $E_N/E_C = 2$ and $E_N/E_C = 10$. One clearly sees that a stiff nucleus ($E_N/E_C = 10$) increases the import of cargo and their accumulation in the nucleus. Note, the initial decrease of the N/C ratio below 1 results from reduction of (especially) the cytoplasmic area due to the cell contraction. The regions on the nuclear envelope with increased permeability can be inferred from the tension Σ_τ on the nucleocytoplasmic boundary (*cf.* 6.3 B for $E_N/E_C = 10$) in mechanical equilibrium, showing that a dilation of NPCs and an increase of the active permeability (as we assume the passive one not to change) is expected at the upper and lower pole of the nucleus. For a soft nucleus ($E_N/E_C = 2$) the distribution of Σ_τ on the nucleus boundary is very similar. Accordingly, the distribution of the cargo concentration $\Phi(c+c_I)$ and $\psi(n+n_I)$ (*cf.* Fig. 6.3 C for $E_N/E_C = 10$ and three different time points) shows a decreased $c + c_I$ concentration near the nucleus where $\Sigma_\tau > 0$. Furthermore, the accumulation of cargo proteins in the nucleus is clearly visible.

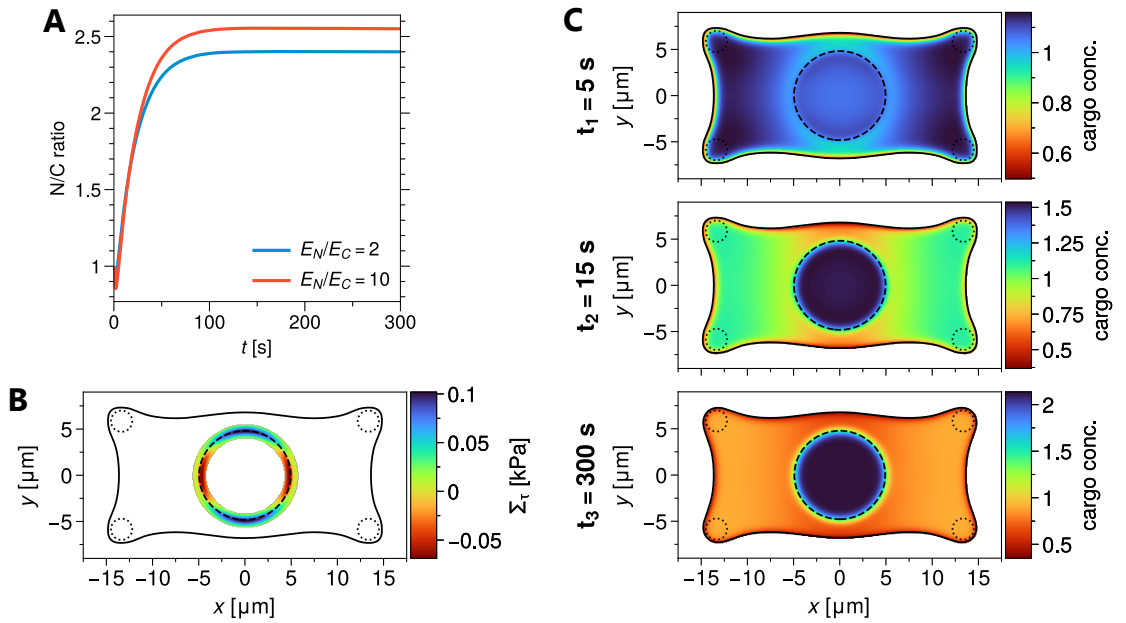

Figure 6.3: Effect of nuclear stiffness on the mechanosensitive nucleocytoplasmic protein transport in isotropically contracting, spread cells of rectangular shape. **A** Shown is the time evolution of the N/C ratio for $E_N/E_C = 2$ (blue) and $E_N/E_C = 10$ (red) with $E_C = 1\,\mathrm{kPa}$ and $k^0_{1/2} = 0.5\,\mathrm{s}^{-1}$. **B** Depicted is Σ_τ (*cf.* Eq. (6.12)) for $|\nabla\psi| > 0.1$ in mechanical equilibrium for a stiff nucleus ($E_N/E_C = 10$), to visualize the nuclear regions of increased active permeability, where $\Sigma_\tau > 0$. **C** Shown is the concentration of cargo proteins $\Phi(c + c_I) + \psi(n + n_I)$ for $\rho \geq 0.5$ for a centred nucleus with $E_N/E_C = 10$ at three different time points: $t_1 = 5\,\mathrm{s}$, $t_2 = 15\,\mathrm{s}$ and $t_3 = 300\,\mathrm{s}$. In (**B**) and (**C**) the adhesion spots of radius r_{adh} are marked by dotted lines, the cell boundary is indicated by the isocontour $\rho = 1/2$ (solid line) and the nuclear boundary by the isocontour $\psi = 1/2$ (dashed line). Other parameters as in Appendix B.4.2 Table B.5.

As a next example, we consider the effect of local straining. We model again the situation as before, *i.e.* a cell which is allowed to adhere to a rectangular shape and which is isotropically contracting with $\sigma_0/E_C = 0.4$. First, the cell is allowed to contract. When mechanical equilibrium has been reached, we apply a localized force of Gaussian shape

$$\boldsymbol{F}(\boldsymbol{x}) = \frac{F_0}{2\pi v_x v_y} \exp\left[-\left(\frac{(x-x_0)^2}{2v_x^2} + \frac{(y-y_0)^2}{2v_y^2}\right)\right] \boldsymbol{e_x}, \tag{6.18}$$

with amplitude F_0 and width in x- and y-direction given by v_x and v_y [10]. This force enters the right-hand side of Eq. (6.14) and pulls on the right edge of the cell at $y = 0$ in positive x-direction. Note that Eq. (6.18) is a boundary force and should always be located in the phase field interface, hence, it should follow its motion, *i.e.* $x_0 = x_0(\rho)$ [10]. As the Gaussian function converges to a Dirac delta function in the sharp

interface limit, it is a suitable choice for a smooth representation of boundary forces in the phase field sense [10]. For reasons of numerical stability, the force was increased by a small amount ΔF per timestep until F_0 had been reached.

Figure 6.4 A shows the N/C ratio with time for a nucleus of stiffness $E_N/E_C = 2$ (blue) and $E_N/E_C = 10$ (red), which is centred in the nucleus (solid, *cf.* Fig. 6.4 B) and shifted to the right (dashed, *cf.* Fig. 6.4 C) for pulling forces $F_0 = 0.5\,\mathrm{nN}$ (top) and $F_0 = 2.5\,\mathrm{nN}$ (bottom). The force magnitude has only small effect and decreases the N/C ratio for increasing force as it counteracts the cell contraction. As in the previous example, the stiffer nucleus shows a higher N/C ratio compared to the softer nucleus. For a nucleus displaced in positive x-direction (*cf.* Fig. 6.4 C) similar observations can be made regarding the relation between the N/C ratios (dashed lines) of a cell with a stiff nucleus ($E_N/E_C = 10$, red) and a cell with a softer nucleus ($E_N/E_C = 2$, blue). Again, the concentration map for the two nucleus positions for $E_N/E_C = 10$ shown in Fig. 6.4 B and C, demonstrate a decreased concentration $\Phi(c+c_I)+\psi(n+n_I)$ where the permeability of the boundary is increased (*cf.* Fig. 6.4 D and E) due to tension $\Sigma_\tau > 0$. Note that shifting the nucleus results in a lowered concentration in the cell-half where the nucleus is present, while the concentration is higher in the other (left) cell-half (*cf.* Fig. 6.4 E). The slightly lower N/C ratio in this case may result from a reduced nuclear boundary area under tension. Nevertheless, an increased nuclear concentration of cargo at the side of higher permeability is visible, while it is lower on the corresponding cytoplasmic side.

Lastly, we consider a rectangular cell which is globally stretched along its long axis. Here, cell contractility is neglected to study the effect of global stretching of the cell (and the nucleus) on the associated nuclear protein accumulation. The forces, which are stretching the cell are applied along the left and right edge of the cell. Both are again of Gaussian-like shape along the x-direction, while they are restricted to the length of the short edges. The initial N/C ratio is again set to 1, with $\Phi c(\boldsymbol{x}, t = 0) = \psi n(\boldsymbol{x}, t = 0) = 1$ and $\Phi c_I(\boldsymbol{x}, t = 0) = \psi n_I(\boldsymbol{x}, t = 0) = 0$.

Figure 6.5 A shows the N/C ratio with time for $E_N/E_C = 2$ and $E_N/E_C = 10$ for different cargo-importin association rates $k^0_{1/2}$, for a nucleus centred in the cell (top panel) and a nucleus shifted to the right in x-direction (bottom panel) (see also Fig. 6.5 B and C). In both cases and for all tested cargo-importin association rates $k^0_{1/2}$, the softer nucleus ($E_N/E_C = 2$) shows a higher protein accumulation in the nucleus as the stiffer one,different to the previous examples of a contractile cell. The higher the association rate, the bigger is the absolute difference. Furthermore, the shifted nucleus accumulates more cargo as it is closer to one of the forced cell edges. In Fig. 6.5 B and C the protein

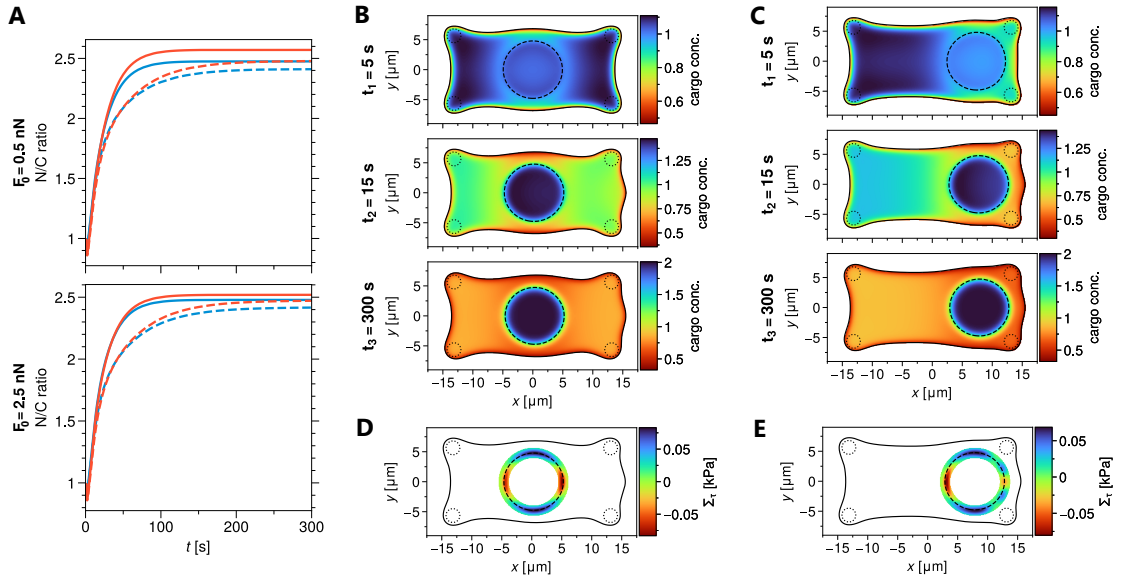

Figure 6.4: Protein import into the nucleus of a rectangular cell adhered to focal adhesions it its corners. The cell first is isotropically contracting with $\sigma_0/E_C = 0.4$ and when mechanical equilibrium is reached a localized force is pulling on its right edge at $y = 0$ in positive x-direction with magnitude F_0. **A** N/C ratio with time for two different forces $F_0 = 0.5\,\text{nN}$ (top) and $F_0 = 2.5\,\text{nN}$ (bottom) with $v_x = 0.5\,\mu\text{m}$ and $v_y = 1.75\,\mu\text{m}$. Shown are the cases of centred nucleus (solid lines) and for a nucleus shifted by to the right by $\Delta x_N = 7.5\,\mu\text{m}$ (dashed lines) with nucleus stiffnesses $E_N/E_C = 2$ (blue) and $E_N/E_C = 10$ (red). **B** Shown is the concentration field of cargo proteins $\Phi(c+c_I)+\psi(n+n_I)$ for $\rho \geq 0.5$ for a centred nucleus with $E_N/E_C = 10$ at three different time points: $t_1 = 5\,\text{s}$, $t_2 = 15\,\text{s}$ and $t_3 = 300\,\text{s}$. **C** as in (**B**) for a shifted nucleus. **D/E** Maps of the tension Σ_τ in the region $|\nabla\psi| > 0.1$ at the nuclear boundary in mechanical equilibrium with the pulling force for the case shown in (**B/C**). In (**B-E**) the adhesion spots of radius r_{adh} are marked by dotted lines, the solid black line marks the cell boundary by the $\rho = 1/2$-isocontour and the dashed black line marks the nuclear boundary by the $\psi = 1/2$-isocontour. If not stated otherwise, the parameters are as in Appendix B.4.2 Table B.5.

concentration for $E_N/E_C = 2$ is shown for three different time points and in Fig. 6.5 D and E the corresponding tension Σ_τ along the nuclear boundary. The observations are similar to the previous cases.

In summary, our modelling approach predicts that nuclear rigidity effects the transport of proteins into the nucleus for contractile and stretched cells. While in contractile cells a stiff nucleus imports more cargo protein, in stretched cells the soft nucleus shows a higher N/C ratio.

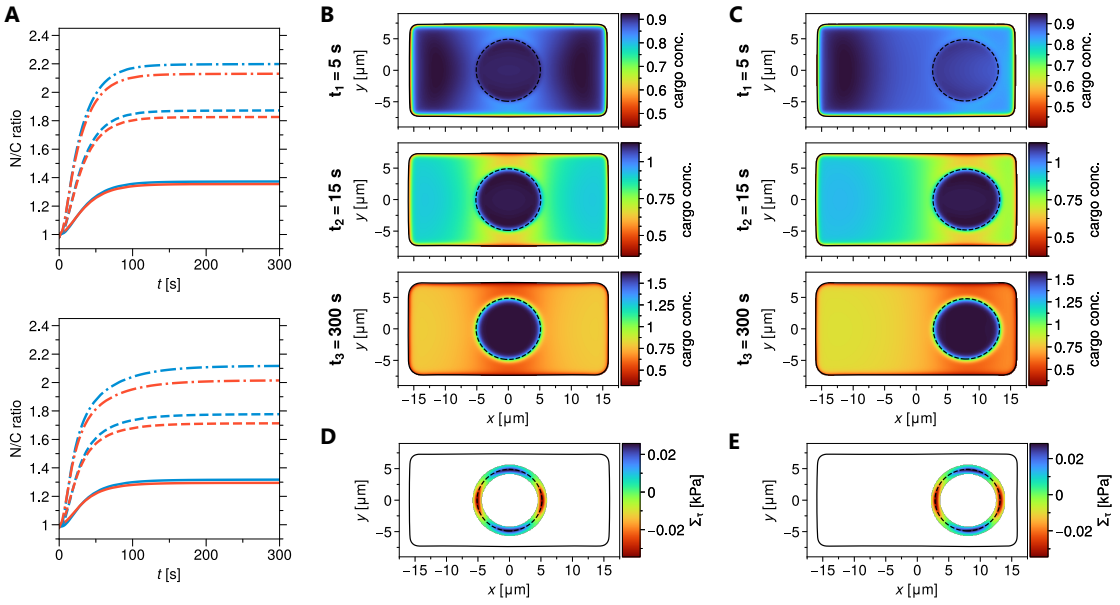

Figure 6.5: Effect of nuclear stiffness on the mechanosensitive nucleocytoplasmic protein transport in a rectangular cell, which is uniaxially stretched by a force of magnitude $F_0/E_C = 0.1$ and $v_x = 0.5\,\mu$m applied at its left and right edge and pulling on them in $\pm x$-direction. **A** Shown is the time evolution of the N/C ratio for $E_N/E_C = 2$ (blue) and $E_N/E_C = 10$ (red) with $E_C = 1$ kPa and cargo-importin association rates $k^0_{1/2} = 0.054\,\mathrm{s}^{-1}$ (solid), $k^0_{1/2} = 0.2\,\mathrm{s}^{-1}$ (dashed) and $k^0_{1/2} = 0.5\,\mathrm{s}^{-1}$ (dashed-dotted). The top panel corresponds to the case of a (B) nucleus centred in the cell and the bottom panel to (C) a nucleus shifted by $\Delta x_N = 7.5\,\mu$m in positive x-direction. **B** Shown is the concentration field of cargo proteins $\Phi(c + c_I) + \psi(n + n_I)$ for $\rho \geq 0.5$ for a centred nucleus with $E_N/E_C = 2$ at three different time points: $t_1 = 5$ s, $t_2 = 15$ s and $t_3 = 300$ s. **C** as in (**B**) for a nucleus shifted by $\Delta x_N = 7.5\,\mu$m in positive x-direction. **D/E** Shown are the maps of the tension Σ_τ in the region $|\nabla\psi| > 0.1$ at the nuclear boundary in mechanical equilibrium for the corresponding cases shown in (**B/C**). In (**B-E**) the adhesion spots of radius r_{adh} are marked by dotted lines, the cell boundary is marked by the $\rho = 1/2$-isocontour (solid line) and the nucleus boundary is indicated by the $\psi = 1/2$-isocontour (dashed line). If not stated otherwise, the parameters are as in Appendix B.4.2 Table B.5.

6.4 Discussion

To react to mechanical stimuli, cells import proteins into their nucleus, which are involved in gene expression and transcription [86]. This import is enabled by the transmission of forces via the cytoskeleton to the nucleus [268]. Forces transmitted to the nucleus can lead to tension-induced stretching of NPCs [6], which is hypothesized to weaken the NPC permeability barrier and thereby facilitating transport through NPCs leading to an accumulation of proteins in the nucleus [8, 9].

In this chapter, we studied the effect of nuclear rigidity on mechanotransduction, *i.e.*

whether the stiffness of the nucleus influences the nuclear import of proteins. We proposed a model that combines the elastic phase field approach for modelling a cell with nucleus from Chapter 5 with a reaction-diffusion system for describing mechanosensitive protein import. The mechanosensitivity of the import process was accounted for by allowing the formation of actively transportable cargo-importin complexes due to stress and a tension-induced increase of the active and passive permeability of the nuclear envelope. For simplicity, we assumed a permeability increase as soon as the nuclear boundary is locally under tension. We restricted the investigation to proteins with a size similar to YAP, which is an important and often studied protein in the context of mechanotransduction [86].

First, we studied the N/C ratio in the case that passive and active permeability are only affected by the geometrical dilation of NPCs, *i.e.* both change by a same factor in response to nuclear tension, keeping their ratio. The result was that passive transport benefits more from an NPC dilation, possibly due to the accumulation of cargo proteins (not in a complex with importins) and a high concentration gradient of cargo between cytoplasm and nucleus. This led to a decrease of the N/C ratio compared to the case without a tension-induced increase of the permeabilities. However, assuming that only the active permeability increases in response to tension, while the passive permeability remains constant resulted in an increase of the N/C ratio. Hence, to allow for increased import due to increased permeability, passive and active transport have to react differently to nuclear tension, as previously suggested [9].

Consequently, we assumed in the following studies that only the active permeability increases while the passive one does not change. This is motivated by the study of Andreu et al. [9], who measured no considerable change of passive influx rates into the nucleus for YAP-sized proteins, while the facilitated influx rates increased in response to force. Hence, the increased facilitated transport is possibly mediated also by other effects, *e.g.* by conformational changes of the NPC in response to tension [6, 256].

Thereafter, we investigated whether nuclear stiffness and position influences the dynamics of nuclear import and the obtained N/C ratios in steady state for a contractile cell on a micropattern. We found that stiff nuclei ($E_N/E_C = 10$) led to increased accumulation of proteins in the nucleus in contractile cells also in presence of localized pulling forces. In contrast, uniaxial cell stretching resulted in a higher accumulation of proteins in soft nuclei ($E_N/E_C = 2$). The position of the nucleus, in our cases closer to focal adhesions in adhered cells, led to a slight decrease of the N/C ratio, possibly due to lower nuclear deformation. In all cases, the concentration in the cytoplasm was lower

at the nuclear boundary with tension, and larger in the nucleus at these sites of higher permeability. In summary, nuclear stiffness impacts the accumulation of cargo, however seemingly in a context-dependent manner, where stiff nuclei have higher import rates in contractile cells and soft nuclei in stretched cells.

Our proposed model is motivated by previously published kinetic models for nucleocytoplasmic transport of proteins by Elosegui-Artola et al. [8] and Kim et al. [264]. While we accounted in a simplified model for spatial mechanical effects on the import process, Kim et al. [264] focussed on the impact of competition between different cargo proteins and Andreu et al. [9] developed a detailed model for the import process, including the RanGTP/GDP cycle (*cf.* Fig. 2.6) and transport kinetics through NPCs, where mechanics entered by increasing NPC translocation rates. To further improve the presented model, one could additionally add these two aspects, cargo competition and the RanGTP/GDP cycle. Further, it should be feasible to also include the export cycle as shown in Fig. 2.6 to extend the model to describe the full transport process. Especially, accounting for a possible feedback of mechanotransduction on cell behaviour/mechanics should be a future goal of previous studies.

Turning from single cell to cell collectives, tissues can be described by resolving the constituting cells and their nuclei by an individual phase field, respectively. It would be highly interesting to study mechanosensitive nucleocytoplasmic transport in such situations, especially in the context of development.

As discussed in the previous chapters, the phase field model could be extended to three dimensions [146, 205]. It would be interesting to study the mechanotransduction for cells in more physiological environments, especially in the context of migration [263] through constrictions, where the nucleus can be heavily deformed and even can even rupture [99, 100, 208].

Nevertheless, in order to get a full picture of the effect of NPC dilation one could think of including resolved holes in the nucleus representing NPCs, instead of considering an effective permeability of the nuclear envelope. How and whether this could be done in the phase field framework should be the subject of future studies.

In summary, the elastic phase field approach is a framework, which can be used to study mechanotransduction and the mechanosensitive nucleocytoplasmic protein shuttling in many different biological situations, ranging from stationary to possibly dynamics ones.

7 Continuum model for mechanosensitive stress fibre formation

In the previous chapters, the role of the nucleus in whole-cell mechanics (*cf.* Chapter 5) and its effect on mechanosensitive nuclear-cytoplasmic protein transport (*cf.* Chapter 6) have been studied by using adapted phase field models. However, the main determinant of cell mechanics is the cytoskeleton, thereby playing a key role in many biological processes. Also recall that it is involved in the transmission of mechanical information to the nucleus. Dynamical reorganization of the cytoskeleton in response to strain and stress, allows a cell to adapt its shape and stiffness to the environment. Especially in stationary, adherent cells the prominent actin filament bundles, called stress fibres, are emerging in a mechanosensitive manner.

Here, we extent the elastic phase field approach of Chapter 4 to model this mechanosensitive stress fibre formation. Instead of discrete stress fibres, we model a continuous orientation field in the cell, which is coupled to elasticity. This orientation field represents the degree of alignment of the actin cytoskeleton, which reorients from an initially isotropic to a locally order state in response to stress. A high degree of alignment can be seen as a precursor for full stress fibre formation. More specifically, we study stress fibre emergence in contractile, stationary cells of various shapes, also investigating a possible mechanical feedback of these cytoskeletal structures on whole-cell elasticity.

7.1 Introduction

In physiological conditions, cells are constantly subject to stresses from their environment, which they have to resist. An important module in this context are thick and stiff actin filament bundles, which can be contractile and mechanically stabilize

cells.[1] Prominent stress fibres have been shown to assemble in cells spreading on micro-engineered substrates of well-defined geometry at non-adhered cell edges, *i.e.* invaginated arcs [201]. Important here is, that the geometry of the adhesive pattern determines the stress fibre distribution and that their transient presence during cell spreading has been associated with a 'memory' for the spreading history [276]. Stress fibres are the main contractile elements in cells [60], whose cross-sectional area apparently linearly correlates with focal adhesion area and thus substrate rigidity [62]. Consistently, the size of focal adhesions correlates with the exerted traction forces, and hence stress fibre contractility, resulting in average shears stresses of approximately 5.5 kPa [69], which are however not constant along the focal adhesions [277].

Stress fibres are especially important in mechanotransduction. They are able to substantially alter nuclear morphology [220], which is a key element in nuclear mechanosensing of the mechanical properties of the ECM. LINC complexes form a direct physical bridge for force transmission between stress fibres and the nuclear envelope [75], which has been shown by severely reduced nuclear accumulation of proteins such as YAP (*cf.* Sect. 2.2.2 and Chapter 6) upon the dissolution of LINC complexes [8]. Although being exceptionally prominent in stationary cells, as this allows for their full maturation, thinner and smaller stress fibres have also been observed in migrating cells [64].

Assembling mostly at focal adhesions where high traction forces are exerted by the cell on the underlying substrate, it is nowadays accepted that these stress fibres form in a mechanosensitive manner [60, 63, 70]. Mechanosensitivity has for instance been observed in micro-pattern experiments involving cyclic straining of the adhered cell, stimulating the assembly of new stress fibres [278]. Recently, it has been demonstrated that they are continuously embedded into the cell cortex and can form out of it through filament bundling and not only from anew polymerization [52]. Nevertheless, many details on their assembly processes are still unknown.

To unravel the complexity of stress fibres, models have been conducted to investigate their mechanical behaviour and assembly process. Models have been proposed for single stress fibres to investigate for instance their mechanics [68, 279] and, more recently, response to tension [280] and stretch [281]. Further, the biochemically-mediated contraction of stress fibres in a cell has been studied in a 1D model [282], where stress fibres were described as viscoelastic materials [283]. Mechanosensitive stress fibre formation has also been studied in higher dimensions, where either stress/tension (in combination with biochemical processes) determines the emergence and orientation of stress

[1] For more details see Sect. 2.1.

fibres [221, 284–288] or mechanical stretch [289]. In contrast to whole-cell mechanical models, stress fibre alignment and mechanical feedback has been investigated using a contour model combined with liquid crystal theory demonstrating cell shape induced stress fibre orientation [290].

We here propose a continuum approach using our now well-developed phase field method for modelling the reorganization of the cytoskeleton, *i.e.* its alignment in response to stress, indicating the location and growth direction of precursors of stress fibres. The mechanosensitive alignment of cytoskeletal filaments is modelled in a continuum fashion by using a nematic liquid crystal as in Ref. [290], which is coupled to whole-cell mechanics described by linear elasticity theory [284] also including a possible feedback of emerging stress fibres on cell rigidity and contractility. The nematic description is motivated by experimental results showing that actin filaments in solution exhibit a transition from an isotropic (unaligned) state to nematic ordering in response to increasing filament density [291–293].

In this chapter, we will first briefly introduce the theory of nematic liquid crystals and then discuss the developed model. Afterwards we study the formation of stress fibres in contractile cells adhered on micro-patterns with and without a feedback of filament bundling on cell stiffness and contractility.

7.2 Overview on nematic liquid crystals

Liquid crystals (LCs) are mesomorphic materials of anisotropic molecules, which show liquid- and crystal-like characteristics [294]. One distinguishes between three main classes: nematics, smectics and columnar phases [294]. Nematic LCs consist of elongated particles with no positional order (like a liquid) but long-range orientational order (similar to a crystal) [294, 295]. This class is further divided into uniaxial and biaxial nematics. In the uniaxial case the constituting molecules are rod-like with rotational symmetry around their long axis [295]. Biaxial nematics are formed by rather plate-like molecules with two symmetry axes [294].

While nematic LCs have three spatial degrees of freedom, for smectic LCs this number is reduced to two by imposing positional order in one dimension [294]. In this case, the constituting molecules can arrange in layers which may slide against each other [296]. If the positional degrees of freedom reduce to one, the considered system is a columnar LC as the particles are further ordered into columns, hence the name [294, 296].

All LC classes have in common, that they show long-range orientational order, which renders them anisotropic systems.

For our purposes, i.e. modelling fibre orientations in strongly spreading quasi-two-dimensional cells, we will use the theory of uniaxial nematic liquid crystals in two dimensions, which will be introduced in the following.

7.2.1 Landau - de Gennes free energy functional

Phase transitions from an unordered (isotropic) to an ordered (nematic) state observed for nematic LCs, for example above a critical particle density or in presence of an external field, can phenomenologically be described by constructing a Landau free energy functional using an order parameter describing the system's orientational state [294]. The most rational choice would be the (local) preferred orientation of uniaxial nematic molecules, given by the director $\boldsymbol{n}$ (*cf.* Fig. 7.1 A). Physically, its sign is irrelevant as it is assumed that no preferential orientation exists regarding the two particle ends [296]. However, no free energy functional can be constructed with the director as it would not be invariant under the transformation $\boldsymbol{n} \rightarrow -\boldsymbol{n}$ [297]. Therefore, a symmetric and traceless tensor is built from the director $\boldsymbol{n}$, describing the nematic crystalline order and being invariant under the aforementioned transformation [294]. In two-dimensions it is defined as

$$\boldsymbol{Q} = S\left(\boldsymbol{n} \otimes \boldsymbol{n} - \frac{1}{2}\mathbf{1}\right) \quad \text{or in index notation} \quad Q_{ij} = S\left(n_i n_j - \frac{1}{2}\delta_{ij}\right), \tag{7.1}$$

where $\mathbf{1}$ is the identity matrix S is a scalar order parameter quantifying the local degree of alignment of molecules [290, 294, 296]. It is defined to be in the range $0 \leq S \leq 1$ [294, 296]. The limiting cases are the isotropic state ($S = 0$) and a state of perfect parallel alignment ($S = 1$) [294–296].

In the two-dimensional case, when $\boldsymbol{Q}$ is known, the order parameter S can be straightforwardly calculated with

$$S = \sqrt{2tr(\mathbf{Q}^2)}, \tag{7.2}$$

where $tr\left(\boldsymbol{Q}^2\right) = Q_{ij}Q_{ij} = 2\left(Q_{11}^2 + Q_{12}^2\right)^2$ [290].

Note, if in 2D the director is written as $\boldsymbol{n} = (\cos(\theta), \sin(\theta))$, the $\boldsymbol{Q}$-tensor can be reformulated as a pseudovector $\boldsymbol{q} = (S/2)(\cos(2\theta), \sin(2\theta))$ using its symmetry properties.

[2]Using that $\boldsymbol{Q}$ is traceless ($Q_{22} = -Q_{11}$) and symmetric ($Q_{21} = Q_{12}$).

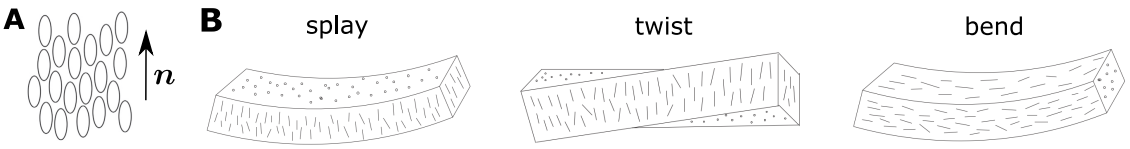

Figure 7.1: A Cartoon of a nematic liquid crystal. The rod-like molecules are oriented in the direction given by the director $\boldsymbol{n}$. Note that under the transformation $\boldsymbol{n} \rightarrow -\boldsymbol{n}$ the nematic state is unchanged. **B** The three elastic modes in a 3D nematic liquid crystal: splay (K_1), twist (K_2) and bend (K_3). In 2D, the twist deformation is not possible. Figure adapted from [296].

A phenomenological free energy functional, the Landau-de Gennes free energy, can be formulated. This has to be done in terms of scalar invariants of $\boldsymbol{Q}$ [294]. Up to fourth order, it reads

$$f_{LdG} = \frac{A}{2} tr\left(\mathbf{Q}^2\right) - \frac{B}{3} tr\left(\mathbf{Q}^3\right) + \frac{C}{4} tr\left(\mathbf{Q}^2\right)^2 + O\left(\mathbf{Q}^5\right), \tag{7.3}$$

where commonly A depends on the state variable under whose change the isotropic-nematic transition occurs and B, C are constants [294, 295].[3] For the two-dimensional case $tr\left(\boldsymbol{Q}^3\right) = 0$ and this holds for all odd powers of $\boldsymbol{Q}$. Consequently, Eq. (7.3) consists solely of invariants in even powers of $\boldsymbol{Q}$ and only second order phase transitions (*i.e.* continuous phase transitions) exist [294, 298]. One can show from Eq. (7.3) that for $A > 0$ the state $S = 0$ is the only equilibrium, while for $A < 0$ the system can spontaneously establish a nematic order $S > 0$ [298].

7.2.2 Distortions in nematic liquid crystals

Changes in local orientation of the LC can be penalized by an additive distortion energy contribution to Eq. (7.3). It is up to second order given in index notation by

$$f_{el}^{2D} = \frac{L_1}{2} \partial_k Q_{ij} \partial_k Q_{ij} + \frac{L_2}{2} \partial_j Q_{ij} \partial_k Q_{ik}. \tag{7.4}$$

The Landau constants L_i are phenomenological and their interpretation is not straightforward.

However, the distortion energy can be described in terms of gradients in the director $\boldsymbol{n}$, which in its most general form is given by

$$\mathcal{F}_{el} = \frac{1}{2} \int K_{ijkl} \left(\nabla_i n_j\right) \left(\nabla_k n_l\right) d\boldsymbol{x}, \tag{7.5}$$

[3] The first order vanishes as $\boldsymbol{Q}$ is traceless, *i.e.* $tr(\boldsymbol{Q}) = 0$.

where K_{ijkl} is a 4-th order tensor containing the elastic constants [297]. For nematic liquid crystals in 3D the distortion energy is given by the Oseen-Frank elastic energy

$$f_{el}^{3D} = \frac{1}{2}K_1(\nabla \cdot \boldsymbol{n})^2 + \frac{1}{2}K_2\left[\boldsymbol{n} \cdot (\nabla \times \boldsymbol{n})\right]^2 + \frac{1}{2}K_3\left[\boldsymbol{n} \times (\nabla \times \boldsymbol{n})\right]^2 \tag{7.6}$$

with the individual terms having a clear physical (and measurable) significance, namely splay (K_1), twist (K_2) and bending (K_3) deformations (*cf.* Fig. 7.1 B) [294–297]. Practically, it is often assumed that the three elastic parameters are equal (so-called *one constant approximation*) [294]. In 2D, twist does not exist and Eq. (7.6) reduces to

$$f_{el}^{3D} = \frac{1}{2}K_1(\nabla \cdot \boldsymbol{n})^2 + \frac{1}{2}K_3\left[(\boldsymbol{n} \cdot \nabla) \cdot \boldsymbol{n}\right]^2, \tag{7.7}$$

where bending (K_3 term) appears in its 2D form [299].

If discontinuous changes of the director $\boldsymbol{n}$ occur, *i.e.* in the case of singularities known as defects, the formulation of the elastic energy in terms of $\boldsymbol{n}$ can diverge. Here, Eq. (7.4) is more suitable. It is possible to relate the phenomenological Landau constants L_i to the Frank constants K_i [295, 296]. One can show (*cf.* Appendix A.4) that Eq. (7.4) leads in two dimensions to the one constant approximation

$$K_1 = K_3 = 2L_1 + L_2. \tag{7.8}$$

Therefore, higher order terms in gradients of $\boldsymbol{Q}$ would be needed in the distortion free energy, Eq. (7.4), to leave the one constant approximation and allow for different K_i values, if required [296, 300].

Since we expect to get defects for fibre orientations in highly symmetric cells, we here employ the Landau-de Gennes free energy as follows:

$$f_{tot} = \frac{L_1}{2}\partial_k Q_{ij}\partial_k Q_{ij} + \frac{L_2}{2}\partial_j Q_{ij}\partial_k Q_{ik} + \frac{A}{2}Q_{ij}Q_{ij} + \frac{C}{4}\left(Q_{ij}Q_{ij}\right)^2. \tag{7.9}$$

7.2.3 Defects in 2D nematic liquid crystals

Discontinuities in the director field $\boldsymbol{n}$ are known as (point) defects and disclinations (line defects) [294]. They are characterized by their topological charge m, stating the number of times the director $\boldsymbol{n}$ rotates when going along a closed contour around the defect core. It is given by

$$\tau = 2\pi m \tag{7.10}$$

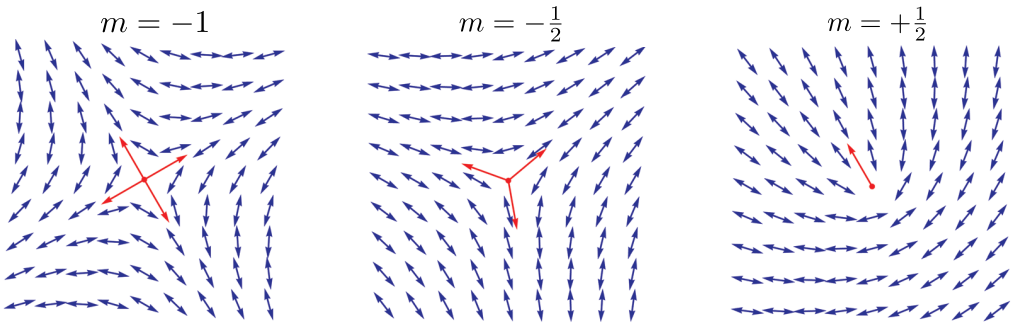

Figure 7.2: Sketches of relevant defects encountered later. Shown are defects of topological charge $m = -1, \pm 1/2$ (left to right). The blue arrows are the LC molecules. Adapted from [301].

where m is a half-integer or integer [294]. Figure 7.2 shows sketches of possible nematic defects with topological charge $m = \pm 1/2$ and $m = -1$.

7.2.4 Boundary conditions - Anchoring energy

Liquid crystals in confinement can show specific orientational order imposed by the confining boundaries of the considered system [294]. This boundary effects can be introduced into the free energy of the system by so-called anchoring energy terms such as

$$\mathcal{F}_{anch} = \frac{W}{2} \int_{\partial\Omega} tr\left[(\boldsymbol{Q} - \boldsymbol{Q}_0)^2\right] dS \tag{7.11}$$

which is a boundary integral [302]. The tensor

$$\boldsymbol{Q}_0 = S_0 \left(\boldsymbol{n}_0 \otimes \boldsymbol{n}_0 - \frac{1}{2}\mathbf{1}\right) \tag{7.12}$$

denotes the imposed orientation, with degree of alignment S_0 and in orientation $\boldsymbol{n}_0$, at the boundary. The prefactor W in Eq. (7.12) is related to the strength of the anchoring and therefore enforcement of the preferred alignment at the domain walls.

7.3 Phase field model including a liquid crystal

We aim at modelling stress-induced cytoskeletal reorientation and stress fibre emergence in a continuum elastic framework. Therefore, we combine the theory of nematic LCs with the elastic phase field model for contractile spread cells in the two-dimensional plane stress approximation as described in Chapter 4.

7.3.1 Model with stresses leading to nematic alignment

Recalling the phase field models of the previous chapters, we describe an elastic and contractile cell by a phase field $\rho(\boldsymbol{x}, t)$, where the interior of the cell is assigned the bulk value $\rho = 1$ and its exterior (empty space) the value $\rho = 0$. The dynamic equation for the phase field is as before

$$\frac{\partial \rho}{\partial t} = D_\rho \Delta \rho - \frac{\partial g(\rho)}{\partial \rho} + D_\rho \kappa_\rho |\nabla \rho| - \frac{1}{\xi} \left(\nabla \cdot \Sigma + \boldsymbol{F} - \gamma(\boldsymbol{x}) \left[1 - h(\rho) \right] \boldsymbol{u} \right) \cdot \nabla \rho, \tag{7.13}$$

where the last term is the driving force due to elasticity. Its evolution is described by the overdamped relaxation equation for the deformation field

$$\xi \frac{\partial \boldsymbol{u}}{\partial t} = \nabla \cdot \Sigma + \boldsymbol{F} - \gamma(\boldsymbol{x}) \left[1 - h(\rho) \right] \boldsymbol{u}. \tag{7.14}$$

Assuming linear elasticity, the total phase field stress tensor is

$$\Sigma_{ij}(\rho) = h(\rho) \left[2\mu \epsilon_{ij} + \lambda \epsilon_{kk} \delta_{ij} + \sigma_{ij}^{act} \right] \tag{7.15}$$

with cell material parameters μ and λ, and an active stress σ_{ij}^{act}. In this chapter cells adhered to micropatterns are modelled. Adhesion is again described by the force

$$\boldsymbol{F}_{adh} = -Y(\boldsymbol{x}) h(\rho) \boldsymbol{u} \tag{7.16}$$

entering the forces in Eqs. (7.13) and (7.14), with locally varying adhesion strength $Y(\boldsymbol{x})$. For more details on these model equations, the reader is referred to Chapters 3 and 4.

As a next step, the nematic liquid crystal has to be coupled to the above phase field model. Starting point is the Landau free energy functional in 2D, *i.e.* Eq. (7.9)

$$f_{tot} = \frac{L_1}{2} \partial_k Q_{ij} \partial_k Q_{ij} + \frac{L_2}{2} \partial_j Q_{ij} \partial_k Q_{ik} + \frac{\epsilon}{2} Q_{ij} Q_{ij} + \frac{1}{4} \left(Q_{ij} Q_{ij} \right)^2, \tag{7.17}$$

where we fixed the constant $C = 1$ and $A = \epsilon \ll 1$. Although small, ϵ has to be larger than zero such that in the absence of any external driving the isotropic state $S = 0$ is a minimum and no spontaneous symmetry breaking, *i.e* no transition to a nematic state with $S > 0$, can occur. The dynamic equation of the nematic LC can then be obtained by a functional derivative of Eq. (7.17)

$$\tau_Q \frac{\partial Q_{ij}}{\partial t} = -\frac{\delta \mathcal{F}}{\delta Q_{ij}} + \left(a_{ij} - a_{ji} \right) + b \delta_{ij} \tag{7.18}$$

where

$$\frac{\delta \mathcal{F}}{\delta Q_{ij}} = -\left(\frac{\partial f}{\partial Q_{ij}} - \nabla_j \cdot \frac{\partial f}{\partial (\nabla_k Q_{ik})} \right) \tag{7.19}$$

and the last two terms

$$a_{ij} - a_{ji} = \frac{L_2}{2} \left(\partial_i \partial_k Q_{jk} - \partial_j \partial_k Q_{ik} \right) \qquad \text{and} \qquad b\delta_{ij} = -\frac{L_2}{2} \partial_l \partial_k Q_{lk} \delta_{ij} \tag{7.20}$$

are Lagrange multipliers ensuring that the symmetry and traceless properties of $\boldsymbol{Q}$ are respected [303, 304]. Performing the calculation leads to

$$\tau_Q \frac{\partial Q_{ij}}{\partial t} = K \Delta Q_{ij} - \epsilon Q_{ij} - \frac{1}{2} S^2 Q_{ij}, \tag{7.21}$$

hence the case of two Landau constants L_i automatically results in a single constant $K = L_1 + L_2/2$.

Assuming that the cytoskeleton described by the $\boldsymbol{Q}$-tensor rearranges in response to stress, we introduce a respective active term into Eq. (7.21), *i.e*

$$\tau_Q \frac{\partial Q_{ij}}{\partial t} = K \Delta Q_{ij} - \epsilon Q_{ij} - \frac{1}{2} S^2 Q_{ij} + \frac{\gamma_Q}{2} \Sigma_{ij}^{dev}, \tag{7.22}$$

where stress and nematic order parameter are coupled via the deviatoric (symmetric and traceless) part of the stress tensor

$$\Sigma_{ij}^{dev} = \Sigma_{ij} - \frac{1}{2} \Sigma_{kk} \delta_{ij}, \tag{7.23}$$

consistent with the properties and symmetries of $\boldsymbol{Q}$. τ_Q in Eq. (7.22) sets the relaxation timescale and $\gamma_Q = 1/E$ is later chosen to be the inverse of the (local) Young's modulus E of the cell to normalize the stress, Eq. 7.23. Otherwise S may get larger one, as no upper bound exists.

Finally, the anchoring term Eq. (7.24) can be added to the dynamic equation. Rewriting it in the phase field sense as [305]

$$\mathcal{F}_{anch} = \frac{W}{2} \int_\Omega tr \left[\left(\mathbf{Q} - \mathbf{Q}_0 \right)^2 \right] |\nabla \rho|^2 d\Omega, \tag{7.24}$$

where Ω is the computational domain, and performing the functional derivative, the resulting full dynamic equation for the nematic LC is

$$\tau_Q \frac{\partial Q_{ij}}{\partial t} = K \Delta Q_{ij} - \epsilon Q_{ij} - \frac{1}{2} S^2 Q_{ij} + \frac{\gamma_Q}{2} \Sigma_{ij}^{dev} - W \left(Q_{ij} - Q_{0,ij} \right) |\nabla \rho|^2. \tag{7.25}$$

Arguing that actin preferentially orients parallel to the cell boundary, as seen for instance for stress fibres forming along invaginated arcs [201, 278], the preferred alignment (*cf.* Eq. (7.12)) is taken to be along the tangent $\boldsymbol{n}_0 = \boldsymbol{t}$ with $S_0 = 1$, for simplicity. Note, the so-constructed $\boldsymbol{Q}_0$ at the phase field interface will be proportional to $|\nabla\rho|^{-2}$, motivating the choice of the boundary description in Eq. (7.24), which facilitates the numerical implementation.

Lastly, we remark that in Eq. (7.25) the dynamics $\boldsymbol{Q}$ is considered for simplicity, not the one of $\rho\boldsymbol{Q}$, because $\boldsymbol{Q}$ does not need to be conserved and is only created inside the cell via stresses.

In summary, the governing equations for the model with stress-induced cytoskeletal fibre orientation are

$$\frac{\partial\rho}{\partial t} = D_\rho\Delta\rho - \frac{\partial g(\rho)}{\partial\rho} + D_\rho\kappa_\rho|\nabla\rho| - \frac{1}{\xi}\left(\nabla\cdot\Sigma + \boldsymbol{F} - \gamma(\boldsymbol{x})\left[1-h(\rho)\right]\boldsymbol{u}\right)\cdot\nabla\rho \tag{7.26}$$

$$\xi\frac{\partial\boldsymbol{u}}{\partial t} = \nabla\cdot\Sigma + \boldsymbol{F} - \gamma(\boldsymbol{x})\left[1-h(\rho)\right]\boldsymbol{u} \tag{7.27}$$

$$\tau_Q\frac{\partial Q_{ij}}{\partial t} = K\Delta Q_{ij} - \epsilon Q_{ij} - \frac{1}{2}S^2Q_{ij} + \frac{\gamma_Q}{2}\Sigma_{ij}^{dev} - W\left(Q_{ij} - Q_{0,ij}\right)|\nabla\rho|^2. \tag{7.28}$$

7.3.2 Adding feedback of alignment on cell mechanics

Up to now, the LC within the cell is describing the expected anisotropic reorientation of the cytoskeleton in response to stress. Besides the polymerization of new stress fibres, the alignment of adjacent actin filaments of the cell cortex can lead to filament bundling and emergence of stress fibres out of the cell cortex [52]. Therefore, we argue that high degrees of alignment S should be associated with a high actin filament density (due to alignment and polymerization) sufficient for bundling into stress fibres. Consequently, we assume that above a certain substantial critical scalar order parameter S_{cr} stress fibres are forming, whose mechanical properties should affect the background elasticity of the cell. This is supported by AFM experiments demonstrating a higher local rigidity of cells, where stress fibres are present [223].

We assume the local stiffness of the cell to change with the degree of alignment S due to the formation of stress fibres according to

$$E(S) = \begin{cases} E_C & \text{for } S < S_{cr} \\ E_C + E_{SF}S^\alpha & \text{for } S \geq S_{cr}. \end{cases} \tag{7.29}$$

Here, E_C is the Young's modulus of the cellular background and E_{SF} models its increase

due to stress fibres. The exponent α captures the dependence of the stiffness on the degree of alignment. It has been shown for entangled, isotropic semiflexible polymer networks, that the shear modulus μ and filament length density ρ_{fil} are related by $\mu \propto \rho_{fil}^{2.2}$ [306–308]. Further, experiments on actin filaments in solution revealed a seemingly linear relationship between the actin filament density and their degree of alignment S [292]. Together, this suggests in Eq. (7.29) that for network formation one expects $\alpha = 2.2$. For stress fibres, which are bundles of highly aligned actin filaments, it is likely that α is even larger 2.2. However, as they can be embedded in the cortical actin network [52], we assume for simplicity and as a lower bound $\alpha = 2$. Note that while we include an increase in stiffness due to stress fibre formation, we do not model the effect that the cell acquires anisotropic elasticity for simplicity. This would be possible, but complicated, and in addition would introduce many more (unknown) elastic constants.

In a similar spirit, the cell's contractility should also change assumed due to the formation of stress fibres. While contracting isotropically with σ_0 until S_{cr} has been reached, the assembling stress fibres introduce an anisotropic stress component due to their myosin II-driven contraction in direction of their orientation $\boldsymbol{n}$. The increase in active stress σ_{SF} is assumed to scale linearly with the alignment S as suggested by earlier studies [76, 168, 304]. We write for the active stress in the phase field formulation

$$\begin{aligned} \sigma_{ij}^{act}(S) &= \sigma_0 \delta_{ij} + \sigma_{SF} S n_i n_j \\ &= \left(\sigma_0 + \frac{1}{2}\sigma_{SF} S\right) \delta_{ij} + \sigma_{SF} Q_{ij}, \end{aligned} \tag{7.30}$$

where in the last step the definition of $\boldsymbol{Q}$ (*cf.* Eq. (7.1)) has been used [290]. In total, the assumed behaviour of the active stress in response to the formation of stress fibres is

$$\sigma_{ij}^{act}(S) = \begin{cases} \sigma_0 \delta_{ij} & \text{for } S < S_{cr} \\ \left(\sigma_0 + \frac{1}{2}\sigma_{SF} S\right) \delta_{ij} + \sigma_{SF} Q_{ij} & \text{for } S \geq S_{cr}. \end{cases} \tag{7.31}$$

which enters Eq. (7.15).

7.4 Model results

Motivated by micropattern experiments showing the appearance of prominent actin stress fibres in spread cells [201], we will consider in the following stationary, spread and contractile cells of distinct geometries. We first study the alignment of the liquid

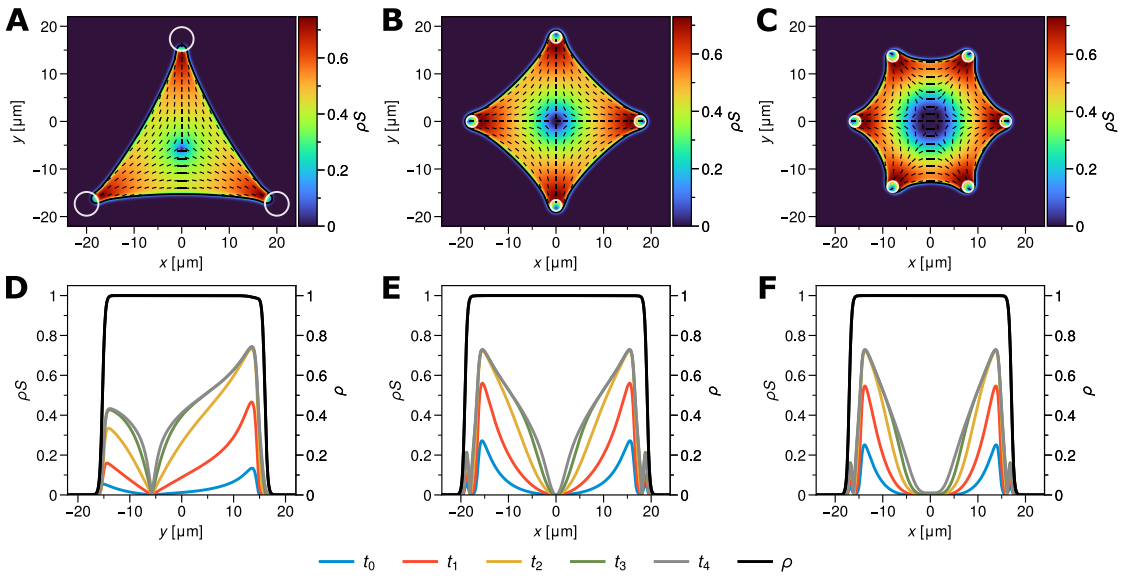

Figure 7.3: Stress-induced alignment of the nematic liquid crystal modelling cytoskeletal orientation without feedback on cell mechanics. Cells are allowed to adhere to adhesive patches (white circles) of radius r_{adh} and spring stiffness density Y in a (**A**) triangular, (**B**) square and (**C**) hexagonal arrangement.Upon an isotropic contractile stress $\sigma_0/E_C = 0.4$ the nematic liquid crystal experiences a phase transition from an isotropic ($S = 0$) to a locally aligned ($S > 0$) state. Shown are the order parameter field S (colour maps) within the cell, *i.e* ρS, and the director field $\boldsymbol{n}$ (short black lines) where $S > 0.01$. The $\rho = 1/2$-isocontours (black solid lines) indicate the cell boundary. The lower panels show ρS along (**D**) the symmetry line $x = 0$ for the triangular-shaped cell and along $y = 0$ for the (**E**) square - and (**F**) hexagonal-shaped cell for different time points $t_0 < ... < t_4$ (blue to grey). The black dashed line shows the phase field profile ρ. For simulation parameters see Appendix B.5 Table B.6.

crystal within the cell, associated with the formation of stress fibres, in response to stresses and localized forces without a mechanical feedback on the cell's rigidity and contractility. This corresponds to the model of Sect. 7.3.1. Later, we investigate the effect of the presence of stress fibres, as described by Eqs. (7.29) and (7.31).

7.4.1 Stress fibre formation without mechanical feedback

Stresses and forces exerted on a cell lead to a reorganization and realignment of the cytoskeleton including stress fibre assembly at focal adhesions. These stress fibres are known to follow non-adhered parts of the cell periphery (peripheral stress fibres) between focal adhesions or by spanning through the interior of the cell.

To see whether our proposed approach, stating that actin filament alignment and fibre formation directly depends on the stress distribution in the cell, captures such

experimental observations, we model contractile cells adhered to adhesive patches arranged in a triangular, square and hexagonal shape (*cf.* Fig. 7.3 A-C). The adhesive spots of radius r_{adh} are described by a smooth (but steep) tanh-like transition from the maximal adhesion strength Y_0 in the interior of the focal adhesion to zero outside of it (*cf.* Eq. (5.8)), with a high Y_0 to prevent slipping from the adhesive spots.[4] For the square and hexagonal cell, the adhesive spots (white circles) are entirely located in the corners of the cells (*cf.* Fig. 7.3 B and C), while in the case of the triangle (*cf.* Fig. 7.3 A) they are centred at the cell corners with a larger radius and adhesion strength to ensure sufficiently strong substrate coupling.

We first consider the situation without a feedback of the liquid crystal alignment, *i.e.* stress fibre assembly, on cell mechanics. Hence, cell stiffness and contractility are not affected and stay constant throughout the cell, *i.e.*

$$E(S) = E_C \qquad \text{and} \qquad \sigma_{ij}^{act}(S) = \sigma_0 \delta_{ij} \qquad \text{for all } S. \tag{7.32}$$

Figure 7.3 A-C show the degree of alignment ρS within the cell for the three different shapes and the respective director fields $\boldsymbol{n}$ for $\rho S > 0.01$. The highest degree of alignment, indicating the presence of (highly) aligned actin filaments that we interpret as stress fibres, are visible close to the focal adhesions. This is consistent with experimental observations, where stress fibres originate from there. From the point of view of a focal adhesion, the orientation of the director $\boldsymbol{n}$ points towards the centre of the cell and parallel to the cell periphery towards adjacent adhesion spot, similar as experimentally observed [201].

In Fig. 7.3 D-F cuts through the ρS-field along the symmetry lines $x = 0$ for the triangular-shaped cell and $y = 0$ for the square-shaped and hexagonal-shaped cells are shown for different times. One sees the growth of ρS towards the cell centre, which in our context can be interpreted as the growth of stress fibres. In the cell centre, where the stress fibres should meet, a nematic defect occurs and ρS drops to zero. Such defects are possible, considering that here stress fibres coming from different directions cross, *i.e.* run over each other, and hence there is no preferential alignment and $S = 0$. The results are qualitatively similar to those obtained in the modelling approach of Deshpande et al. [284]. We note that the director field $\boldsymbol{n}$ coincides with the direction of the principal stresses in the cell (*cf.* Appendix Fig. B.9), because the principal stresses of the deviatoric stress tensor σ_{ij}^{dev} are equal to those of the full stress tensor σ_{ij}.

[4] As discussed in Chapter 5, this improves numerical stability compared to imposing fixed boundary conditions (*cf.* Eq. (4.14)).

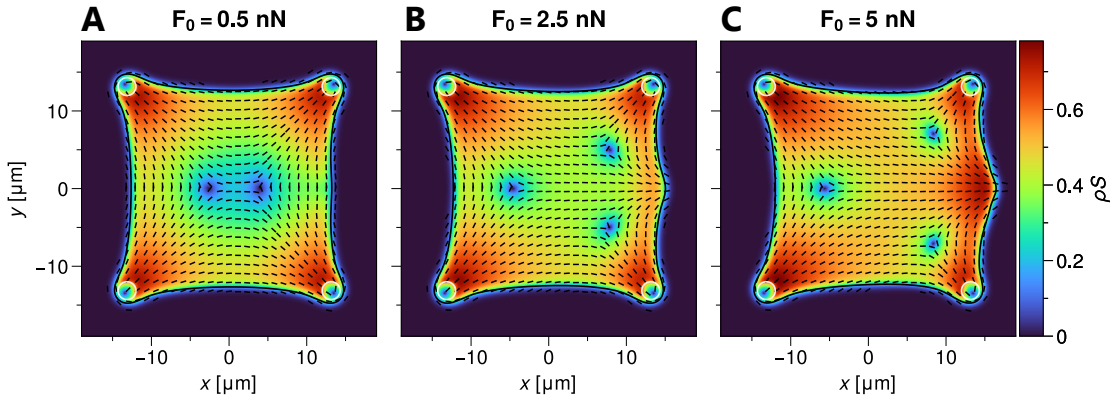

Figure 7.4: A contractile cell on a square-shaped adhesive pattern (white circles) is pulled in positive x-direction by a Gaussian force of magnitude F_0 at its right edge and $y = 0$. Shown is the degree of alignment ρS within the cell and the director field $\boldsymbol{n}$ for $\rho S > 0.01$ (short black lines). The cell boundary is indicated by the isocontour $\rho = 0.5$ (black solid line). The force increases from **A** to **C** with F_0 =0.5 nN, F_0 =2.5 nN and F_0 =5 nN with $v_x = 0.5\,\mu$m and $v_y = 1.75\,\mu$m. The stationary configurations at mechanical equilibrium are shown. For other parameters see Appendix B.5 Table B.6.

We also tested if nematic anchoring, as described by the last term in Eq. (7.25), changes these observations (*cf.* Appendix Fig. B.8). We assumed preferred tangential alignment to the cell periphery and set the preferred degree of alignment $S_0 = 1$. Anchoring has only a limited effect, mainly by increasing S at the cell edge, becoming considerable only for very strong anchoring, *i.e.* high W. The director field $\boldsymbol{n}$ remains in general unchanged. If sufficiently strong, anchoring in the above implementation will lead to filament alignment at the cell periphery also in the absence of stresses or focal adhesions. However, the stress itself is sufficient to enforce a peripheral alignment of the nematic LC parallel to the cell edge (*cf.* Fig. 7.3 A-C). Consequently, we will neglect explicit anchoring, as described by Eq. (7.24), in the following.

Straining of adhered cells, *e.g.* by displacing one of the micropillars they are adhered to, induces the formation of additional stress fibres and reinforcement of existing ones, which are connected to the displaced adhesion spot (*cf.* Fig. 7.5 B) [278]. Inspired by this experimental setup, we modelled a square cell adhered at its corners to adhesive spots as before. First, a contractile stress $\sigma_0/E_C = 0.4$ is applied and the cell is allowed

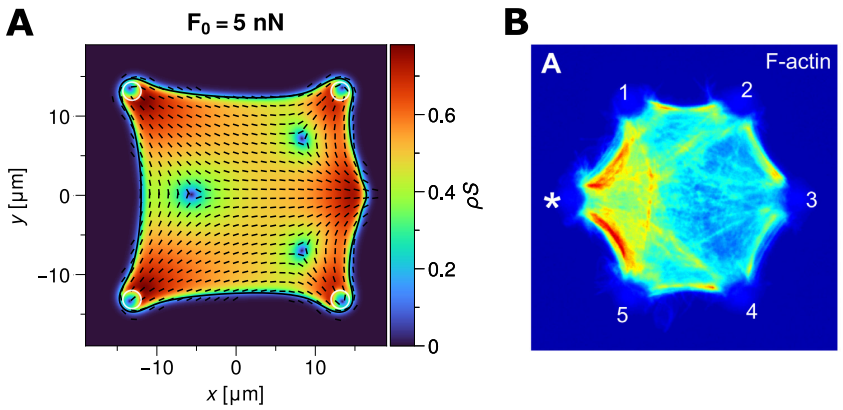

Figure 7.5: Comparison between the (**A**) numerical pulling experiment with $F_0 = 5\,\mathrm{nN}$ and the (**B**) periodic stretching experiment in Ref. [278]. In the experimental figure the cell is of hexagonal shape hold by movable pillars. The pillar marked by the star is periodically pulled. The colour map marks the signal intensity for actin from lowest (blue) to highest (red). As in the experiment, the pulling at the cell edge in **A** leads to increased alignment and stress fibre formation at the pulled edge. Panel **B** adapted from [278].

to relax into mechanical equilibrium. Subsequently, a force of Gaussian shape [10]

$$\boldsymbol{F}(\boldsymbol{x}) = \frac{F_0}{2\pi v_x v_y} \exp\left[-\left(\frac{(x-x_0)^2}{2v_x^2} + \frac{(y-y_0)^2}{2v_y^2}\right)\right] \boldsymbol{e_x}, \tag{7.33}$$

with F_0 being the force amplitude and v_x and v_y the width in x and y direction, is added that pulls at the right edge and $y = 0$ of the cell in x-direction. Recall, that $x_0 = x_0(\rho)$ as the force is always located in the phase field interface, moving with it [10]. The Gaussian shape has been chosen, as it is a smooth representation of a boundary force in the phase field sense, converging to a Dirac delta function in the sharp interface limit [10]. Similar to Sect. 6.3.3, the force was increased by a small amount ΔF every time step until F_0 had been reached, for numerical stability. Figure 7.4 shows the ρS-field and the director field $\boldsymbol{n}$ in the cell for different applied force amplitudes (A) $F_0 = 0.5$ nN, (B) $F_0 = 2.5$ nN and (C) $F_0 = 5$ nN in mechanical equilibrium. With increasing force, the degree of alignment ρS increases where the force is applied, *i.e.* at the tip of the force-induced protrusion. Furthermore, an increase of ρS is visible at the cell edge connecting the protrusion with the upper and lower focal adhesion. Hence, here a reinforcement/ assembly of stress fibres occurs in response to the force, consistent with experimental results in Ref [278] (*cf.* also the direct comparison shown in Fig. 7.5).

Interestingly, the nematic defect in the centre of the cell is also affected by the pulling

force. As soon as the force is applied, the defect of topological charge $m = -1$ (*cf.* Fig. 7.2), breaks up into multiple defects. Their distance to each other increases with the applied force. Note that the total topological charge is conserved. One can see this, by considering Fig. 7.4 C for $F_0 = 5\,\mathrm{nN}$. Here, three $-1/2$-defects (in the cell interior) and one $+1/2$-defect (outside of the cell at the protrusion tip; not shown) are forming. Hence, the total topological charge stays $m = -1$ as for the case without applied force.

In summary, the straightforward coupling of the nematic alignment to the internal stress in the cell is able to recover the main observations with regard to stress fibre orientation and distribution on a qualitative level.

7.4.2 Feedback of stress fibre mechanics

The presence of stress fibres influences the mechanics of cells by increased local cell stiffness [223] and contractility. This is evident by an increase of the traction forces exerted by spreading cells, correlating with the focal adhesion size [69] and therefore stress fibre thickness [62].

This mechanical feedback is incorporated on the phenomenological, macroscopic level by Eqs. (7.29) and (7.31), assuming (as previously explained) that actin filament bundling into stress fibres occurs above a (high) critical alignment parameter S_{cr}. Above this critical value the emerging stress fibre increases local cell elasticity and contractility. We model cells on a square-shaped and hexagonal micropatterns, initially subject to an isotropic stress $\sigma_0/E_C = 0.4$, where $E_C = 1\,\mathrm{kPa}$ is the background Young's modulus of the cell. Indentation experiments via atomic force microscopy (AFM) on living cells resulted in an effective local stiffness of cell regions where stress fibres are present of around $E = 11\,\mathrm{kPa}$ [223]. Assuming that in the case of perfect alignment ($S = 1$) the local cell stiffness should reach this rigidity, we set $E_{SF} = 10\,\mathrm{kPa}$ in Eq. (7.29). For the contractility of the stress fibres, we set $\sigma_{SF} = 3.5\,\mathrm{kPa}$ in Eq. (7.31) such that for $S = 1$ the maximal contractile stress is $\sigma_{max} = 3.9\,\mathrm{kPa}$, a value which has been used previously in the literature [284]. Additionally, the prefactor $\gamma_Q = 1/E(S)$ in Eq. (7.22) is adjusted to ensure that $S \leq 1$. Note that according to the foregoing results, no explicit nematic anchoring is considered, *i.e.* $W = 0$.

Figure 7.6 shows local stiffness maps $E(S)$ for the square-shaped cell (Fig. 7.6 A-C) and the hexagonal cell (Fig. 7.6 D-F) for critical alignment parameters $S_{cr} = 0.6$, $S_{cr} = 0.7$ and for the case without mechanical feedback for comparison. One can see the expected decrease of the stiff, stress fibre associated, area (yellow areas) with increasing S_{cr}. In the absence of mechanical feedback, the cell stiffness is uniform and equal to $E_C = 1\,\mathrm{kPa}$.

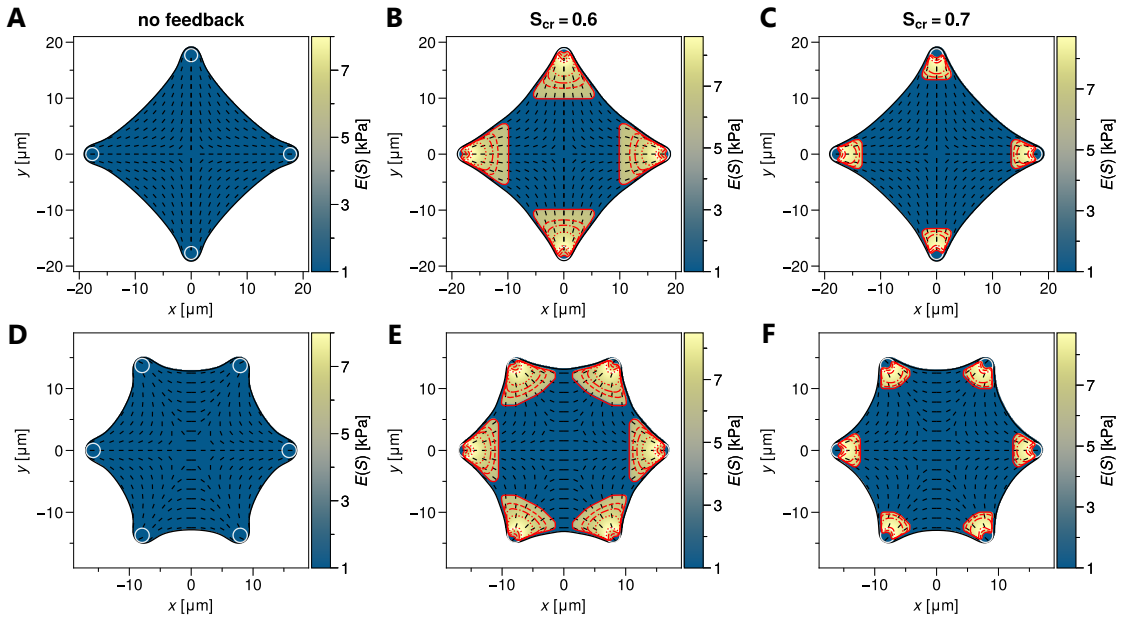

Figure 7.6: Contractile cells are adhering to adhesive spots (white circles) to (**A**-**C**) a square and (**D**-**F**) a hexagonal shape. Shown is the local stiffness $E(S)$ for $\rho \geq 0.5$, which increases with the degree of alignment S according to Eq. (7.29). For reference, (**A**/**D**) show the case without this mechanical feedback while **B**/**E** show the case for $S_{cr} = 0.6$ and (**C**/**F**) for $S_{cr} = 0.7$. Stiffnesses above the background rigidity $E_C = 1\,\text{kPa}$ are associated with increased filament bundling. Note, these regions are also subject to an increased, anisotropic contractile stress (*cf.* Eq. (7.31)). Additionally, the red lines show growth of the regions of increased stiffness at different time points. The short black lines show the director field $\boldsymbol{n}$ and the black curve gives the isoline $\rho = 1/2$ indicating the cell boundary. For parameters see Appenidx B.5 Table B.6.

The red lines within the cell demonstrate the growth of the stress fibre area by marking the respective contour lines $S = S_{cr}$ at different time points. Again, the stress fibres start to grow from the focal adhesions and grow towards the cell centre. No major changes in the director field $\boldsymbol{n}$ compared to the case of no mechanical feedback is visible.

As a last example, we again model the square-shaped cell subject to a boundary force as in Fig. 7.4, but now with stress fibres modulating cell mechanics. Again, a Gaussian-shaped force (*cf.* Eq. 7.33) is pulling on the right edge of the cell. In Fig. 7.7 the local stiffness $E(S)$ in mechanical equilibrium for different pulling forces $F_0 = 2.5\,\text{nN}$, $F_0 = 3.75\,\text{nN}$ and $F_0 = 5\,\text{nN}$ (A-c) and critical alignment parameter $S_{cr} = 0.6$ is visualized. First, a more extended and asymmetric growth of the stress fibre region (yellow areas and red lines) at the two left focal adhesions towards the pulled edge is visible for increasing pulling force. In particular, in Fig. 7.7 C a stiffness increase at the pulled cell edge is visible, *i.e.* stress fibres are forming along the pulled edge. This corresponds to

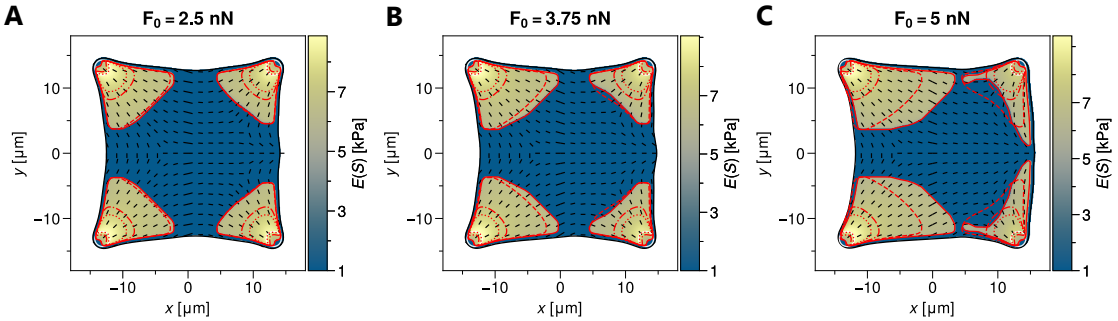

Figure 7.7: A square-shaped cell adheres to adhesive spots (white circles) and is contracting isotropically. After reaching mechanical equilibrium a Gaussian shaped force of strength (A) $F_0 = 2.5\,\text{nN}$, (B) $F_0 = 3.75\,\text{nN}$ and (C) $F_0 = 5\,\text{nN}$ is applied at the right cell boundary at $y = 0$, pulling on it towards the positive x-direction. Shown is the local stiffness $E(S)$ for $\rho \geq 0.5$ increasing with the degree of alignment S if it is above a critical value $S_{cr} = 0.6$ (*cf.* Eq. (7.29)). Regions with a rigidity above the background $E_C = 1\,\text{kPa}$ are associated with enhanced filament bundling and stress fibre formation. Furthermore, they exhibit increased and anisotropic contraction (*cf.* Eq. (7.31)). The red lines show the growth of the stiff region (stress fibres) from the focal adhesions at different time points. The short black lines are the director field $\boldsymbol{n}$ and the solid black line the isocountor $\rho = 0.5$ indicating the cell boundary. For $F_0 = 5\,\text{nN}$ (C) the pulling force is sufficiently strong to induce stress fibre formation along the pulled edge. The force width is $v_x = 0.5\,\mu\text{m}$ and $v_y = 1.75\,\mu\text{m}$. For other parameters see Appendix B.5 Table B.6.

experimental observations [278], as shown in Fig. 7.5 B. Note, the increased stiffness at the pulled cell edge leads to a disappearance of the invaginated arc and the force-induced protrusion (*cf.* Fig. 7.4 C and Fig. 7.7 C).

7.5 Discussion

Spread cells are known to develop prominent actin filament bundles (*cf.* Sect. 2.1.1). These stress fibres are essential cytoskeletal structures when it comes to providing mechanical stability, the generation of forces and the transduction of external mechanical stimuli. Albeit many aspects of their assembly process are still unravelled, it is nowadays undebated that mechanical cues play a vital role. Stress fibre assembly is initiated at focal adhesions, which represent regions of stress accumulation, and have been also shown to form out of the cell cortex by filament bundling, demonstrating their embedding in the 'cytoskeletal continuum' [52]. Because they are stiff and (mostly) contractile (*cf.* Sect. 2.1.1), they alter the overall mechanical behaviour of a cell, as evidenced by increased local cell stiffness in presence of these fibres [223].

Motivated by these results, we proposed a model for mechanosensitive stress fibre

formation in a continuum framework. Several models have already been proposed regarding stress fibre appearance and orientation in response to cell mechanics and shape [284, 288–290]. Resorting to the elastic phase field approach, which already proved its usefulness in the previous chapters, we proposed a model for mechanosensititve stress fibre formation in cells by coupling the continuum elasticity of the cell and the alignment dynamics of a nematic liquid crystal representing the cytoskeleton. This was inspired by Ref. [284], where the cell is modelled as an elastic continuum, and Ref. [290], where stress fibre orientation is described by a nematic liquid crystal in a contour model framework for cell shape. We accounted for the mechanosensitive alignment and assembly of stress fibres by direct coupling of the deviatoric part of the stress tensor to the dynamic equation for the orientation order parameter of the nematic, where a high degree of alignment S is associated with the emergence of stress fibres. Furthermore, a feedback of appearing stress fibres was introduced into cell mechanics by increased local stiffness and increased as well as anisotropic contractility.

In the first study in Sect. 7.4.1 stationary adhered cell were studied without a feedback of stress fibres mechanics on whole-cell mechanics. Our approach was able to capture qualitative features as observed in experiments, *i.e.* high filament alignment associated with stress fibres at focal adhesions and parallel alignment to the cell edge of the cytoskeleton/stress fibres [201]. Interestingly, no anchoring of the liquid crystal is needed to achieve this alignment; it is solely dictated by the internal cellular stress. A pulling experiment, where one edge of the cell was deformed by a localized force, showed reinforced nematic alignment (hence possible stress fibres) at the pulled edge, consistent to similar experimental studies [278]. Our modelling strengthens the idea that the stress fibre distribution follows the stress distribution in the cell [284]. Topological defects visible in these numerical studies, arise naturally and (depending on the context and geometry of the cell) can be interpreted as crossing of actin stress fibres, where in this case low or vanishing order would be expected.

In Sect. 7.4.2 the mechanical feedback of the forming stress fibres on cell stiffness and contractility has been introduced. To our knowledge such a feedback has not yet been modelled before. It was assumed that filament bundling into stress fibres occurs at high degrees of alignment S, hence the mechanical feedback was turned on only when degree of alignment S exceeded some critical value S_{cr}. Besides leading to increased alignment at focal adhesions, regions near focal adhesions stiffened due to the assembly of stress fibres. Performing again a pulling experiment showed, that the force influences the direction of stress fibre growth and (depending on the critical degree of alignment

S_{cr} and magnitude of the pulling force) stress fibres formed along the pulled cell edge, leading to a disappearance of the localized, force-induced protrusion. This supports the idea that stress fibres protect cells from high (local) strains.

It has to be emphasized that the continuous framework proposed here, although successful in capturing essential observations, has some limitations. Most importantly, stress fibres are discrete structures, whose formation out of a continuum cannot be described correctly with the current continuum approach. Nevertheless, a continuum model leading at least to band-like structures in the stress distribution in a cell, associated with stress fibres, has been proposed some years ago [287].

Another aspect is that physiologically stress fibres are embedded in a three-dimensional environment. In principle, a corresponding three-dimensional description has to be used, which would allow to model stress fibres going over each other without crossing; in two-dimensions this is not possible (*cf.* nematic defects in the current approach). Going into this direction, a quasi-3D continuum model for stress fibre formation in adhered cells of axial symmetric geometry has already been published [221].

A discretization of stress fibres, while still remaining in a continuum framework, could be to describe their assembly by the association of elongated particles which are implemented as smooth fields and represent stress fibre elements. How exactly such a particle-field approach [309] can describe stress fibre growth and the associated mechanical effects may be a subject of a different study. However, a better (and more realistic) modelling philosophy would be to consider the cell as a composite material with *e.g* implicitly embedded discrete structures [310].

The proposed model can be extended by additional details. In Ref. [221], the cell nucleus has been included as an internal elastic compartment. Such an extension is achievable by a conjunction with the phase field approach for cells with nucleus presented in Chapter 5. This would allow to study how the nucleus is affected by the formation of stress fibres and vice versa. Here, also the effect on protein import (*Cf.* Chapter 6) could be of interest. Furthermore, chemical details like *e.g.* the Rho-pathway involved in stress fibre assembly could be implemented as well as adhesion dynamics. The latter would be especially of interest for spreading or migrating cells with transient stress fibres [64, 276].

In summary, the phase field approach presented in this chapter provides an alternative framework to model mechanically-driven stress fibre formation, which also allows the addition of further assembly details. It should be useful and provide additional insight, in particular, if stress fibre assembly in dynamic situations is of interest.

8 Summary and Outlook

Biological cells sense the mechanical properties of their surrounding by constantly generating forces, in order to adapt their own mechanics accordingly. The response of cells to external mechanical stimuli is mainly determined by the stiff, but dynamically reorganizing cytoskeleton and the nucleus. Both intracellular structures are linked with each other, allowing a mechanosensitive transport of proteins through pores into the nucleus, which are involved in triggering cellular reactions.

In this thesis, we developed models based on a diffuse interface approach to investigate several aspects in the context of cell mechanics. More precisely, using an elastic phase field method, we studied the effect of nuclear mechanics on whole-cell elasticity and its implications on facilitated nucleocytoplasmic transport of proteins due to a tension-mediated increase of the permeability of the nuclear boundary. Further, we considered the stress-induced realignment of the cytoskeleton and the emergence of (precursors of) stress fibres in spread cells in a continuum framework, using the theory of nematic liquid crystals. We here provide a brief summary of this thesis and discuss future perspectives.

In **Chapter 2**, we gave an overlook on the cellular structures determining cell mechanical responses, namely the cytoskeleton and the nucleus. Regarding the latter, we described the nucleocytoplasmic transport process through nuclear pore complexes, essential for cellular mechanical sensing, *i.e* mechanotransduction. We closed the chapter with a brief review on the theory of continuum elasticity and its linearization, which we used to describe cell deformations.

The approach used throughout this thesis to model elastic cells in various geometries and situations is a diffuse interface approach: the phase field method. Therefore, we continued in **Chapter 3** by introducing the concept of interface methods for modelling moving boundary problems and discussed the phase field method in more detail.

Chapter 4 was concerned with the coupling of the phase field method and continuum elasticity. It was discussed that the standard, energy-based formulation cannot recover the reversibility of elastic deformations upon release of forces. We therefore

presented an alternative, force-based formulation which is able to account for this reversibility [10]. Considering standard experimental geometries of spread single cells and cell monolayers, we verified the method by comparison to available analytical solutions. Importantly, we found out how analytical solutions to elastic problems can be compared to the respective phase field solutions, where the displacement field moves with the domain. Over this, the elastic phase field method can capture prominent experimental observations in cell morphology, such as the formation of invaginated arcs for cells on micropatterned substrates. All in all, it is a method suited for describing biological situations involving cell mechanics.

In **Chapter 5**, we extended the elastic phase field model from Chapter 4 by an additional phase field describing an elastic nucleus and verified the model against a derived analytical solution. First, we investigated the role of the nucleus in cell mechanics by considering spread cells on different adhesion geometries. We found that the transmission of forces to the nucleus is highly dependent on the actual adhesion geometry and that nuclear rigidity has the potential to considerably perturb cell morphology, such as the formation of invaginated arcs. Interestingly, nuclear position and increasing nuclear stiffness changed the stress distribution in cells and was associated with the appearance of 'stress bridges' connecting nucleus and focal adhesions, reminiscent of stress fibres, which may have important implications on the process of mechanotransduction and determining cell polarity.

We then turned to the question how nuclear mechanics influences the measurement of effective elastic moduli of the cell-nucleus composite. Therefore, we considered two experimental setups which are frequently used to determine cell stiffness, namely the compression of cells between two plates and micropipette aspiration. Our modelling approach allowed us to extracted effective stiffnesses for spherical cells in axial symmetry in both modelled experiments. We found that in global straining of cells, as in compression experiments, the impact of the nucleus on the measured effective modulus is greater than in the case of local straining, as in micropipette aspiration. Hence, the measured effective moduli depend on the experimental setup and the internal structure of the cell. Our model provides evidence, that the nucleus is a cellular structure which should be considered in models for whole-cell mechanics.

In **Chapter 6**, we looked at possible effect of nuclear rigidity on mechanosensitive protein transport into the nucleus through nuclear pore complexes (NPCs) perforating the nuclear boundary. We proposed a system of reaction-diffusion equations in the phase field framework of the previous chapters, allowing to consider spatiotempo-

ral import dynamics. Motivated by a recent experimental study suggesting that force transmission to the nucleus leads to a stretch of NPCs facilitating the transport through them [9], we assumed an increase in the permeability of the nuclear envelope in regions where the nuclear boundary is under tension. Our model for spread cells shows that if passive and active transport efficiency benefit equally from a tension-induced opening of NPCs, passive diffusion dominates leading to smaller nucleocytoplasmic signal ratios (N/C ratio) of the considered protein compared to the case without NPC stretch. Only a differential effect, leading to an increase of the ratio between active and passive import efficiency can lead to an increase of the N/C ratio, consistent with recent experimental results [9]. Furthermore, we found that nuclear stiffness influences the obtained steady state N/C ratio in a context-dependent manner, where contractile cells (also in presence of localized pulling forces) showed a slightly larger N/C ratio for stiff nuclei compared to softer ones, while in uniaxially stretched cells this observation was reversed. Here, softer nuclei had a larger N/C ratio. Nuclear positioning can influence the signal ratio as well by determining the extend of nuclear deformation.

In **Chapter 7**, we were interested in the mechanosensitive formation of stress fibres in spread cells on micropatterns. To model stress fibre emergence, we coupled the elastic phase field model from Chapter 4 with a continuous orientation field from the theory of nematic liquid crystals. Increased alignment, induced by the stress within the cell, was interpreted as the formation of (precursors of) stress fibres, where the orientation field indicated their growth direction. Additionally, we implemented a feedback of the forming stress fibres on the local contractility and stiffness of the cell. We found that our model, predicting that the stress field in the cell directly determines stress fibre growth, is able to qualitatively capture experimental observations, such as stress fibre formation originating at focal adhesions and along invaginated arcs.

Regarding the above projects, a future validation of the made predictions by experiments is highly desirable to further support the modelling approach. Nevertheless, **in the future**, the elastic phase field approach should prove useful in studying a large variety of different biological situations in complex geometries, which can be easily described by this method. The phase field model could be extended to multicellular systems in which each cell is described by a separate phase field [151, 152]. This would allow a more detailed description of tissue mechanics and dynamics. Similarly, more internal structures could be resolved, possibly with different material laws. Here the phase field method could prove very efficient to understand the cell as a composite material. Important in this context is a more discrete description of cytoskeletal structures

and their dynamics, such as stress fibres and their assembly process. Features such as cell motility or adhesion dynamics could be implemented by coupling additional fields to the existing model [142, 145].

An extension to three-dimensions should be feasible and would allow to model cells and their mechanics in physiological environments, such as fibrous networks [148, 205]. It would be highly interesting to investigate the effect of nuclear mechanics and positioning in three-dimensional cells, especially in cells migrating through narrow constrictions as the phase field approach is well-suited for such moving boundary problems. Complemented by a model containing all nucleocytoplasmic transport cycles, the phase field approach could shed light on mechanotransduction in dynamic situations.

In summary, the elastic phase field method is a very versatile approach allowing an incorporation of different cellular features also involving dynamics, with the potential of providing many interesting new insights in the context of biomechanics.

Appendices

A Analytical calculations

A.1 Asymptotic analysis of the elastic phase field method

Phase field models are diffuse interface approximations of originally sharp boundary PDEs and their respective boundary conditions. Therefore, the underlying sharp boundary system has to be recovered from the phase field model in the limit of an infinitely thin interface ($D \longrightarrow 0$ or equivalently the interface width $\epsilon \longrightarrow 0$). To check whether a proposed phase field formulation properly describes the system of interest an asymptotic analysis (also known as sharp interface limit) has to be performed. We here perform such an asymptotic analysis for the elastic phase field method as proposed in Chapter 4. However, we examine the generalized version with two elastic phases. Equivalent calculations can be made for the phase field model for cells with elastic nuclei as presented in Chapter 5. During the analysis, we follow the procedure and partially the notation as described in Jamet & Misbah (2008) [162] and the PhD thesis of Julien Beaucourt [311].

The governing equations for the elastic phase field method we will examine analytically are the phase field and elastodynamic equation for the displacement field $\boldsymbol{u}$

$$\frac{\partial \rho}{\partial t} = D\Delta\rho - \frac{\partial g(\rho)}{\partial \rho} + D\kappa|\nabla\rho| - \frac{1}{\xi}\left(\nabla\cdot\Sigma + \boldsymbol{F} + F_S\nabla\rho\right) \tag{A.1}$$

$$\xi\frac{\partial \boldsymbol{u}}{\partial t} = \nabla\cdot\Sigma + \boldsymbol{F} + F_S\nabla\rho \tag{A.2}$$

where $\boldsymbol{F}$ are general bulk (body) forces and $F_S\nabla\rho$ are boundary forces acting only at the ρ-interface. Recall, our double well potential of choice is $g(\rho) = \rho^2(1-\rho)^2$, distinguishing two bulk phases via assigning its minima values $\rho = 0$ and $\rho = 1$ to each of them, respectively. In our cases of interest, these are the interior ($\rho = 1$) and exterior ($\rho = 0$) of a cell. Assuming that the mechanics of both bulk phases can be described by standard linear elasticity, the respective stress tensor in each phase is given by Hooke's

law

$$\sigma_{ij} = 2\mu\epsilon_{ij} + \lambda\epsilon_{kk}\delta_{ij} \tag{A.3}$$

with material parameters μ and λ and strain tensor

$$\epsilon_{ij} = \frac{1}{2}\left(\frac{\partial u_i}{\partial x_j} + \frac{\partial u_j}{\partial x_i}\right). \tag{A.4}$$

The interpolated phase field stress tensor in Eq. (A.2) is defined as

$$\Sigma = h(\rho)\boldsymbol{\sigma}^{\mathbf{1}} + [1 - h(\rho)]\boldsymbol{\sigma}^{\mathbf{0}} \tag{A.5}$$

with $h(\rho)$ being an interpolation function fulfilling the conditions $h(0) = 0$, $h(1) = 1$ and $\partial_\rho h_{|\rho=0} = \partial_\rho h_{|\rho=1} = 0$. Further, it should poses only these two extrema. Otherwise, its exact form is arbitrary [1] and insignificant for the asymptotic expansion.

We are interested in recovering the sharp interface equilibrium equations. Therefore, we perform the asymptotic analysis in steady state, such that eqs. (A.1) and (A.2) become

$$0 = D\Delta\rho - \frac{\partial g(\rho)}{\partial\rho} + D\kappa|\nabla\rho| \tag{A.6}$$

$$0 = \nabla\cdot\Sigma + \boldsymbol{F} + F_S\nabla\rho. \tag{A.7}$$

This simplifies the following calculations enormously. [2]

A.1.1 Curvilinear coordinates

Phase field models allow an efficient treatment of problems involving complex shapes. To facilitated the analysis, it is essential to perform the sharp interface limit in a coordinate system best suited for the phase field approach. Except for the special case of planar interfaces, an asymptotic expansion in Cartesian coordinates would become to cumbersome. The natural choice are curvilinear coordinates with orthogonal basis vectors normal and tangential to the phase field interface.

Consider a curve Γ coinciding with the phase field isocline $\rho = 0.5$ representing the position of the interface [3]. The coordinate variables are the arclength s along the curve Γ and the radial (normal) coordinate r. On the isocline $\rho = 0.5$ the radial coordinate can

[1] Recall, our choice for the interpolation function is $h(\rho) = \rho^2(3 - 2\rho)$.

[2] An example of an asymptotic analysis of a dynamical system is given in Ref. [162]

[3] For a phase field model with bulk values ρ_I and ρ_{II} the isocontour $(\rho_I + \rho_{II})/2$ can be associated with the sharp boundary position [162].

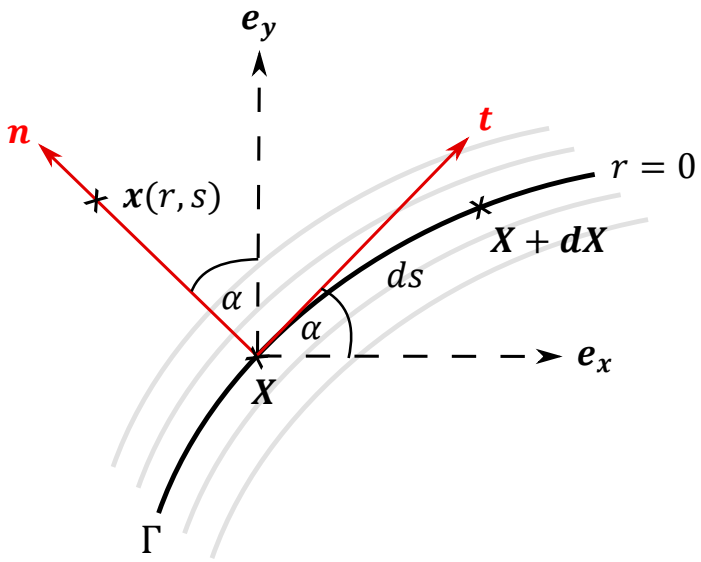

Figure A.1: Curvilinear coordinate system for the asymptotic analysis of the *reversible elastic phase field method* with orthogonal basis vectors $\boldsymbol{n}$ and $\boldsymbol{t}$, being the local normal and tangential vectors of a curve Γ, which is chosen as baseline. The orthogonal system is locally tilted by an angle α with respect to the Cartesian coordinate system defined by $\boldsymbol{e_x}$ and $\boldsymbol{e_y}$. Γ coincides with the phase field isocontour $\rho = 1/2$ (black curve), interpreted as the sharp interface position, and is set to $r = 0$. Starting from a point $\boldsymbol{X}$, any point in space can be reached by shifting $\boldsymbol{X}$ along Γ by the arc length ds and by displacing it along the normal $\boldsymbol{n}$ by a distance r. Figure inspired by [162].

be set to $r = 0$, without loss of generality. The curvilinear coordinate system, with the normal vectors $\boldsymbol{n}$ and tangent vectors $\boldsymbol{t}$ of Γ as orthogonal basis, is locally tilted by an angle α with respect to the Cartesian coordinate system, i.e. $\boldsymbol{e}_x \cdot \boldsymbol{t} = \cos(\alpha)$ (*cf.* Fig. A.1).

Consider a point $\boldsymbol{X} = (X, Y)$ lying on Γ. Any point in the two-dimensional plane can be reached by combining a translation along and normal to Γ of $\boldsymbol{x}$. We will consider both translations separately. First, we shift $\boldsymbol{X}$ along Γ by an arc length ds to a new position $\boldsymbol{X} + \boldsymbol{dX}$. This is given by

$$\boldsymbol{X} \rightarrow \boldsymbol{X} + \boldsymbol{dX} = \begin{pmatrix} X + \cos(\alpha) ds \\ Y + \sin(\alpha) ds \end{pmatrix} \tag{A.8}$$

while a normal translation of a point $\boldsymbol{X}(s)$ on Γ about a distance r to a point $\boldsymbol{x}$ in the domain is described by

$$\boldsymbol{X} \rightarrow \boldsymbol{x}(r,s) = \begin{pmatrix} X(s) - r\sin(\alpha) \\ Y(s) + r\cos(\alpha) \end{pmatrix}. \tag{A.9}$$

In order to transform all differential operators into the new coordinate system, so-called scale factors have to be calculated, relating length changes in the different coordinate systems with each other. They are given by $h_i = |\partial \boldsymbol{x}/\partial q_i|$, where q_i are the curvilinear coordinates r and s. Using eqs. (A.8) and (A.9) the scale factors in the given curvilinear coordinate system are

$$h_r = \left[\left(\frac{\partial x}{\partial r}\right)^2 + \left(\frac{\partial y}{\partial r}\right)^2\right]^{1/2} = 1 \tag{A.10}$$

$$h_s = \left[\left(\frac{\partial x}{\partial s}\right)^2 + \left(\frac{\partial y}{\partial s}\right)^2\right]^{1/2} = |1 - r\kappa| \tag{A.11}$$

where κ is the curvature of the curve s at $r = 0$ defined as $\kappa = \partial\alpha/\partial s$. The differential operators acting on a scalar field ϕ and vector field $\mathbf{v} = (\mathrm{v}_r, \mathrm{v}_s)$ in curvilinear coordinates with above scale factors are

$$\nabla\phi = \boldsymbol{n}\partial_r\phi + \boldsymbol{t}h_s^{-1}\partial_s\phi \tag{A.12}$$

$$\nabla \cdot \mathbf{v} = h_s^{-1}\left[\partial_r(h_s\mathrm{v}_r) + \partial_s\mathrm{v}_s\right] \tag{A.13}$$

$$\Delta\phi = \partial_{rr}\phi - \kappa h_s^{-1}\partial_r\phi + h_s^{-2}\partial_{ss}\phi + rh_s^{-3}(\partial_s\kappa)\partial_s\phi. \tag{A.14}$$

A.1.2 Outer expansion

First, we will consider the elastic phase field method in the bulk phases far away from the phase field interface. This is called the outer expansion. We begin by expanding all base quantities of the model up to first order in the interface width ϵ :

$$\begin{aligned} \rho &= \rho_0 + \epsilon\rho_1 + O\left(\epsilon^2\right) \\ \boldsymbol{u} &= \boldsymbol{u}_0 + \epsilon\boldsymbol{u}_1 + O\left(\epsilon^2\right) \\ \boldsymbol{F} &= \boldsymbol{F}_0 + \epsilon\boldsymbol{F}_1 + O\left(\epsilon^2\right) \end{aligned} \tag{A.15}$$

From the linearity of the elastic constitutive equation (A.3) and the differential operator, it follows that the expansion of $\boldsymbol{u}$ results in

$$\boldsymbol{\sigma} = \boldsymbol{\sigma}_0 + \epsilon\boldsymbol{\sigma}_1 + O\left(\epsilon^2\right). \tag{A.16}$$

Further, for any allowed interpolation function $h(\rho)$ the expansion of ρ will result in

$$h(\rho) = h_0(\rho_0) + \epsilon h_1(\rho_0, \rho_1) + O\left(\epsilon^2\right) \tag{A.17}$$

where the lowest order term $h_0(\rho_0)$ is of the same form as the original function $h(\rho)$.[4] By inserting the expansions (A.15) into eqs. (A.6) and (A.7) and sorting the resulting terms by powers of ϵ, we are able to analyse them order by order to see, if the sharp boundary system is recovered. We will restrict the expansion of each equation up to the first non-vanishing order. It is important to keep in mind, that the phase field diffusion coefficient D and the interface width ϵ are related by $D \propto \epsilon^2$.

order $O(0)$

For the phase field equation (A.6) we find in lowest order

$$2\rho_o(1 - 3\rho_0 + 2\rho_0^2) = \frac{\partial g(\rho_0)}{\partial \rho_0} = 0 \tag{A.18}$$

which is simply the derivative of the chosen double well potential with respect to the phase field variable. The solutions are given by the stable minima $\rho_0 = 0$ and $\rho_0 = 1$, assigned to the bulk phases, and the unstable maximum at $\rho_0 = 1/2$, associated with the sharp interface position. However, as we are interested for the bulk phases far away from the interface only $\rho \in \{0, 1\}$ are of importance for now.

The lowest order term for the elastic equation (A.7) is

$$\nabla \cdot \left\{ h_0(\rho_0)\boldsymbol{\sigma}_0^{\mathbf{1}} + [1 - h_0(\rho_0)]\, \boldsymbol{\sigma}_0^{\mathbf{0}} \right\} + \boldsymbol{F}_0 + F_S \nabla \rho_0 = 0. \tag{A.19}$$

From the conditions $h(\rho = 0) = 0$ and $h(\rho = 1) = 1$ for the interpolation function, it follows that $h_0(\rho_0 = 0) = 0$ and $h_0(\rho_0 = 1) = 1$ and this yields

$$\begin{cases} \nabla \cdot \boldsymbol{\sigma}_0^{\mathbf{1}} + \boldsymbol{F}_0 = 0 & \text{for } \rho_0 = 1 \\ \nabla \cdot \boldsymbol{\sigma}_0^{\mathbf{0}} + \boldsymbol{F}_0 = 0 & \text{for } \rho_0 = 0. \end{cases} \tag{A.20}$$

The interfacial force drops out as $\nabla \rho = 0$ in the bulk phases far away from the interface, where ρ is constant. Only body forces survive. We have therefore recovered in each bulk phase the mechanical equilibrium equations.

[4] Consider for example our choice $h(\rho) = \rho^2(3 - 2\rho)$. Inserting the expansion of ρ from Eq. (A.15) gives $h(\rho) = \rho_0^2(3 - 2\rho_0) + \epsilon 6\rho_0\rho_1(1 - \rho_0) + O\left(\epsilon^2\right) = h_0(\rho_0) + \epsilon h_1(\rho_0, \rho_1) + O\left(\epsilon^2\right)$.

order $O(\epsilon)$

In the next order we have for the phase field equation

$$6\rho_0^2\rho_1 - 12\rho_0\rho_1 + 2\rho_1^2 = 0 \tag{A.21}$$

which has the trivial solution $\rho_1 = 0$. The corresponding order for the mechanical equation is

$$\nabla \cdot \left\{ h_0(\rho_0)\boldsymbol{\sigma}_1^{\mathbf{1}} + [1 - h_0(\rho_0)]\, \boldsymbol{\sigma}_1^{\mathbf{0}} \right\} + \boldsymbol{F}_1 + F_S \nabla \rho_1 = 0. \tag{A.22}$$

Knowing from above that $\rho_1 = 0$, interfaces forces drop out again and we can further infer that $h_1(\rho_0, \rho_1) = 0$ as all terms in $O(\epsilon)$ and higher for the interpolation function will contain a factor ρ_1. Considering the bulk phases, we again find the equations of mechanical equilibrium

$$\begin{cases} \nabla \cdot \boldsymbol{\sigma}_1^{\mathbf{1}} + \boldsymbol{F}_1 = 0 & \text{for } \rho_0 = 1 \\ \nabla \cdot \boldsymbol{\sigma}_1^{\mathbf{0}} + \boldsymbol{F}_1 = 0 & \text{for } \rho_0 = 0 \end{cases} \tag{A.23}$$

as before. Therefore, this order has not given us any additional information, and we shift all the problems complexity into the lowest order $O(0)$ by setting $\boldsymbol{F}_1 = 0$ and $\boldsymbol{u}_1 = 0$ (and by linearity $\boldsymbol{\sigma}_1^{\mathbf{1}} = \boldsymbol{\sigma}_1^{\mathbf{0}} = 0$).

A.1.3 Inner expansion

Having analysed the phase field model equations in the bulk (outer) regions where the phase field ρ is (nearly) constant, we now focus on the interface (inner) region. Here ρ is subject to strong variations. For the following steps, we need to renormalise the radial coordinate r in the inner region by the interface width ϵ

$$\bar{r} = r/\epsilon. \tag{A.24}$$

As for the outer expansion, we expand all fields in the inner region up to first order in the interface width ϵ

$$\begin{aligned} \bar{\rho} &= \bar{\rho}_0 + \epsilon\bar{\rho}_1 + O\left(\epsilon^2\right) \\ \bar{\boldsymbol{u}} &= \bar{\boldsymbol{u}}_0 + \epsilon\bar{\boldsymbol{u}}_1 + O\left(\epsilon^2\right) \\ \bar{\boldsymbol{F}} &= \bar{\boldsymbol{F}}_0 + \epsilon\bar{\boldsymbol{F}}_1 + O\left(\epsilon^2\right) \end{aligned} \tag{A.25}$$

Further, we define that in the limit $\bar{r} \to -\infty$ we leave the interface into the bulk

phase $\rho = 1$, while for $\bar{r} \to +\infty$ we enter the bulk phase $\rho = 0$. The solutions of the asymptotic expansions in the outer and inner regions have to be matched in the above limits.[5] These matching conditions are

$$\lim_{\bar{r}\to\pm\infty} \bar{\rho}_0(\bar{r}, s) = \begin{cases} 1 & \text{for } \bar{r} \to -\infty \\ 0 & \text{for } \bar{r} \to +\infty \end{cases} \qquad \lim_{\bar{r}\to\pm\infty} \bar{\rho}_1(\bar{r}, s) = 0 \tag{A.26}$$

$$\lim_{\bar{r}\to\pm\infty} \bar{\boldsymbol{u}}_0(\bar{r}, s) = \boldsymbol{u}_0(0^{\pm}, s) \qquad \lim_{\bar{r}\to\pm\infty} \bar{\boldsymbol{u}}_1(\bar{r}, s) = 0 \tag{A.27}$$

$$\lim_{\bar{r}\to\pm\infty} \bar{\boldsymbol{F}}_0(\bar{r}, s) = \boldsymbol{F}_0(0^{\pm}, s) \qquad \lim_{\bar{r}\to\pm\infty} \bar{\boldsymbol{F}}_1(\bar{r}, s) = 0 \tag{A.28}$$

where the superscript for $0^{\pm}$ indicates, to which inner expansion limit for $\bar{r} \to \pm\infty$ the outer solution of the respective phase is approached. Additionally, the scale factors and differential operators have to be transformation into the new interface coordinate $\bar{r}$. While the scale factor $h_r = 1$ remains unchanged, the second one becomes $h_s = 1 + \epsilon\bar{r}\kappa$. Recalling the differential operators in curvilinear coordinates (A.12), we approximate

$$h_s^{-1} = \frac{1}{1 - \epsilon\bar{r}\kappa} \approx 1 + \epsilon\bar{r}\kappa + O\left(\epsilon^2\right). \tag{A.29}$$

Together with $\partial_r = \epsilon^{-1}\partial_{\bar{r}}$, the differential operators can be approximated as

$$\nabla f = \frac{1}{\epsilon}\boldsymbol{n}\partial_{\bar{r}} f + \boldsymbol{t}(1 + \epsilon\bar{r}\kappa)\partial_s f + O\left(\epsilon^2\right) \tag{A.30}$$

$$\nabla \cdot \boldsymbol{V} = \frac{1}{\epsilon}\partial_{\bar{r}} V_{\bar{r}0} + \partial_{\bar{r}}\left(V_{\bar{r}1} - \kappa\bar{r}V_{\bar{r}0}\right) - \bar{r}\kappa\partial_{\bar{r}} V_{\bar{r}0} + \partial_s V_{s0} + O\left(\epsilon\right) \tag{A.31}$$

$$\Delta f = \frac{1}{\epsilon^2}\partial_{\bar{r}\bar{r}} f - \frac{1}{\epsilon}\kappa(1 + \bar{r}\kappa)\partial_{\bar{r}} f + O\left(\epsilon^0\right). \tag{A.32}$$

and

$$|\nabla\rho| = \frac{1}{\epsilon}\partial_{\bar{r}}\bar{\rho}_0 + \partial_{\bar{r}}\bar{\rho}_1 + O\left(\epsilon\right) \tag{A.33}$$

up to the second lowest order in ϵ. Moreover, it can be shown that the normal vector is $\boldsymbol{n} = \nabla\rho/|\nabla\rho| = \boldsymbol{n_0} + O\left(\epsilon\right)$ and the curvature approximates as $\kappa = -\nabla \cdot \boldsymbol{n} = \kappa_0 + O\left(\epsilon\right)$ [162].

We repeat the procedure from above and examine the governing equations in the inner interface region up to second non-vanishing order in ϵ by using the expansions (A.25)-(A.33), sorting terms in powers of ϵ and examining them individually. Due to different leading orders in ϵ, each equation is now examined separately, for convenience.

[5] Therefore the asymptotic analysis is also known as matched asymptotic expansion.

Phase field equation

We begin with expanding the phase field equation as the informations we get here will become useful when treating the expansion of the elastodynamic equations.

order $O(\epsilon^0)$: The dominating term in the phase field equation is

$$\partial_{\bar{r}\bar{r}}\bar{\rho}_0 - \frac{\partial g(\bar{\rho}_0)}{\partial \bar{\rho}_0} = 0. \tag{A.34}$$

Solving this equation under the matching conditions (A.26) for $\bar{\rho}_0$ yields

$$\bar{\rho}_0(\bar{r}) = \frac{1}{2}\left[1 + \tanh\left(\frac{\bar{r}}{\sqrt{2}}\right)\right], \tag{A.35}$$

hence the stationary phase field profile is recovered in lowest order (cf. appendix section A.2).

order $O(\epsilon)$: In the next highest order $O(\epsilon)$ we find for the phase field equation

$$\partial_{\bar{r}\bar{r}}\bar{\rho}_1 + 8\bar{\rho}_0\bar{\rho}_1 - 4\bar{\rho}_0^2\bar{\rho}_1 + \kappa_0\partial_{\bar{r}}\bar{\rho}_0 - \kappa_0\partial_{\bar{r}}\bar{\rho}_0 = 0 \tag{A.36}$$

which has the trivial solution $\bar{\rho}_1 = 0$. Remark, that the surface tension term proportional to the curvature κ_0 appears naturally in the expansion. It's balancing by the respective counter term, as introduced by Folch et al. (1999) (third term in Eq. (A.1)), ensures a stationary phase field profile. It is worth noting, that the balancing term used here cannot be related to an energy and is therefore not thermodynamic consistent. For cases where this consistency is required, Jamet and Misbah (2008) [162] proposed an alternative balancing term which is $\sqrt{2Dg(\rho)}\kappa$ [6], which they showed to be up to first order in ϵ equivalent to the expression by Folch et al. (1999) [160].

Equations of mechanical equilibrium

Now, we turn to the inner expansion of the equation of mechanical equilibrium (A.7). To analyse these equations, one has to refer to the specific form of the strain and stress tensor in curvilinear coordinates. For generalized coordinates q_i the strain tensor com-

[6] The respective energy is $\mathcal{F} = -\int_V \sqrt{2Dg(\rho)}|\nabla\rho|d\boldsymbol{x}$ [162].

ponents are

$$\epsilon_{ii} = \frac{\partial u_i}{h_i \partial q_i} \qquad \text{and} \qquad \epsilon_{ij} = \frac{1}{2}\left(\frac{\partial u_i}{h_j \partial q_j} + \frac{\partial u_j}{h_i \partial q_i}\right) \tag{A.37}$$

with scale factors (A.10) and (A.11) for the in section A.1.1 defined local orthogonal system. By using the approximations $h_r = 1$ and Eq. (A.29) of the scale factors in the new coordinate $\bar{r} = r/\epsilon$ the strain components yield

$$\begin{aligned} \bar{\epsilon}_{\bar{r}\bar{r}} &= \frac{1}{\epsilon}\partial_{\bar{r}}\bar{u}_{\bar{r}} \\ \bar{\epsilon}_{ss} &= (1 + \epsilon\bar{r}\kappa)\partial_s\bar{u}_s \\ \bar{\epsilon}_{\bar{r}s} &= \frac{1}{2}\left[(1 + \epsilon\bar{r}\kappa)\partial_{\bar{r}}\bar{u}_{\bar{r}} + \frac{1}{\epsilon}\partial_{\bar{r}}\bar{u}_s\right] \end{aligned} \tag{A.38}$$

which is needed for transforming the stress tensor with respect to the new coordinate. The stress tensor components in the local normal-tangential coordinate system are

$$\begin{aligned} \sigma_{\bar{r}\bar{r}} &= (2\mu + \lambda)\bar{\epsilon}_{\bar{r}\bar{r}} + \lambda\bar{\epsilon}_{ss} \\ \bar{\sigma}_{ss} &= (2\mu + \lambda)\bar{\epsilon}_{ss} + \lambda\bar{\epsilon}_{\bar{r}\bar{r}} \\ \bar{\sigma}_{\bar{r}s} &= 2\mu\bar{\epsilon}_{\bar{r}s} \end{aligned} \tag{A.39}$$

Further, one can expand the divergence of the phase field stress tensors Σ by noting that

$$\nabla\cdot\Sigma = \begin{cases} \nabla\cdot\begin{pmatrix}\bar{\Sigma}_{\bar{r}\bar{r}}\\ \bar{\Sigma}_{\bar{r}s}\end{pmatrix} = \frac{1}{\epsilon}\partial_{\bar{r}}\bar{\Sigma}_{\bar{r}\bar{r}} + [1+\epsilon\bar{r}\kappa]\partial_s\bar{\Sigma}_{\bar{r}s} - \kappa[1+\epsilon\bar{r}\kappa]\bar{\Sigma}_{\bar{r}\bar{r}} \\ \\ \nabla\cdot\begin{pmatrix}\Sigma_{rs}\\ \Sigma_{ss}\end{pmatrix} = \frac{1}{\epsilon}\partial_{\bar{r}}\bar{\Sigma}_{\bar{r}\bar{s}} + [1+\epsilon\bar{r}\kappa]\partial_s\bar{\Sigma}_{ss} - \kappa[1+\epsilon\bar{r}\kappa]\bar{\Sigma}_{\bar{r}s} \end{cases} \tag{A.40}$$

where the expanded differential operator Eq. (A.31) has been used.

Finally, inserting the previous eqs. (A.39) in the displacement formulation (with the help of eqs. (A.38)) into the equation of mechanical equilibrium (A.7), together with the expansions of the body forces $\boldsymbol{F}$ (A.25), the weighting function $h(\rho)$ (being the same as Eq. A.17) and the approximated gradient (A.30) for the surface forces $F_S\nabla\rho$, one can expand the governing equation up to second lowest order.

order $O(\epsilon^{-2})$: In leading order we get

$$\begin{cases} \left[\left(2\mu^1+\lambda^1\right)-\left(2\mu^0+\lambda^0\right)\right]\left(\partial_{\bar{r}}h_0\partial_{\bar{r}}\bar{u}_{\bar{r}0}+h_0\partial_{\bar{r}\bar{r}}\bar{u}_{\bar{r}0}\right)+\left(2\mu^0+\lambda^0\right)\partial_{\bar{r}\bar{r}}\bar{u}_{\bar{r}0}=0 \\ \left(\mu^1-\mu^0\right)\left(\partial_{\bar{r}}h_0\partial_{\bar{r}}u_{s0}+h_0\partial_{\bar{r}\bar{r}}\bar{u}_{s0}\right)+\mu_0\partial_{\bar{r}\bar{r}}\bar{u}_{s0}=0 \end{cases} \tag{A.41}$$

which both can be written as

$$\begin{cases} \partial_{\bar{r}}\left\{\left[h_0\left(2\mu^1+\lambda^1\right)-\left(1-h_0\right)\left(2\mu^0+\lambda^0\right)\right]\partial_{\bar{r}}\bar{u}_{\bar{r}0}\right\}=0 \\ \partial_{\bar{r}}\left\{\left[h_0\mu^1+(1-h_0)\mu^0\right]\partial_{\bar{r}}u_{s0}\right\}=0 \end{cases} \tag{A.42}$$

by using the product rule. Neither body nor surface forces enter the leading order. Further, only radial gradients of the stress tensor components $\bar{\Sigma}_{\bar{r}\bar{r}}$ and $\bar{\Sigma}_{ss}$ appear in dominating order. Tangential derivatives or the shear component $\bar{\Sigma}_{\bar{r}s}$, do not appear. Since $h_0 = h_0(\bar{\rho}_0)$ is not constant (or vanishes) in the interfacial region, it follows from eqs. (A.42) that

$$\partial_{\bar{r}}\bar{u}_{\bar{r}0}=0 \qquad \text{and} \qquad \partial_{\bar{r}}\bar{u}_{s0}=0 \tag{A.43}$$

for all h_0. Integrating both across the interface width $\bar{r}\longrightarrow\pm\infty$ yields

$$\begin{cases} \bar{u}_{\bar{r}0}(\infty,s)=\bar{u}_{\bar{r}0}(-\infty,s) \quad\Longrightarrow\quad u_{\bar{r}0}(0^+,s)=u_{\bar{r}0}(0^-,s) \\ \bar{u}_{s0}(\infty,s)=\bar{u}_{s0}(-\infty,s) \quad\Longrightarrow\quad u_{s0}(0^+,s)=u_{s0}(0^-,s) \end{cases} \tag{A.44}$$

where the matching conditions (A.27) have been used. Therefore, in leading order, the reversible elastic phase field method describes the desired continuity of the deformation normal to the boundary between two elastic media, i.e. their cohesion. Otherwise, an induced deformation could lead to their break up and physical distancing, *i.e* appearance of a third void phase, or unphysical deformation into each other.

order $O(\epsilon^{-1})$: For examining the next order, knowledge from the previous one can help to facilitate it. [7] Similar to the dominating order, we can reduce the remaining terms to

$$\begin{cases} \partial_{\bar{r}}\Big\{\left[h_0\left(2\mu^1+\lambda^1\right)+\left(1-h_0\right)\left(2\mu^0+\lambda^0\right)\right]\partial_{\bar{r}}\bar{u}_{\bar{r}1} \\ \qquad +\left[h_0\lambda^1+\left(1-h_0\right)\lambda^0\right]\partial_s\bar{u}_{s0}+F_S\rho_0\Big\}=0 \\ \partial_{\bar{r}}\left\{\left[h_0\mu^1+\left(1-h_0\right)\mu^0\right]\left(\partial_s\bar{u}_{\bar{r}0}+\partial_{\bar{r}}\bar{u}_{s1}\right)\right\}=0 \end{cases} \tag{A.45}$$

[7] In the full expansions terms containing eqs. (A.43) will automatically drop out. The same holds for terms proportional to $\partial_{s\bar{r}}\bar{u}_{s0}=\partial_{\bar{r}s}\bar{u}_{s0}=0$, which immediately follows from eqs. (A.43).

where it is worth noting, that in the mechanical equilibrium equation for the radial coordinate the surface force appears for the first time. The coupling between normal and tangential displacement components in both equations, makes them more complicated than the previous ones and impossible to directly infer information on the terms in the curly brackets, as has been done before. To further analyse these equations, we integrate both along the interface width. This procedure is further motivated by noting, that all relevant information on the displacement field itself has been achieved in leading order. Recall, that in the outer expansion $\boldsymbol{u}_0 = 0$ bears all information, while $\boldsymbol{u}_1 = 0$. This renders the $\bar{u}_{\bar{r}1}$ and $\bar{u}_{s1}$ irrelevant through the matching conditions. Again, the integration along the interface normal is performed in the limits $\bar{r} \longrightarrow \pm\infty$ giving

$$\begin{cases} \left\{\left[h_0\left(2\mu^1+\lambda^1\right)+\left(1-h_0\right)\left(2\mu^0+\lambda^0\right)\right]\partial_{\bar{r}}\bar{u}_{\bar{r}1} \right. \\ \left. +\left[h_0\lambda^1+\left(1-h_0\right)\lambda^0\right]\partial_s\bar{u}_{s0}+F_S\rho_0\right\}\Big|_{-\infty}^{+\infty}=0 \\ \\ \left\{\left[h_0\mu^1+\left(1-h_0\right)\mu^0\right]\left(\partial_s\bar{u}_{\bar{r}0}+\partial_{\bar{r}}\bar{u}_{s1}\right)\right\}\Big|_{-\infty}^{+\infty}=0 \end{cases} \tag{A.46}$$

which simplifies to

$$\begin{cases} \lambda^0\partial_s\bar{u}_{s0}(\infty,s)-\lambda^1\partial_s\bar{u}_{s0}(-\infty,s)-F_S=0 \\ \mu^0\partial_s\bar{u}_{\bar{r}0}(\infty,s)-\mu^1\partial_s\bar{u}_{\bar{r}0}(-\infty,s)=0 \end{cases} \tag{A.47}$$

by using the matching conditions (A.26) on ρ_0, resulting in $h_0(\rho_0(+\infty)) = 0$ and $h_0(\rho_0(+\infty)) = 1$, and the displacement components, yielding $\partial_{\bar{r}}\bar{u}_{\bar{r}1}(\pm\infty,s) = \partial_{\bar{r}}\bar{u}_{s1}(\pm\infty,s) = 0$. For deductive purposes, we did not match the non-vanishing deformation gradients in eqs. A.47 yet. Finally, carrying out the matching for the remaining terms with the respective conditions (A.26) we find

$$\begin{cases} \lambda^0\partial_s\bar{u}_{s0}(0^+,s)-\lambda^1\partial_s\bar{u}_{s0}(0^-,s)-F_S=0 \\ \mu^0\partial_s\bar{u}_{\bar{r}0}(0^+y,s)-\mu^1\partial_s\bar{u}_{\bar{r}0}(0^-,s)=0 \end{cases} \tag{A.48}$$

which state that the displacement may exhibit a discontinuity along the boundary when approaching it from each elastic phase. This jump occurs in the tangential displacement component due to surface forces and, as for the normal component, due to differences in the elastic parameters of the considered materials. Therefore, shear is not described (at least up to first order) by our proposed elastic phase field method.

A.2 One-dimensional phase field profile

The stead-state profile of the phase field can be derived by solving the leading order equation of the inner asymptotic expansion of the phase field dynamics (A.34) under matching conditions (A.26) for ρ, which is similar to the solution of the one-dimensional phase field equation

$$\frac{\partial \rho}{\partial t} = D\frac{\partial^2 \rho}{\partial x^2} - \frac{\partial g(\rho)}{\partial \rho} \tag{A.49}$$

with $g(\rho) = \rho^2(1-\rho)^2$ under the conditions $\rho(x \to -\infty) = 0$ and $\rho(x \to +\infty) = 1$. Consider the stationary case

$$D\frac{\partial^2 \rho}{\partial x^2} - \frac{\partial g(\rho)}{\partial \rho} = 0. \tag{A.50}$$

By multiplying both sides of the equation with $\partial\rho/\partial x$, we get the expression

$$\begin{aligned} & D\frac{\partial^2 \rho}{\partial x^2}\frac{\partial \rho}{\partial x} - \frac{\partial g(\rho)}{\partial \rho}\frac{\partial \rho}{\partial x} = 0 \\ \Rightarrow \quad & \frac{d}{dx}\left[\frac{D}{2}\left(\frac{d\rho}{dx^2}\right)^2 - g(\rho)\right] = 0. \end{aligned} \tag{A.51}$$

This gives

$$\frac{D}{2}\left(\frac{d\rho}{dx^2}\right)^2 - g(\rho) = const, \tag{A.52}$$

where we can set the constant to zero due to the above conditions on ρ. Now, we can solve this equation for

$$\frac{\partial \rho}{\partial x} = \sqrt{\frac{D}{2}g(\rho)} = \sqrt{\frac{D}{2}}\rho(1-\rho), \tag{A.53}$$

where we have used the exact form of the double well potential $g(\rho)$ used in this thesis. A separation of variables leads to

$$\frac{d\rho}{\rho(1-\rho)} = \sqrt{\frac{D}{2}}dx. \tag{A.54}$$

Performing a partial fraction decomposition

$$\frac{d\rho}{\rho} - \frac{d\rho}{1-\rho} = \sqrt{\frac{D}{2}}dx \tag{A.55}$$

and integrating, gives

$$\log\left(\frac{\rho}{1-\rho}\right) = \sqrt{\frac{D}{2}}x + k \tag{A.56}$$

which leads to

$$\frac{\rho}{1-\rho} = \exp\left(\sqrt{\frac{2}{D}}x + k\right). \tag{A.57}$$

Solving for the phase field variable ρ results in

$$\rho(r) = \left[1 + \exp\left(-\sqrt{\frac{2}{D}}x - k\right)\right]^{-1} \tag{A.58}$$

which fulfils the above mentioned limiting conditions on ρ. The integration constant k can now be specified by noting that the interface position x_0 can be identified with the isocontour of the phase field $\rho = 1/2$ for our chosen double-well potential. Finally, we arrive at

$$\rho(x) = \left[1 + \exp\left(-\sqrt{\frac{2}{D}}(x - x_0)\right)\right]^{-1} = \frac{1}{2}\left[1 + \tanh\left(\frac{x - x_0}{\sqrt{2D}}\right)\right] \tag{A.59}$$

where in the last step we have used the relation

$$\tanh(x) = 1 - \frac{2}{1 + e^{2x}}. \tag{A.60}$$

For $D = 1$ and $x_0 = 0$, the Eq. (A.35) given in the asymptotic expansion of the previous section is recovered.

A.3 Analytical solution for a contractile cell with nucleus adhered to a substrate in radial symmetry

In section 5.3.1 a radial symmetric contractile cell homogeneously adhered to a compliant substrate was discussed. We here give the calculation of the analytical solution to the corresponding sharp interface problem, being an extension of the model presented by Edwards & Schwarz [191], due to the incorporation of an elastic nucleus.

A strongly spread cell of height d, much smaller than its extensions in the other two spatial directions, can be approximated as a thin elastic sheet in plane stress (*cf.* Fig. 5.2 A). Consider a radial symmetric cell of radius R_C, split into two compartments: a concentric nucleus (N) of radius R_N and the cytoplasm (C), *i.e* the rest of the cell without the nucleus. Both are assumed to be linear elastic. Young's moduli E_N and E_C as well as Poisson's ratio ν_N and ν_C of these two compartments can differ from each other. Corresponding to the model described in section 5.3.1, we assume the cell to be subjected to a homogeneous and isotropic active contractile stress $\boldsymbol{\sigma}_{act} = -\sigma_0 \mathbf{1}$, where $\sigma_0 > 0$ is the magnitude of the active stress and $\mathbf{1}$ is the identity matrix. The cell is coupled to an underlying substrate by modelling the engaged adhesions as a homogeneous density of springs with spring stiffness density Y. This elastic foundation evokes a restoring force $\boldsymbol{F} = -Y\boldsymbol{u}$ upon deformation.

In each compartment the equation of mechanical equilibrium

$$\nabla \cdot \boldsymbol{\sigma}^\alpha - Y\boldsymbol{u}^\alpha = 0 \tag{A.61}$$

has to be solved under appropriate boundary conditions, where $\alpha \in \{C, N\}$ denotes the compartment, *i.e.* cytoplasm (C) or nucleus (N). Due to the radial symmetric geometry, the only non-vanishing displacement component in polar coordinates is the radial one, *i.e.* $\boldsymbol{u} = u_r(r)\boldsymbol{e}_r$ with $\boldsymbol{e}_r$ being the radial basis vector. From this symmetry consideration it follows, that in polar coordinates Eq. A.61 reduces to

$$r^2 \frac{\partial^2 u_r^\alpha}{\partial r^2} + r\frac{\partial u_r^\alpha}{\partial r} - \left(1 + \frac{r^2}{l_\alpha^2}\right) u_r^\alpha = 0 \tag{A.62}$$

where $l_\alpha = \sqrt{E_\alpha d / \left[Y\left(1-\nu_\alpha^2\right)\right]}$ is the localization length [191] for the respective cell compartment α. The localization lengths l_α are a characteristic length scale, describing

how far forces can propagate through a body in the above configuration. Equation A.62 is a modified Bessel function, whose general solution

$$u_r^{\alpha}(r) = AI_1\left(\frac{r}{l_\alpha}\right) + BK_1\left(\frac{r}{l_\alpha}\right) \tag{A.63}$$

is a superposition of modified Bessel functions of the first kind $I_1(x)$ and second kind $K_1(x)$ [215]. A and B are constants which have to be determined through the boundary conditions specifying the problem.

A.3.1 Subproblem I: Nucleus

We start with the nuclear compartment for which $l_N = \sqrt{E_N d/\left[Y\left(1-\nu_N^2\right)\right]}$. The boundary conditions are

$$\text{(I)} \quad u_r^N(0) = 0 \qquad \text{and} \qquad \text{(II)} \quad \sigma_{rr}^N(R_N) = -\sigma_N d, \tag{A.64}$$

where σ_N is the a priori unknown radial stress at the nuclear boundary which will be specified later. By using the above conditions (I) and (II), the displacement field in the nuclear compartment can be determined to be

$$u_r^N(r) = -\frac{\sigma_N d l_N}{2\mu_N + \lambda_N} \frac{I_1\left(\frac{r}{l_N}\right)}{I_0\left(\frac{R_N}{l_N}\right) - \frac{2\mu_N}{2\mu_N+\lambda_N}\frac{l_N}{R_N} I_1\left(\frac{R_N}{l_N}\right)} \tag{A.65}$$

where in the derivation it has to be used that [215]

$$\frac{\partial}{\partial r} I_1\left(\frac{r}{l_N}\right) = \frac{1}{l_N}\left[I_0\left(\frac{r}{l_N}\right) - \frac{l_N}{r} I_1\left(\frac{r}{l_N}\right)\right]. \tag{A.66}$$

Equation A.65 is of the same form as derived by Edwards & Schwarz [191] for a adhered contractile disk-like cell.

A.3.2 Subproblem II: Cytoplasm

For the cytoplasmic compartment with outer radius R_C and $l_C = \sqrt{E_C d/\left[Y\left(1-\nu_C^2\right)\right]}$, the boundary conditions are

$$\text{(III)} \quad \sigma_{rr}(R_C) = -\sigma_0 d \qquad \text{and} \qquad \text{(IV)} \quad u_r^N(R_N) - u_r^C(R_N) = 0, \tag{A.67}$$

where σ_0 is the contractile stress appearing as boundary force. Boundary condition (IV) enforces a continuous displacement field in the cell, exhibiting no jumps at the nucleus-cytoplasm interface. Otherwise, the cell would loose its coherency, what would be equivalent to a rupture at the interface of the two cell compartments.

Determining the constants in Eq. (A.63) via the boundary conditions (A.67) (III) and (IV) lead to the displacement field in the cytoplasm

$$u_r^C(r) = \left(u_r^N(R_N) - \frac{\sigma_0 d l_C}{2\mu_C + \lambda_C} \frac{K_1\left(\frac{R_N}{l_C}\right)}{\tilde{K}} \right) \times \frac{I_1\left(\frac{r}{l_C}\right) + \frac{\tilde{I}}{\tilde{K}} K_1\left(\frac{r}{l_C}\right)}{I_1\left(\frac{R_N}{l_C}\right) + \frac{\tilde{I}}{\tilde{K}} K_1\left(\frac{R_N}{l_C}\right)} + \frac{\sigma_0 d l_C}{2\mu_C + \lambda_C} \frac{K_1\left(\frac{r}{l_C}\right)}{\tilde{K}}. \tag{A.68}$$

Here, $u_r^N(R_N)$ is the displacement field at the cytoplasm-nucleus boundary and

$$\begin{aligned} \tilde{I} &= I_0\left(\frac{R_C}{l_C}\right) - \frac{2\mu_C}{2\mu_C + \lambda_C} \frac{l_C}{R_C} I_1\left(\frac{R_C}{l_C}\right) \\ \tilde{K} &= K_0\left(\frac{R_C}{l_C}\right) + \frac{2\mu_C}{2\mu_C + \lambda_C} \frac{l_C}{R_C} K_1\left(\frac{R_C}{l_C}\right). \end{aligned} \tag{A.69}$$

In the derivation of Eq. (A.68) it has to be used that [215]

$$\frac{\partial}{\partial r} K_1\left(\frac{r}{l_N}\right) = -\frac{1}{l_C}\left[K_0\left(\frac{r}{l_C}\right) + \frac{l_C}{r} K_1\left(\frac{r}{l_C}\right) \right], \tag{A.70}$$

additionally to Eq. (A.66).

Lastly, the stress at the nucleus-cytoplasm boundary σ_N has to be specified. We use that in the mechanical equilibrium the internal stress at the nucleus-cytoplasm interface, when approaching it from the cytoplasm and the nucleus domain, have to balance each other, *i.e.*

$$\sigma_{rr}^N\Big|_{r\to R_N} = \sigma_{rr}^C\Big|_{r\to R_N}. \tag{A.71}$$

By taking advantage of the von Neumann boundary condition (A.64) (II), it follows from Eq. (A.71)

$$\sigma_N = \frac{\sigma_0}{\tilde{K}} \frac{\alpha K_1\left(\frac{R_N}{l_C}\right) + K_0\left(\frac{R_N}{l_C}\right)}{1 - \frac{l_N}{2\mu_N + \lambda_N} \frac{I_1\left(\frac{R_N}{l_N}\right)}{I_0\left(\frac{R_N}{l_N}\right) - \frac{2\mu_N}{2\mu_N + \lambda_N} I_1\left(\frac{R_N}{l_N}\right) \frac{l_N}{R_N}} \left[\frac{2\mu_C + \lambda_C}{l_C} \alpha - \frac{2\mu_C}{R_N} \right]} \tag{A.72}$$

with

$$\alpha = \frac{I_0\left(\frac{R_N}{l_C}\right) - \frac{\tilde{I}}{\tilde{K}} K_0\left(\frac{R_N}{l_C}\right)}{I_1\left(\frac{R_N}{l_C}\right) + \frac{\tilde{I}}{\tilde{K}} K_1\left(\frac{R_N}{l_C}\right)}. \tag{A.73}$$

The full solution is hence given by

$$u_r(r) = \begin{cases} -\frac{\sigma_N dl_N}{2\mu_N+\lambda_N} \frac{I_1\left(\frac{r}{l_N}\right)}{I_0\left(\frac{R_N}{l_N}\right) - \frac{2\mu_N}{2\mu_N+\lambda_N}\frac{l_N}{R_N} I_1\left(\frac{R_N}{l_N}\right)} & \text{for } 0 \le r \le R_N \\ \left(u_r^N(R_N) - \frac{\sigma_0 dl_C}{2\mu_C+\lambda_C}\frac{K_1\left(\frac{R_N}{l_C}\right)}{\tilde{K}}\right) \times \frac{I_1\left(\frac{r}{l_C}\right)+\frac{\tilde{I}}{\tilde{K}}K_1\left(\frac{r}{l_C}\right)}{I_1\left(\frac{R_N}{l_C}\right)+\frac{\tilde{I}}{\tilde{K}}K_1\left(\frac{R_N}{l_C}\right)} + \frac{\sigma_0 dl_C}{2\mu_C+\lambda_C}\frac{K_1\left(\frac{r}{l_C}\right)}{\tilde{K}} & \text{for } R_N < r \le R_C \end{cases} \tag{A.74}$$

together with Eqs. (A.69), (A.72) and (A.73).

A.4 On the relation between Frank and Landau elastic constants in 2D

In Sect. 7.2.2 Eq. (7.8) we gave the relation between the Frank elastic constants in 2D an the respective phenomenlogical constants in an Landau expansion up to second order in gradients of the $\boldsymbol{Q}$-tensor. Here, we want to demonstrate the procedure to obtain these relation.

Distortions in the nematic order can be phenomenological described in an Landau expansion in gradients of the order parameter

$$Q_{ij} = S\left(n_i n_j - \frac{1}{2}\delta_{ij}\right), \tag{A.75}$$

which is a symmetric and traceless tensor. Up to second order, as used in this work, the Landau distortional energy is

$$f_{el}^{2D} = \frac{L_1}{2}\partial_k Q_{ij}\partial_k Q_{ij} + \frac{L_2}{2}\partial_j Q_{ij}\partial_k Q_{ik}, \tag{A.76}$$

with phenomenological elastic constants L_i.

Alternatively, distortions can be described by gradients in the director $\boldsymbol{n}$. The so-called Oseen-Frank elastic energy for distortions in the nematic orientation in 2D reads

$$f_{el}^{3D} = \frac{1}{2}K_1(\nabla\cdot\boldsymbol{n})^2 + \frac{1}{2}K_3\left[(\boldsymbol{n}\cdot\nabla)\cdot\boldsymbol{n}\right]^2, \tag{A.77}$$

describing splay (K_1) and bending (K_3) deformations [299]. Here, the Frank elastic constants K_i have a clear physical meaning. Note that in 2D twist deformations (K_2) are

not possible and the term describing bending appears in its 2D form (*cf.* Eq. (7.6)) [299].

We now want to establish a relation between the phenomenological elastic constants of Eq. (A.76) and the Frank elastic constants in Eq. (A.77) in 2D. For simplicity we assume that the scalar order parameter S in Eq. (A.75), which describes the degree of alignment of the nematic liquid crystal, is $S = const = 1$. Inserting the expression of the $\boldsymbol{Q}$-tensor, Eq. (A.75) in the Landau distortional energy Eq. (A.76) leads to

$$\begin{aligned} f_{el} &= \frac{L_1}{2}\left[\partial_k\left(n_i n_j\right)\partial_k\left(n_i n_j\right)\right] + \frac{L_2}{2}\left[\partial_j\left(n_i n_j\right)\partial_k\left(n_i n_k\right)\right] \\ &= \frac{L_1}{2}\left[\left(\partial_k n_i\right)n_j + n_i\left(\partial_k n_j\right)\right]^2 + \frac{L_2}{2}\left[\left(\partial_j n_i\right)n_j + n_i\left(\partial_j n_j\right)\right]\left[\left(\partial_k n_i\right)n_k + n_i\left(\partial_k n_k\right)\right] \\ &= \frac{L_1}{2}\left[\left(\partial_k n_i\right)^2 + \left(\partial_k n_j\right)^2\right] + \frac{L_2}{2}\left[\left(n_j\partial_j n_i\right)\left(n_k\partial_k n_i\right) + \left(\partial_j n_j\right)^2\right] \\ &= L_1\left(\partial_k n_i\right)^2 + \frac{L_2}{2}\left[\left(n_k\partial_k n_i\right)^2 + \left(\partial_j n_j\right)^2\right], \end{aligned} \tag{A.78}$$

where in the third step $n_i\partial_k n_i = 0$ was used. Furthermore, in the last step and the second L_1-term we relabeled j to i and in the first L_2-term j was relabeled to k. Using the identity $\partial_k n_i = n_k\left[\left(n_j\partial_j\right)n_i\right] + \left(\partial_j n_j\right)\left(\delta_{ki} - n_k n_i\right)$ in the last step of Eq. (A.78) and rearranging the resulting terms leads to

$$f_{el} = \left(L_1 + \frac{L_2}{2}\right)\left(\partial_j n_j\right)^2 + \left(L_1 + \frac{L_2}{2}\right)\left[\left(n_j\partial_j\right)n_i\right]^2. \tag{A.79}$$

This can be written in vector notation

$$f_{el} = \left(L_1 + \frac{L_2}{2}\right)\left(\nabla\cdot\boldsymbol{n}\right)^2 + \left(L_1 + \frac{L_2}{2}\right)\left[\left(\boldsymbol{n}\cdot\nabla\right)\cdot\boldsymbol{n}\right]^2. \tag{A.80}$$

and compared to the Frank free energy, Eq. (A.77). We find that

$$K_1 = K_3 = 2L_1 + L_2. \tag{A.81}$$

Hence, a Landau expansion of the distortional energy up to second order effectively results in a one constant approximation. To break this degeneracy and to allow for different K_i values, higher order terms in the Landau expansion Eq. (A.76) are needed.

B Supplementary material

B.1 Supplementary material to Chapter 3

The following tables contain the computational parameters to Figs. 3.2, 3.3 and 3.4 in Chapter 3.

Table B.1: Simulation parameters for Fig. 3.2 C.

Description	Symbol	Value
number of grid points	N	2048
domain size	L	100
time step size	Δt	0.001
extension of domain $\rho = 1$	L_x	25
Phase field diffusion coefficient	D_ρ	$0.25 - 2$

Table B.2: Simulation parameters for Fig. 3.3 and Fig. 3.4.

Description	Symbol	Value
number of grid points	$N_x \times N_y$	1024×512
domain size	L	100
time step size	Δt	0.01
extension of rectangle	$L_x \times L_y$	30×15
Phase field diffusion coefficient	D_ρ	1

B.2 Supplementary material to Chapter 4

This appendix contains supplementary information on Chapter 4, *i.e* supplementary figures and parameters used for the simulations presented in the main text.

B.2.1 Supplementary figures

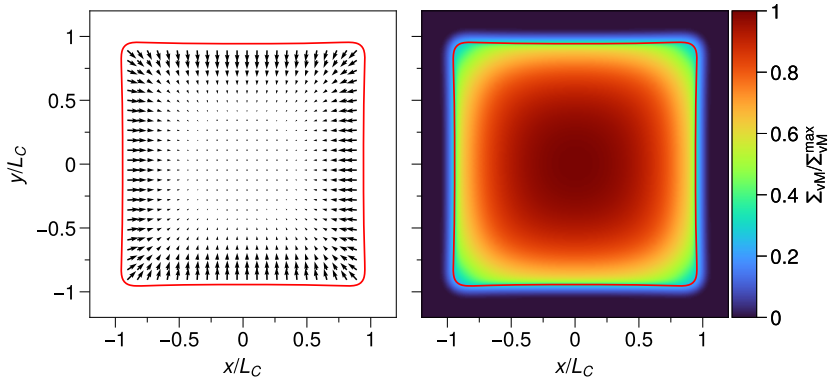

Figure B.1: A contractile cell (E_C, ν_C) of half-edge length L_C is homogeneously adhered to an underlying substrate via a spring stiffness density Y. The cell contracts isotropically due to an active stress $\sigma_0/E_C = 0.4$. Shown is the displacement field $\boldsymbol{u}(\boldsymbol{x})$ (left) and the (phase field) von Mises stress Σ_{vM}^{max}, Eq. (4.20), normalized by the maximal stress value Σ_{vM}^{max} (right). The red line is the $\rho = 1/2$-isocontour marking the cell boundary. The vectors in the left panel are scaled by a factor of 2 for better visibility. Simulations were performed on $N = 512 \times 512$ grid points on a domain of size $100\,\mu\text{m} \times 100\,\mu\text{m}$. If not specified above, relevant mechanical parameters are $L_C = 25\,\mu\text{m}$, $E_C = 1\,\text{kPa}$, $\nu_C = 0.5$ and $Y = 0.003\,\text{nN}/\mu\text{m}^3$. Further parameters as in Appendix B.2.2 Table B.3.

B.2.2 Parameters for simulations

The table below lists the default values for additional parameters used for the simulations in Chapter 4, if not stated otherwise in the respective figure captions.

Table B.3: Additional simulation parameters to Chapter 4

Description	Symbol	Value
time step size*	Δt	$10^{-3} - 10^{-6}$
diffusion coefficient phase field**	D_ρ	1
friction coefficient	ξ	1
global suppression coefficient**	γ_0	0.35
force-dependent friction coefficient	$\gamma_1(\boldsymbol{F})$	0
cell/monolayer height***	d	0.1

*Fig. 4.2 B: $\Delta t = 10^{-4}$: ($\Delta t = 10^{-5}$ for $Y = 0.25\,\mathrm{nN/\mu m^3}$); Fig. 4.3: $\Delta t = 10^{-3}$; Fig. 4.4 and Fig. B.1: $\Delta t = 10^{-6}$; Fig. 4.2 C and Fig. 4.5: $\Delta t = 10^{-5}$.
** In Fig. 4.2 C $D_\rho = 0.5$ and $\gamma_0 = 0$.
*** In Fig. 4.2 $d = 1$.
Note, characteristic length scale for cell simulations is $L_0 = 1\,\mu\mathrm{m}$ and for monolayer simulations $L_0 = 10\,\mu\mathrm{m}$.

B.3 Supplementary material to Chapter 5

This appendix contains supplementary information on Chapter 5, *i.e* supplementary figures and parameters used for the simulations presented in the main text.

B.3.1 Supplementary figures

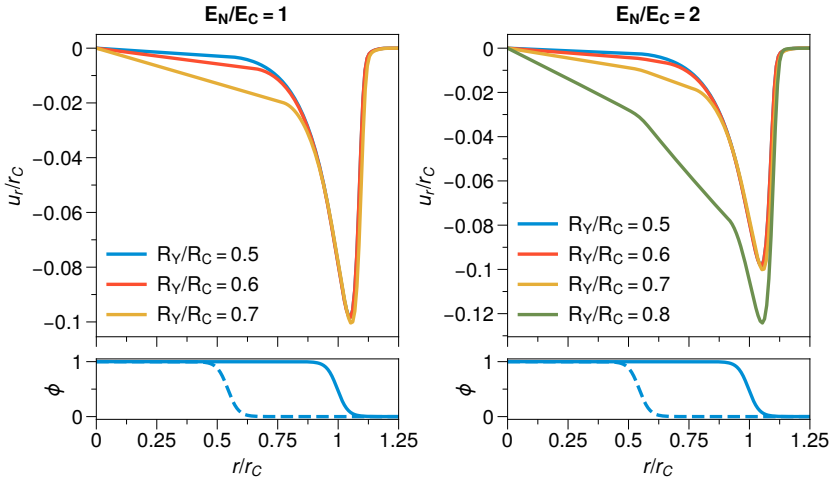

Figure B.2: Adhesion on an outer ring only. In the upper panel phase field solutions for u_r/r_C are shown for $E_N/E_C = 1$ (left panel) and $E_N/E_C = 2$ (right panel). In both cases $R_N/R_C = 0.5$. For $E_N/E_C = 1$ the solutions for adhesive ring radii $R_Y/R_C = 0.5, 0.6, 0.7$ (blue to yellow) are shown. For $E_N/E_C = 2$ the cases $R_Y/R_C = 0.5, 0.6, 0.7$ (blue to yellow) are shown. The lower panel shows the phase field profiles for ρ (solid)and ψ (dashed) for the case $R_Y/R_C = 0.5$. All simulations were performed on $N = 512 \times 512$ grid points on a domain of $50\,\mu\text{m} \times 50\,\mu\text{m}$. If not specified above, the other mechanical parameters are $R_C = 12.5\,\mu\text{m}$, $d = 1\,\mu\text{m}$, $E_C = \sigma_0 = 1\,\text{kPa}$, $\nu_C = \nu_N = 0.5$ and $Y_0 = 0.8\,\text{nN}/\mu\text{m}^3$. Further parameters as in Appendix B.3.2 Table B.4.

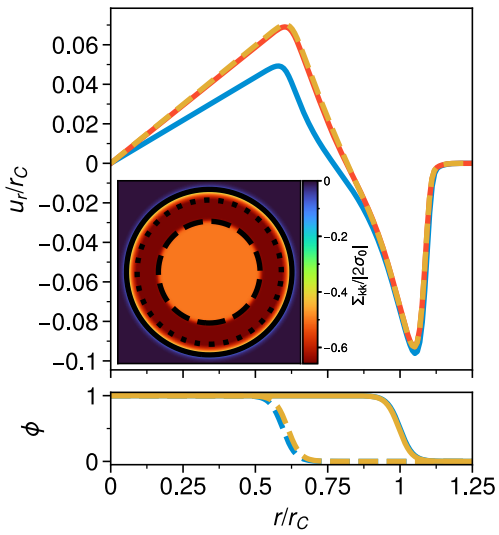

Figure B.3: A contractile, disk-like cell is adhered on an outer ring of radius R_Y for nuclear-cytoplasmic coupling degree $f = 1$ (*cf.* Eq. (5.4)). The upper panel shows phase field solutions for the radial displacement field u_r/r_C, normalized by the cell radius in mechanical equilibrium, for $E_N/E_C = 2$, $R_N/R_C = 0.5$ with varying $R_Y/R_C = 0.56$ (blue), 0.7 (red) and 0.8 (yellow). The inset shows the normalized stress for $R_Y/R_C = 0.8$ and the lower panel the radial phase field profiles for $R_Y/R_C = 0.56$ (blue) and $R_Y/R_C = 0.8$ (yellow), where the ψ-profile is shown as dashed line and the ρ-profile as solid line. Further parameters as in Fig. 5.2 and Appendix B.3.2 Table B.4

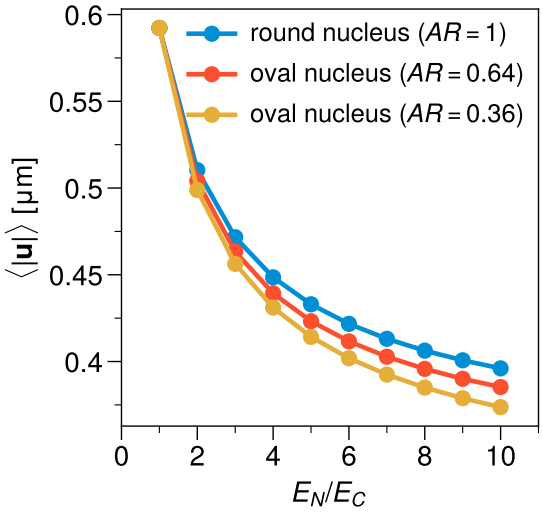

Figure B.4: A rectangular cell is adhered at its corners to a micropattern and is subject to an isotropic contractile stress, as shown in Fig. 5.3 **A**-**C**. Shown is the average deformation $\langle|\boldsymbol{u}|\rangle$ of the cell with a circular nucleus (aspect ratio $AR = 1$) and an oval nucleus ($AR = 0.64$ and $AR = 0.36$) for different nucleus rigidities E_N/E_C. The average deformation decreases with the aspect ratio and stiffness of the nucleus. Parameters as in Fig. 5.3 and Appendix B.3.2 Table B.4.

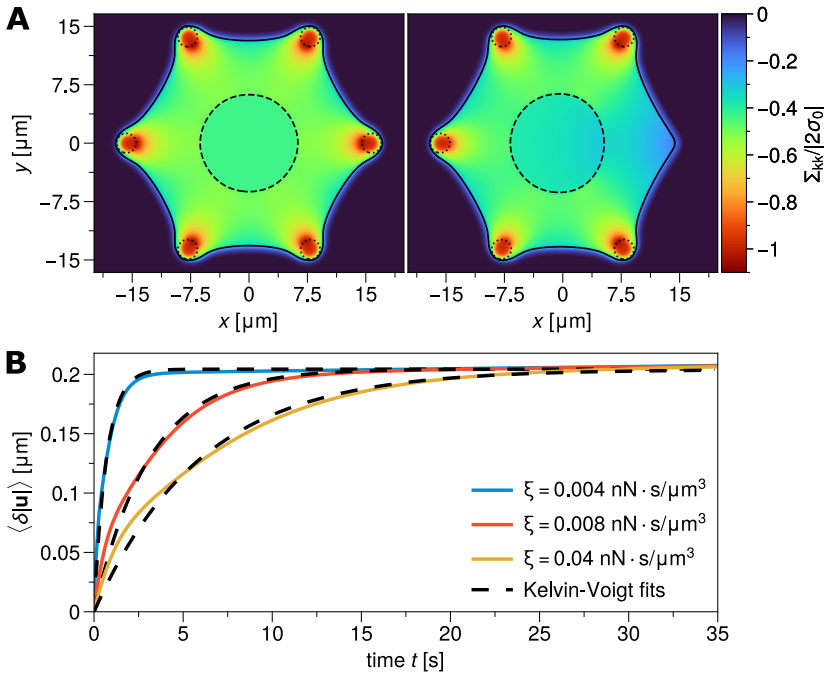

Figure B.5: A A cell with nucleus of stiffness $E_N/E_C = 2$ was allowed to spread in a hexagonal adhesion pattern and to contract isotropically with $\sigma_0/E_C = 0.4$ until it reached mechanical equilibrium (left panel). Subsequently, the most right adhesion spot was removed and the cell evolved towards a new mechanical equilibrium (right panel). The colour map shows the normalized trace of the stress tensor. The cell shape (isocline $\rho = 0.5$, solid black) and nucleus shape ($\psi = 0.5$, dashed black) are also shown. **B** Shown is the average displacement $\langle\delta|\boldsymbol{u}|\rangle$, with respect to the initial reference displacement in (A), as a function of time t for different friction coefficients ξ. For all tested ξ, the behaviour is the one of a Kelvin-Voigt model. Parameters as in Fig. 5.4 and Appendix B.3.2 Table B.4.

B.3.2 Parameters for simulations

The table below lists the default values for additional parameters used for the simulations in Chapter 5, if not stated otherwise in the respective figure captions.

Table B.4: Additional simulation parameters for Chapter 5

Parameter	Symbol	Value	Unit
time step*	Δt	0.001	s
diffusion coefficient phase field (PF)**	D_ϕ	1.25	$\mu m^2/s$
friction coefficient***	ξ	0.004	$nN \cdot s/\mu m^3$
local suppression coeff.***	$\gamma(\boldsymbol{x})$	$0.014 - 0.04$	$nN \cdot s/\mu m^3$
regularization parameter	ϵ	0.0025	μm^2
diffusion coefficient adhesion PF	D_Y	0.25	$\mu m^2/s$
diffusion coefficient obstacle PF	D_φ	0.625	$\mu m^2/s$
degree of nucleocytoplasmic coupling	f	0	

*For Fig. 5.2 $\Delta t = 10^{-4}$ s. Chosen time scale is $\tau = 0.1$ s in all simulations.
**For $\phi \in \{\rho, \psi\}$, i.e. cell and nucleus. Sets the interface width to 0.5 µm.
***Note, in plane strain and axial symmetry the unit is $nN \cdot s/\mu m^4$.

B.4 Supplementary material to Chapter 6

This appendix contains supplementary information on Chapter 6, *i.e* supplementary figures and parameters used for the simulations presented in the main text.

B.4.1 Supplementary figures

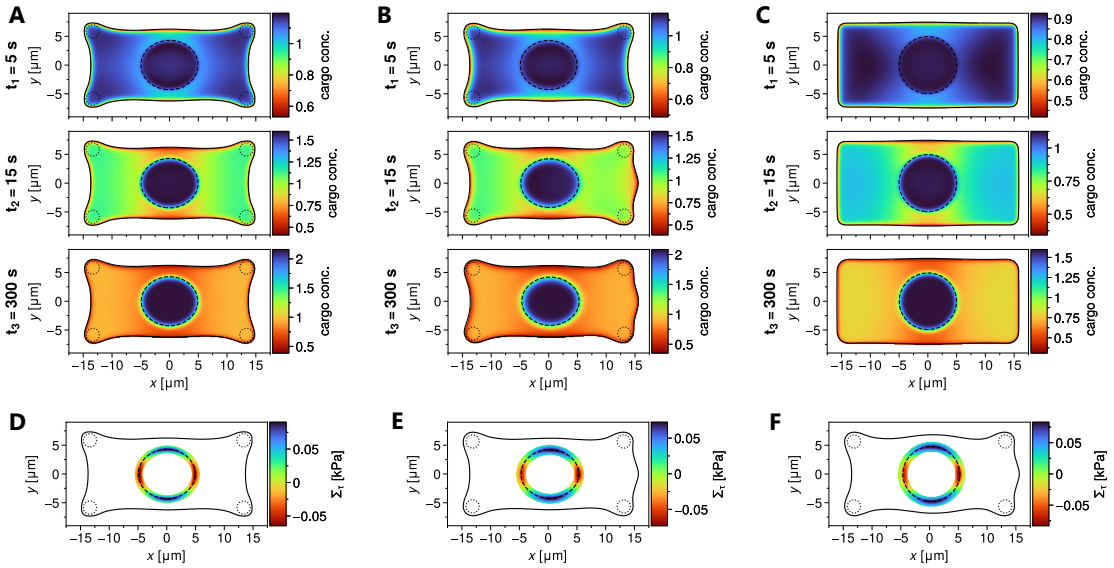

Figure B.6: Additional figures to simulations in Sect. 6.3.3. **A-C** Concentration maps for $\rho \geq 0.5$ and three different time points for an (**A**) only contracting, adhered cell with nucleus stiffness $E_N/E_C = 2$, (**B**) a contractile, adhered cell pulled at its right edge at $y = 0$ in positive x-direction with nucleus stiffness $E_N/E_C = 2$ and (**C**) a uniaxially stretched cell with $E_N/E_C = 2$. **D-F** Tension Σ_τ for $|\nabla\psi| > 0.1$ at the nuclear boundary for the corresponding panels above. Adhesion spots are marked by dotted lines, the cell boundary is indicated by the isocontour $\rho = 1/2$ (solid line) and the nuclear boundary by the isocontour $\psi = 1/2$ (dashed line). For further parameters for (**A/D**) see Fig. 6.3, for (**B/E**) see Fig. 6.4 and for (**C/F**) see Fig. 6.5. Other parameters as in in Appendix B.4.2 Table B.5.

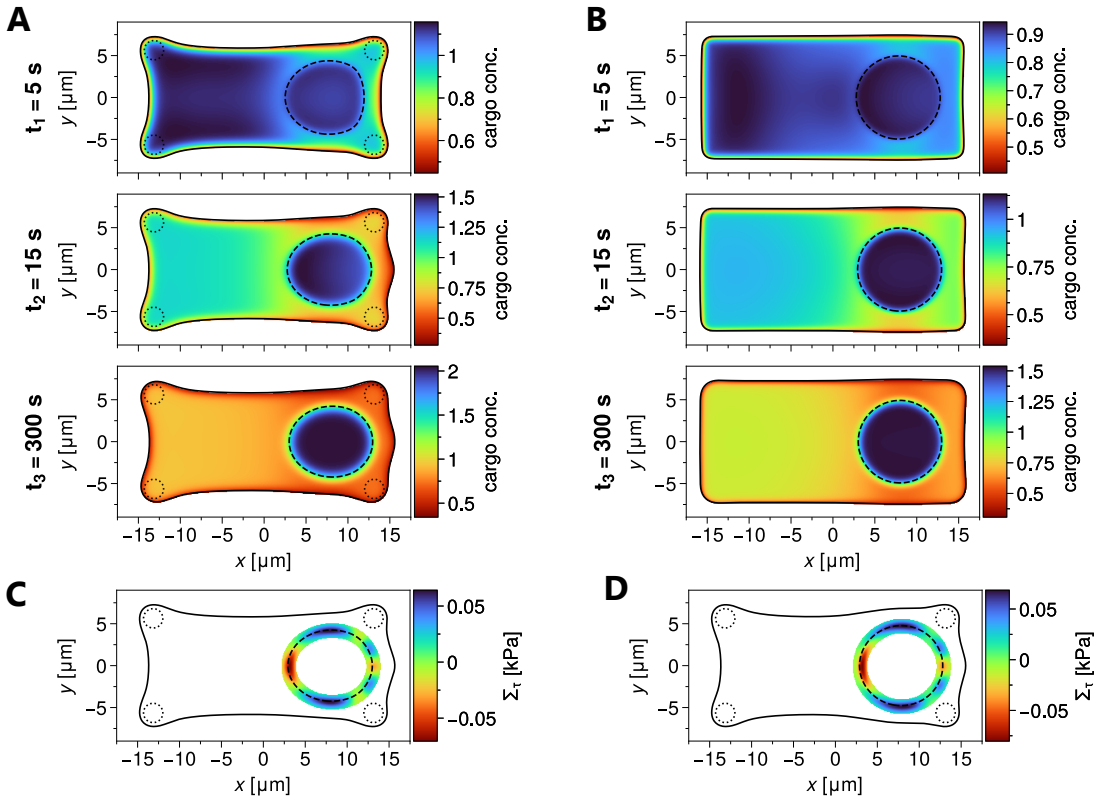

Figure B.7: Additional figures to simulations in Sect. 6.3.3 **A**-**B** Concentration maps for $\rho \geq 0.5$ and three different time points for a (**A**) contractile, adhered cell, which is pulled by a force $F_0 = 2.5\,\mathrm{nN}$ at $y = 0$ at the right edge. The nucleus has a stiffness $E_N/E_C = 2$ and is shifted by $\Delta x_N = 7.5\,\mu\mathrm{m}$. (**B**) a uniaxially stretched cell with a nucleus shifted as in (**A**) with stiffness $E_N/E_C = 10$. **C**-**D** Tension Σ_τ for $|\nabla\psi| > 0.1$ at the nuclear boundary for the corresponding panels above. Adhesion spots are marked by dotted lines, the cell boundary is indicated by the isocontour $\rho = 1/2$ (solid line) and the nuclear boundary by the isocontour $\psi = 1/2$ (dashed line). For further parameters for (**A/C**) see Fig. 6.4 and for (**B/D**) see Fig. 6.5. Other parameters as in in Appendix B.4.2 Table B.5.

B.4.2 Parameters for simulations

The table below lists the default values for additional parameters used for the simulations in Chapter 6, if not stated otherwise in the respective figure captions.

Table B.5: Default simulation parameters for Chapter 6

Description	Symbol	Value	Units	Ref.
number grid points	$N_x \times N_y$	512×256		
domain size	$L_x \times L_y$	50×25	$\mu m \times \mu m$	
time step	Δt	0.01	s	
diff. coeff. phase fields *	D_ϕ	0.125	$\mu m^2/s$	
friction coefficient	ξ	0.04	$nN \cdot s/\mu m^3$	
local suppression coeff.	$\gamma(\boldsymbol{x})$	$0.14 - 0.4$	$nN \cdot s/\mu m^3$	
Stiffness cytoplasm	E_C	1	kPa	
Poisson ratio nucleus and cytoplasm	$\nu_{C/N}$	0.5		
isotropic cell contractility	σ_0	0.4	kPa	
diff. coeff. adhesion PF	D_Y	0.025	$\mu m/s$	
spring stiffness density**	Y_0	16	$nN/\mu m^3$	
focal adhesion radius**	r_{adh}	1.15	μm	
diff. coeff. cargo in (cytoplasm)	D_c	10	$\mu m^2/s$	[272]
diff. coeff. cargo in (nucleus)	D_n	10	$\mu m^2/s$	[272]
diff. coeff. cargo-complex (cytoplasm)	D_{c_I}	2	$\mu m^2/s$	[272]
diff. coeff. cargo-complex (nucleus)	D_{n_I}	2	$\mu m^2/s$	[272]
passive permeability	P_p	0.075	$\mu m/s$	[9]
passive permeability with tension	P'_p	0.075	$\mu m/s$	[9]
active permeability	P_a	0.2	$\mu m/s$	[9]
active permeability with tension	P'_a	0.5	$\mu m/s$	[102]
cargo-importin association rates	$k^0_{1/2}$	0.5	s^{-1}	[9, 273]
cytoplasmic dissociation rate	k^-_1	0.05	s^{-1}	[9]
nuclear dissociation rate	k^-_2	5	s^{-1}	[9, 265]
critical stress for association	$\Sigma_{vM,cr}$	0.1	kPa	[261]
critical tension for NPC dilation	τ_{cr}	0		

* For the simulations of Fig. 6.4, $D_\phi = 0.25\,\mu m^2/s$.

B.5 Supplementary material to Chapter 7

This appendix contains supplementary information on Chapter 7, *i.e* supplementary figures and parameters used for the simulations presented in the main text.

B.5.1 Supplementary figures

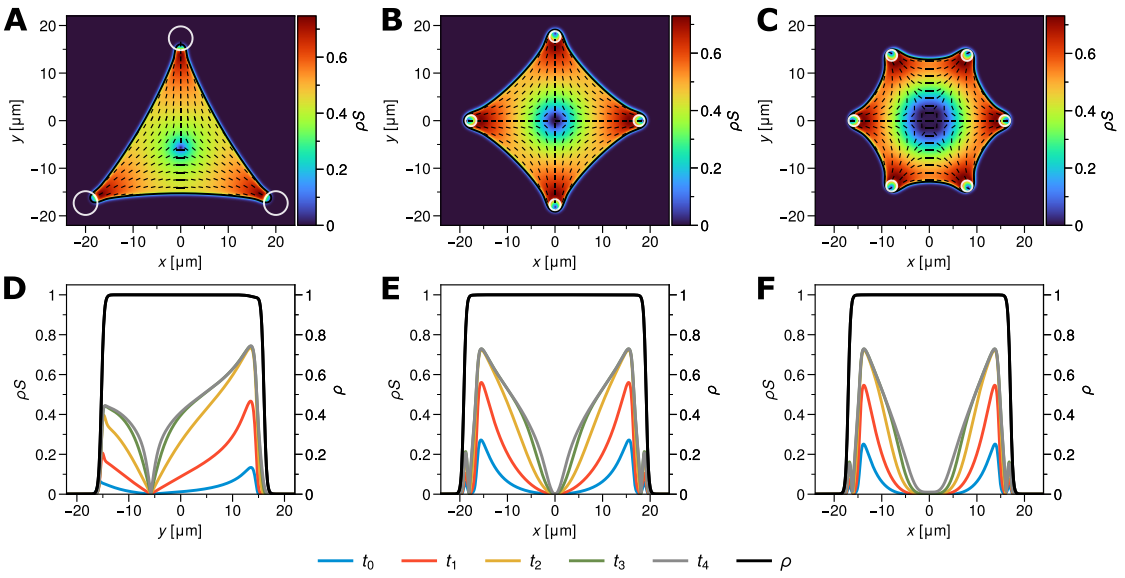

Figure B.8: Stress-induced alignment of the nematic liquid crystal without feedback on cell mechanics and with anchoring strength $W = 0.8$. Cells are allowed to adhere to adhesive patches (white circles) of radius r_{adh} and spring stiffness density Y in a (**A**) triangular, (**B**) square and (**C**) hexagonal arrangement. Upon an isotropic contractile stress $\sigma_0/E_C = 0.4$ the nematic liquid crystal experiences a phase transition from an isotropic ($S = 0$) to a locally aligned ($S > 0$) state. Shown are the order parameter field ρS (colour maps) the director field $\boldsymbol{n}$ (short black lines) for $\rho S > 0.01$. The $\rho = 1/2$-isocontours (black solid lines) indicate the cell boundary. The lower panels show ρS along (**D**) the symmetry line $x = 0$ for the triangular-shaped cell and along $y = 0$ for the (**E**) square - and (**F**) hexagonal-shaped cell for different time points $t_0 < ... < t_4$ (blue to grey). The black dashed line shows the phase field profile ρ. For simulation parameters see Appendix B.5 Table B.6.

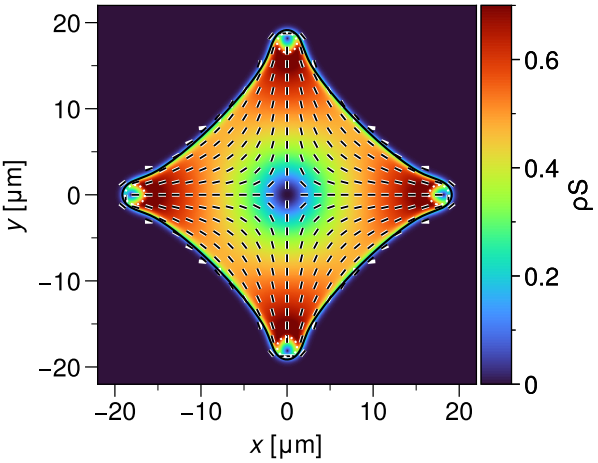

Figure B.9: A contractile cell is adhered to a square-shaped micropattern. No feedback of the forming stress fibres on cell mechanics is assumed. Shown is the degree of alignment ρS, the director field $\boldsymbol{n}$ (black lines) and the direction of principal stresses (white lines, below the director lines) for $\rho S > 0.01$. Director field and direction of local principal stress are the same within the cell. For simulation parameters see Table B.6.

B.5.2 Parameters for simulations

The table below lists the default values for additional parameters used for the simulations in Chapter 7, if not stated otherwise in the respective figure captions.

Table B.6: Default simulation parameters for Chapter 7

Description	Symbol	Value	Units	Ref.
grid points	$N \times N$	512×512		
domain length $L_x \times L_y$	50×50	$\mu m \times \mu m$		
time step*	Δt	0.001	s	
diffusion coeff. phase field (PF)*	D_ϕ	1.25	$\mu m/s$	
friction coefficient	ξ	0.004	$nN \cdot s/\mu m^3$	
local suppression coeff.	$\gamma(\boldsymbol{x})$	$0.014 - 0.04$	$nN \cdot s/\mu m^3$	
cell stiffness	E_C	1	kPa	
Addition to stress fibre stiffness	E_{SF}	10	kPa	[223]
Poisson ratio	ν_C	0.5		
isotropic cell contractility	σ_0	0.4	kPa	
Addition to stress fibre contractility	σ_{SF}	3.5	kPa	[284]
diffusion coeff. adhesion PF	D_Y	0.25	$\mu m/s$	
spring stiffness density**	Y_0	16	$nN/\mu m^3$	
focal adhesion radius**	r_{adh}	1.15	μm	
Nematic relaxation time scale*	τ_Q	0.1	s	
LC elastic constant	K	0.2	$\mu m^2/s$	[142]
Nematic first order term coeff.*	ϵ	0.1	s^{-1}	
Nematic second order term coeff.*	α	0.1	s^{-1}	
Nematic anchoring strength	W	0	$\mu m^2 s^{-1}$	

* With time sclae set to $\tau = 0.1$ s.
** For Fig. 7.3 A and D and Fig. B.9 A and D: $Y = 40 nN/\mu m^3$ and $r_{adh} = 2.5\,\mu m$.

C Numerical methods

In this chapter we briefly introduce the numerical methods used to solve the model equations in this thesis.

C.1 (Semi-implicit) pseudo-spectral method

Several model equations in this thesis are numerically solved using a pseudo-spectral method. These are the phase field equations (*cf.* for example Eq. (4.8) or Eq. (5.1)), the reaction-diffusion system of Chapter 6 (*cf.* Eqs. (6.5)-(6.8)) and the dynamic equation of the nematic order parameter $\boldsymbol{Q}$ in Chapter 7 (*cf.* Eq. (7.25)). We here briefly describe the implementation of an explicit version of the spectral method used in Chapter 4 and a semi-implicit scheme used in Chapters 5-7.

Pseud-spectral method

Consider as an example the phase field equation (*cf.* Eq. (4.8))

$$\frac{\partial \rho}{\partial t} = D\Delta\rho - \frac{\partial g(\rho)}{\partial \rho} + \sqrt{2Dg(\rho)}\kappa - \frac{1}{\xi}\left(\nabla \cdot \Sigma + \boldsymbol{F}\right) \cdot \nabla\rho, \tag{C.1}$$

which has to be solved in a domain Ω of size $L_x \times L_y$ with $N_x \times N_y$ grid points. We can split the equation into a linear part $\mathcal{L}[\rho]$ and a non-linear part $\mathcal{N}[\rho]$. $\mathcal{L}[\rho]$ always contains the derivative of highest order, *i.e.* the Laplacian term (first term of Eq. (C.1)), while we consider the rest to be part of $\mathcal{N}[\rho]$.

In the explicit spectral scheme, first the linear part

$$\frac{\partial \rho}{\partial t} = D\Delta\rho \tag{C.2}$$

is solved in Fourier space, which gives

$$\hat{\rho} = \exp\left(-k^2 D\Delta t\right) \tag{C.3}$$

with $k^2 = k_x^2 + k_y^2$ where the wave numbers are given by [147]

$$k_i = \begin{cases} \frac{2\pi}{L_i} m \quad for \quad 0 \leq m \leq \frac{N_i}{2} \\ \frac{2\pi}{L_i}(m - N_i) \quad for \quad \frac{N_i}{2} \leq m \leq N_i \end{cases} \tag{C.4}$$

with $i \in \{x, y\}$ and m the respective grid point coordinate.

The nonlinear part

$$\frac{\partial \rho}{\partial t} = \mathcal{N}[\rho] \tag{C.5}$$

is solved in real space by a finite difference method and Euler integration. This solution is then Fourier transformed [312] and multiplied with the Fourier space solution of the linear part, *i.e.*

$$\hat{\rho}^{n+1} = exp\left(-k^2 D\Delta t\right) FFT\{\rho^n + \Delta t \mathcal{N}[\rho]\} \tag{C.6}$$

where $\hat{\rho}^{n+1}$ is the full solution in Fourier space. FFT denotes the Fast Fourier transform [312] and the expression in its brackets is the real space solution of the nonlinear part. In the last step, one has to perform an inverse Fourier transform on Eq. (C.6) to obtain the full solution in real space, *i.e.*

$$\rho^{n+1} = FFT\{\hat{\rho}^{n+1}\}. \tag{C.7}$$

Semi-implicit pseudo-spectral method

We also used a semi-implicit spectral method described in Camley et al. [147] for better numerical stability. Here, we follow the description in Camley et al. [147]. To apply the semi-implicit method, Eq. (C.1) (which we now abbreviate as $\partial\rho/\partial t = D\Delta t\rho + \mathcal{N}[\rho]$) has to be discretized and written as

$$\rho^{n+1} - \Delta D\Delta t\rho^{n+1} = \rho^n - \Delta t\mathcal{N}[\rho^n], \tag{C.8}$$

where Δt is the time step, ρ^n is known from the current time point n and ρ^{n+1} is the solution in the next timestep which has to be calculated. Performing a Fourier transformation yields

$$\left(1 + k^2 D\Delta t\right)\hat{\rho}^{n+1} = FFT\{\rho^n - \Delta t\mathcal{N}[\rho^n]\}, \tag{C.9}$$

where $k^2 = k_x^2 + k_y^2$, $\hat{\rho}$ is the Fourier transformed solution we want to determine, and FFT denotes that the expression in brackets is transformed via a Fast Fourier Transfor-

mation [312]. Equation (C.9) can be solved for $\hat{\rho}^{n+1}$

$$\hat{\rho}^{n+1} = \left(1 + k^2 D\Delta t\right)^{-1} FFT\{\rho^n - \Delta t \mathcal{N}[\rho^n]\}, \tag{C.10}$$

which is the solution in Fourier space. To obtain the solution in real space, one has to take the inverse Fourier transform of Eq. (C.10), *i.e.*

$$\rho^{n+1} = FFT\{\hat{\rho}^{n+1}\}. \tag{C.11}$$

Solving the equations of the reaction-diffusion system

When solving the equations of the reaction-diffusion system Eqs. (6.5)-(6.8)), one has to pay attention to two aspects. Consider a concentration c in a phase field domain ϕ with

$$\frac{\partial \phi c}{\partial t} = \nabla \left[D\phi \nabla c\right] + \mathcal{N}[\phi c]. \tag{C.12}$$

In order to be able to perform the Fourier transformation without encountering convolutions, we can write Eq (C.12) as [147]

$$\frac{\partial \phi c}{\partial t} = \nabla \left[D\phi \nabla c\right] + \mathcal{N}[\phi c] = D\Delta \left(\phi c\right) - D\nabla \left[c \nabla \phi\right] + \mathcal{N}[\phi c] \tag{C.13}$$

for $D = const$, where the second term in the last step will join the nonlinear part $\mathcal{N}[\phi c]$, *i.e.* the remaining terms. Performing the semi-implicit spectral method from above, one solves for $(\phi c)^{n+1}$. c^{n+1}, which is needed for the permeability terms in Eqs. (6.5)-(6.8)) and the gradient of c in the second term of Eq. (C.13) can be extracted by [147, 266]

$$c = \begin{cases} \dfrac{\phi c}{\phi} & \text{if } \phi > 10^{-5} \\ c & \text{else.} \end{cases} \tag{C.14}$$

C.2 Iterative SOR matrix relaxation method

We here briefly describe the Successive overrealxation method (SOR method) used to solve the elastodynamic equation Eq. (4.11) [163]. This section follows the explanation in Press et al. [313].

The iterative SOR method is used to solve linear equations of the form

$$\boldsymbol{A}\boldsymbol{x} = \boldsymbol{b} \tag{C.15}$$

where $\boldsymbol{A}$ is a sparse $N_x \times N_y$ matrix, $\boldsymbol{x}$ is the desired solution and $\boldsymbol{b}$ is a vector with known entries. Assume, Eq. (C.15) can be written as

$$a_{j,l}x_{j+1,l} + b_{j,l}x_{j-1,l} + c_{j,l}x_{j,l+1} + d_{j,l}x_{j,l-1} + e_{j,l}x_{j,l} = f_{j,l} \tag{C.16}$$

which represents one row of the system of equations. The iterative procedure so solve the above equation is

$$x^*_{j,l} = \frac{1}{e_{j,l}} \left(f_{j,l} - a_{j,l}x_{j+1,l} - b_{j,l}x_{j-1,l} - c_{j,l}x_{j,l+1} - d_{j,l}x_{j,l-1} \right). \tag{C.17}$$

It is now possible to weight the residual $\xi_{j,l}$ (term in brackets in Eq. (C.17) times (-1)) in order to accelerate the convergence of the iterative method to the desired solution, *i.e.*

$$x^{new}_{j,l} = x^{old}_{j,l} - \omega \frac{\xi_{j,l}}{e_{j,l}}, \tag{C.18}$$

where ω is the weighting factor. The iteration terminates when the right-hand side of (C.18) reaches a termination condition, *i.e.* when it gets smaller than a threshold ϵ_{cr}. This is the Successive overrelaxation method (SOR) used in this thesis. For $\omega = 1$ one gets the Gauss-Seidel algorithm, which is used in Chapter 4 to solve the elastodynamic equations of the elastic phase field method. In other cases a weighting factor $\omega = 1.6$ is used.

C.3 Time and space discretization schemes

C.3.1 Crank-Nicolson time discretization

For the time discretization of the elastodynamic equations of our elastic phase field approach we use the second order accurate in time [313]. Consider a model function $u(\boldsymbol{x}, t)$, which may be one coordinate of the displacement field. The associated elastodynamic equation has the general form

$$\frac{\partial u}{\partial t} = f(u) \tag{C.19}$$

where $f(u)$ is a function which depends on $u(x,t)$ and possibly its derivatives. The Crank-Nicolson scheme is a semi-implicit one that reads

$$\frac{u^{n+1}-u^n}{\Delta t} = \frac{1}{2}\left[f(u^{n+1}) + f(u^n)\right], \tag{C.20}$$

where Δt is the time step size, u^{n+1} is the desired solution in the next time step $n+1$ and u^n is the current known solution ate time point n [313].

C.3.2 Isotropic finite differences

For the numerical calculation of the curvature

$$\kappa_\rho = -\nabla \cdot \frac{\nabla \rho}{|\nabla \rho|} \tag{C.21}$$

of the phase fields we use an isotropic finite difference scheme for the discretization of the derivatives to prevent potential artefacts of the regular discretization grid. The isotropic finite difference scheme for the gradient of a phase field $\rho(\boldsymbol{x})$ in 2D is

$$\frac{\partial \rho}{\partial x} = \frac{1}{12\Delta x}\left[4\left(\rho_{i+1,j} - \rho_{i-1,j}\right) + \rho_{i+1,j+1} - \rho_{i-1,j+1} + \rho_{i+1,j-1} - \rho_{i-1,j-1}\right] \tag{C.22}$$

$$\frac{\partial \rho}{\partial x} = \frac{1}{12\Delta y}\left[4\left(\rho_{i,j+1} - \rho_{i,j-1}\right) + \rho_{i+1,j+1} - \rho_{i+1,j-1} + \rho_{i-1,j+1} - \rho_{i-1,j-1}\right], \tag{C.23}$$

where Δx and Δy are the grid spacings in x- and y-direction [314]. Due to the use of the spectral method for solving the phase field equation, we always use $\Delta x = \Delta y$.

Bibliography

[1] Milo, R. and Phillips, R. *Cell biology by the numbers*. New York, NY ; Abingdon: Garland Science, Taylor & Francis Group, 2016, pp. xlii, 356. New York, NY ; Abingdon.

[2] Ingber, D. "Mechanobiology and diseases of mechanotransduction". *Annals of Medicine* 35.8 (2003). PMID: 14708967, pp. 564–577.

[3] Maniotis, A. J., Chen, C. S., and Ingber, D. E. "Demonstration of mechanical connections between integrins, cytoskeletal filaments, and nucleoplasm that stabalizes nuclear structure". *Proceedings of the National Academy of Sciences* 94.3 (1997), pp. 849–854.

[4] Crisp, M., Liu, Q., Roux, K., Rattner, J., Shanahan, C., Burke, B., Stahl, P. D., and Hodzic, D. "Coupling of the nucleus and cytoplasm: Role of the LINC complex ". *Journal of Cell Biology* 172.1 (2005), pp. 41–53.

[5] Lombardi, M. L., Jaalouk, D. E., Shanahan, C. M., Burke, B., Roux, K. J., and Lammerding, J. "The Interaction between Nesprins and Sun Proteins at the Nuclear Envelope Is Critical for Force Transmission between the Nucleus and Cytoskeleto". *Journal of Biological Chemistry* 286.30 (2011), pp. 26743–26753.

[6] Zimmerli, C. E., Allegretti, M., Rantos, V., et al. "Nuclear pores dilate and constrict in cellulo". *Science* 374.6573 (2021), eabd9776.

[7] Schuller, A. P., Wojtynek, M., Mankus, D., et al. "The cellular environment shapes the nuclear pore complex architecture". *Nature* 598.7882 (2021), pp. 667–671.

[8] Elosegui-Artola, A., Andreu, I., Beedle, A. E. M., et al. "Force Triggers YAP Nuclear Entry by Regulating Transport across Nuclear Pores". *Cell* 171.6 (2017), 1397–1410.e14.

[9] Andreu, I., Granero-Moya, I., Chahare, N. R., et al. "Mechanical force application to the nucleus regulates nucleocytoplasmic transport". *Nature Cell Biology* 24.6 (2022), pp. 896–905.

[10] Chojowski, R., Schwarz, U. S., and Ziebert, F. “Reversible elastic phase field approach and application to cell monolayers”. *European Physical Journal E* 43.10 (2020), p. 63.

[11] Pelham, R. J. and Wang, Y.-l. “Cell locomotion and focal adhesions are regulated by substrate flexibility”. *Proceedings of the National Academy of Sciences* 94.25 (1997), pp. 13661–13665.

[12] Tee, S.-Y., Fu, J., Chen, C. S., and Janmey, P. A. “Cell Shape and Substrate Rigidity Both Regulate Cell Stiffness”. *Biophysical Journal* 100.5 (2011), pp. L25–L27.

[13] Nisenholz, N., Rajendran, K., Dang, Q., Chen, H., Kemkemer, R., Krishnan, R., and Zemel, A. “Active mechanics and dynamics of cell spreading on elastic substrates”. en. *Soft Matter* 10.37 (2014), pp. 7234–7246.

[14] Charras, G. and Sahai, E. “Physical influences of the extracellular environment on cell migration”. *Nature Reviews Molecular Cell Biology* 15.12 (2014), pp. 813–824.

[15] Lo, C.-M., Wang, H.-B., Dembo, M., and Wang, Y.-l. “Cell Movement Is Guided by the Rigidity of the Substrate”. *Biophysical Journal* 79.1 (2000), pp. 144–152.

[16] Isenberg, B. C., DiMilla, P. A., Walker, M., Kim, S., and Wong, J. Y. “Vascular Smooth Muscle Cell Durotaxis Depends on Substrate Stiffness Gradient Strength”. *Biophysical Journal* 97.5 (2009), pp. 1313–1322.

[17] Sunyer, R., Conte, V., Escribano, J., et al. “Collective cell durotaxis emerges from long-range intercellular force transmission”. *Science* 353.6304 (2016), pp. 1157–1161.

[18] Solon, J., Levental, I., Sengupta, K., Georges, P. C., and Janmey, P. A. “Fibroblast Adaptation and Stiffness Matching to Soft Elastic Substrates”. *Biophysical Journal* 93.12 (2007), pp. 4453–4461.

[19] Schwarz, U. “Soft matters in cell adhesion: rigidity sensing on soft elastic substrates”. *Soft Matter* 3.3 (2007), pp. 263–266.

[20] McBeath, R., Pirone, D. M., Nelson, C. M., Bhadriraju, K., and Chen, C. S. “Cell Shape, Cytoskeletal Tension, and RhoA Regulate Stem Cell Lineage Commitment”. *Developmental Cell* 6.4 (2004), pp. 483–495.

[21] Engler, A. J., Sen, S., Sweeney, H. L., and Discher, D. E. “Matrix Elasticity Directs Stem Cell Lineage Specification”. *Cell* 126.4 (2006), pp. 677–689.

[22] Rianna, C., Radmacher, M., and Kumar, S. “Direct evidence that tumor cells soften when navigating confined spaces”. *Molecular Biology of the Cell* 31.16 (2020). PMID: 31995446, pp. 1726–1734.

[23] Guck, J., Schinkinger, S., Lincoln, B., et al. “Optical Deformability as an Inherent Cell Marker for Testing Malignant Transformation and Metastatic Competence”. *Biophysical Journal* 88.5 (2005), pp. 3689–3698.

[24] Heisenberg, C.-P. and Bellaïche, Y. “Forces in Tissue Morphogenesis and Patterning”. *Cell* 153.5 (2013), pp. 948–962.

[25] Kaliman, S., Hubert, M., Wollnik, C., et al. “Mechanical Regulation of Epithelial Tissue Homeostasis”. *Physical Review X* 11.3 (2021), p. 031029.

[26] Poujade, M., Grasland-Mongrain, E., Hertzog, A., Jouanneau, J., Chavrier, P., Ladoux, B., Buguin, A., and Silberzan, P. “Collective migration of an epithelial monolayer in response to a model wound”. *Proceedings of the National Academy of Sciences* 104.41 (2007), pp. 15988–15993.

[27] Vishwakarma, M., Di Russo, J., Probst, D., Schwarz, U. S., Das, T., and Spatz, J. P. “Mechanical interactions among followers determine the emergence of leaders in migrating epithelial cell collectives”. *Nature Communications* 9.1 (2018), p. 3469.

[28] Guillot, C. and Lecuit, T. “Mechanics of Epithelial Tissue Homeostasis and Morphogenesis”. *Science* 340.6137 (2013), pp. 1185–1189.

[29] Trepat, X. and Sahai, E. “Mesoscale physical principles of collective cell organization”. *Nature Physics* 14.7 (2018), pp. 671–682.

[30] Alberts, B., Johnson, A., Lewis, J., Morgan, D., Raff, M., Roberts, K., and Walter, P. *Molecular biology of the cell.* 6. ed. New York, NY [u.a.]: Garland Science, 2015.

[31] Svitkina, T. M. “Actin Cell Cortex: Structure and Molecular Organization”. *Trends in Cell Biology* 30.7 (2020), pp. 556–565.

[32] Fletcher, D. and Mullins, R. “Cell mechanics and the cytoskeleton”. *Nature* 463.7280 (2010), pp. 485–492.

[33] Pegoraro, A. F., Janmey, P., and Weitz, D. A. “Mechanical Properties of the Cytoskeleton and Cells”. *Cold Spring Harbor Perspectives in Biology* 9.11 (2017).

[34] Huber, F., Boire, A., López, M. P., and Koenderink, G. H. "Cytoskeletal crosstalk: when three different personalities team up". *Current Opinion in Cell Biology* 32 (2015), pp. 39–47.

[35] Iskratsch, T., Wolfenson, H., and Sheetz, M. P. "Appreciating force and shape — the rise of mechanotransduction in cell biology". *Nature Reviews Molecular Cell Biology* 15.12 (2014), pp. 825–833.

[36] Murrell, M., Oakes, P. W., Lenz, M., and Gardel, M. L. "Forcing cells into shape: the mechanics of actomyosin contractility". *Nature Reviews Molecular Cell Biology* 16.8 (2015), pp. 486–498.

[37] Howard, J. *Mechanics of Motor Proteins and the Cytoskeleton*. Sinauer, Sunderland, 2001.

[38] Smith, P. G., Deng, L., Fredberg, J. J., and Maksym, G. N. "Mechanical strain increases cell stiffness through cytoskeletal filament reorganization". *American Journal of Physiology-Lung Cellular and Molecular Physiology* 285.2 (2003). PMID: 12704020, pp. L456–L463.

[39] Deng, L., Trepat, X., Butler, J. P., Millet, E., Morgan, K. G., Weitz, D. A., and Fredberg, J. J. "Fast and slow dynamics of the cytoskeleton". *Nature Materials* 5.8 (2006), pp. 636–640.

[40] Stamenović, D., Rosenblatt, N., Montoya-Zavala, M., Matthews, B. D., Hu, S., Suki, B., Wang, N., and Ingber, D. E. "Rheological Behavior of Living Cells Is Timescale-Dependent". *Biophysical Journal* 93.8 (2007), pp. L39–L41.

[41] Trepat, X., Deng, L., An, S. S., Navajas, D., Tschumperlin, D. J., Gerthoffer, W. T., Butler, J. P., and Fredberg, J. J. "Universal physical responses to stretch in the living cell". *Nature* 447.7144 (2007), pp. 592–595.

[42] Étienne, J., Fouchard, J., Mitrossilis, D., Bufi, N., Durand-Smet, P., and Asnacios, A. "Cells as liquid motors: Mechanosensitivity emerges from collective dynamics of actomyosin cortex". *Proceedings of the National Academy of Sciences* 112.9 (2015), pp. 2740–2745.

[43] Stricker, J., Falzone, T., and Gardel, M. L. "Mechanics of the F-actin cytoskeleton". *Journal of Biomechanics* 43.1 (2010). Special Issue on Cell Mechanobiology, pp. 9–14.

[44] Lappalainen, P., Kotila, T., Jégou, A., and Romet-Lemonne, G. "Biochemical and mechanical regulation of actin dynamics". *Nature Reviews Molecular Cell Biology* 23.12 (2022), pp. 836–852.

[45] Herrmann, H., Bär, H., Kreplak, L., Strelkov, S. V., and Aebi, U. "Intermediate filaments: from cell architecture to nanomechanics". *Nature Reviews Molecular Cell Biology* 8.7 (2007), pp. 562–573.

[46] Lowery, J., Kuczmarski, E. R., Herrmann, H., and Goldman, R. D. "Intermediate Filaments Play a Pivotal Role in Regulating Cell Architecture and Function*". *Journal of Biological Chemistry* 290.28 (2015), pp. 17145–17153.

[47] Herrmann, H. and Aebi, U. "Intermediate Filaments: Structure and Assembly". *Cold Spring Harbor Perspectives in Biology* 8.11 (2016).

[48] Hawkins, T., Mirigian, M., Selcuk Yasar, M., and Ross, J. L. "Mechanics of microtubules". *Journal of Biomechanics* 43.1 (2010). Special Issue on Cell Mechanobiology, pp. 23–30.

[49] Brouhard, G. J. and Rice, L. M. "Microtubule dynamics: an interplay of biochemistry and mechanics". *Nature Reviews Molecular Cell Biology* 19.7 (2018), pp. 451–463.

[50] Logan, C. M. and Menko, A. S. "Microtubules: Evolving roles and critical cellular interactions". *Experimental Biology and Medicine* 244.15 (2019), pp. 1240–1254.

[51] Gudimchuk, N. B. and McIntosh, J. R. "Regulation of microtubule dynamics, mechanics and function through the growing tip". *Nature Reviews Molecular Cell Biology* 22.12 (2021). Special Issue on Cell Mechanobiology, pp. 777–795.

[52] Vignaud, T., Copos, C., Leterrier, C., et al. "Stress fibers are embedded in a contractile cortical network". *Nature Materials* 20.3 (2021), pp. 410–420.

[53] Pogoda, K., Byfield, F., Deptuła, P., et al. "Unique Role of Vimentin Networks in Compression Stiffening of Cells and Protection of Nuclei from Compressive Stress". *Nano Letters* 22.12 (2022), pp. 4725–4732.

[54] Vukušić, K., Buđa, R., Bosilj, A., Milas, A., Pavin, N., and Tolić, I. M. "Microtubule Sliding within the Bridging Fiber Pushes Kinetochore Fibers Apart to Segregate Chromosomes". *Developmental Cell* 43.1 (2017), 11–23.e6.

[55] Letort, G., Ennomani, H., Gressin, L., Théry, M., and Blanchoin, L. "Dynamic reorganization of the actin cytoskeleton [version 1; peer review: 2 approved]". *F1000Research* 4.940 (2015).

[56] Phillips, R., Kondev, J., Theriot, J., and Garcia, H. G. *Physical biology of the cell.* Second edition. Includes bibliographical references and index. London ; New York: Garland Science, Taylor & Francis Group, 2013.

[57] Ziebert, F., Löber, J., and Aranson, I. S. *Physical Models of Cell Motility.* Ed. by Aranson, I. S. 1st ed. 2016. Cham: Springer, 2016. Chap. Macroscopic Model of Substrate-Based Cell Motility.

[58] Pellegrin, S. and Mellor, H. "Actin stress fibres". *Journal of Cell Science* 120.20 (2007), pp. 3491–3499.

[59] Naumanen, P., Lappalainen, P., and Hotulainen, P. "Mechanisms of actin stress fibre assembly". *Journal of Microscopy* 231.3 (2008), pp. 446–454.

[60] Tojkander, S., Gateva, G., and Lappalainen, P. "Actin stress fibers – assembly, dynamics and biological roles". *Journal of Cell Science* 125.8 (2012), pp. 1855–1864.

[61] Kassianidou, E. and Kumar, S. "A biomechanical perspective on stress fiber structure and function". *Biochimica et Biophysica Acta (BBA) - Molecular Cell Research* 1853.11, Part B (2015). Mechanobiology, pp. 3065–3074.

[62] Livne, A. and Geiger, B. "The inner workings of stress fibers - from contractile machinery to focal adhesions and back". *Journal of Cell Science* 129.7 (2016), pp. 1293–1304.

[63] Burridge, K. and Guilluy, C. "Focal adhesions, stress fibers and mechanical tension". *Experimental Cell Research* 343.1 (2016), pp. 14–20.

[64] Lehtimäki, J. I., Rajakylä, E. K., Tojkander, S., and Lappalainen, P. "Generation of stress fibers through myosin-driven reorganization of the actin cortex". *eLife* 10 (2021). Ed. by Fässler, R., Akhmanova, A., Fässler, R., and Schnorrer, F., e60710.

[65] Khatau, S. B., Hale, C. M., Stewart-Hutchinson, P. J., Patel, M. S., Stewart, C. L., Searson, P. C., Hodzic, D., and Wirtz, D. "A perinuclear actin cap regulates nuclear shape". *Proceedings of the National Academy of Sciences* 106.45 (2009), pp. 19017–19022.

[66] Hotulainen, P. and Lappalainen, P. "Stress fibers are generated by two distinct actin assembly mechanisms in motile cells ". *Journal of Cell Biology* 173.3 (2006), pp. 383–394.

[67] Deguchi, S., Ohashi, T., and Sato, M. "Tensile properties of single stress fibers isolated from cultured vascular smooth muscle cells". *Journal of Biomechanics* 39.14 (2006), pp. 2603–2610.

[68] Bathe, M., Heussinger, C., Claessens, M. M., Bausch, A. R., and Frey, E. "Cytoskeletal Bundle Mechanics". *Biophysical Journal* 94.8 (2008), pp. 2955–2964.

[69] Balaban, N. Q., Schwarz, U. S., Riveline, D., et al. "Force and focal adhesion assembly: a close relationship studied using elastic micropatterned substrates". *Nature Cell Biology* 3.5 (2001), pp. 466–472.

[70] Chrzanowska-Wodnicka, M. and Burridge, K. "Rho-stimulated contractility drives the formation of stress fibers and focal adhesions". *Journal of Cell Biology* 133.6 (1996), pp. 1403–1415.

[71] Schwarz, U. S. and Safran, S. A. "Physics of adherent cells". *Reviews of Modern Physics* 85.3 (2013), pp. 1327–1381.

[72] Brangwynne, C. P., MacKintosh, F. C., Kumar, S., Geisse, N. A., Talbot, J., Mahadevan, L., Parker, K. K., Ingber, D. E., and Weitz, D. A. "Microtubules can bear enhanced compressive loads in living cells because of lateral reinforcement". *Journal of Cell Biology* 173.5 (2006), pp. 733–741.

[73] Mitchison, T. and Kirschner, M. "Dynamic instability of microtubule growth". *Nature* 312.5991 (1984), pp. 237–242.

[74] Ishikawa, H., Bischoff, R., and Holtzer, H. "Mitosis and intermediate-sized filaments in developing skeletal muscle". *Journal of Cell Biology* 38.3 (1968), pp. 538–555.

[75] Kalukula, Y., Stephens, A. D., Lammerding, J., and Gabriele, S. "Mechanics and functional consequences of nuclear deformations". *Nature Reviews Molecular Cell Biology* 23.9 (2022), pp. 583–602.

[76] Xi, W., Saw, T. B., Delacour, D., Lim, C. T., and Ladoux, B. "Material approaches to active tissue mechanics". *Nature Reviews Materials* 4.1 (2019), pp. 23–44.

[77] Kechagia, J. Z., Ivaska, J., and Roca-Cusachs, P. "Integrins as biomechanical sensors of the microenvironment". *Nature Reviews Molecular Cell Biology* 20.8 (2019), pp. 457–473.

[78] Ladoux, B., Mège, R.-M., and Trepat, X. "Front–Rear Polarization by Mechanical Cues: From Single Cells to Tissues". *Trends in Cell Biology* 26.6 (2016), pp. 420–433.

[79] Lammerding, J. *Mechanics of the Nucleus*. John Wiley & Sons, Ltd, 2011, pp. 783–807.

[80] Neumann, F. R. and Nurse, P. "Nuclear size control in fission yeast ". *Journal of Cell Biology* 179.4 (2007), pp. 593–600.

[81] Wu, Y., Pegoraro, A. F., Weitz, D. A., Janmey, P., and Sun, S. X. "The correlation between cell and nucleus size is explained by an eukaryotic cell growth model". *PLOS Computational Biology* 18.2 (2022), pp. 1–26.

[82] Guilak, F., Tedrow, J. R., and Burgkart, R. "Viscoelastic Properties of the Cell Nucleus". *Biochemical and Biophysical Research Communications* 269.3 (2000), pp. 781–786.

[83] Caille, N., Thoumine, O., Tardy, Y., and Meister, J.-J. "Contribution of the nucleus to the mechanical properties of endothelial cells". *Journal of Biomechanics* 35.2 (2002), pp. 177–187.

[84] Kirby, T. J. and Lammerding, J. "Emerging views of the nucleus as a cellular mechanosensor". *Nature Cell Biology* 20.4 (2018), pp. 373–381.

[85] Janota, C. S., Calero-Cuenca, F. J., and Gomes, E. R. "The role of the cell nucleus in mechanotransduction". *Current Opinion in Cell Biology* 63 (2020). Cell Signalling (2020), pp. 204–211.

[86] Dupont, S., Morsut, L., Aragona, M., et al. "Role of YAP/TAZ in mechanotransduction". *Nature* 474.7350 (2011), pp. 179–183.

[87] Halder, G., Dupont, S., and Piccolo, S. "Transduction of mechanical and cytoskeletal cues by YAP and TAZ". *Nature Reviews Molecular Cell Biology* 13.9 (2012), pp. 591–600.

[88] Hoogenboom, B. W., Hough, L. E., Lemke, E. A., Lim, R. Y. H., Onck, P. R., and Zilman, A. "Physics of the nuclear pore complex: Theory, modeling and experiment". *Physics Reports* 921 (2021), pp. 1–53.

[89] Swift, J., Ivanovska, I. L., Buxboim, A., et al. "Nuclear Lamin-A Scales with Tissue Stiffness and Enhances Matrix-Directed Differentiation". *Science* 341.6149 (2013), p. 1240104.

[90] Kim, D.-H., Li, B., Si, F., Phillip, J. M., Wirtz, D., and Sun, S. X. "Volume regulation and shape bifurcation in the cell nucleus". *Journal of Cell Science* 128.18 (2015), pp. 3375–3385.

[91] Kim, D.-H. and Wirtz, D. “Cytoskeletal tension induces the polarized architecture of the nucleus”. *Biomaterials* 48 (2015), pp. 161–172.

[92] Venturini, V., Pezzano, F., Castro, F. C., et al. “The nucleus measures shape changes for cellular proprioception to control dynamic cell behavior”. *Science* 370.6514 (2020), eaba2644.

[93] Lomakin, A. J., Cattin, C. J., Cuvelier, D., et al. “The nucleus acts as a ruler tailoring cell responses to spatial constraints”. *Science* 370.6514 (2020), eaba2894.

[94] Güttinger, S., Laurell, E., and Kutay, U. “Orchestrating nuclear envelope disassembly and reassembly during mitosis”. *Nature Reviews Molecular Cell Biology* 10.3 (2009), pp. 178–191.

[95] Wang, N., Tytell, J. D., and Ingber, D. E. “Mechanotransduction at a distance: mechanically coupling the extracellular matrix with the nucleus”. *Nature Reviews Molecular Cell Biology* 10.1 (2009), pp. 75–82.

[96] Davidson, P. M., Battistella, A., Déjardin, T., Betz, T., Plastino, J., Borghi, N., Cadot, B., and Sykes, C. “Nesprin-2 accumulates at the front of the nucleus during confined cell migration”. *EMBO reports* 21.7 (2020), e49910.

[97] Watson, J. D. and Crick, F. H. C. “Molecular Structure of Nucleic Acids: A Structure for Deoxyribose Nucleic Acid”. *Nature* 171.4356 (1953), pp. 737–738.

[98] Nava, M. M., Miroshnikova, Y. A., Biggs, L. C., et al. “Heterochromatin-Driven Nuclear Softening Protects the Genome against Mechanical Stress-Induced Damage”. *Cell* 181.4 (2020), 800–817.e22.

[99] Denais, C. M., Gilbert, R. M., Isermann, P., et al. “Nuclear envelope rupture and repair during cancer cell migration”. *Science* 352.6283 (2016), pp. 353–358.

[100] Raab, M., Gentili, M., Belly, H. de, et al. “ESCRT III repairs nuclear envelope ruptures during cell migration to limit DNA damage and cell death”. *Science* 352.6283 (2016), pp. 359–362.

[101] Shah, P., Hobson, C. M., Cheng, S., Colville, M. J., Paszek, M. J., Superfine, R., and Lammerding, J. “Nuclear Deformation Causes DNA Damage by Increasing Replication Stress”. *Current Biology* 31.4 (2021), 753–765.e6.

[102] Ribbeck, K. and Görlich, D. “Kinetic analysis of translocation through nuclear pore complexes”. *The EMBO Journal* 20.6 (2001), pp. 1320–1330.

[103] Yang, W., Gelles, J., and Musser, S. M. "Imaging of single-molecule translocation through nuclear pore complexes". *Proceedings of the National Academy of Sciences* 101.35 (2004), pp. 12887–12892.

[104] Rout, M. P. and Blobel, G. "Isolation of the yeast nuclear pore complex." *Journal of Cell Biology* 123.4 (1993), pp. 771–783.

[105] Reichelt, R., Holzenburg, A., Buhle E L, J., Jarnik, M., Engel, A., and Aebi, U. "Correlation between structure and mass distribution of the nuclear pore complex and of distinct pore complex components." *Journal of Cell Biology* 110.4 (1990), pp. 883–894.

[106] Gall, J. G. "Octagonal nuclear pores". *Journal of Cell Biology* 32.2 (1967), pp. 391–399.

[107] Löschberger, A., Linde, S. van de, Dabauvalle, M.-C., Rieger, B., Heilemann, M., Krohne, G., and Sauer, M. "Super-resolution imaging visualizes the eightfold symmetry of gp210 proteins around the nuclear pore complex and resolves the central channel with nanometer resolution". *Journal of Cell Science* 125.3 (2012), pp. 570–575.

[108] Chowdhury, R., Sau, A., and Musser, S. M. "Super-resolved 3D tracking of cargo transport through nuclear pore complexes". *Nature Cell Biology* 24.1 (2022), pp. 112–122.

[109] Hoelz, A., Glavy, J. S., and Beck, M. "Toward the atomic structure of the nuclear pore complex: when top down meets bottom up". *Nature Structural & Molecular Biology* 23.7 (2016), pp. 624–630.

[110] Mosalaganti, S., Obarska-Kosinska, A., Siggel, M., et al. "AI-based structure prediction empowers integrative structural analysis of human nuclear pores". *Science* 376.6598 (2022), eabm9506.

[111] Cautain, B., Hill, R., Pedro, N. de, and Link, W. "Components and regulation of nuclear transport processes". *The FEBS Journal* 282.3 (2015), pp. 445–462.

[112] Nachury, M. V. and Weis, K. "The direction of transport through the nuclear pore can be inverted". *Proceedings of the National Academy of Sciences* 96.17 (1999), pp. 9622–9627.

[113] Landau, L. D. and Lifschitz, E. M. *Elastizitätstheorie.* 7., unveränd. Aufl. Berlin: Akad.-Verl., 1991.

[114] Howell, P., Kozyreff, G., and Ockendon, J. R. *Applied solid mechanics*. Cambridge texts in applied mathematics. Cambridge [u.a.]: Cambridge Univ. Press, 2009.

[115] Sadd, M. H. *Elasticity - Theory, Applications, and Numerics*. Elsevier Butterworth-Heinemann, 2005. Burlington, MA.

[116] Sadd, M. H. *Continuum mechanics modeling of material behavior*. London, United Kingdom ; San Diego, CA, United States ; Cambridge, MA, United States ; Oxford, United Kingdom: Elsevier, Academic Press, 2019.

[117] Osher, S. and Sethian, J. A. "Fronts propagating with curvature-dependent speed: Algorithms based on Hamilton-Jacobi formulations". *Journal of Computational Physics* 79.1 (1988), pp. 12–49.

[118] Sussman, M., Smereka, P., and Osher, S. "A Level Set Approach for Computing Solutions to Incompressible Two-Phase Flow". *Journal of Computational Physics* 114.1 (1994), pp. 146–159.

[119] Wolgemuth, C. W. and Zajac, M. "The moving boundary node method: A level set-based, finite volume algorithm with applications to cell motility". *Journal of Computational Physics* 229.19 (2010), pp. 7287–7308.

[120] Yang, L., Effler, J. C., Kutscher, B. L., Sullivan, S. E., Robinson, D. N., and Iglesias, P. A. "Modeling cellular deformations using the level set formalism". *BMC Systems Biology* 2.1 (2008), p. 68.

[121] Osher, S. and Fedkiw, R. P. "Level Set Methods: An Overview and Some Recent Results". *Journal of Computational Physics* 169.2 (2001), pp. 463–502.

[122] Sethian, J. A. and Smereka, P. "LEVEL SET METHODS FOR FLUID INTERFACES". *Annual Review of Fluid Mechanics* 35.1 (2003), pp. 341–372.

[123] Ziebert, F. and Aranson, I. S. "Computational approaches to substrate-based cell motility". *npj Computational Materials* 2.1 (2016), p. 16019.

[124] Kobayashi, R. "Modeling and numerical simulations of dendritic crystal growth". *Physica D: Nonlinear Phenomena* 63.3 (1993), pp. 410–423.

[125] Karma, A. and Rappel, W.-J. "Quantitative phase-field modeling of dendritic growth in two and three dimensions". *Physical Review E* 57.4 (1998), pp. 4323–4349.

[126] Steinbach, I. "Phase-Field Model for Microstructure Evolution at the Mesoscopic Scale". *Annual Review of Materials Research* 43.1 (2013), pp. 89–107.

[127] Boettinger, W. J., Warren, J. A., Beckermann, C., and Karma, A. "Phase-Field Simulation of Solidification". *Annual Review of Materials Research* 32.1 (2002), pp. 163–194.

[128] Warren, J. A., Kobayashi, R., Lobkovsky, A. E., and Craig Carter, W. "Extending phase field models of solidification to polycrystalline materials". *Acta Materialia* 51.20 (2003), pp. 6035–6058.

[129] Laghmach, R., Candau, N., Chazeau, L., Munch, E., and Biben, T. "Phase field modelling of strain induced crystal growth in an elastic matrix". *The Journal of Chemical Physics* 142.24 (2015), p. 244905.

[130] Aranson, I. S., Kalatsky, V. A., and Vinokur, V. M. "Continuum Field Description of Crack Propagation". *Physical Review Letters* 85.1 (2000), pp. 118–121.

[131] Karma, A., Kessler, D. A., and Levine, H. "Phase-Field Model of Mode III Dynamic Fracture". *Physical Review Letters* 87.4 (2001), p. 045501.

[132] Spatschek, R., Müller-Gugenberger, C., Brener, E., and Nestler, B. "Phase field modeling of fracture and stress-induced phase transitions". *Physical Review E* 75.6 (2007), p. 066111.

[133] Henry, H. "Study of three-dimensional crack fronts under plane stress using a phase field model". *Europhysics Letters* 92.4 (2010), p. 46002.

[134] Kassner, K. and Misbah, C. "A phase-field approach for stress-induced instabilities". *Europhysics Letters* 46.2 (1999), p. 217.

[135] Kassner, K., Misbah, C., Müller, J., Kappey, J., and Kohlert, P. "Phase-field modeling of stress-induced instabilities". *Physical Review E* 63.3 (2001), p. 036117.

[136] Mokbel, D., Abels, H., and Aland, S. "A phase-field model for fluid–structure interaction". *Journal of Computational Physics* 372 (2018), pp. 823–840.

[137] Emmerich, H. "Advances of and by phase-field modelling in condensed-matter physics". *Advances in Physics* 57.1 (2008), pp. 1–87.

[138] Biben, T. and Misbah, C. "Tumbling of vesicles under shear flow within an advected-field approach". *Physical Review E* 67.3 (2003), p. 031908.

[139] Biben, T., Kassner, K., and Misbah, C. "Phase-field approach to three-dimensional vesicle dynamics". *Physical Review E* 72.4 (2005), p. 041921.

[140] John, K., Peyla, P., Kassner, K., Prost, J., and Misbah, C. "Nonlinear Study of Symmetry Breaking in Actin Gels: Implications for Cellular Motility". *Physical Review Letters* 100.6 (2008), p. 068101.

[141] Shao, D., Rappel, W.-J., and Levine, H. "Computational Model for Cell Morphodynamics". *Physical Review Letters* 105.10 (2010), p. 108104.

[142] Ziebert, F., Swaminathan, S., and Aranson, I. S. "Model for self-polarization and motility of keratocyte fragments". *Journal of The Royal Society Interface* 9.70 (2012), pp. 1084–1092.

[143] Ziebert, F. and Aranson, I. S. "Effects of Adhesion Dynamics and Substrate Compliance on the Shape and Motility of Crawling Cells". *PLOS ONE* 8.5 (2013), p. 64511.

[144] Marth, W., Praetorius, S., and Voigt, A. "A mechanism for cell motility by active polar gels". *Journal of The Royal Society Interface* 12.107 (2015), p. 20150161.

[145] Löber, J., Ziebert, F., and Aranson, I. S. "Modeling crawling cell movement on soft engineered substrates". *Soft Matter* 10.9 (2014), pp. 1365–1373.

[146] Moure, A. and Gomez, H. "Phase-field model of cellular migration: Three-dimensional simulations in fibrous networks". *Computer Methods in Applied Mechanics and Engineering* 320 (2017), pp. 162–197.

[147] Camley, B. A., Zhao, Y., Li, B., Levine, H., and Rappel, W.-J. "Crawling and turning in a minimal reaction-diffusion cell motility model: Coupling cell shape and biochemistry". *Physical Review E* 95.1 (2017), p. 012401.

[148] Moure, A. and Gomez, H. "Three-dimensional simulation of obstacle-mediated chemotaxis". *Biomechanics and Modeling in Mechanobiology* 17.5 (2018), pp. 1243–1268.

[149] Moure, A. and Gomez, H. "Phase-Field Modeling of Individual and Collective Cell Migration". *Archives of Computational Methods in Engineering* 28.2 (2021), pp. 311–344.

[150] Zadeh, P. and Camley, B. A. "Picking winners in cell-cell collisions: Wetting, speed, and contact". *Physical Review E* 106.5 (2022), p. 054413.

[151] Nonomura, M. "Study on Multicellular Systems Using a Phase Field Model". *PLOS ONE* 7.4 (2012), pp. 1–9.

[152] Löber, J., Ziebert, F., and Aranson, I. S. "Collisions of deformable cells lead to collective migration". *Scientific Reports* 5.1 (2015), p. 9172.

[153] Najem, S. and Grant, M. "Phase-field model for collective cell migration". *Physical Review E* 93.5 (2016), p. 052405.

[154] Mueller, R., Yeomans, J. M., and Doostmohammadi, A. "Emergence of Active Nematic Behavior in Monolayers of Isotropic Cells". *Physical Review Letters* 122.4 (2019), p. 048004.

[155] Wenzel, D. and Voigt, A. "Multiphase field models for collective cell migration". *Physical Review E* 104.5 (2021), p. 054410.

[156] Jain, H. P., Voigt, A., and Angheluta, L. "Robust statistical properties of T1 transitions in a multi-phase field model of cell monolayers". *Scientific Reports* 13.1 (2023), p. 10096.

[157] Monfared, S., Ravichandran, G., Andrade, J., and Doostmohammadi, A. "Mechanical basis and topological routes to cell elimination". *eLife* 12 (2023), e82435.

[158] Kuang, X., Guan, G., Tang, C., and Zhang, L. "MorphoSim: an efficient and scalable phase-field framework for accurately simulating multicellular morphologies". *npj Systems Biology and Applications* 9.1 (2023), p. 6.

[159] Zhang, G. and Yeomans, J. M. "Active Forces in Confluent Cell Monolayers". *Physical Review Letters* 130.3 (2023), p. 038202.

[160] Folch, R., Casademunt, J., Hernández-Machado, A., and Ramírez-Piscina, L. "Phase-field model for Hele-Shaw flows with arbitrary viscosity contrast. I. Theoretical approach". *Physical Review E* 60.2 (1999), pp. 1724–1733.

[161] Huisken, G. "Flow by mean curvature of convex surfaces into spheres". *Journal of Differential Geometry* 20.1 (1984), pp. 237–266.

[162] Jamet, D. and Misbah, C. "Thermodynamically consistent picture of the phase-field model of vesicles: Elimination of the surface tension". *Physical Review E* 78.4 (2008), p. 041903.

[163] Chojowski, R. *Phase field approach for elastic cell sheets.* Master thesis. Heidelberg University. 2019.

[164] Burnette, D. T., Manley, S., Sengupta, P., Sougrat, R., Davidson, M. W., Kachar, B., and Lippincott-Schwartz, J. "A role for actin arcs in the leading-edge advance of migrating cells". *Nature Cell Biology* 13.4 (2011), pp. 371–382.

[165] Ballestrem, C., Hinz, B., Imhof, B. A., and Wehrle-Haller, B. "Marching at the front and dragging behind: differential αVβ3-integrin turnover regulates focal adhesion behavior". *Journal of Cell Biology* 155.7 (2001), pp. 1319–1332.

[166] Salbreux, G., Charras, G., and Paluch, E. "Actin cortex mechanics and cellular morphogenesis". *Trends in Cell Biology* 22.10 (2012), pp. 536–545.

[167] Krndija, D., Marjou, F. E., Guirao, B., Richon, S., Leroy, O., Bellaiche, Y., Hannezo, E., and Vignjevic, D. M. "Active cell migration is critical for steady-state epithelial turnover in the gut". *Science* 365.6454 (2019), pp. 705–710.

[168] Jülicher, F., Grill, S. W., and Salbreux, G. "Hydrodynamic theory of active matter". en. *Reports on Progress in Physics* 81.7 (2018), p. 076601.

[169] Trepat, X., Wasserman, M. R., Angelini, T. E., Millet, E., Weitz, D. A., Butler, J. P., and Fredberg, J. J. "Physical forces during collective cell migration". *Nature Physics* 5.6 (2009), pp. 426–430.

[170] Petitjean, L., Reffay, M., Grasland-Mongrain, E., Poujade, M., Ladoux, B., Buguin, A., and Silberzan, P. "Velocity Fields in a Collectively Migrating Epithelium". *Biophysical Journal* 98.9 (2010), pp. 1790–1800.

[171] Trepat, X. and Fredberg, J. J. "Plithotaxis and emergent dynamics in collective cellular migration". *Trends Cell Biology* 21.11 (2011), pp. 638–646.

[172] Vincent, R., Bazellières, E., Pérez-González, C., Uroz, M., Serra-Picamal, X., and Trepat, X. "Active Tensile Modulus of an Epithelial Monolayer". *Physical Review Letters* 115.24 (2015), p. 248103.

[173] Harris, A. R., Peter, L., Bellis, J., Baum, B., Kabla, A. J., and Charras, G. T. "Characterizing the mechanics of cultured cell monolayers". *Proceedings of the National Academy of Sciences* 109.41 (2012), pp. 16449–16454.

[174] Khalilgharibi, N., Fouchard, J., Asadipour, N., et al. "Stress relaxation in epithelial monolayers is controlled by the actomyosin cortex". *Nature Physics* 15.8 (2019), pp. 839–847.

[175] Blanch-Mercader, C., Vincent, R., Bazellières, E., Serra-Picamal, X., Trepat, X., and Casademunt, J. "Effective viscosity and dynamics of spreading epithelia: a solvable model". *Soft Matter* 13.6 (2017), pp. 1235–1243.

[176] Serra-Picamal, X., Conte, V., Vincent, R., Anon, E., Tambe, D. T., Bazellieres, E., Butler, J. P., Fredberg, J. J., and Trepat, X. "Mechanical waves during tissue expansion". *Nature Physics* 8.8 (2012), pp. 628–634.

[177] Banerjee, S., Utuje, K. J. C., and Marchetti, M. C. "Propagating Stress Waves During Epithelial Expansion". *Physical Review Letters* 114.22 (2015), p. 228101.

[178] Blanch-Mercader, C. and Casademunt, J. "Hydrodynamic instabilities, waves and turbulence in spreading epithelia". *Soft Matter* 13.38 (2017), pp. 6913–6928.

[179] Alert, R., Blanch-Mercader, C., and Casademunt, J. "Active Fingering Instability in Tissue Spreading". *Physical Review Letters* 122.8 (2019), p. 088104.

[180] Tlili, S., Durande, M., Gay, C., Ladoux, B., Graner, F., and Delanoë-Ayari, H. "Migrating Epithelial Monolayer Flows Like a Maxwell Viscoelastic Liquid". *Physical Review Letters* 125.8 (2020), p. 088102.

[181] Kim, J. H., Serra-Picamal, X., Tambe, D. T., et al. "Propulsion and navigation within the advancing monolayer sheet". *Nature Materials* 12.9 (2013), pp. 856–863.

[182] Ravasio, A., Cheddadi, I., Chen, T., et al. "Gap geometry dictates epithelial closure efficiency". *Nature Communications* 6.1 (2015), p. 7683.

[183] Ajeti, V., Tabatabai, A. P., Fleszar, A. J., et al. "Wound healing coordinates actin architectures to regulate mechanical work". *Nature Physics* 15.7 (2019), pp. 696–705.

[184] Oakes, P. W., Wagner, E., Brand, C. A., Probst, D., Linke, M., Schwarz, U. S., Glotzer, M., and Gardel, M. L. "Optogenetic control of RhoA reveals zyxin-mediated elasticity of stress fibres". *Nature Communications* 8 (2017), p. 15817.

[185] Schiedung, R., Steinbach, I., and Varnik, F. "Multi-phase-field method for surface tension induced elasticity". *Physical Review B* 97.3 (2018), p. 035410.

[186] Lecuit, T., Lenne, P.-F., and Munro, E. "Force Generation, Transmission, and Integration during Cell and Tissue Morphogenesis". *Annual Review of Cell and Developmental Biology* 27.1 (2011), pp. 157–184.

[187] Ruprecht, V., Monzo, P., Ravasio, A., et al. "How cells respond to environmental cues – insights from bio-functionalized substrates". *Journal of Cell Science* 130.1 (2017), pp. 51–61.

[188] Schwarz, U. S. and Soiné, J. R. D. "Traction force microscopy on soft elastic substrates: A guide to recent computational advances". *Biochimica et Biophysica Acta (BBA) - Molecular Cell Research.* Mechanobiology 1853.11, Part B (2015), pp. 3095–3104.

[189] Roca-Cusachs, P., Conte, V., and Trepat, X. "Quantifying forces in cell biology". *Nature Cell Biology* 19.7 (2017), pp. 742–751.

[190] Edwards, C. M. and Chapman, S. J. "Biomechanical Modelling of Colorectal Crypt Budding and Fission". *Bulletin of Mathematical Biology* 69.6 (2007), pp. 1927–1942.

[191] Edwards, C. M. and Schwarz, U. S. "Force Localization in Contracting Cell Layers". *Physical Review Letters* 107.12 (2011), p. 128101.

[192] Banerjee, S. and Marchetti, M. C. "Contractile Stresses in Cohesive Cell Layers on Finite-Thickness Substrates". *Physical Review Letters* 109.10 (2012), p. 108101.

[193] Hanke, J., Probst, D., Zemel, A., Schwarz, U. S., and Köster, S. "Dynamics of force generation by spreading platelets". *Soft Matter* 14.31 (2018), pp. 6571–6581.

[194] Solowiej-Wedderburn, J. and Dunlop, C. M. "Sticking around: Cell adhesion patterning for energy minimization and substrate mechanosensing". *Biophysical Journal* 121.9 (2022), pp. 1777–1786.

[195] Bement, W. M., Forscher, P., and Mooseker, M. S. "A novel cytoskeletal structure involved in purse string wound closure and cell polarity maintenance." *Journal of Cell Biology* 121.3 (1993), pp. 565–578.

[196] Anon, E., Serra-Picamal, X., Hersen, P., Gauthier, N. C., Sheetz, M. P., Trepat, X., and Ladoux, B. "Cell crawling mediates collective cell migration to close undamaged epithelial gaps". *Proceedings of the National Academy of Sciences* 109.27 (2012), pp. 10891–10896.

[197] Klarlund, J. K. "Dual modes of motility at the leading edge of migrating epithelial cell sheets". *Proceedings of the National Academy of Sciences* 109.39 (2012), pp. 15799–15804.

[198] Cochet-Escartin, O., Ranft, J., Silberzan, P., and Marcq, P. "Border Forces and Friction Control Epithelial Closure Dynamics". *Biophysical Journal* 106.1 (2014), pp. 65–73.

[199] Nier, V., Deforet, M., Duclos, G., Yevick, H. G., Cochet-Escartin, O., Marcq, P., and Silberzan, P. "Tissue fusion over nonadhering surfaces". *Proceedings of the National Academy of Sciences* 112.31 (2015), pp. 9546–9551.

[200] Chen, C. S., Mrksich, M., Huang, S., Whitesides, G. M., and Ingber, D. E. "Geometric Control of Cell Life and Death". *Science* 276.5317 (1997), pp. 1425–1428.

[201] Théry, M., Pépin, A., Dressaire, E., Chen, Y., and Bornens, M. "Cell distribution of stress fibres in response to the geometry of the adhesive environment". *Cell Motility and the Cytoskeleton* 63.6 (2006), pp. 341–355.

[202] Lehnert, D., Wehrle-Haller, B., David, C., Weiland, U., Ballestrem, C., Imhof, B. A., and Bastmeyer, M. "Cell behaviour on micropatterned substrata: limits of extracellular matrix geometry for spreading and adhesion". *Journal of Cell Science* 117.1 (2004), pp. 41–52.

[203] Marth, W. and Voigt, A. "Signaling networks and cell motility: a computational approach using a phase field description". *Journal of Mathematical Biology* 69.1 (2014), p. 91.

[204] Palmieri, B., Bresler, Y., Wirtz, D., and Grant, M. "Multiple scale model for cell migration in monolayers: Elastic mismatch between cells enhances motility". *Scientific Reports* 5.1 (2015), p. 11745.

[205] Winkler, B., Aranson, I. S., and Ziebert, F. "Confinement and substrate topography control cell migration in a 3D computational model". *Communications Physics* 2.1 (2019), p. 82.

[206] Chojowski, R., Schwarz, U. S., and Ziebert, F. "The role of the nucleus for cell mechanics: an elastic phase field approach". *arXiv preprint arXiv:2309.12777* (2023).

[207] Chojowski, R., Schwarz, U. S., and Ziebert, F. *Phase field modelling of the mechanics of nucleated cells in confined spaces*. Contributed Talk at APS March Meeting 2023, Las Vegas (Nevada, USA). 2023.

[208] Thiam, H.-R., Vargas, P., Carpi, N., et al. "Perinuclear Arp2/3-driven actin polymerization enables nuclear deformation to facilitate cell migration through complex environments". *Nature Communications* 7.1 (2016), p. 10997.

[209] Fuhs, T., Wetzel, F., Fritsch, A. W., et al. "Rigid tumours contain soft cancer cells". *Nature Physics* (2022). Publisher: Nature Publishing Group, pp. 1–10.

[210] Wolf, K., Lindert, M. te, Krause, M., et al. "Physical limits of cell migration: Control by ECM space and nuclear deformation and tuning by proteolysis and traction force". *Journal of Cell Biology* 201.7 (2013), pp. 1069–1084.

[211] Harada, T., Swift, J., Irianto, J., et al. "Nuclear lamin stiffness is a barrier to 3D migration, but softness can limit survival". *Journal of Cell Biology* 204.5 (2014), pp. 669–682.

[212] Kristal-Muscal, R., Dvir, L., and Weihs, D. “Metastatic cancer cells tenaciously indent impenetrable, soft substrates”. *New Journal of Physics* 15.3 (2013), p. 035022.

[213] Camley, B. A., Zhang, Y., Zhao, Y., Li, B., Ben-Jacob, E., Levine, H., and Rappel, W.-J. “Polarity mechanisms such as contact inhibition of locomotion regulate persistent rotational motion of mammalian cells on micropatterns”. *Proceedings of the National Academy of Sciences* 111.41 (2014), pp. 14770–14775.

[214] Moure, A. and Gomez, H. “Dual role of the nucleus in cell migration on planar substrates”. *Biomechanics and Modeling in Mechanobiology* 19.5 (2020), pp. 1491–1508.

[215] Abramowitz, M. and Stegun, I. A. *Handbook of mathematical functions. with formulas, graphs, and mathematical tables.* 9. Dover pr. Dover books on advanced mathematics. New York: Dover Publ., 1972.

[216] Zamir, E. and Geiger, B. “Molecular complexity and dynamics of cell-matrix adhesions”. *Journal of Cell Science* 114.20 (2001), pp. 3583–3590.

[217] Andersen, T., Wörthmüller, D., Probst, D., Wang, I., Moreau, P., Fitzpatrick, V., Boudou, T., Schwarz, U. S., and Balland, M. “Cell size and actin architecture determine force generation in optogenetically activated cells”. *Biophysical Journal* 122.4 (2023), pp. 684–696.

[218] Link, R., Weißenbruch, K., Tanaka, M., Bastmeyer, M., and Schwarz, U. S. “Cell Shape and Forces in Elastic and Structured Environments: From Single Cells to Organoids”. *Advanced Functional Materials* n/a.n/a (2023), p. 2302145.

[219] Bischofs, I. B., Klein, F., Lehnert, D., Bastmeyer, M., and Schwarz, U. S. “Filamentous Network Mechanics and Active Contractility Determine Cell and Tissue Shape”. *Biophysical Journal* 95.7 (2008), pp. 3488–3496.

[220] Jana, A., Tran, A., Gill, A., Kiepas, A., Kapania, R. K., Konstantopoulos, K., and Nain, A. S. “Sculpting Rupture-Free Nuclear Shapes in Fibrous Environments”. *Advanced Science* 9.25 (2022), p. 2203011.

[221] Ronan, W., Deshpande, V. S., McMeeking, R. M., and McGarry, J. P. “Cellular contractility and substrate elasticity: a numerical investigation of the actin cytoskeleton and cell adhesion”. *Biomechanics and Modeling in Mechanobiology* 13.2 (2014), pp. 417–435.

[222] Hofmann, U. G., Rotsch, C., Parak, W. J., and Radmacher, M. "Investigating the Cytoskeleton of Chicken Cardiocytes with the Atomic Force Microscope". *Journal of Structural Biology* 119.2 (1997), pp. 84–91.

[223] Lu, L., Oswald, S. J., Ngu, H., and Yin, F. C.-P. "Mechanical Properties of Actin Stress Fibers in Living Cells". *Biophysical Journal* 95.12 (2008), pp. 6060–6071.

[224] Yoneda, M. "Tension At The Surface of Sea-Urchin Egg: A Critical Examination Of Cole's Experiment". *Journal of Experimental Biology* 41.4 (1964), pp. 893–906.

[225] Thoumine, O. and Ott, A. "Time scale dependent viscoelastic and contractile regimes in fibroblasts probed by microplate manipulation". *Journal of Cell Science* 110.17 (1997), pp. 2109–2116.

[226] Ofek, G., Wiltz, D. C., and Athanasiou, K. A. "Contribution of the Cytoskeleton to the Compressive Properties and Recovery Behavior of Single Cells". *Biophysical Journal* 97.7 (2009), pp. 1873–1882.

[227] Mitrossilis, D., Fouchard, J., Guiroy, A., Desprat, N., Rodriguez, N., Fabry, B., and Asnacios, A. "Single-cell response to stiffness exhibits muscle-like behavior". *Proceedings of the National Academy of Sciences* 106.43 (2009), pp. 18243–18248.

[228] Fischer-Friedrich, E., Toyoda, Y., Cattin, C. J., Müller, D. J., Hyman, A. A., and Jülicher, F. "Rheology of the Active Cell Cortex in Mitosis". *Biophysical Journal* 111.3 (2016), pp. 589–600.

[229] Evans, E. and Yeung, A. "Apparent viscosity and cortical tension of blood granulocytes determined by micropipet aspiration". *Biophysical Journal* 56.1 (1989), pp. 151–160.

[230] Chesla, S. E., Selvaraj, P., and Zhu, C. "Measuring Two-Dimensional Receptor-Ligand Binding Kinetics by Micropipette". *Biophysical Journal* 75.3 (1998), pp. 1553–1572.

[231] Evans, E., Leung, A., Heinrich, V., and Zhu, C. "Mechanical switching and coupling between two dissociation pathways in a P-selectin adhesion bond". *Proceedings of the National Academy of Sciences* 101.31 (2004), pp. 11281–11286.

[232] Herant, M., Heinrich, V., and Dembo, M. "Mechanics of neutrophil phagocytosis: behavior of the cortical tension". *Journal of Cell Science* 118.9 (2005), pp. 1789–1797.

[233] Tinevez, J.-Y., Schulze, U., Salbreux, G., Roensch, J., Joanny, J.-F., and Paluch, E. "Role of cortical tension in bleb growth". *Proceedings of the National Academy of Sciences* 106.44 (2009), pp. 18581–18586.

[234] Luo, T., Mohan, K., Iglesias, P. A., and Robinson, D. N. "Molecular mechanisms of cellular mechanosensing". *Nature Materials* 12.11 (2013), pp. 1064–1071.

[235] Desprat, N., Guiroy, A., and Asnacios, A. "Microplates-based rheometer for a single living cell". *Rev. Sci. Instrum.* 77.5 (2006), p. 055111.

[236] Mokbel, M., Hosseini, K., Aland, S., and Fischer-Friedrich, E. "The Poisson Ratio of the Cellular Actin Cortex Is Frequency Dependent". 118.8 (2020), pp. 1968–1976.

[237] Liu, Y.-J., Le Berre, M., Lautenschlaeger, F., Maiuri, P., Callan-Jones, A., Heuzé, M., Takaki, T., Voituriez, R., and Piel, M. "Confinement and Low Adhesion Induce Fast Amoeboid Migration of Slow Mesenchymal Cells". *Cell* 160.4 (2015), pp. 659–672.

[238] Johnson, K. L. *Contact Mechanics*. Cambridge [u.a.]: Cambridge University Press, 1985.

[239] Hertz, H. "Ueber die Berührung fester elastischer Körper." *Journal für die reine und angewandte Mathematik* 92 (1882), pp. 156–171.

[240] Hoeprich, M. R. and Zantopulos, H. "Line Contact Ddeformation: A Cylinder Between Two Flat Plates". *Journal of Lubrification Technology* 103.1 (1981), pp. 21–25.

[241] Hochmuth, R. M. "Micropipette aspiration of living cells". *Journal of Biomechanics* 33.1 (2000), pp. 15–22.

[242] Drury, J. L. and Dembo, M. "Hydrodynamics of Micropipette Aspiration". *Biophysical Journal* 76.1 (1999), pp. 110–128.

[243] Theret, D. P., Levesque, M. J., Sato, M., Nerem, R. M., and Wheeler, L. T. "The Application of a Homogeneous Half-Space Model in the Analysis of Endothelial Cell Micropipette Measurements". *Journal of Biomechanical Engineering* 110.3 (1988), pp. 190–199.

[244] McGregor, A. L., Hsia, C.-R., and Lammerding, J. "Squish and squeeze—the nucleus as a physical barrier during migration in confined environments". *Current Opinion in Cell Biology* 40 (2016). Cell nucleus, pp. 32–40.

[245] Estabrook, I. D., Thiam, H. R., Piel, M., and Hawkins, R. J. "Calculation of the force field required for nucleus deformation during cell migration through constrictions". *PLOS Computational Biology* 17.5 (2021), pp. 1–26.

[246] Thomas, D. G., Yenepalli, A., Denais, C. M., et al. "Non-muscle myosin IIB is critical for nuclear translocation during 3D invasion". *Journal of Cell Biology* 210.4 (2015), pp. 583–594.

[247] Keys, J., Cheung, B. C., Wu, M., and Lammerding, J. "Rear cortex contraction aids in nuclear transit during confined migration by increasing pressure in the cell posterior". *bioRxiv* (2022).

[248] Stoeberl, S., Flommersfeld, J., Kreft, M., Benoit, M., Broedersz, C., and Raedler, J. O. "Nuclear deformation and dynamics of migrating cells in 3D confinement reveal adaptation of pulling and pushing forces". *bioRxiv* (2023).

[249] Gonthier, A. R., Botvinick, E. L., Grosberg, A., and Mohraz, A. "Effect of Porous Substrate Topographies on Cell Dynamics: A Computational Study". *ACS Biomater. Sci. Eng.* 9.10 (2023), pp. 5666–5678.

[250] Kim, S., Amini, R., and Campàs, O. "A nuclear jamming transition in vertebrate organogenesis". *bioRxiv* (2022).

[251] Jacobson, E. C., Perry, J. K., Long, D. S., Olins, A. L., Olins, D. E., Wright, B. E., Vickers, M. H., and O'Sullivan, J. M. "Migration through a small pore disrupts inactive chromatin organization in neutrophil-like cells". *BMC Biology* 16.1 (2018), p. 142.

[252] Bley, C. J., Nie, S., Mobbs, G. W., et al. "Architecture of the cytoplasmic face of the nuclear pore". *Science* 376.6598 (2022), eabm9129.

[253] Zhu, X., Huang, G., Zeng, C., et al. "Structure of the cytoplasmic ring of the Xenopus laevis nuclear pore complex". *Science* 376.6598 (2022), eabl8280.

[254] Petrovic, S., Samanta, D., Perriches, T., et al. "Architecture of the linker-scaffold in the nuclear pore". *Science* 376.6598 (2022), eabm9798.

[255] Fontana, P., Dong, Y., Pi, X., Tong, A. B., Hecksel, C. W., Wang, L., Fu, T.-M., Bustamante, C., and Wu, H. "Structure of cytoplasmic ring of nuclear pore complex by integrative cryo-EM and AlphaFold". *Science* 376.6598 (2022), eabm9326.

[256] Andreu, I., Granero-Moya, I., Garcia-Manyes, S., and Roca-Cusachs, P. "Understanding the role of mechanics in nucleocytoplasmic transport". *APL Bioengineering* 6.2 (2022), p. 020901.

[257] Fay, N. and Panté, N. “Nuclear entry of DNA viruses”. *Frontiers in Microbiology* 6 (2015).

[258] Zila, V., Margiotta, E., Turoňová, B., et al. “Cone-shaped HIV-1 capsids are transported through intact nuclear pores”. *Cell* 184.4 (2021), 1032–1046.e18.

[259] Pocaterra, A., Romani, P., and Dupont, S. “YAP/TAZ functions and their regulation at a glance”. *Journal of Cell Science* 133.2 (2020). jcs230425.

[260] Sudol, M., Chen, H. I., Bougeret, C., Einbond, A., and Bork, P. “Characterization of a novel protein-binding module — the WW domain”. *FEBS Letters* 369.1 (1995), pp. 67–71.

[261] Elosegui-Artola, A., Oria, R., Chen, Y., Kosmalska, A., Pérez-González, C., Castro, N., Zhu, C., Trepat, X., and Roca-Cusachs, P. “Mechanical regulation of a molecular clutch defines force transmission and transduction in response to matrix rigidity”. *Nature Cell Biology* 18.5 (2016), pp. 540–548.

[262] Li, Y., Zhong, Z., Xu, C., Wu, X., Li, J., Tao, W., Wang, J., Du, Y., and Zhang, S. “3D micropattern force triggers YAP nuclear entry by transport across nuclear pores and modulates stem cells paracrine”. *National Science Review* 10.8 (2023), nwad165.

[263] Koushki, N., Ghagre, A., Srivastava, L. K., Molter, C., and Ehrlicher, A. J. “Nuclear compression regulates YAP spatiotemporal fluctuations in living cells”. *Proceedings of the National Academy of Sciences* 120.28 (2023), e2301285120.

[264] Kim, S. and Elbaum, M. “A Simple Kinetic Model with Explicit Predictions for Nuclear Transport”. *Biophysical Journal* 105.3 (2013), pp. 565–569.

[265] Görlich, D., Seewald, M. J., and Ribbeck, K. “Characterization of Ran-driven cargo transport and the RanGTPase system by kinetic measurements and computer simulation”. *The EMBO Journal* 22.5 (2003), pp. 1088–1100.

[266] Kockelkoren, J., Levine, H., and Rappel, W.-J. “Computational approach for modeling intra- and extracellular dynamics”. *Physical Review E* 68.3 (2003), p. 037702.

[267] Li, X., Lowengrub, J., Rätz, A., and Voigt, A. “Solving PDEs in complex geomtries: a diffuse domain approach”. *Communications in mathematical sciences* 7.1 (2009), pp. 81–107.

[268] Driscoll, T. P., Cosgrove, B. D., Heo, S.-J., Shurden, Z. E., and Mauck, R. L. “Cytoskeletal to Nuclear Strain Transfer Regulates YAP Signaling in Mesenchymal Stem Cells”. *Biophysical Journal* 108.12 (2015), pp. 2783–2793.

[269] MacLellan, A. G. and Born, M. “A statistical-mechanical theory of surface tension”. *Proceedings of the Royal Society of London. Series A. Mathematical and Physical Sciences* 213.1113 (1952), pp. 274–284.

[270] McLellan, A. G. “The stress tensor, surface tension and viscosity”. *Proceedings of the Royal Society of London. Series A. Mathematical and Physical Sciences* 217.1128 (1953), pp. 92–96.

[271] Lacoste, D., Menon, G. I., Bazant, M. Z., and Joanny, J. F. “Electrostatic and electrokinetic contributions to the elastic moduli of a driven membrane”. *The European Physical Journal E* 28.3 (2009), pp. 243–264.

[272] Baum, M., Erdel, F., Wachsmuth, M., and Rippe, K. “Retrieving the intracellular topology from multi-scale protein mobility mapping in living cells”. *Nature Communications* 5.1 (2014), p. 4494.

[273] Catimel, B., Teh, T., Fontes, M. R., Jennings, I. G., Jans, D. A., Howlett, G. J., Nice, E. C., and Kobe, B. “Biophysical Characterization of Interactions Involving Importin-α during Nuclear Import”. *Journal of Biological Chemistry* 276.36 (2001), pp. 34189–34198.

[274] Riddick, G. and Macara, I. G. “A systems analysis of importin-α–β mediated nuclear protein import”. *Journal of Cell Biology* 168.7 (2005), pp. 1027–1038.

[275] Paine, P. L., Moore, L. C., and Horowitz, S. B. “Nuclear envelope permeability”. *Nature* 254.5496 (1975), pp. 109–114.

[276] Kassianidou, E., Probst, D., Jäger, J., Lee, S., Roguet, A.-L., Schwarz, U. S., and Kumar, S. “Extracellular Matrix Geometry and Initial Adhesive Position Determine Stress Fiber Network Organization during Cell Spreading”. *Cell Reports* 27.6 (2019), pp. 1897–1909.

[277] Raz-Ben Aroush, D. and Wagner, H. D. “Shear-Stress Profile along a Cell Focal Adhesion”. *Advanced Materials* 18 (2006), pp. 1537–1540.

[278] Scheiwe, A. C., Frank, S. C., Autenrieth, T. J., Bastmeyer, M., and Wegener, M. “Subcellular stretch-induced cytoskeletal response of single fibroblasts within 3D designer scaffolds”. *Biomaterials* 44 (2015), pp. 186–194.

[279] Heussinger, C., Bathe, M., and Frey, E. “Statistical Mechanics of Semiflexible Bundles of Wormlike Polymer Chains”. *Physical Review Letters* 99.4 (2007), p. 048101.

[280] Ni, H., Ni, Q., Papoian, G. A., Trache, A., and Jiang, Y. "Myosin and α-actinin regulation of stress fiber contractility under tensile stress". *Scientific Reports* 13.1 (2023), p. 8662.

[281] Bernal, R., Van Hemelryck, M., Gurchenkov, B., and Cuvelier, D. "Actin Stress Fibers Response and Adaptation under Stretch". *International Journal of Molecular Sciences* 23.9 (2022).

[282] Besser, A. and Schwarz, U. S. "Coupling biochemistry and mechanics in cell adhesion: a model for inhomogeneous stress fiber contraction". *New Journal of Physics* 9.11 (2007), pp. 425–425.

[283] Kumar, S., Maxwell, I. Z., Heisterkamp, A., Polte, T. R., Lele, T. P., Salanga, M., Mazur, E., and Ingber, D. E. "Viscoelastic Retraction of Single Living Stress Fibers and Its Impact on Cell Shape, Cytoskeletal Organization, and Extracellular Matrix Mechanics". *Biophysical Journal* 90.10 (2006), pp. 3762–3773.

[284] Deshpande, V. S., McMeeking, R. M., and Evans, A. G. "A bio-chemo-mechanical model for cell contractility". *Proceedings of the National Academy of Sciences* 103.38 (2006), pp. 14015–14020.

[285] Deshpande, V. S., McMeeking, R. M., and Evans, A. G. "A model for the contractility of the cytoskeleton including the effects of stress-fibre formation and dissociation". *Proceedings of the Royal Society A: Mathematical, Physical and Engineering Sciences* 463.2079 (2007), pp. 787–815.

[286] Deshpande, V. S., Mrksich, M., McMeeking, R. M., and Evans, A. G. "A bio-mechanical model for coupling cell contractility with focal adhesion formation". *Journal of the Mechanics and Physics of Solids* 56.4 (2008), pp. 1484–1510.

[287] Chandran, P. L., Wolf, C. B., and Mofrad, M. R. K. "Band-like Stress Fiber Propagation in a Continuum and Implications for Myosin Contractile Stresses". *Cellular and Molecular Bioengineering* 2.1 (2009), pp. 13–27.

[288] Farsad, M. and Vernerey, F. J. "An XFEM-based numerical strategy to model mechanical interactions between biological cells and a deformable substrate". *International Journal for Numerical Methods in Engineering* 92.3 (2012), pp. 238–267.

[289] Kaunas, R. and Hsu, H.-J. "A kinematic model of stretch-induced stress fiber turnover and reorientation". *Journal of Theoretical Biology* 257.2 (2009), pp. 320–330.

[290] Schakenraad, K., Ernst, J., Pomp, W., Danen, E. H. J., Merks, R. M. H., Schmidt, T., and Giomi, L. “Mechanical interplay between cell shape and actin cytoskeleton organization”. *Soft Matter* 16.27 (2020), pp. 6328–6343.

[291] Viamontes, J. and Tang, J. X. “Continuous isotropic-nematic liquid crystalline transition of F-actin solutions”. *Physical Review E* 67.4 (2003), p. 040701.

[292] Viamontes, J., Narayanan, S., Sandy, A. R., and Tang, J. X. “Orientational order parameter of the nematic liquid crystalline phase of *F*-actin”. *Physical Review E* 73.6 (2006), p. 061901.

[293] Viamontes, J., Oakes, P. W., and Tang, J. X. “Isotropic to Nematic Liquid Crystalline Phase Transition of *F*-Actin Varies from Continuous to First Order”. *Physical Review Letters* 97.11 (2006), p. 118103.

[294] de Gennes, P.-G. and Prost, J. *The physics of liquid crystals*. 2. ed. International series of monographs on physics. Includes bibliographical references and index. Oxford [u.a.]: Clarendon Press, 1993.

[295] Stephen, M. J. and Straley, J. P. “Physics of liquid crystals”. *Reviews of Modern Physics* 46.4 (1974), pp. 617–704.

[296] Andrienko, D. “Introduction to liquid crystals”. *Journal of Molecular Liquids* 267 (2018). Special Issue Dedicated to the Memory of Professor Y. Reznikov, pp. 520–541.

[297] Chaikin, P. M. and Lubensky, T. C. *Principles of condensed matter physics*. 1. paperback ed. (with corr.), 3. pr. Includes bibliographical references and index. Cambridge [u.a.]: Cambridge Univ. Press, 2006.

[298] Kleman, M. and Lavrentovich, O. D. *Soft Matter Physics. An Introduction*. eng. New York, Berlin, Heidelberg: Springer, 2003.

[299] Selinger, J. V. “Interpretation of saddle-splay and the Oseen-Frank free energy in liquid crystals”. *Liquid Crystals Reviews* 6.2 (2018), pp. 129–142.

[300] Longa, L., Monselesan, D., and Trebin, H.-R. “An extension of the Landau-Ginzburg-de Gennes theory for liquid crystals”. *Liquid Crystals* 2.6 (1987), pp. 769–796.

[301] Tang, X. and Selinger, J. V. “Orientation of topological defects in 2D nematic liquid crystals”. *Soft Matter* 13.32 (2017), 5481–5490".

[302] Nobili, M. and Durand, G. “Disorientation-induced disordering at a nematic-liquid-crystal–solid interface”. *Physical Review A* 46.10 (1992), R6174–R6177.

[303] Iyer, G., Xu, X., and Zarnescu, A. D. "Dynamic cubic instability in a 2D Q-tensor model for liquid crystals". *Mathematical Models and Methods in Applied Sciences* 25.8 (2015), pp. 1477–1517.

[304] Doostmohammadi, A., Ignés-Mullol, J., Yeomans, J. M., and Sagués, F. "Active nematics". *Nature Communications* 9.1 (2018), p. 3246.

[305] Giomi, L. and DeSimone, A. "Spontaneous Division and Motility in Active Nematic Droplets". *Physical Review Letters* 112.14 (2014), p. 147802.

[306] Broedersz, C. P. and MacKintosh, F. C. "Modeling semiflexible polymer networks". *Reviews of Modern Physics* 86.3 (2014), pp. 995–1036.

[307] Morse, D. C. "Viscoelasticity of Concentrated Isotropic Solutions of Semiflexible Polymers. 1. Model and Stress Tensor". *Macromolecules* 31.20 (1998), pp. 7030–7043.

[308] Tharmann, R., Claessens, M. M. A. E., and Bausch, A. R. "Viscoelasticity of Isotropically Cross-Linked Actin Networks". *Physical Review Letters* 98.8 (2007), p. 088103.

[309] Großmann, R., Aranson, I. S., and Peruani, F. "A particle-field approach bridges phase separation and collective motion in active matter". *Nature Communications* 11.1 (2020), p. 5365.

[310] Hansbo, P., Larson, M. G., and Larsson, K. "Cut Finite Element Methods for Linear Elasticity Problems". *Geometrically Unfitted Finite Element Methods and Applications*. Ed. by Bordas, S. P. A., Burman, E., Larson, M. G., and Olshanskii, M. A. Cham: Springer International Publishing, 2017, pp. 25–63.

[311] Beaucourt, J. "Modélisation numérique de problèmes hydrodynamiques aux frontières libres". PhD Thesis. Université Joseph-Fourier - Grenoble I, 2005.

[312] Frigo, M. and Johnson, S. G. "The design and implementation of FFTW3". *Proceedings of the IEEE* 93.2 (2005), pp. 216–231.

[313] Press, W. H., Teukolsky, S. A., Vetterling, W. T., and Flannery, B. P. *Numerical recipes. the art of scientific computing*. 3. ed. Cambridge [u.a.]: Cambridge Univ. Press, 2007.

[314] Kumar, A. "Isotropic finite-differences". *Journal of Computational Physics* 201.1 (2004), pp. 109–118.

List of Publications

The manuscripts listed below have been prepared, submitted or published during the course of this thesis. The respective chapters based on these manuscripts are indicated in the right column.

1	Robert Chojowski, Ulrich S. Schwarz, and Falko Ziebert **Reversible elastic phase field approach and application to cell monolayers** *The European Physical Journal E* 43.10 (2020), p.63	Chapter 4
2	Robert Chojowski, Ulrich S. Schwarz, and Falko Ziebert **The role of the nucleus for cell mechanics: an elastic phase field approach** *Submitted to Soft Matter* (2023)	Chapter 5
3	Robert Chojowski, Falko Ziebert, and Ulrich S. Schwarz **Modelling the spatiotemporal dynamics of nucleocytoplasmic transport in mechanically strained cells** *In preparation* (2023)	Chapter 6

Danksagungen

An dieser Stelle möchte ich mich herzlich bei allen Personen bedanken, die zum Gelingen dieser Arbeit durch ihren Rat und ihre Unterstützung beigetragen haben.

Zuallererst gilt mein besonderer Dank meinem Doktorvater Ulrich Schwarz, der es mir ermöglicht hat diese Arbeit zu erstellen, mir mit seiner fachlichen Kompetenz zur Seite stand und immer ein offenes Ohr für meine Ideen hatte. Dank ihm habe ich immer wieder neue Themen und Blickwinkel in der Physik kennengelernt. Darüber hinaus danke ich ihm dafür, dass ich durch seine Unterstützung meine Projekte auf verschiedensten wissenschaftlichen Tagungen präsentieren konnte und die es mir erlaubten meine Kompetenzen in der wissenschaftlichen Kommunikation zu erweitern. Hier möchte ich besonders die Reise zur APS Tagung nach Las Vegas (meinem ersten Aufenthalt in den USA) hervorheben, die ohne ihn so nicht möglich gewesen wäre.

Tristan Bereau danke ich für sein Interesse an meiner Arbeit und für seine Bereitschaft diese als Zweitgutachter zu bewerten. Auch die kurzweiligen Gespräche mit ihm waren mir immer eine Freude.

Ich bedanke mich auch bei Christine Selhuber-Unkel und Selim Jochim dafür, dass sie sich bereiterklärt haben, Teil meines Disputationskomitees zu sein.

Falko Ziebert danke ich sehr für die Zweitbetreuung dieser Arbeit. Seine Unterstützung und sein Rat waren immer eine große Hilfe. Auch er hat sich immer Zeit für meine Fragen genommen und stand immer mit einer neuen Idee bereit.

Besonders danken möchte ich auch der gesamten AG Schwarz in deren freundschaftlichen Atmosphäre diese Arbeit entstanden ist. Auch eine Covid-Pandemie und Lockdowns haben unserem Austausch keinen Abbruch getan. Dieser Dank gilt Allen deren Weg sie in die AG Schwarz geführt hat und die ich während meiner Zeit in dieser Arbeitsgruppe kennenlernen durfte. Bei meinen Bürokollegen Felix Frey, Justin Grewe, Dennis Wörthmüller und Santiago Gomez Melo möchte ich mich für die tollen Diskussionen über alle möglichen Themen, für die tolle Büroatmosphäre und für die unterhaltsamen Kaffeepausen bedanken. Oliver Drozdowski möchte ich besonders für das gemeinsame und unvergessliche Abenteuer in den USA danken.

Mein Dank gilt auch all jenen, die bereit waren meine Doktorarbeit Korrektur zu lesen, und viele hilfreiche Verbesserungsvorschläge hatten. Hierfür möchte ich besonders Falko Ziebert, Clara Coursier und Susanne Chojowski danken.

Ein großer Dank geht auch an Sonja Bartsch, Melanie Steiert, Anja Kamp und Besma Klinger-Araifa, die mich immer wieder durch das Formulardickicht geleitet haben.

Dem Excellenzcluster STRUCTURES möchte ich für die finanzielle Unterstützung und das fachliche Umfeld danken.

Mein ganz besonderer Dank gilt meiner Familie, die mich durch diese Zeit begleitet und unterstützt hat. Meinen Eltern Izabela und Henryk, meiner Schwester Susanne, meiner Freundin Clara, ihren Eltern Dominique und Philippe und ihren Geschwistern Diane, Gwladys, Hadrien und Matthieu möchte ich aus ganzem Herzen für ihre bedingungslose Unterstützung, für ihre ermutigenden Worte und für ihren Glauben an mich danken. Unendlich dankbar bin ich meiner Liebe Clara, die unermüdlich an meiner Seite steht. *Kocham cię!*